ISQI, Faculty of Physics

Adam Mickiewicz University Poznań

Szymon Mieszczak

Spin waves in magnonic systems: localization and propagation

PhD thesis

Supervisor: dr hab. Jarosław W. Kłos, prof. UAM

September 2022

Declaration

Declaration of the author of this dissertation:

I hereby declare that except where specific reference is made to the work of others, the contents of this dissertation are original and have not been submitted in whole or in part for consideration for any other degree or qualification in this, or any other university. This dissertation is my own work and all the contents of the dissertation have been obtained by legal means.

Szymon Mieszczak, 19.03.22
Mgr Szymon Mieszczak

Declaration of the thesis Supervisor:

This dissertation is ready to be reviewed.

John Kłos, 19.03.22
dr hab. Jarosław W. Kłos, prof. UAM

Acknowledgements

I was very fortunate that during my studies I could meet so many great people.

In the beginning, I want to express gratitude to my supervisor Prof. UAM Jarosław Kłos, for his tireless help and guidance over all these years. Thank You for allowing me to conduct my studies and that You decided to invest so much of your time into me. Also, I want to thank Prof. Maciej Krawczyk for sharing his optimism and great ideas that always boost my research. I could always rely on your advice. Heartfelt thanks to my talented colleagues from the Department of Physics of Nanostructures: Dr. Piotr Graczyk, Dr. Paweł Gruszecki, Prof. UAM Sławomir Mamica, Prof. UAM Andriy Serebryannikov, Krzysztof Szulc, Dr. Justyna Rychły, Dr. Vishal Vashistha, and Dr. Mateusz Zelent. You made the lab a truly vibrant space.

I want to thank my collaborators, Prof. Raanan Tobey, Dr. Chia-Lin Chang, Dr. Oksana Busel, Prof. Andriy N. Kuchko, and all co-authors of the publications. It was an honor to work with You.

During my studies, I had opportunities to visit labs around Europe, and I would like to thank the hosts and amazing teams with that I could work together.

I spent one month in Kyiv under the supervision of Prof. Oksana Gorobets from Igor Sikorsky Kyiv Polytechnic Institute. I appreciate the knowledge transfer about analytical tools in magnetism. I want to thank also Dr. Oksana Busel for taking care of me and showing me what means the phrase *fortes fortuna adiuvat*.

I visited for one month Prof. Bartel Van Waeyenberge, Dr. Jonathan Leliaert, and Dr. Jeroen Mulkers at Ghent University. This internship was an important step in my understanding of micromagnetic simulations.

At the end of my studies, I had the pleasure to spend six months in Lausanne and working with Prof. Dirk Grundler, Andrea Mucchietto, and Dr. Mingran Xu. It was a stimulating time. I really appreciate that You included me in your tight agenda. Also, I want to thank the rest team members, Axel Deen, Huixin Guo, Mohammad Hamdi, Shreyas Joglekar, and Yuko Kagata. You all made my stay a very memorable time.

I can proudly announce that in my research, I used solely Open Source tools. I want to thank all people behind the projects: Linux, Python (with all its amazing libraries), Inkscape, Blender, LibreOffice, and Łukasz Hryniuk for being a lighthouse in this world.

Last but not least, I want to thank my family for their great support.

That was a pleasant adventure.

Abstract

Magnonics is a field of research and technology which uses magnetic nanostructures to control the *propagation and localization* of magnetic excitations, called spin waves. This control is realized by tailoring the geometry of nanostructure and modifying the internal landscape of the magnetic field, or by coupling the spin waves to external biases. The steering of localization and propagation is essential for information transmission. The interplay between wave localization and propagation determines the speed and direction of the wave signal, and even then whether the signal will be transmitted at all. The information, however, is encoded not only in the amplitude of the waves but also in their phase. The controlling of phase is essential for the implementation of wave phenomena and performing the information processing within the paradigm of so-called wave computing. Spin waves are very interesting candidates for the realization of the *wave computing in nanoscale* due to: the complexity of the dispersion relation, the possibility of interacting with other kinds of waves (e.g., elastic waves), and the tunability by on-demand applied external biases (magnetic field, voltage, and temperature). On one side, all these features are very handy if one wants to achieve specific behavior, there are many options to play with. However, from another angle, spin waves are sometimes hard to enslave and intensive studies on how to manipulate them are necessary.

The objective of my thesis is theoretical studies on spin waves in typical *magnonic systems* in the form of planar nanostructures, like waveguides, magnonic crystals, and quasicrystals. In my research, I worked on the coherent spin wave guiding in magnonic waveguides and on the spin wave localization in patterned layers in the presence of defects and interfaces. I was also interested in the steering of spin waves by non-magnetic signals. The *thesis contains four publications* covering these topics. The papers are ordered by the date of publication. In the first publication, I discussed the relation between the spatial distribution of spin waves in magnonic crystals and the coupling with surface acoustic waves. We found that the change of the direction of the external magnetic field modifies the amplitude of the *spin waves pumped by acoustic waves*. The effect is attributed to the *modification of the anisotropy of magnetoelastic interaction in magnonic crystal*. In the next work, I presented the studies on the *spin wave propagation in curved waveguides*. The method of coherent transmission

of the spin wave signal through the bent is proposed in the work. We used the *lens of graded refractive index* to coherently refract the spin waves at the bent of the waveguide. The later publication focuses on the *spin wave localization at the interface between two magnonic crystals*. We formulated the condition of existence magnonic interface state using the topological concept: *Zak phase*. In the last paper included in the thesis, I discussed the *impact of disorder in magnonic quasicrystal on the spin wave localization*. We introduced the *localization measure, based on Shannon information entropy*, which evaluates the spatial (non)uniformity of the modes. We performed the numerical simulations for different levels of disorder, related to the presence of so-called *phasonic defects*, and then observed the enhancement of localization with increasing levels of disorder.

Streszczenie

Magnonika to dziedzina wiedzy, która wykorzystuje struktury w nanoskali do kontrolowania *propagacji i lokalizacji fal spinowych*. Może się to odbywać poprzez kształtowanie geometrii nanostruktury lub modyfikację jej wewnętrznego pola magnetycznego. Kontrola propagacji i lokalizacji jest kluczowa z punktu widzenia przesyłania informacji. Determinują one prędkość oraz kierunek propagacji, a nawet to czy propagacja w ogóle następuje. W przypadku ruchu falowego, informacja jest zakodowana nie tylko w amplitudzie, ale także w fazie fali. W szczególności, to właśnie faza jest bardzo istotna dla *obliczeń analogowych z wykorzystaniem fal*. Fale spinowe są tutaj ciekawym kandydatem do takich obliczeń, gdyż złożoność ich relacji dyspersyjnej, możliwość oddziaływania fal spinowych z innymi wzbudzeniami, takimi jak fale elastyczne, czy kontrola poprzez zewnętrzne parametry, takie jak pole magnetyczne, pole elektryczne, temperatura, stwarza duże możliwości do projektowania układów. Tak duża elastyczność ma także swoje minusy, gdyż czasem zależność od wielu parametrów jest trudna do kontroli. Rozeznanie tych procesów wymaga intensywnych badań podstawowych.

Celem mojej pracy doktorskiej są teoretyczne badania fal spinowych w *układach magnonicznych*, takich jak falowody, kryształy i kwazikryształy. Rozważałem propagację fal spinowych, lokalizację na defektach, czy interfejsach, a także to, jaki ma ona wpływ na oddziaływania magnetoelastyczne. *Dysertacja zawiera cztery artykuły naukowe*, które są uporządkowane w kolejności ich publikacji. Pierwsza praca dotyczy związku pomiędzy przestrzennym rozkładem fal spinowych oraz sprzężeniem z powierzchniowymi falami akustycznymi. W pracy pokazaliśmy, że kierunek zewnętrznego pola magnetycznego zmienia amplitudę *wzbudzanej magnetoelastycznie fali spinowej*. Wynika to ze *zmiany anizotropii oddziaływań magnetoelastycznych w krysztale magnonicznym*. W następnej pracy rozważałem *przesyłanie fal spinowych przez zakrzywiony falowód*. W celu zachowania koherentności sygnału, umieściliśmy na zagięciu falowodu *element o zmiennym współczynniku załamania dla fal spinowych*, który ugina czoło fali zgodnie z geometrią falowodu. Następna praca dotyczy *lokalizacji fal spinowych na interfejsie pomiędzy dwoma kryształami magnonicznymi*. W pracy zostały sformułowane warunki na powstanie stanów interfejsowych, wykorzystujące pojęcie tzw. *fazy Zaka*. W ostatniej pracy dołączonej do rozprawy,

poruszona jest tematyka *nieporządku w kwazikryształach magnonicznych oraz wynikająca z tego lokalizacja*. Wprowadziliśmy miarę lokalizacji opartą na *entropii informacyjnej Shannona*, która określa niejednorodność rozkład amplitudy modu. Wykonane zostały obliczenia dla różnych poziomów nieporządku, wprowadzonego jako *defekty fazonowe*. Pokazaliśmy jak nieporządek wpływa na wzrost lokalizacji fal spinowych.

Table of contents

Chapter 1

Preface

The concept of spin waves is dated to 1930 when Felix Bloch found that low-energy excitations in ferromagnets are delocalised[15]. He used the coupling in a spin system, called exchange interaction, that was derived by Werner Heisenberg[44]. The phenomenological, i.e., quasi-classical theory of spin waves as small perturbations around the equilibrium state, which actually is used nowadays, was introduced in 1935 by Lev Landau and Evgeny Lifshitz[73]. It is remarkable that key concepts after almost 100 years are still valid and are able to explain more and more phenomena, even for atomistic spin dynamics[27]. What is more, this field still attracts the attention of scientists and is a valid topic to write a dissertation. Indeed, following 'Scopus', the scientific database indexing research, the amount of papers with the keyword: *spin waves* and *magnonics* increases exponentially till now. To be fair, this can be said also about other topics, like electromagnetic waves[96], spintronics[46], plasmonics[36], etc. since science expands tremendously. Nevertheless, it seems that magnonics[67, 77, 62], a field of research that exploit spin wave dynamics in nano-structures, is well established in the scientific community. Despite the fact that fundamental theory is there for almost 100 years[10], the studies on spin waves in nanostructures face intriguing fundamental problems and inspire novel applications[9, 19]. One of the reasons is that the magnetic moments interact with themselves in a nontrivial way. Due to the interplay between the exchange, dipolar interactions, and Dzyaloshinskii-Moriya, magnetization can form complex textures, even in relatively simple systems like plane film. Therefore, developing new materials with re-configurable magnetic textures which support the complex magnetization dynamic[134] is a vital part of the field of magnonics[108]. Not to mention, that development in fabrication techniques[29] opens many ways to achieve desired properties, by shaping the geometry at nanometer sizes. The magnonic subsystem can also interact with others, like the phononic subsystem, which is an area of intensive research as well[129]. We should not also forget about the fact that the Landau-Lifshitz equation [72] is intrinsically

nonlinear[56]. So, the field was established almost a century ago, but the real potential is exploited recently when scientists' dreams can come true in laboratories with state-of-the-art technologies[9, 19].

The driving force behind the progress in magnonics is the belief that current technology, i.e. Complementary Metal Oxide Semiconductor (CMOS) technology[1], needs to be substituted by some alternative, offering breakthroughs in terms of speed and efficiency. The progress in the semiconductor industry is made now with increasing struggle and we are inevitably approaching physical limits in terms of reducing the size of a single transistor, and its density. This limitation is described by Moore's law[83], which refers to the empirical rule that the number of transistors on a microchip doubles every two years. At the moment, current technology, that already revolutionized our world most likely will not bring us another breakthrough[88]. Much research is centered around some specific kinds of excitations and quasiparticles, which could substitute the transport of electrons out there. And all of them have unique properties. Among them, one can distinguish the use of the spin degree of freedom for representing and transmitting information in the form of collective excitation, spin waves. Magnonics, at first glance, seems to be a very interesting candidate, because spin waves carry low energies, and they are operating with high frequency[25, 85, 21]. However, it should be stated clearly that this concept is dramatically different, in the sense that spin wave is a wave phenomenon and thus making a circuit would require different philosophy in design, that so well established semiconductor industry operating with billion dollar budgets and business plans for next decade would not be willing to support it. As I think that the paradigm of CMOS as a central concept remains true for my generation, I believe also that we can observe some spectacular achievements in a nontrivial application, that could be integrated with existing technology and used in some applications. Maybe we are still waiting for discovery. Unconventional computing[126, 91] or quantum magnonics[135] just to mention few examples, are starting to be explored.

In my thesis, I focused on the essential properties related to *propagation and localization of spin waves*. In other words, the publications included in the dissertation are concentrated on the fundamental research in the field of magnonics, though the gained knowledge can be potentially used in the application. I investigated the *building blocks of magnonics*[77], namely *magnonic waveguides*, and *magnonic crystals*. The first object is an indispensable part of any circuit since the signal must flow between elements performing operations. As a 'passive' element in the system, ideally, it should not disturb the properties of the signal. In the case of wave phenomena, information can be encoded into the phase and amplitude, so keeping them not perturbed is essential. Magnonic crystals are artificially ordered materials, where magnetic properties are periodic and in the case of quasicrystals have non-periodic

long-range order in one- two-, or three- dimensions. They can be used as an 'active' part of the circuit, that process the spin wave signal.

The complexity of the spin wave dynamics in partially confined systems: planes and wires, is manifested by the interplay between the *propagation and localization*. The relation between these two competitive features determines how the information encoded in spin waves is transmitted and distributed.

The term wave localization refers to the situation when waves are spatially nonuniform and one can distinguish the area of concentration. Controlling the localization of coherent waves is essential for wave computing[126]. In the dissertation, I look at this property from different angles, i.e., by considering different systems, and mechanisms that eventually lead to localization. The diversity of the magnonic systems and the mechanisms of localization for spin waves is particularly large.

The term wave propagation is related to the transmission of waves, their velocity, and their direction. One can directly extract a lot of information about the propagation of spin waves from the dispersion relation, which links the wavevector and the frequency of the wave. The dispersion relation for spin waves can have many unusual features which are responsible for: field-controlled anisotropy of propagation, non-reciprocal propagation, and long waves at high frequencies. Also, in the case of crystals and quasicrystals, the dispersion relation reveals the position of the band gaps -– the range of the frequency at which propagation through the crystal is forbidden, and only localized modes can be observed if some conditions are fulfilled.

I think that magnonics is a promising field and spin wave computing in the nanoscale can provide some solutions for the bottlenecks in the development of conventional electronics[88]. I hope that magnonics initiates a new direction in information processing in a similar way[20] as the discovery of semiconductors revolutionized electronics[8].

The thesis is composed of five chapters, two appendixes, and a bibliography. Below, a short description of the content is presented.

Chapter 1 (current one) is a preface containing an introductory part to the thesis. It presents the motivation for the studies and outlines the content of the dissertation.

Chapter 2 introduces the topic of spin waves and presents the basic theoretical background needed to understand the work, like the concept of dispersion relation in the confined system, or mechanisms of localization. There is also presented the derivation of interaction-specific components of effective field used in numerical calculations.

Chapter 3 is focused on numerical methods and tools used in my research. It discusses two numerical methods I used. In the case of the plane wave expansion method, I presented the derivation of the eigenvalue problem and discussed the implementation of this method

in a programming language. For micromagnetic simulations, there are presented the key assumptions and workflow that I developed to calculate spin wave spectra.

Chapter 4 presents the research conducted during my studies, related to the topic of the dissertation. I selected and included in the thesis four peer-reviewed publications, where my contribution was meaningful. Before each paper, the motivation for the studies, the main findings of this work, and my contribution are presented. For the convenience of cross-reference within the dissertation, I index these publications with the 'P' symbol.

- **P1** - *Driving magnetization dynamics in an on-demand magnonic crystal via the magnetoelastic interactions*, discuss the role of spin wave localization within the magnonic crystal by changing the angle of the in-plane external magnetic field with respect to the periodicity direction. Surface acoustic waves that are induced in the system, via magnetoelastic coupling can parametrically induce spin waves. The dependency of the strength of this coupling in the function of the angle between the in-plane magnetic field and wave vector in the thin magnetic film is known and can be theoretically predicted. However, in the case of a magnonic crystal, the spatial distribution of spin waves starts to be nontrivial and we report how it can additionally affect the magnetoelastic coupling.

- **P2** - *Anomalous refraction of spin waves as a way to guide signals in curved magnonic multimode waveguides* address the issue of signal transmission by the spin wave in the curved multimode magnonic waveguide. We exploit the concept of graded-index material to propose a design of the waveguide's bent that can tilt the wavefront and thus avoid scattering of fundamental mode into the quantized modes.

- **P3** - *Interface modes in planar one-dimensional magnonic crystals* is devoted to the topic of interface states induced between two joint semi-infinite magnonic crystals. We exploit the works of Zak[137, 138], to derive the existence condition for inducing the interface state that can appear in the common band gap of the two subsystems. We verify the theoretical prediction numerically and discuss the results for the exchange spin waves and exchange-dipolar spin waves.

- **P4** - *Spin-wave localization on phasonic defects in one-dimensional magnonic quasicrystal* explore the disorder in the quasiperiodic structure. We investigated the impact of so-called phasonic defects on the spectrum of spin waves. We show how frequency gaps are narrowing and localization of the spin wave modes is enhanced with increasing levels of disorder.

Chapter 5 is a summary that presents concluding remarks.

Appendix 1, contains the list of my publications, including the works which are discussed in the thesis.

Appendix 2, includes the statements about the contribution other co-authors to the publications P1-P4. My contribution to the works P1-P4 are described in Chapter 4, in the commentaries preceding each publication.

Chapter 2

Introduction to spin waves

2.1 Landau-Lifshitz equation

The dynamics of the magnetic moment $\mathscr{M}$ can be classically described by the Landau-Lifshitz equation[38, 111]:

$$\frac{d\mathscr{M}}{dt} = -\mu_0 |\gamma| \mathscr{M} \times \mathbf{H}_{\text{eff}},$$ (2.1)

where $\mathbf{H}_{\text{eff}}$ is an effective field. The effective field includes both the external field $\mathbf{H}_0$, and the internal field $\mathbf{H}_{\text{int}}$, resulting from the interactions between magnetic moments or other subsystems in the material. The coefficient γ is called the gyro-magnetic ratio and relates the magnetic moments to the angular momentum: $\gamma = \mathscr{M}/\mathbf{J}$. For negatively charged particles (e.g., for electron) the angular momentum (spin) is oriented opposite to the direction of the magnetic moment and therefore their gyro-magnetic ratio is negative. The equation (2.1) can be classically derived from the equation of motion for angular momentum:

$$\frac{d\mathbf{J}}{dt} = \mathscr{T},$$ (2.2)

where the torque $\mathscr{T}$ has magnetic origin: $\mathbf{T} = \mathscr{M} \times \mathbf{B}_{\text{eff}} = \mu_0 \mathscr{M} \times \mathbf{H}_{\text{eff}}$. The Landau-Lifshitz equation (2.1) describes dynamics that conserve the length of the magnetic moment vector. It can be noticed after calculations of scalar product of both sides of the equation (2.1) with $\mathscr{M}(t)$ which gives the relation: $\partial |\mathscr{M}(t)|^2/\partial t = 0 \implies |\mathscr{M}(t)| = const$.

For continuous medium the equation can be written in the local form, where the magnetization vector $\mathbf{M}$, as a magnetic moment $\mathscr{M}$ per unit of volume v ($\mathbf{M} = d\mathscr{M}/dv$),

is introduced:

$$\frac{\partial \mathbf{M}(\mathbf{r},t)}{\partial t} = \gamma(\mathbf{r}) \underbrace{\mu_0 \mathbf{M}(\mathbf{r},t) \times \mathbf{H}_{\text{eff}}(\mathbf{r},t)}_{\mathbf{T}(\mathbf{r},t)}, \tag{2.3}$$

where $\mathbf{T}$ is a torque per unit volume of the magnetic material. The internal components of effective field are determined by the spatial distribution and temporal changes of magnetization vector: $\mathbf{H}_{\text{int}}(\mathbf{r},t) = \mathbf{H}_{\text{int}}(\mathbf{M}(\mathbf{r},t))$. This feature makes the equation (2.3) non-linear in the general case. Therefore, the Landau-Lifshitz equation describes the variety of dynamical effects including both the non-linear and linear phenomena, e.g., magnetization switching[68], domain wall motion[51, 31], vortex dynamics[40], and spin wave propagation[111].

The magnetization in the solids results primarily from the presence of magnetic moments of electronic spins. Therefore in further consideration we assume that $\gamma(\mathbf{r}) < 0$.

2.2 Effective field

In the following section, I will describe several components of the effective field, that I took into consideration during my calculations.

2.2.1 Exchange field

Despite the fact that electrons interact electrostatically with each other, the dominant force in the very short range results from the Pauli exclusion principle. Thus, the theoretical framework describing ferromagnetism is based on this principle. Spontaneous configuration of magnetic moments is the parallel alignment of the electron's spins, so one can model the Hamiltonian of electronic spins[44]: $\mathscr{H}_{\text{ex},i,j} = -J_{i,j}\mathbf{S}_i \cdot \mathbf{S}_j$. The parameter $J_{i,j}$ is called exchange integral and depends on the overlapping of electron wave functions located at the neighboring sites i and j.

In the semi-classical interpretation, the exchange energy of selected magnetic moment (macrospin) $\gamma\hbar\mathbf{S}_i$ in the field of neighboring macrospins $\gamma\hbar\mathbf{S}_j$ is given by the formula:

$$\mathscr{H}_{\text{ex},i} = - \sum_{\substack{j \\ (NN \text{ of } i)}} J_{i,j}\mathbf{S}_i \cdot \mathbf{S}_j, \tag{2.4}$$

where the summation is done over all of the nearest neighbors (NN). The vectors $\mathbf{S}_i, \mathbf{S}_j$ can be oriented arbitrary in space, without the constraints describing the quantization of the angular momentum. However, in the case of application of Eq. (2.4) to the continuous model of magnetization dynamics, i.e., to the Landau-Lifshitz equation (2.3), the following

assumptions are made: (i) the exchange interaction is isotropic, i.e., $J_{i,j} = J$ for any pair of *NN*, (ii) there is a continuous function describing the magnetic moments in the ferromagnets, (iii) the angle between *NN* are small, that after expanding mathematical function in Taylor series we can limit ourselves only to the linear component. We start derivation from defining the magnetization vector, that combine the values of $\mathbf{S}_l$ at discrete locations $\mathbf{r}_l$ with continuous function $\mathbf{M}(\mathbf{r}_l)$:

$$\mathbf{M}(\mathbf{r}_l) = \frac{N}{V} \mu_B g \mathbf{S}_l, \tag{2.5}$$

where N is a number of spin in volume V of the unit cell, $\mu_B g$ is Bohr magneton, and $g = \hbar/\mu_B \gamma$ is the so-called g-factor. After expanding the magnetization vector (2.5) into the Taylor series, to describe the small spatial changes of the orientation in the vicinity of position $\mathbf{r}_l$, and assuming that the exchange integral is the same for all pairs of neighboring spins as well as the distances between them are equal, we can derive the formula for the density of exchange energy $\varepsilon_{\text{ex}}(\mathbf{r}_l) = d\mathcal{H}_{\text{ex},l}/dv$ in the form:

$$\varepsilon_{\text{ex}} = \lambda M_S^2 + \frac{A}{M_S^2} \sum_i (\partial_{x_i} \mathbf{M})^2. \tag{2.6}$$

Equation introduces to the model a parameter A that is called exchange stiffness constant, which reflects the microscopic origin of the formula. It is related to the exchange integral $A = \frac{JS^2 n}{a}$ (for cubic lattices), where $S = |\mathbf{S}_1| = |\mathbf{S}_2|$, a is the lattice constant and $N = n/a^3$ is a number of spins/atoms per unit cell. The saturation magnetization can also be related to microscopic parameters: $M_S = N \mu_B g S$. In the continuous model, the material parameters can be, in general, spatially dependent: $M_S(\mathbf{r})$, $A(\mathbf{r})$. The parameter λ is equal to: $-\frac{ZJ}{N\mu_B^2 g^2}$ (where Z is the number of NN for the selected spin).

Total exchange energy stored in magnetic material can be calculated as an integral of density energy over volume:

$$E_{\text{ex}} = \int_v \varepsilon_{\text{ex}} d^3 r = \int_v \lambda M^2 d^3 r + \int_v A \left[\left(\partial_x \frac{\mathbf{M}}{M} \right)^2 + \left(\partial_y \frac{\mathbf{M}}{M} \right)^2 + \left(\partial_z \frac{\mathbf{M}}{M} \right)^2 \right] d^3 r. \tag{2.7}$$

In a linear regime, the magnetization vector can be separated into static and dynamic parts. We assume that the material is magnetically saturated which means that the static component of magnetization is lying along the static effective magnetic field. Thus $M_z \equiv M_S(\mathbf{r}) \equiv M_S$. Dynamical components can be presented as a vector: $\mathbf{m} = (m_x, m_y)$. Total exchange energy can be then rewritten as:

$$E_{\text{ex}} = \int_v \lambda M_S^2 d^3 r + \int_v A \left(\nabla \frac{\mathbf{m}}{M_S} \right)^2 d^3 r \tag{2.8}$$

Calculating derivatives and assuming that magnetization saturation is described by Heaviside function θ, i.e., in the considered system is composed of the domains of materials that have sharp interfaces:

$$M_S(\mathbf{r}) = (M_{S,A} - M_{S,B})\,\theta\,(\mathbf{r} - \mathbf{r}_{\text{interface}})\,, \tag{2.9}$$

we present a formula for the exchange energy:

$$E_{ex} = \int_v \lambda M_S^2(\mathbf{r})\,d^3r + \int_v \frac{A}{M_S^2(\mathbf{r})}\,(\nabla\mathbf{m})^2\,d^3r. \tag{2.10}$$

The effective field is calculated as a functional derivative of the density of exchange interaction with respect to magnetization vector[66]:

$$\mathbf{H}_{\text{ex}}(\mathbf{r}) = -\frac{1}{\mu_S}\frac{\delta E_{\text{ex}}}{\delta \mathbf{M}} = -\frac{1}{\mu_0}\left[\frac{\delta E_{\text{ex}}}{\delta m_x},\frac{\delta E_{\text{ex}}}{\delta m_y},\frac{\delta E_{\text{ex}}}{\delta M_S}\right]. \tag{2.11}$$

The effective field reads as:

$$\mathbf{H}_{\text{ex}} = \frac{1}{\mu_0}\nabla\left(\frac{2A}{M_S^2}\right)\nabla\mathbf{M}, \tag{2.12}$$

where the first term in Eq. (2.10) is the static part and thus is irrelevant for the derivation of the exchange field (2.12) [66]. Concluding, in the uniformly magnetized sample, the static component of the exchange field is equal to zero, and the exchange field is expressed only by the dynamic part, which for the spin wave of the frequency ω is:

$$\mathbf{H}_{\text{ex}}(\mathbf{r},t) = \mathbf{h}_{\text{ex}}(\mathbf{r},t), = \frac{1}{\mu_0}\nabla\left(\frac{2A}{M_S^2}\right)\nabla\mathbf{m}(\mathbf{r},t) \tag{2.13}$$

2.2.2 Dipolar field

The dipolar interaction can be described using the principles of classical electromagnetism. The energy of dipolar interaction between the pair of spins can be described by the formula derived on the ground of magnetostatics[48]:

$$\mathcal{H}_{d,i,j} = \mu_0 \frac{(g\mu_B)^2}{4\pi}\left(\frac{\mathbf{S}_i\cdot\mathbf{S}_j}{r_{i,j}^3} - 3\frac{(\mathbf{S}_i\cdot\mathbf{r}_{i,j})(\mathbf{S}_j\cdot\mathbf{r}_{i,j})}{r_{i,j}^5}\right), \tag{2.14}$$

where $\mathbf{r}_{i,j}$ is a vector connecting $\mathbf{S}_i$ and $\mathbf{S}_j$. The energy (2.14) depends strongly on the relative orientation of the spins. The dipolar interaction (2.14) can be repulsive, when $\mathbf{r}_{i,j} \perp \mathbf{S}_i, \mathbf{S}_j$ or attractive for $\mathbf{r}_{i,j} \parallel \mathbf{S}_i, \mathbf{S}_j$, which illustrates the anisotropic character of this interaction.

In order to calculate the dipolar energy of i-th spin in the magnetic system, we need to sum up the contributions from all dipoles:

$$\mathscr{H}_{\mathrm{d},i} = \sum_{\substack{j \\ (j \neq i)}} \mathscr{H}_{\mathrm{d},i,j}. \tag{2.15}$$

Due to the long range of dipolar interactions, the sum (2.15) above is strongly dependent on the shape of the magnetic body.

Equation (2.14) can be applied for magnonics, because the investigated range is within several or dozens of GHz, where the retardation effect is still marginal, and we do not need to solve the full electromagnetic problem[125] where the electromagnetic coupling and Lorentz invariance are granted. Thus, we can assume that the electric field is not induced by varying in time the magnetization within the magnetic body. The lack of feedback from a magnetic field to an electric field in magnonics means that the electric currents and electric fields can be only the sources of the external magnetic field but they are not involved in the mediation of interactions between processing magnetic moments.

The effective magnetic field related to dipolar interaction can be derived in a continuous medium from the energy formulated in the lattice model (2.14), in a similar way as it was presented for the effective exchange field in Sec.2.2.1. However, we will use a much simpler approach based on so-called magnetostatic approximation[111], which reflects the omission of retardation effect. In the magnetostatic approximation, the Maxwell equation for the rotation of magnetic field **H** reduces to:

$$\nabla \times \mathbf{H} = 0. \tag{2.16}$$

For such field, called magnetostatic field $\mathbf{H}_{\mathrm{d}}$, we can introduce the scalar potential Φ [38, 111]:

$$\mathbf{H}_{\mathrm{d}} = -\nabla \Phi, \tag{2.17}$$

called magnetostatic potential. From another Maxwell equation, the Gauss equation for magnetism:

$$\nabla \cdot \mathbf{B} = 0, \tag{2.18}$$

we obtain the Poisson(Laplace) equation for magnetostatic potential inside Φ_{in} (outside Φ_{out}) the magnetic material:

$$\begin{cases} \Delta \Phi_{\mathrm{in}} = \nabla \cdot \mathbf{M}, \\ \Delta \Phi_{\mathrm{out}} = 0. \end{cases} \tag{2.19}$$

The requirement of the continuity of the normal component of the **B**-field and the tangential component of the **H**-field on the interface leads to the following boundary conditions for magnetostatic potential:

$$
\begin{aligned}
\Phi_{\text{in}} - \Phi_{\text{out}} &= 0, \\
\frac{\partial \Phi_{\text{in}}}{\partial \hat{\mathbf{n}}_0} - \frac{\partial \Phi_{\text{out}}}{\partial \hat{\mathbf{n}}_0} &= \mathbf{M} \cdot \hat{\mathbf{n}}_0,
\end{aligned}
\tag{2.20}
$$

where $\hat{\mathbf{n}}_0$ is the unit vector normal to the interface. The solution of Eqs. (2.19) can be written in a form[48]:

$$
\Phi(\mathbf{r}) = -\frac{1}{4\pi} \int_V \frac{\nabla' \cdot \mathbf{M}(\mathbf{r}')}{|\mathbf{r} - \mathbf{r}'|} dV' + \frac{1}{4\pi} \oint_S \frac{\hat{\mathbf{n}}'_0 \cdot \mathbf{M}(\mathbf{r}')}{|\mathbf{r} - \mathbf{r}'|} dS',
\tag{2.21}
$$

where V and S are the volume and the surface of the magnetic body, respectively. The first term in (2.21) describes the contribution of the volume magnetic charges which appear in non-collinear magnetic configurations where $\nabla \cdot \mathbf{M}(\mathbf{r}) \neq 0$. The second term in (2.21) is related to the presence of surface magnetic charges induced on the interfaces where the normal component of magnetization is discontinuous. It refers also to the surfaces of the magnetic body separating magnetic ($\mathbf{M} \neq 0$) and nonmagnetic medium ($\mathbf{M} = 0$).

In the linear approximation, the demagnetizing field can be presented as a sum of static component and dynamic $\mathbf{H}_d(\mathbf{r}, t) = \mathbf{H}_d(\mathbf{r}) + \mathbf{h}_d(\mathbf{r})e^{i\omega t}$, where the static component lies along the direction of the external magnetic field, and two dynamic components are perpendicular. In the general case, finding of demagnetizing field must be done via the self-consistent procedure, since demagnetizing field affects magnetization dynamics and *vice versa*. It is clear from the formula (2.21), where the dipolar interactions are nonlocal and depend on geometrical factors like shape or size but also on the magnetic configuration. However, the magnetic configuration is determined not only by the geometry of a magnetic body but also by the external magnetic field. Therefore, the interplay between the geometry and applied field is responsible for forming the magnetic landscape in which the magnetic interactions couple the precessing magnetic moments.

For periodic structures in saturation state, i.e., for magnetically saturated magnonic crystals, the calculations of demagnetizing field can be performed semi-analytically by applying the Fourier transform to Eqs. (2.19). The most common form of magnonic crystals is the planar structure where the ferromagnetic film is periodically patterned in one or two directions. The demagnetizing field in these structures can be presented in terms of auxiliary functions $\psi^{(x)}$, $\psi^{(z)}$, $\psi^{(z)}$, strictly related to magnetostatic potential Φ, as it was presented in

the work by Kaczer and Murtinova[54]:

$$\Phi(\mathbf{r}) = -\left(\frac{\partial \psi^{(x)}(\mathbf{r})}{\partial x} + \frac{\partial \psi^{(y)}(\mathbf{r})}{\partial y} + \frac{\partial \psi^{(z)}(\mathbf{r})}{\partial z} \right), \qquad (2.22)$$

For thin film (of the thickness $2a$) and periodic distribution of magnetization $\mathbf{M}$ (described by the Fourier components $\mathbf{M}(\mathbf{G})$), the formulas read as, for the external area:

$$\psi_{\text{out}}^{(\alpha)}(\mathbf{r}) = \sum_{\mathbf{G} \neq 0} \frac{M_\alpha(\mathbf{G})}{G^2} \frac{\sinh(Ga)}{\sinh(Ga) + \cosh(Ga)} e^{i\mathbf{G} \cdot \mathbf{r}_\parallel} e^{-G(z-a)}, \qquad (2.23)$$

and internal area:

$$\psi_{\text{in}}^{(\alpha)}(\mathbf{r}) = \sum_{\mathbf{G}} \frac{M_\alpha(\mathbf{G})}{G^2} \left(1 - \frac{\sinh(Ga)}{\sinh(Ga) + \cosh(Ga)} \right) e^{i\mathbf{G} \cdot \mathbf{r}_\parallel} - \frac{1}{2} M_\alpha(0) \left(z^2 - a^2 \right), \quad (2.24)$$

where $\alpha = \{x, y, z\}$, $\mathbf{G} = [G_x, G_y]$, and $\mathbf{r}_\parallel = [x, y]$.

To obtain the demagnetizing field $\mathbf{H}_{\text{ms}} = \left[H_{\text{d},x}, H_{\text{d},y}, H_{\text{d},z} \right]$ one needs evaluating the following expressions:

$$H_{\text{d},x} = \frac{\partial^2 \psi^{(x)}}{\partial x^2} + \frac{\partial^2 \psi^{(y)}}{\partial x \partial y} + \frac{\partial^2 \psi^{(z)}}{\partial x \partial z},$$
$$H_{\text{d},y} = \frac{\partial^2 \psi^{(x)}}{\partial y \partial x} + \frac{\partial^2 \psi^{(y)}}{\partial y^2} + \frac{\partial^2 \psi^{(z)}}{\partial y \partial z},$$
$$H_{\text{d},z} = \frac{\partial^2 \psi^{(x)}}{\partial z \partial x} + \frac{\partial^2 \psi^{(y)}}{\partial z \partial y} + \frac{\partial^2 \psi^{(z)}}{\partial z^2}. \qquad (2.25)$$

The Eqs. (2.23-2.25) can be used for finding the static and dynamic components of demagnetizing field magnetization independently. The mathematical form of the formulas (2.23-2.25) is convenient for implementing them in the plane wave expansion method (see Sec. 3.1), for the calculation the spin wave dispersion relation in magnonic crystals.

2.2.3 Magnetoelastic field

Every nanostructure is characterized by elastic properties, regardless if it is magnetic or not[101]. The most common realization of a magnonic system is planar ferromagnetic nanostructure deposited on a non-magnetic substrate – see Fig. 2.1. The characteristic dimensions of the planar magnonic nanostructure are hundredths of nm (for in-plane dimensions: widths of stripes, sizes of dots/holes) and single tens of nm (for out-of-plane dimensions: thicknesses of layers). For such systems, the coupling between dipolar-dominated SWs and surface

acoustic waves (SAWs) can be observed. The SAWs have the amplitude concentrated close to the surface of the elastic substrate, where the magnonic structure is deposited. The spatial concentration of SAWs and SWs in the same area, and the compatible range of frequencies with wavevectors for both excitations make the dynamical coupling between SAWs and SWs possible if the magnetic medium is magnetostrictive.
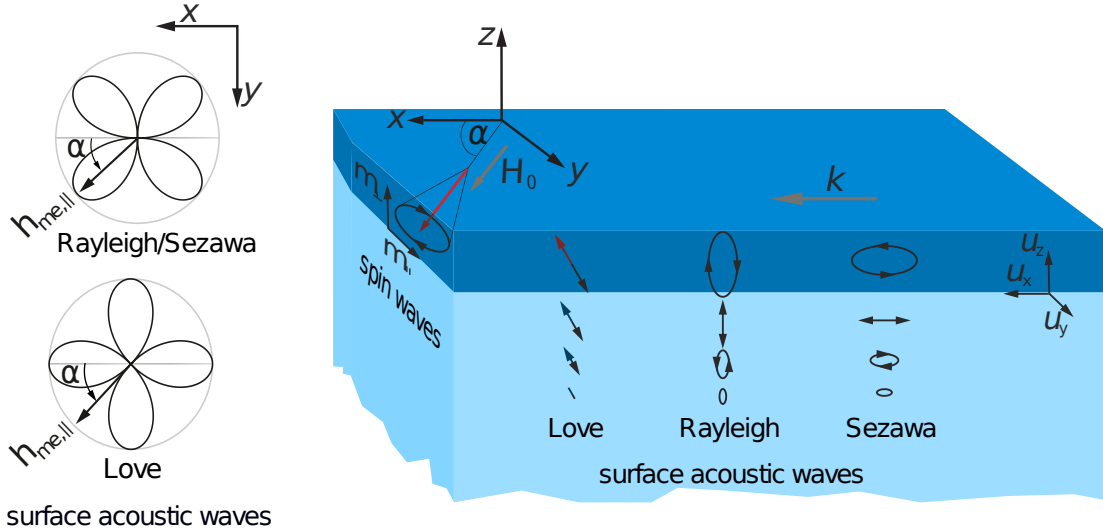

Fig. 2.1 An exemplary system where SW and SAW can mutually propagate. Dark blue is a magnetic layer with finite thickness, and light blue is a substrate that is assumed to have an infinite thickness in comparison to the wavelength of the excitation. The SW can propagate only in the magnetic top layer, and the directions of the dynamical components are perpendicular to the in-plane external magnetic field. Sketch presents polarization of three kinds to SAW, namely Love, Rayleigh, Sezawa. Polar plots on the left show the angular dependence of magnetoelastic coupling (expressed the corresponding component of effective field) for those three SAWs.

Here, I outline the formal description of the impact of the elastic waves on the SW dynamics. For the magnetoelastic systems presented above, the continuous model[95, 101] will be appropriate to describe the dynamics of elastic waves and their coupling to SWs.

The displacement vector is a continuous function of position $\mathbf{u}(\mathbf{r})$ and expresses the deformation of the medium:

$$\mathbf{u}(\mathbf{r}) = \mathbf{r} - \mathbf{r}_0,$$

i.e., the difference between the initial position $\mathbf{r}_0$, and the corresponding position in deformed medium $\mathbf{r}_0$. The homogeneous displacement $\mathbf{u} = \text{const}(\mathbf{r})$ is equivalent to the translation of the whole body and does not generate mechanical stress. Therefore, we need to consider the gradient of $\mathbf{u}(\mathbf{r})$, which is a tensor: $\nabla \mathbf{u}(\mathbf{r})$. The asymmetric component of $\nabla \mathbf{u}(\mathbf{r})$ expresses

the rotation of medium. The uniform rotation must be neglected because is equivalent to the rotation of the whole body. The non-uniform rotation is usually small[131], referring to the symmetric component of the displacement gradient, and can be neglected. Therefore, the stress results predominately from the presence of the symmetric component of $\nabla\mathbf{u}(\mathbf{r})$, which is called strain tensor:

$$\varepsilon = \frac{1}{2}\left(\nabla\mathbf{u} + \nabla\mathbf{u}^T\right), \qquad\qquad \varepsilon_{pq} = \frac{1}{2}\left(\frac{\partial u_p}{\partial x_q} + \frac{\partial u_q}{\partial x_p}\right), \qquad (2.26)$$

where the later expression in (2.26) is valid in Cartesian coordinates ($\mathbf{r} = [x_1, x_2, x_3]$). The equation of motion in elastodynamics is a local formulation of Newton's second law of dynamics. In the absence of external forces, we can write:

$$\rho\frac{\partial^2\mathbf{u}}{\partial t^2} = \mathbf{f}_{\text{el}}, \qquad (2.27)$$

where ρ denotes mass density and $\mathbf{f}_{\text{el}}$ is body force density – the net, internal, elastic forces density coming from the environment of the point $\mathbf{r}$. The body force density can be formally expressed as a divergence of the so-called Cauchy strain tensor: $\mathbf{f}_{\text{el}} = \nabla \cdot \sigma$, which gives full information about the stress at point $\mathbf{r}$. For small deformations, i.e., in a linear regime, we can write a local version of Hook's law, which relates stress and strain tensors: $\sigma = \mathbf{c} \cdot \varepsilon$. The symbol $\mathbf{c}$ is stiffness tensor, which is a four-rank tensor describing the material properties of the elastic medium and contains, in the general case, 21 independent components (due to the symmetry of strain and stress tensors). The elastodynamic equation of motion can be then written in Cartesian coordinates in the following form:

$$\rho\frac{\partial^2 u_p}{\partial t^2} = \sum_{q,l,m} c_{pqlm}\frac{\partial^2 u_m}{\partial x_q \partial x_l}. \qquad (2.28)$$

The microscopic mechanisms leading to the (dynamical) coupling between magnetic and elastic systems are complex[38]. In the continuous model, we can use the phenomenological description of magnetoelastic interaction. If we limit our considerations to the case when the deformation is expressed only by strain tensor (i.e., when we neglect the magneto-rotation coupling[131]) then the equation for magnetoelastic energy density has the following form in Cartesian coordinates:

$$f_{\text{me}} = \frac{1}{M_S^2}\sum_{i,j=1}^{3}\varepsilon_{ij}M_i M_j\left(b_1\delta_{ij} + b_2\left(1 - \delta_{ij}\right)\right). \qquad (2.29)$$

This intrinsic magnetoelastic coupling can be observed in a selected class of materials, characterized by non-zero magnetoelastic coupling constants b_1 and b_2.

The coupling between the equations of motion for SWs (2.3) and elastic waves (2.27) can be formally implemented by addind magnetoleastic contribution to effective magnetic field $\mathbf{h}_{\mathrm{me}}$ and to the stress tensor σ_{me}, respectively:

$$h_{\mathrm{me},l} = -\frac{1}{\mu_0}\frac{\partial f_{\mathrm{me}}}{\partial M_l}, \qquad\qquad \sigma_{\mathrm{me},pq} = \frac{\partial f_{\mathrm{me}}}{\partial \varepsilon_{pq}} \qquad (2.30)$$

The solution of the full magnetoelastic problem gives information about the spectrum and profiles of hybrid magnetoelastic modes. In my research, however, I used the simplified approach. In work P1, I assumed that SAWs are generated in the film and pump SWs. In these calculations, we neglect the feedback from magnetization dynamics to elastic dynamics, and took for granted that SWs are excited dynamically by given magnetoelastic field $\mathbf{h}_{\mathrm{me}}$. In work P1, we looked for the condition which has to be fulfilled to observe the pumping of SWs by SAW, in a non-homogeneous magnetic layer deposited on a nonmagnetic substrate.

From the general formula (2.30), we can derive the amplitudes of the magnetoelastic field which drives the SWs in in-plane magnetized film. The equations for in-plane and out-of-plane components of $\mathbf{h}_{\mathrm{me}}$ in Cartesian coordinates (see Fig. 2.1) take a form:

$$\begin{cases} \mu_0 h_{\mathrm{me},\parallel} = 2b_2\left(\varepsilon_{xz}\cos\phi + \varepsilon_{yz}\sin\phi\right), \\ \mu_0 h_{\mathrm{me},\perp} = b_1\left(\varepsilon_{xx} - \varepsilon_{yy}\right)\sin 2\phi - 2b_2\varepsilon_{xy}\cos 2\phi, \end{cases} \qquad (2.31)$$

where ϕ is the angle between the in-plane applied external magnetic field and wave vector. The polar plots on the left side of Fig. 2.1 present schematically strength of magnetoelastic coupling. We can see that only at specific angles ϕ can the SWs can be effectively excited by the SAW of specific polarization (i.e., by Rayleigh SAW or by Love SAW [17, 6]).

2.3 Magnonic structures and their dispersion relations

This section introduces the description of the magnonic systems that were by in the thesis. Analysis of dispersion relation is crucial since it governs the way of propagation.

2.3.1 Thin film

The magnonic system is typically considered with the confinement in at least one direction, mostly due to constraints in fabrication and characterization techniques. Moreover, the

appearance of surfaces and interfaces is crucial for the activation of dipolar interaction in magnetically saturated samples. In bulk, homogeneous, and magnetically saturated material the demagnetizing fields are absent and the spin wave dynamics is governed only by exchange interaction[38].

In this section, the considered system is a plane film, where the magnetization dynamics is confined to one dimension, while the SW can freely propagate in the plane of the film. The most general analytical theory of SW dispersion relation in the ferromagnetic film was developed in the 80s of the last century by Kalinikos and Slavin[55]. The equation describing the dispersion relation in thin film with the arbitrary angle between the direction of SW propagation and the external magnetic field (strong enough to saturate the sample) takes the form:

$$\omega(\mathbf{k}) = \omega(k, \phi, \theta) = \gamma\mu_0 \sqrt{\left(H_0 - M_S + M_S l_{ex}^2 k^2\right)\left(H_0 - M_S + M_S l_{ex}^2 k^2 + M_S F(\phi, \theta, k)\right)}, \tag{2.32}$$

where auxiliary function $F(\phi, \theta, k)$ can be written as:

$$F(\phi, \theta, k) = P(kd) + \sin^2\theta \left[1 - P(kd)\left(1 + \cos^2\phi\right) + \frac{M_S P(kd)\left[1 - P(kd)\right]}{H_0 + M_S l_{ex}^2 k^2}\sin^2\phi\right],$$

with the function $P(kd)$ defined as:

$$P(kd) = 1 - \frac{1 - e^{-kd}}{kd}. \tag{2.33}$$

The symbol d is the thickness of the film, θ is the polar angle (out-of-plane angle) between external magnetic field $\mathbf{H}_0$ and direction of SW propagation $\mathbf{k}/k$ and ϕ is azimuthal angle between in-plane projection of $\mathbf{H}_0$ and $\mathbf{k}/k$. The parameter $l_{ex} = 1/M_S\sqrt{2A/\mu_0}$ denotes so-called exchange length. While the SW can freely propagate in the plane of the film, the perpendicular component (k_{oop} - out-of-plane) is quantized, i.e., only SW with wavelengths that are multiple of thickness d is allowed:

$$k_{oop} = \frac{\pi(n-1)}{d}, \tag{2.34}$$

where $n = 1, 2, 3, \ldots$. For $n > 1$ Eq. (2.32) describe so-called perpendicular standing spin waves (PSSW). Formula (2.32) assumes no pinning on the interface and is simplified to the case when there is no surface anisotropy[94] – see Sec.2.3.2 for more information about quantization and pinning of SWs in confined dimensions. In my research, I mostly neglected PSSW: the considerations were limited only to the case $n = 1$.

The equation (2.32) reflects the complexity of SW dispersion relation, illustrated in Fig.2.2. The analysis of Eq. (2.32) can give some insight to the interplay between dipolar and exchange interaction (see also Sec. 2.2.1 and 2.2.2 for more information about these interactions). The terms proportional to k^2 come from the exchange field, and they are independent on the geometrical factors. The terms associated with the dipolar field have a more complex form. The dipolar terms scale with kd, which means that thickness of film d is critical. They are expressed by function $P(kd)$ (2.33) containing the exponential function e^{-kd}, which makes the dispersion relation $\omega(\mathbf{k})$ linear in the vicinity of $\mathbf{k} = 0$, and non-analytic at $\mathbf{k} = 0$ (the slope of $\omega(\mathbf{k})$ must change a sign at $\mathbf{k} = 0$ when $\phi \to \phi + \pi$, because of reciprocity of SWs' propagation: $\omega(\mathbf{k}) = \omega(-\mathbf{k})$ resulting from the conservation of time-reversal symmetry). For small wave vectors the slope of the dispersion relation, which is the measure of the strength of interaction, increases linearity with the changes in the film's thickness d. The function $P(kd)$ ranges from 0 (for $k = 0$) to 1 (for $k \to \infty$), as the system transits from dipolar to exchange regime. For $k = 0$ the dispersion relation (2.32) reproduces the Kittel formula[59] for ferromagnetic resonance frequency and includes only static demagnetizing fields, dependent on the orientation of the external field saturating the sample. For $k \to \infty$ the dispersion relation is isotropic (do not depends on θ nor ϕ) and quadratic in k (the dipolar terms responsible for spin wave dynamics are non-active: $P(kd) = 0$).

It is worth noting that the dispersion relation in dipolar dominated regime (i.e., for small $\mathbf{k}$ when quadratic exchange terms can be neglected) is strongly anisotropic for small values of θ (i.e., when the external field is applied with a significant in-plane component). The slope of dispersion relation changes substantially with the polar angle ϕ (angle between the wave vector and in-plane projection of external field), which can even lead to the reverse of its sign and form a saddle-like shape of dispersion relation in the vicinity of $\mathbf{k} = 0$ (see Fig.2.2(a)). For dipolar-dominated SWs propagating in-plane, three canonical configurations (geometries) can be distinguished (see Fig.2.2):

- **Damon-Eshbach geometry** (surface spin waves): k and H_0 lies in-plane ($\theta = 0°$) and they are perpendicular to each other ($\phi = 90°$),

- **Backward volume geometry** (volume backward spin waves): k and H_0 lies in-plane ($\theta = 0°$) and they are parallel to each other ($\phi = 0°$),

- **Forward volume geometry** (volume forward spin waves): H_0 lies out-of-plane ($\theta = 90°$).

The Demon-Eshbach configuration is also called surface spin waves configuration because the amplitude of the SW across the thickness is non-uniform, is located at one interface and
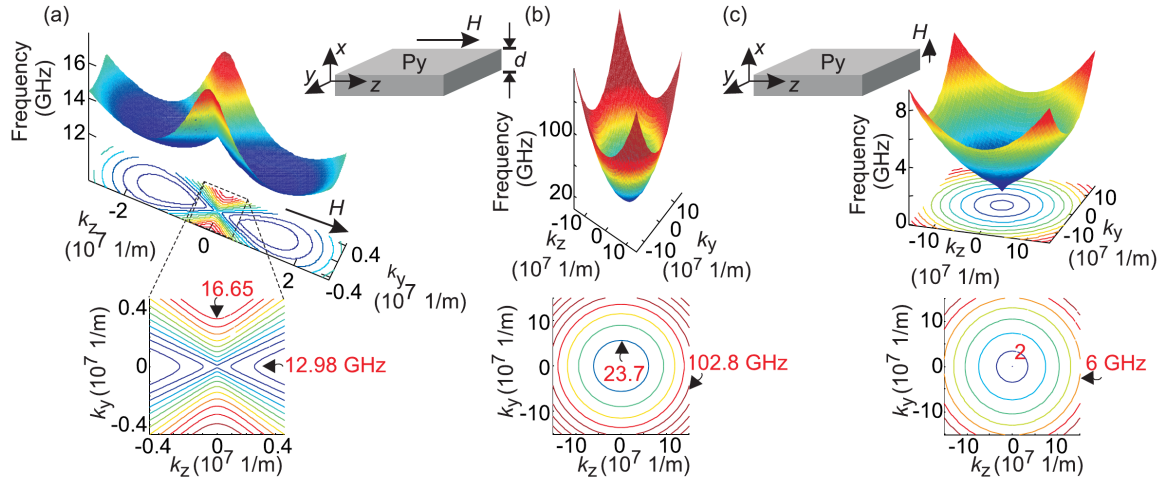
Fig. 2.2 Dispersion relations of spin waves as a function of in-plane wavevectors calculated from analytical formula (2.32) (a) the considered film is made from Py and has a thickness of 50 nm, external magnetic field $\mu_0 H_0 = 0.2T$ is applied along the z axis. Line along k_y, for $k_z = 0$ is dispersion relation for Demon-Eshbach configuration, while line along k_z, for $k_y = 0$ for backward-volume. (b) the considered film is made from Py and has a thickness 1 nm, external magnetic field $\mu_0 H_0 = 0.2T$ is applied along the z axis. The plot presents the same magnetic configurations, however now, the minimum for backward-volume configuration is not pronounced due to the dominance of the exchange field. (c) To 50 nm Py film external magnetic field $\mu_0 H_0 = 1.5T$ is applied along the normal to the film. The dispersion relation is characterized by isotropic isocontours. (Reproduced from *J. Phys.: Condens. Matter* **26**, 123202 (2014) [62], © 2014 IOP Publishing Ltd.)

decays towards the second one[22]. The dispersion relation of Demon-Eshbach is presented in Fig. 1(a), where one needs to make a cross-section along the k_y-axis at position $k_z = 0$. Dispersion relation there is calculated for Py film of 50 nm thickness and for magnetic field $\mu_0 H_0 = 0.2T$ applied along the z axis. The backward volume configuration is characterized by a minimum dispersion relation function for $k \neq 0$. This lead to backward propagation for some range of k with a negative slope, where group velocity is negative (see cross section along k_z axis, for $k_x = 0$). Different behavior of SW in both of the configurations shows strong shape anisotropy of the magnonic system, which is a consequence of the dipolar field. Due to the scaling dipolar field with kd, changing the thickness can dramatically modify the properties of the system. This is visualized in Fig. 2.2(b), where dispersion relation is calculated for Py film of thickness 1 nm and applied magnetic field $\mu_0 H_0 = 0.02T$. The function resembles parabolic dependence, which means the dominance of the exchange field in the equation (2.32). In the case of forward volume configuration, presented in Fig. 2.2(c) dispersion relation is isotropic. The magnetic field is applied perpendicular to the interface,

so a static demagnetizing field exists in the system in the form of magnetic charges on the surfaces. One needs to apply an external magnetic field that can overcome them, and thus saturate film in the desired direction. Naturally, it is difficult to set the static component of magnetization out-of-plane and this fact is reflected in the name: hard axis, meaning that this configuration is not favorable for minimizing the energy of the system. In-plane configuration for the film is thus called easy plane configuration.

2.3.2 Magnonic waveguides

The confinement in the second dimension leads to forming a waveguide – the structure that is finite in two directions (thickness and width) but unconstrained in a third one. Shaping the waveguide not necessarily means the physical constraints of the magnetic medium. The magnonic waveguide[42] can be induced in the film, by shaping the internal the magnetic film, for example by: modifying the magnetic anisotropy[128], placing another magnetic structure on top of the film[93], pattering the structure[90] or designing the magnetic texture in the form of domain walls[58].

The finite sizes lead to the quantization of the wavevector. As an illustration, let's discuss the case of a flat waveguide. For simplicity, we will consider only the system with the exchange interactions – see Fig. 2.3. The wavelengths related to the quantization across the thickness of the waveguide d are small and this quantization is relevant only for SWs of very high frequencies[43]. Therefore, we can consider the modes which are homogeneous across the thickness and quantized in the width of the waveguide $w \gg d$ with discrete components of the wavevector: $k_n = \frac{\pi(n-1)}{w}$, where $n = 1, 2, 3, \ldots$. Only the wavevector's component along the waveguide k can change continuously. So, we can plot dispersion relation $\omega(k)$ for this component, assuming specific quantization in the width, i.e for $n = 1, 2, 3, \ldots$.

In narrow waveguide, the separation between the sucessive branches: $\delta\omega = \omega(k + k_n) - \omega(k + k_{n-1})$ is meaningful, and the range of frequency accessible only for fundamental mode ($n = 1$) is large – see the range 6-10.5 GHz in Fig. 2.3(a) *vs.* 6-7 GHz Fig. 2.3(b). A narrower waveguide is easier to operate in a regime called *single-mode*, where the scattering between perpendicularly quantized modes are excluded in the wide frequency range. The coherence of SWs is preserved, even if the waveguide is curved. With increasing width, the quantized modes appear at a lower frequency and the single-mode regime becomes narrower. Considering the fact that around $k = 0$ group velocity of exchange-dominated SW is close to zero, such a single-mode waveguide is practically inoperable – one needs to increase the frequency, and then higher quantized modes come into play, i.e., the waveguide becomes multi-mode.
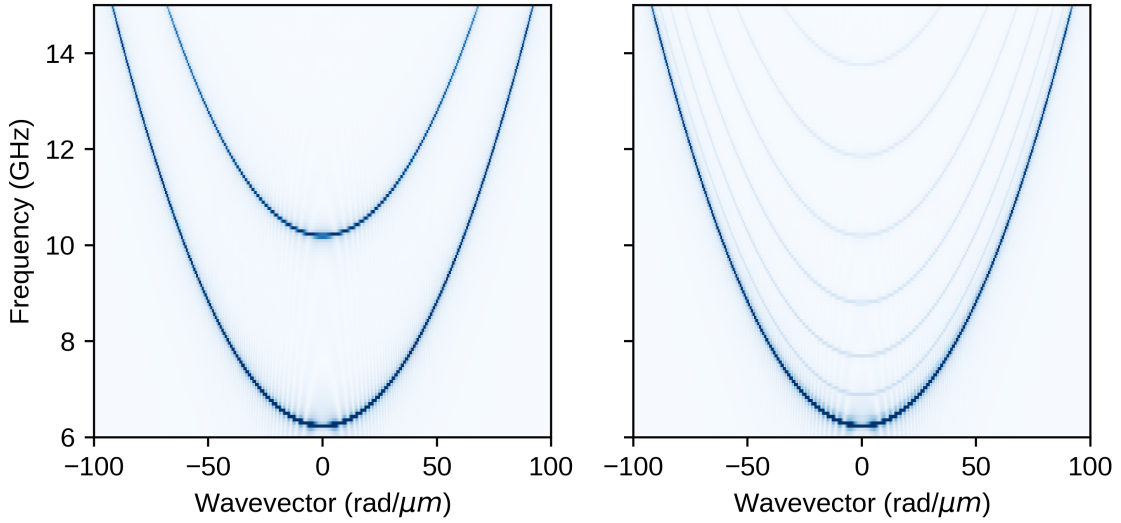
Fig. 2.3 Dispersion relations of waveguides with only exchange interaction taken into account. The calculation was done for two different widths: (a) 100 nm, and (b) 500 nm. The rest of the parameters, thickness: 20 nm, external magnetic field: $\mu_0 H_0 = 0.2$ T, were the same for (a) and (b). The waveguides were assumed to be made of Py ($M_{S,Py} = 860$ kA/m, $\lambda_{ex,Py} = 5.29$ nm).

It should be pointed out, that any potential magnonic circuit[57] would require changing the direction of SW propagation since it is not possible to imagine any device that can be designed along one line. Thus, the single-mode waveguides are intensively exploited in research since they do not disturb the coherence of signal, and they can be used in the application that relay wave computing[85]. Nevertheless, multimode-waveguide are characterized by higher bandwidth, since they are not limited in frequency. The work P2 contributes to the field of multimode-waveguide by presenting the method of guiding the SW through the bent in the multimode waveguide.

By including the dipolar interaction, the SW dispersion relation is much more complex, even for the fundamental mode ($n = 0$). One needs to consider the fact, that even for fundamental mode, the amplitude of SW is no more uniform across the width. The analytical formula for the thin waveguide (where aspect ratio $p = d/w$ is small, and the width is bigger than λ_{ex}) was derived by Guslienko[39, 41]. He found that the spin wave dynamics are partially pinned (i.e., spin wave amplitude is reduced) at the lateral edges of the stripes and the fundamental mode is not uniform anymore. The effect is caused by a dynamic demagnetizing field produced by elliptically precessing magnetization in confined geometries (mostly due to the presence of dynamic magnetic surface charges at lateral edges)[18]. To describe SW pinning, he introduced the parameter w_{eff}, standing for the effective width of

the waveguide, which is always smaller than the geometrical w. The parameter w_{eff} is the fictitious width at which the sin-like/cos-like SW profile is completely pinned ($\mathbf{m} = 0$), if the profile would be extended outside the width w of the real waveguide. In general case, the SW is partially pinned at the edges of the waveguide, and the limits $w_{\text{eff}} = \infty$ ($w_{\text{eff}} = w$) correspond to the totally free $\partial_{\mathbf{n}}\mathbf{m} = 0$ (completely pinned $\mathbf{m} = 0$) SW, where $\partial_{\mathbf{n}}$ denotes the spatial derivative in the direction normal to the lateral edges.

The effective width w_{eff} is related to dipolar pinning parameter $D_{\text{dip}} = \partial_{\mathbf{n}}\mathbf{m}/\mathbf{m}$. The parameter D_{dip} is expressed by aspect ratio p and for flat stripes ($p \ll 1$) takes the value:

$$D_{\text{dip}} = \frac{2\pi}{p\left[1 + 2\ln\left(1/p\right)\right]},$$

In the range $p \ll 1$, the relation between w_{eff} and D_{dip} can be expressed as:

$$w_{\text{eff}} = w\left(\frac{D_{\text{dip}}}{D_{\text{dip}} - 2}\right).$$

Recently, with the progress of experimental techniques that allowed the fabrication of nanoscopic magnonic structure, there was a need to derive a theory that could describe SWs' dispersion relation in waveguide at any aspect ratio, not only for $p \ll 1$. The theory, as well as comparison with experimental results was presented in the paper[127], where the authors discussed truly nanoscopic waveguide, showing the exchange dispersion relation.

2.3.3   Magnonic crystals

The idea of periodic modulation of the material is very old and was possibly considered for the first time by Lord Rayleigh in 1887 for one-dimensional photonic crystals in the form of multi-layered dielectric film[81]. He could demonstrate that such a system possesses band gaps: regions of frequency that completely halt transmission through the system. After several decades, the theory of propagating electronic waves in crystal lattices was developed[14], and it become a fundamental theory for any wave propagation in periodic potential[61, 60, 5]. (The sketch of the derivation of the Bloch theorem is presented in the Subsection below.)

In terms of magnetic material, the topic is also not new. The pioneering paper discussing the periodization can be dated around 50 years ago[113], where the spin wave transmission through the film of yttrium-iron-garnet with the array of grooves at the top surface was investigated. The revolution in the investigation of the periodic systems, however, can be pointed out in the paper of Yablonovitch[132] who considered periodic structures that could

shape the propagation of light. This paper opened many frontiers in physics and in September 2022 is cited over 10000 times. Photonic crystals[53] brought many ideas that eventually were applied to many other wave-like excitations in media, among them also to the spin waves and the concept of magnonic crystal was renewed at the end of XX century[62]. Over the course of a few decades, different approaches for the fabrication of magnonic crystals were used: arranging nanoelements (strips[75, 74], dots[133, 34]), pattering the films in the form of antidot lattices[119, 115], changing the magnetic properties (by material deposition or ion implantation[128]), or modifying the boundary conditions[13].

New levels of complexity concerning the magnonic crystals are explored, e.g., 3D structures[63, 37], and periodic textures[7]. In the dissertation are presented 3 works contributing to the field of magnonic crystals: P1, P3, and P4. The details of dispersion relation are presented in Chapter 3, where numerical tools are presented. Especially Sec. 3.1 because it contains the implementation of the plane wave expansion method for spin waves[123, 65]. There are also presented exemplary results of the dispersion relation.

Bloch theorem

The Floquet theorem[30], known in condensed matter physics as a Bloch theorem[14], states that the solution of the homogeneous linear differential equation with periodic coefficients has the following form:

$$\varphi(\mathbf{r}) = e^{i\mathbf{k}\cdot\mathbf{r}} u(\mathbf{r}), \tag{2.35}$$

where the function $u(\mathbf{r})$ is periodic with the same periodicity as the coefficients of the differential equation. The parameter $\mathbf{k}$ is interpreted in condensed matter physics as a wave vector and the function $\varphi(\mathbf{r})$, called the Bloch function, is a wave-like eigenmode propagating in a periodic medium. The properties of the inhomogeneous medium (e.g. saturation magnetization M_S, exchange stiffens constant A) are described by periodic coefficients of the differential equation. The Bloch function can be understand as plane wave $e^{i\mathbf{k}\cdot\mathbf{r}}$ modulated by periodic factor $u(\mathbf{r}+\mathbf{a}) = u(\mathbf{r})$ with the periodicity of the medium.

It can be proved that the Bloch function is strictly periodic in the space of the parameter $\mathbf{k}$, i.e., in the space of the wave number or so-called reciprocal space:

$$\varphi_{\mathbf{k}}(\mathbf{r}) = \varphi_{\mathbf{k}+\mathbf{G}}(\mathbf{r}), \tag{2.36}$$

where $\mathbf{G}$ is the reciprocal lattice vector. The same periodicity shows the eigenvalues (energies or frequencies) corresponding to the Bloch functions:

$$\omega(\mathbf{k}) = \omega(\mathbf{k}+\mathbf{G}). \tag{2.37}$$

which is equivalent to the folding of the dispersion ration $\omega(\mathbf{k})$ into the confined region of reciprocal space called the first Brillouin zone. Another important remark that should be emphasized is that Bloch function $\varphi_{\mathbf{k},n}(\mathbf{r})$ should be labeled by index n, because for given $\boldsymbol{k}$ there are infinite and countable amount branches of dispersion relation folded into the first Brillouin zone.

2.3.4   Magnonic quasicrystals

Quasicrystals are a special class of structures exhibiting, similarly to crystals, long-range order and thus deserving a separated section to discuss them. In 1992, The International Union of Crystallography provided the definition of crystal which states that crystal is *"any solid having an essentially discrete diffraction diagram"*[23]. This definition was modified to fit quasicrystal into it, because they are characterized by long-range order (they have discrete diffraction diagram), however, they lack translation symmetry. Before, the definition of crystal was stricter: *"a crystal is a substance in which the constituent atoms, molecules, or ions are packed in a regularly ordered, repeating three-dimensional pattern"*, which assumes that crystal is constructed by unit cell, possessing translation symmetry. The discovery of quasicrystal by Schechtman in 1984[107], destroyed a long-standing paradigm, which exclude from consideration other fold symmetries than 2-, 3-, 4-, and 6-. Scientist for ~100 years, overlooked the fact that it is possible to fill the space also with other fold symmetries like 5 or 10, however more than one unit cells need to be used.

Quasicrystals[50] possess several very interesting properties, that make them the object of study in photonics or magnonics. I will discuss them on the example of Fibonacci quasicrystal[122, 99], that I studied in the work P4. The easiest way to understand how the Fibonacci sequence can be created is to present one technique, called "cut&projection"[50]. From two-dimensional square lattice, that plays a role of hyperspace for Fibonacci quasicrystal, a straight line is drawn at the slope τ to one the principal direction of the lattice (τ is an irrational number, equal to golden ratio $\tau = \left(1 + \sqrt{5}\right)/2$). Then, the lattice points from the stripe of the width $a(\tau+1)\sqrt{\tau+2}$, projected at the line give Fibonacci quasicrystal being a sequence of long ($L = a\tau/\sqrt{\tau+2}$) and short ($S = a/\sqrt{\tau+2}$), where a is a square lattice constant. Due to a lack of translation symmetry, we cannot define "a unit cell" which can be used in numerical calculations to represent the whole structure. It is then necessary to consider approximates of the Fibonacci sequence containing the finite number of S and L sections. Moreover, the quasicrystal composed of short S and L sections can be decorated by two distinct sections A and B of the same length, differing e.g. in material properties. In the inset of Fig. 2.4(a) is presented such approximate built from 21 elements. The structure there

is composed of two kinds of strips that have the same size but differ in magnetic parameters leading to inducing the contrast. The discussed sequence can be understood as a decorated Fibonacci sequence, with strips made of sequences *SLLS* and *SLS* that share *S* section with the ratio: $(2 - \tau)/(2 + \tau)$.

The quasiperiodic structures are self-similar, which means that some fraction of the structure reveals the same pattern as the whole structure. This feature is especially interesting from the perspective of the dynamic properties of the system. Eigenmode that would be associated with this pattern shall be degenerated due to the appearance of the same pattern several times, aperiodically within the structure.
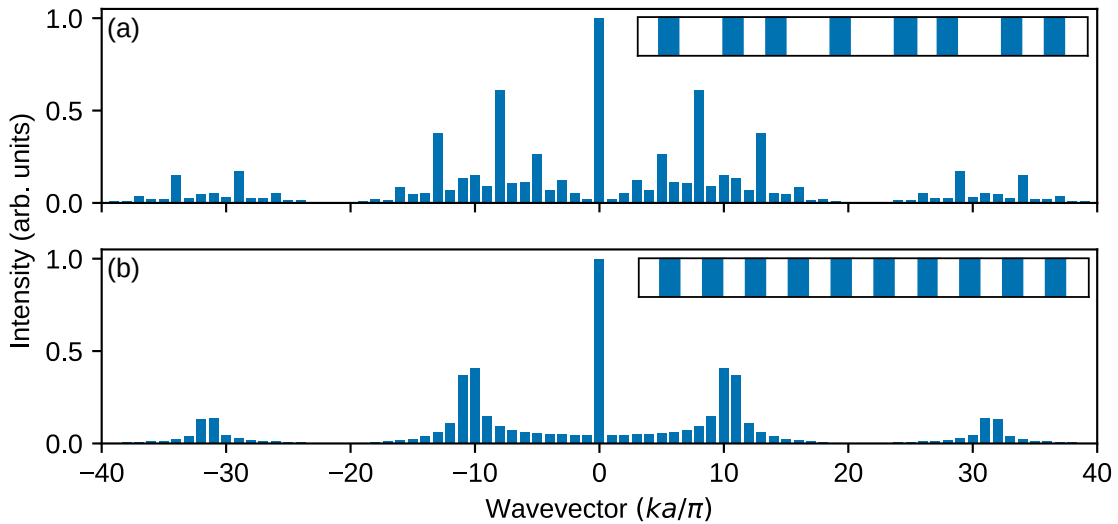

Fig. 2.4 Fourier transform corresponds to the diffraction of a pattern of (a) Fibonacci sequence, and (b) periodic sequence presented in the insets. Calculations were done for the systems composed of 21 elements in both cases. (a) The Fibonacci sequence has a complex spectrum of peaks, while (b) the periodic sequence is related to the periodic arrangement of isolated peaks in the spectrum (the finite width of the peaks, results from the finite size of the structure).

Another important feature is a dense fractal spectrum (i.e., Fourier transform) of quasiperiodic structure, composed of Dirac-delta peaks, which can be interpreted as a diffraction pattern of scattered waves. The approximated spectra for finite structures (i.e., containing 21 elements) are showed in Fig. 2.4, where Fig. 2.4(a) presents Fourier transform of Fibonacci sequence, while Fig. 2.4(b) – the spectrum periodic structure, showed for reference. In Fig. 2.4(a) we can notice several bunches of pronounced peaks, but in (b) we have only single peaks (widened due to the finite size of the structures), shifted by successive reciprocal lattice vectors $G_n = n2\pi/a$, where a is a lattice constant of the periodic structure. This feature of

quasicrystal leads to the opening large number of frequency gaps in the spectrum, due to the fact that Bragg condition for reflection is fulfilled for a dense set of wave vectors. The consequence of the lack of translation symmetry is that the wavevector cannot be interpreted as quasimomentum, and the eigenfrequencies are not periodic in reciprocal space. Therefore, we used the integrated density of states: IDOS(f) (IDOS is equal to the amount of solution (eigenfrequencies) below given frequency) instead of dispersion relation $f(k)$ to present the frequency spectrum of quasicrystals. The plateaus in IDOS(f) denote the frequency ranges corresponding to the frequency gaps – see e.g. Fig.3 in the work P4.

2.4   Spin wave localization

This section is devoted to one important property of wave dynamics, namely localization. The localization of SW can be the result of the evanescent solutions of the LLE (characterized by complex wavevector) which appear in the regions where propagating SWs, i.e., the oscillatory solutions (characterized by real wavevector) cannot exist for a given range of frequencies. This exponential decay in space can be observed in the areas where the precession frequency is below the minimum of dispersion relation: $\min(f(k))$, determined for real values of the wavevector – see e.g. Fig. 2.2, or in the frequency gaps (e.g. in the spectrum of magnonic crystals or quasicrystals) – see works P3 and P4. The homogeneous systems or the systems with long-range order, which are unconstrained in size, cannot support the localization of this kind. It is due to the exponential (i.e., physically unlimited) growth of the wave's amplitude which accompanies the decay in opposite direction. The SW modes can be, however, *exponentially localized at defects* introduced into these systems. The presence of defects (which can also take the form of interfaces or surfaces[70, 97] – see also work P3) can guarantee the exponential decay of SW when one moves away from the defect in opposite directions. The *confinement in constrained geometries and on magnetization textures*[124, 7] can be also understood as a kind of localization because the SW amplitude can be focused on these objects at selected frequencies. Some modes can be also *naturally localized in ordered and infinite systems* due to the different and more complex mechanisms, not mentioned above. This is e.g., the case of the localized modes that can be observed in the quasicrystal – see work P4.

This arbitrary taxonomy of SW localization is neither strict nor complete. The mixing of mentioned types of localization is also possible. One can consider the SW localization at the interface of two magnonic crystals composed of magnetic nanoelements (strips, dots) in which the SWs can be internally localized, or the SWs localized in defected magnonic

quasicrystals where the intrinsic localization in the structure of quasicrystal can be altered by the presence of defects.

Below, I would like to discuss broader some of these localization types with an indication that was under my investigation and is included in the dissertation.

Nonuniform of magnetic material

The SW dispersion relation depends on material parameters like magnetization saturation, exchange length, or anisotropy energy density. The molding of material properties is an important method in designing magnonic crystals. SW scattering on the periodic pattern induces Bragg reflection and opens related frequency gaps. A similar strategy is also used in photonics and phononics, however, there are peculiarities of this approach, specific to magnonics. If the dipolar interactions are active, the minimum of dispersion relation (and not only its slope df/dk) is sensitive to the material parameters, and some modes can be localized only in the material, where they oscillate spatially while decaying exponentially in another part of the system[98]. It is because the frequency of the given mode is above (below) the minimum frequency for oscillatory (evanescent) solutions in respective components. This type of localization is discussed in the work P3.

By adjusting the geometry, we can affect the static effective field inside the magnetic structure, mostly due to the demagnetizing field, which is strongly dependent on the shape of the structure. The SWs' dispersion and the profiles of SW modes are also dependent on the static effective field. Its increase leads, at some point, to the transition from oscillatory to evanescent profile. Therefore, both the distribution of material parameters and the landscape of static effective field are important for the determination of the regions where the SW of a given frequency has an oscillatory or evanescent profile. In planar structures, with sharp interfaces and magnetic field perpendicular to them, this mechanism can lead to the appearance of additional modes in the spectrum, called edge modes[115, 116]. The magnonic crystals can be fabricated by the decoration of the uniform film by the periodic array of magnetic nanoelements (dots, strips). The periodicity in this system is provided not only by the array of magnetic nanoelements (i.e., by the periodic distribution of material parameters) but also by the periodic profile internal field within the film produced by the array. This is visualized in Fig. 2.5, where the out-of-plane component of the static demagnetizing field is plotted. The considered system is built from the uniform yttrium-iron-garnet (YIG) film with a thickness of 112 nm. On top of the YIG film, the Ni strip is placed, which is 112 nm thick and 800 nm wide. The system is magnetically saturated by the out-of-plane applied external field of the value 0.5 T. We can notice a significant change in the static demagnetizing field

in the system. The internal field in the uniform YIG layer is lowered in the central region, below the Ni strip.
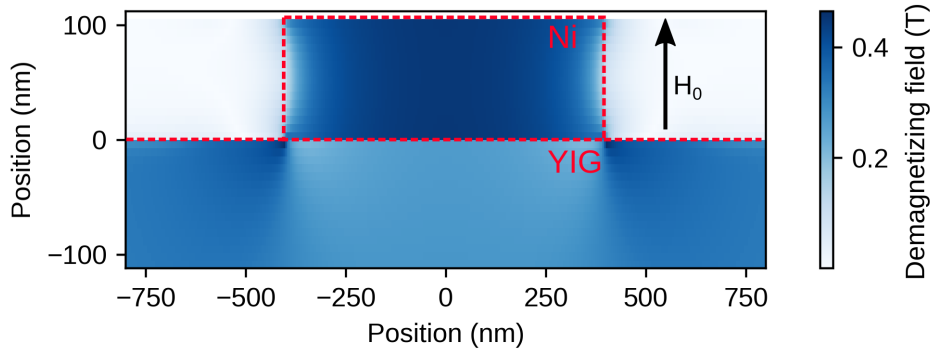

Fig. 2.5 The distribution of static demagnetizing field (out-of-plane component) for the structure composed of the uniform film made of yttrium-iron-garnet (YIG) and Ni strip, placed on the top. The following material parameters were assumed: YIG layer ($M_{\text{S,YIG}} = 143$ kA/m, $\lambda_{\text{ex,YIG}} = 14.5$ nm), Ni strip ($M_{\text{S,Ni}} = 480$ kA/m, $\lambda_{\text{ex,Ni}} = 7.7$ nm). YIG layer and Ni strip have the same thickness 112 nm. The width of the strip is 800 nm. An external magnetic field of the value 0.5 T is applied along the vertical axis, saturating the magnetization in the out-of-plane direction.

Critical localization in quasicrystals

Quasicrystals possess a rich spectrum of modes that reflects the complexity of their structure. In the frequency spectrum of wave excitations in quasicrystals, there is a group of the modes called critically localized modes[82, 49], that are occupying specific arrangements of the constituent elements of quasicrystals. The critically localized modes exhibit self-similarity, like the structure of the quasicrystal itself. Due to this, it is not straightforward to define their localization measure, it cannot be described simply by the rate of exponential decay. Thus, there is a need to derive other, global type of localization measure that reflects complex forms for the modes in quasicrystals. This type of localization, considered for SW in Fibonacci magnonic quasicrystal, is a subject of research in the work P4.

Localization in magnetic texture

Magnetic moments can form nontrivial texture when the system is not saturated by an external magnetic field. The complex textures are the results of the interplay between Dzyaloshinskii–Moriya interactions, magnetic anisotropy, and dipolar interactions[108]. The magnetization dynamics on magnetic textures are also intensively studied, and the localization properties of the SW modes exited on the complex curvilinear magnetic configurations

were reported. For example, the domain walls were exploited to use them as very narrow waveguides[33, 45], or they can form regular pattern making magnonic crystals[7]. In magnetic dot, where vortex state can be induced, the existence of whispering gallery modes was reported. Although the confinement at the vortex, the mode is propagating one, because it is formed from the interference of the clockwise and counterclockwise SWs, differing in wavelengths. Its amplitude is localized next to the edge of the vortex[103]. Very intensive studies are done on skyrmions due to their unique properties and potential application[28]. They can form a periodic lattice. The chirality that is embedded in the texture of skyrmions can lead to the appearance of topological edge states in their lattice[24].

Termination of the periodicity – interfaces and surfaces of magnonic crystals

Another reason that can lead to the localization of SW is the termination of crystal, that suppose to be infinite to sustain the translational symmetry. Explanations of this behavior were given for the electronic state in the 30'ties of XX century, by Tamm[117] and Schockley[109]. Nowadays, Shockley states refer to states induced directly on the termination, while Tamm states appear in the system that additionally has defects in the unit cells located at the edges. The mathematical construction of the mode is based on the matching boundary condition between two evanescent solutions on both sides of the interface. In the case of electronic states, one can assume that electronic wavefunction decay exponentially in the vacuum, however, SWs cannot exist outside of the magnetic material, and proper boundary condition must be implemented. This was discussed with detailed in the paper of Rychły[97]. In work P3, I discussed the existence condition for magnonic interface states localized at the junction of two different semi-infinite magnonic crystals. The paper presents how from the bulk properties, i.e., symmetries of the eigenmodes, one can predict in which frequency gap interface mode would appear. The mathematical description of bulk-edge correspondence of SW in magnonic crystals is based on the work of Zak[137, 138].

Defects

The appearance of defects in the crystal also leads to the localized of the waves. The mechanism is similar to that described for interface and surface modes. The defect mode is constructed from two evanescent waves decaying exponentially in opposite directions. Investigation of the defect modes is a long subject, also in magnonics, where many ways of defecting the ordered magnonic nanostructures (magnonic crystals and quasicrystals) were considered, e.g.: changing the geometry of constituent elements[87, 139, 32] or local reversal

of magnetization[11]. I contributed to this investigation with the work P4, where defected magnonic Fibonacci sequence is investigated.

A special type of localization, that is the result of the disorder, is Anderson localization. It was suggested for the first time by Philip Anderson[3, 2], who investigated electron wavefunction in the crystal with the disorder introduced in lattice potential. He showed that when the strength of disorder exceeds some threshold, then electronic transport completely halts, and the wavefunction of electrons becomes localized with the exponential rate of decay. This is a wave phenomenon and is the consequence of interference of the wave function due to the wave's scattering on different paths. This could not be explained by the ballistic approach when one would expect a gradual degradation of the transmission. Due to the wave nature of this phenomenon, it was observed also in other types of excitation, like electromagnetic waves[104, 71] or acoustic waves[47].

Particularly interesting was a demonstration of Anderson localization of light. The considered system was in the so-called transverse localization scheme[106, 84]. The light in the form of localized modes is propagating along the waveguides that are forming photonic crystals. Position along the waveguides plays the role of time in the original problem formulated by Anderson. Waveguides are coupled to each other and the distance between pairs of waveguides is proportional to coupling strength. Introducing disorder in the lattice, i.e., when distances are different, the coupling is different as well. The system can be solved by the Maxwell equation in paraxial approximation. This formulation of the problem is analogous to the original one, which was described by Schrödinger equation and can be even solved by the same techniques, for example, the tight-binding model. The Anderson localization in the transverse scheme is localized wave spatially. The signal is concentrated and decays exponentially.

This kind of localization is the subject of my recent studies conducted during my internship at the Swiss Federal Institute of Technology – EPFL in Lausanne, realized in the framework of the NCN program ETIUDA (grant No 2020/36/T/ST3/00542). The research is being done with the experimental team from EPFL: Prof. Dirk Grudler, Andrea Mucchietto, and Dr. Mingran Xu. In our studies, we want to exploit transverse localization in one-dimensional magnonic crystals with the induced disorder.

Chapter 3

Numerical tools

In this chapter, I present the description of two numerical methods that I used in my research projects, namely the plane wave expansion method (PWEM) and the micromagnetic simulations (MS).

The PWEM is used in works P1, P3, and P4. The first implementation of PWEM for 3D magnonic crystals, in exchange dominated regime, was done by Maciej Krawczyk and Henryk Puszkarski[65]. The method was then extended for planar magnonic crystals with dipolar interactions taken into account[110] and used widely in the Department of Physics of Nanostructures in different variants and for different applications[114, 70, 64, 35, 86]. I developed the current version of the code of PWEM for magnonic systems. The software, written in Python, is publicly available and distributed under the MIT license.

For the MS[76], I used software called MuMax3 that was developed by the Dynamat group from Ghent University in Belgium with the leading role of Arne Vansteenkiste[121]. The software is distributed with an open source license GNU General Public License. Micromagnetic simulations were used in P2 work.

3.1   Plane wave expansion method

The PWEM is typically used for periodic structures, where the Bloch boundary condition might be applied. To illustrate the principles of PWEM, I decided to present the derivation of this method for one-dimensional magnonic crystal, where an external magnetic field is applied along the strips, and both the exchange and dipolar interactions are included.

The starting point is LLE (2.3):

$$\frac{\partial \mathbf{M}}{\partial t} = -\mu_0 \, |\gamma| \, \mathbf{M} \times \mathbf{H}_{\text{eff}}, \qquad (3.1)$$

where γ stands for gyromagnetic ratio, and μ_0 magnetic permeability. The PWEM is dedicated to linear systems. Therefore, we need to linearize LLE and write the magnetization vector in the form:

$$\mathbf{M}(\mathbf{r},t) = [m_x(\mathbf{r},t), M_s(\mathbf{r}), m_z(\mathbf{r},t)], \tag{3.2}$$

where x, z components point towards excitation directions, while the external magnetic field lies along the y axis. For linearized LLE, the solutions are monochromatic waves and dynamical components of the magnetization vector can be written as:

$$\begin{cases} m_x(\mathbf{r},t) = m_x(\mathbf{r}) e^{i\omega t}, \\ m_z(\mathbf{r},t) = m_z(\mathbf{r}) e^{i\omega t}. \end{cases} \tag{3.3}$$

In the further derivations, we skip explicit notation on the spatial dependence, i.e., $m_x \equiv m_x(\mathbf{r})$ and $m_z \equiv m_z(\mathbf{r})$. The left side of (3.1) is the derivative of time from the magnetization vector, that can be now calculated:

$$\frac{\partial \mathbf{M}}{\partial t} = i\omega [m_x, 0, m_z] e^{i\omega t}. \tag{3.4}$$

The effective field is assumed to have sources in three kinds of fields, namely external magnetic field, dipolar field, and exchange field:

$$\mathbf{H}_{\text{eff}}(\mathbf{r},t) = \mathbf{H}_0 + \mathbf{H}_d(\mathbf{r},t) + \mathbf{H}_{\text{ex}}(\mathbf{r},t). \tag{3.5}$$

The external magnetic field H_0 is static and uniform in the space, thus explicit dependence on position and time can be neglected. Dipolar interaction are incorporated into the model as a demagnetizing field, both static $\mathbf{H}_d(\mathbf{r})$, and dynamic one $\mathbf{h}_d(\mathbf{r},t)$. In the framework of linear approximation, the dynamic component of the demagnetizing field is also considered to be harmonic in time, similarly to the dynamic component of the magnetization vector: $\mathbf{h}_d(\mathbf{r},t) = \mathbf{h}_d(\mathbf{r}) e^{i\omega t}$. Effective field can be now presented in the form:

$$\begin{aligned} \mathbf{H}_{\text{eff}}(\mathbf{r},t) = \big[&H_{d,x} + h_{d,x} e^{i\omega t} + \nabla \lambda_{\text{ex}}^2 \nabla (m_x e^{i\omega t}), H_{d,y} + h_{d,y} e^{i\omega t} + \nabla \lambda_{\text{ex}}^2 \nabla (m_y e^{i\omega t}) + H_0, \\ &H_{d,z} + h_{d,z} e^{i\omega t} + \nabla \lambda_{\text{ex}}^2 \nabla (m_z e^{i\omega t}) \big]. \end{aligned} \tag{3.6}$$

Having defined all of the components of the effective field, we can write right side of the equation (3.1):

$$
\begin{cases}
(\mathbf{M} \times \mathbf{H}_{\text{eff}})_x = M_S \left(H_{\text{d},z} + h_{\text{d},z} e^{i\omega t} + \nabla \lambda_{\text{ex}}^2 \nabla \left(m_z e^{i\omega t} \right) \right) + \\
-m_z e^{i\omega t} \left(H_{\text{d},y} + \nabla \lambda_{\text{ex}}^2 \nabla M_S + H_0 \right), \\
(\mathbf{M} \times \mathbf{H}_{\text{eff}})_y = 0, \\
(\mathbf{M} \times \mathbf{H}_{\text{eff}})_x = m_x e^{i\omega t} H_{d,y} + m_x e^{i\omega t} \nabla \lambda_{\text{ex}}^2 \nabla M_S + m_x e^{i\omega t} H_0 + \\
-M_S h_{\text{d},x} e^{i\omega t} - M_S \nabla \lambda_{\text{ex}}^2 \nabla \left(m_x e^{i\omega t} \right).
\end{cases}
\tag{3.7}
$$

Since the external magnetic is oriented along the strips, all the interfaces are parallel to the H_0, and the static demagnetizing field can be neglected. Having the left and right sides of the LLE written down, we can now define the coupled equations of dynamical components in the following form:

$$
\begin{cases}
i\Omega m_x = \frac{M_S h_{\text{d},z}}{H_0} + \frac{M_S}{H_0} \nabla \lambda_{\text{ex}}^2 \nabla m_z - \frac{m_z}{H_0} \nabla \lambda_{\text{ex}}^2 \nabla M_S - m_z, \\
i\Omega m_z = -\frac{M_S h_{\text{d},x}}{H_0} - \frac{M_S}{H_0} M_S \nabla \lambda_{\text{ex}}^2 \nabla m_x + \frac{m_x}{H_0} \nabla \lambda_{\text{ex}}^2 \nabla M_S + m_x,
\end{cases}
\tag{3.8}
$$

where $\Omega = \frac{\omega}{\mu_0 H_0 |\gamma|}$.

In PWEM differential equation is solved in reciprocal space, which means that to both Bloch function (dynamic components of magnetization) and material parameters (magnetization saturation and exchange length) the Fourier transform is applied. In the next step, components M_s, m_z, m_x, $h_{\text{d},x}$, $h_{\text{d},z}$ are expanded into Fourier series with reciprocal vector being in this case one dimensional: $\mathbf{G}_n = \left[\frac{2\pi n}{a}, 0, 0 \right]$. After expansion, the dynamic components: m_β ($\beta = \{x, z\}$) of magnetization vector take following form:

$$
m_\beta = \sum_{\mathbf{G}} m_{\mathbf{k}} (\mathbf{G}) e^{i(\mathbf{k}+\mathbf{G}) \cdot \mathbf{r}},
\tag{3.9}
$$

where $\mathbf{k}$ is a wavevector of SW. $m_{\mathbf{k}}$ is a vector of Fourier coefficients, and $e^{i(\mathbf{k}+\mathbf{G}) \cdot \mathbf{r}}$ plane wave.

We need also expand material parameters M_s and λ_{ex} in the Fourier series:

$$
M_S = \sum_{\mathbf{G}} M_S (\mathbf{G}) e^{i\mathbf{G} \cdot \mathbf{r}},
\tag{3.10}
$$

$$
l_{\text{ex}} = \sum_{\mathbf{G}} l_{\text{ex}} (\mathbf{G}) e^{i\mathbf{G} \cdot \mathbf{r}}.
\tag{3.11}
$$

The dynamic component of demagnetizing field along the x (in-plane direction) axis has a form[54]:

$$
\begin{aligned}
h_{\mathrm{d},x} &= h_{\mathrm{d},x}^{(x)} + h_{\mathrm{d},x}^{(y)} + h_{\mathrm{d},x}^{(z)} = -\sum_{G \neq 0} \frac{m_x(\mathbf{G})}{|\mathbf{G}+\mathbf{k}|^2} (G_x + k_x)^2 \times \\
&\times \left(1 - \frac{\cosh\left[(\mathbf{G}+\mathbf{k})z\right]}{\sinh\left[(\mathbf{G}+\mathbf{k})a\right] + \cosh\left[(\mathbf{G}+\mathbf{k})a\right]}\right) M_{\mathrm{S}} \\
&+ \sum_{G \neq 0} \frac{\sinh\left[(\mathbf{G}+\mathbf{k})z\right]}{\sinh\left[(\mathbf{G}+\mathbf{k})a\right] + \cosh\left[(\mathbf{G}+\mathbf{k})a\right]} \frac{m_z(\mathbf{G})}{|\mathbf{G}+\mathbf{k}|} \times \\
& e^{i(\mathbf{G}+\mathbf{k})\cdot\mathbf{r}} (G_x + k_x),
\end{aligned} \tag{3.12}
$$

while along z axis (out-of-plane direction):

$$
\begin{aligned}
h_{\mathrm{d},z} &= h_{\mathrm{d},z}^{(x)} + h_{\mathrm{d},z}^{(y)} + h_{\mathrm{d},z}^{(z)} = \\
&= -\sum_{\mathbf{G}} m_z(\mathbf{G}) \frac{\cosh\left[(\mathbf{G}+\mathbf{k})z\right]}{\sinh\left[(\mathbf{G}+\mathbf{k})a\right] + \cosh\left[(\mathbf{G}+\mathbf{k})a\right]} e^{i(\mathbf{G}+\mathbf{k})\cdot\mathbf{r}} + \\
&+ \sum_{\mathbf{G} \neq 0} m_x(\mathbf{G}) \frac{\sinh\left[(\mathbf{G}+\mathbf{k})z\right]}{\sinh\left[(\mathbf{G}+\mathbf{k})a\right] + \cosh\left[(\mathbf{G}+\mathbf{k})a\right]} \frac{(\mathbf{G}+\mathbf{k})}{|\mathbf{G}+\mathbf{k}|} e^{i(\mathbf{G}+\mathbf{k})\cdot\mathbf{r}}.
\end{aligned} \tag{3.13}
$$

Having expanded components into the Fourier series, now we can attempt to derive expressions from (3.8), that are products of the Fourier series. We present the derivation for $\frac{1}{H_0} M_{\mathrm{S}} \nabla \lambda_{\mathrm{ex}}^2 \nabla m_\alpha$, where $\alpha = \{x,z\}$ The expression contain three Fourier series, that need to be multiplied. We use here properties that sum of two reciprocal vectors give another reciprocal vector:

$$
\begin{aligned}
\frac{1}{H_0} M_{\mathrm{S}} \nabla \lambda_{\mathrm{ex}}^2 \nabla m_\alpha &= \frac{1}{H_0} \sum_{\mathbf{G}} M_{\mathrm{S}}(\mathbf{G}) e^{i\mathbf{G}\cdot\mathbf{r}} \nabla \sum_{\mathbf{G}'} \lambda_{\mathrm{ex}}^2(\mathbf{G}') e^{i\mathbf{G}'\cdot\mathbf{r}} \nabla \sum_{\mathbf{G}''} m_\alpha(\mathbf{G}'') e^{i(\mathbf{G}''+\mathbf{k})\cdot\mathbf{r}} = \\
&= \frac{1}{H_0} \sum_{\mathbf{G}} M_{\mathrm{S}}(\mathbf{G}) e^{i\mathbf{G}\cdot\mathbf{r}} \nabla \sum_{\mathbf{G}',\mathbf{G}''} \lambda_{\mathrm{ex}}^2(\mathbf{G}') e^{i\mathbf{G}'\cdot\mathbf{r}} (\mathbf{G}''+\mathbf{k}) m_\alpha(\mathbf{G}'') e^{i(\mathbf{G}''+\mathbf{k})\cdot\mathbf{r}} \underset{\left|\mathbf{G}''' \to \mathbf{G}''+\mathbf{G}'\right|}{=} \\
&= \frac{1}{H_0} \sum_{\mathbf{G}} M_{\mathrm{S}}(\mathbf{G}) e^{i\mathbf{G}\cdot\mathbf{r}} \sum_{\mathbf{G}''',\mathbf{G}''} \lambda_{\mathrm{ex}}^2(\mathbf{G}''' - \mathbf{G}'') \times \\
&\times e^{i(\mathbf{G}'''+\mathbf{k})\cdot\mathbf{r}} (\mathbf{G}''+\mathbf{k}) \cdot (\mathbf{G}'''+\mathbf{k}) m_\alpha(\mathbf{G}'') \underset{\left|\substack{\mathbf{G}' \to \mathbf{G}'''+\mathbf{G} \\ \mathbf{G}'' \to \mathbf{G}'-\mathbf{G}, \mathbf{G}'' \to \mathbf{G}}\right|}{=} \\
&= \frac{1}{H_0} \sum_{\mathbf{G}'',\mathbf{G}',\mathbf{G}} M_{\mathrm{S}}(\mathbf{G}' - \mathbf{G}'') \lambda_{ex}^2(\mathbf{G}'' - \mathbf{G}) \times \\
&\times m_\alpha(\mathbf{G}) e^{i(\mathbf{G}'+\mathbf{k})\cdot\mathbf{r}} (\mathbf{G}+\mathbf{k}) \cdot (\mathbf{G}''+\mathbf{k}).
\end{aligned} \tag{3.14}
$$

Following the decoration of Eq.(3.8), we can write:

$$\frac{1}{H_0} m_\alpha \nabla \lambda_{\text{ex}}^2 \nabla M_S = \frac{1}{H_0} \sum_{\mathbf{G}'',\mathbf{G}',\mathbf{G}} M_S \left(\mathbf{G}' - \mathbf{G}'' \right) \lambda_{ex}^2 \left(\mathbf{G}'' - \mathbf{G} \right) \times$$
$$\times m_\alpha \left(\mathbf{G} \right) e^{i(\mathbf{G}'+\mathbf{k})\cdot\mathbf{r}} \left(\mathbf{G}' - \mathbf{G}'' \right) \cdot \left(\mathbf{G}' - \mathbf{G} \right). \tag{3.15}$$

The dynamic components of demagnetizing field and magnetization saturation are expanded into Fourier series, so now their product in the equation (3.8) can be defined:

$$
\begin{aligned}
\frac{M_S h_{\text{d},z}}{H_0} \;=\; & -\frac{1}{H_0} \sum_{\mathbf{G},\mathbf{G}'} m_z \left(\mathbf{G} \right) e^{i\mathbf{G}\cdot\mathbf{r}} \frac{\cosh\left[(\mathbf{G}+\mathbf{k})\,z \right]}{\sinh\left[(\mathbf{G}+\mathbf{k})\,a \right] + \cosh\left[(\mathbf{G}+\mathbf{k})\,a \right]} M_S \left(\mathbf{G}' \right) e^{i\mathbf{G}'\cdot\mathbf{r}} + \\
& -\frac{1}{H_0} \sum_{\mathbf{G},\mathbf{G}'} m_x \left(\mathbf{G} \right) e^{i\mathbf{G}\cdot\mathbf{r}} \frac{\sinh\left[(\mathbf{G}+\mathbf{k})\,z \right]}{\sinh\left[(\mathbf{G}+\mathbf{k})\,a \right] + \cosh\left[(\mathbf{G}+\mathbf{k})\,a \right]} \times \\
& \times M_S \left(\mathbf{G}' \right) e^{i\mathbf{G}'\cdot\mathbf{r}} \frac{(G_x + k_x)}{|\mathbf{G}+\mathbf{k}|} \\
\;=\; & -\frac{1}{H_0} \sum_{\mathbf{G},\mathbf{G}'} M_S \left(\mathbf{G}' - \mathbf{G} \right) e^{i(\mathbf{G}'+\mathbf{k})\cdot\mathbf{r}} \times \\
& \times \left[m_z \left(\mathbf{G} \right) C \left(\mathbf{G}+\mathbf{k} \right) + m_x \left(\mathbf{G} \right) S \left(\mathbf{G}+\mathbf{k} \right) \frac{(G_x + k_x)}{|\mathbf{G}+\mathbf{k}|} \right],
\end{aligned}
\tag{3.16}
$$

while the product of magnetization saturation and x component of the dynamic demagnetizing field takes the following form:

$$
\begin{aligned}
\frac{M_S h_{\text{d},x}}{H_0} \;=\; & -\frac{1}{H_0} \sum_{\mathbf{G},\mathbf{G}'} M_S \left(\mathbf{G}' - \mathbf{G} \right) e^{i(\mathbf{G}'+\mathbf{k})\cdot\mathbf{r}} \times \\
& \times \left[\frac{m_x \left(\mathbf{G} \right)}{|\mathbf{G}+\mathbf{k}|^2} (G_x + k_x)^2 \left(1 - C \left(\mathbf{G}+\mathbf{k} \right) \right) + \frac{m_z \left(\mathbf{G} \right)}{|\mathbf{G}+\mathbf{k}|} (G_x + k_x) S \left(\mathbf{G}+\mathbf{k} \right) \right].
\end{aligned}
\tag{3.17}
$$

The auxiliary functions were used in (3.17) and (3.18):

$$C \left(\mathbf{k}, x \right) = \cosh\left(|\mathbf{k}| x \right) e^{-|q|d/2}, \qquad S \left(\mathbf{k}, x \right) = \sinh\left(|\mathbf{k}| x \right) e^{-|q|d/2} \tag{3.18}$$

The procedure of Fourier expansion is finished and two coupled linear equations that were defined in (3.8) have the following form:

$$
\begin{aligned}
i\Omega m_x \left(\mathbf{G}' \right) \;\; = \;\; & -\frac{1}{H_0} \sum_{\mathbf{G}} M_\text{S} \left(\mathbf{G}' - \mathbf{G} \right) \times \\
& \times \left[m_z \left(\mathbf{G} \right) C \left(\mathbf{G} + \mathbf{k} \right) + m_x \left(\mathbf{G} \right) S \left(\mathbf{G} + \mathbf{k} \right) \frac{\left(G_x + k_x \right)}{\left| \mathbf{G} + \mathbf{k} \right|} \right] + \\
& + \frac{1}{H_0} \sum_{\mathbf{G}'', \mathbf{G}} M_\text{S} \left(\mathbf{G}' - \mathbf{G}'' \right) \lambda_\text{ex}^2 \left(\mathbf{G}'' - \mathbf{G} \right) m_z \left(\mathbf{G} \right) \times \\
& \times \left[\left(\mathbf{G} + \mathbf{k} \right) \cdot \left(\mathbf{G}'' + \mathbf{k} \right) - \left(\mathbf{G}' - \mathbf{G}'' \right) \cdot \left(\mathbf{G}' - \mathbf{G} \right) \right] + \\
& - m_z \left(\mathbf{G}' - \mathbf{G} \right).
\end{aligned}
\tag{3.19}
$$

$$
\begin{aligned}
i\Omega m_z \left(\mathbf{G}' \right) \;\; = \;\; & \frac{1}{H_0} \sum_{\mathbf{G}} M_\text{S} \left(\mathbf{G}' - \mathbf{G} \right) \times \\
& \times \left[\frac{m_x \left(\mathbf{G} \right)}{\left| \mathbf{G} + \mathbf{k} \right|^2} \left(G_x + k_x \right)^2 \left(1 - C \left(\mathbf{G} + \mathbf{k} \right) \right) + \frac{m_z \left(\mathbf{G} \right)}{\left| \mathbf{G} + \mathbf{k} \right|} \left(G_x + k_x \right) S \left(\mathbf{G} + \mathbf{k} \right) \right] + \\
& + \frac{1}{H_0} \sum_{\mathbf{G}'', \mathbf{G}} M_\text{S} \left(\mathbf{G}' - \mathbf{G}'' \right) \lambda_\text{ex}^2 \left(\mathbf{G}'' - \mathbf{G} \right) m_x \left(\mathbf{G} \right) \times \\
& \times \left[\left(\mathbf{G} + \mathbf{k} \right) \cdot \left(\mathbf{G}'' + \mathbf{k} \right) - \left(\mathbf{G}' - \mathbf{G}'' \right) \cdot \left(\mathbf{G}' - \mathbf{G} \right) \right] + m_x.
\end{aligned}
\tag{3.20}
$$

In the next step, LLE is presented in the form of an eigenproblem, where Ω is sought frequency of modes, and $\hat{M}$ is eigen matrix with eigenvectors:

$$
i\Omega \mathbf{m_k} = \hat{M} \mathbf{m_k},
\tag{3.21}
$$

The eigenvector contains Fourier coefficients for both (x and z) components of magnetization. Thus, the eigenproblem is twice as big as the number of reciprocal vectors $\mathbf{G}$:

$$
\mathbf{m_k}^T = \left[\mathbf{m}_{x,\mathbf{k}} \left(\mathbf{G}_1 \right), \ldots, \mathbf{m}_{x,\mathbf{k}} \left(\mathbf{G}_N \right), \mathbf{m}_{y,\mathbf{k}} \left(\mathbf{G}_1 \right), \ldots, \mathbf{m}_{y,\mathbf{k}} \left(\mathbf{G}_N \right) \right].
\tag{3.22}
$$

Please note the index $\mathbf{k}$ next to vector $\mathbf{m}$. Wavevector now is a parameter, that is given externally for numerical calculations. The matrix $\hat{M}$ has a form:

$$
\hat{M} = \begin{pmatrix} \hat{M}^{xx} & \hat{M}^{xy} \\ \hat{M}^{yx} & \hat{M}^{yy} \end{pmatrix},
\tag{3.23}
$$

and is constructed from Eq. (3.19) and (3.20). Matrix elements are defined as:

$$M_{ij}^{xx} = -\frac{1}{H_0} M_S \left(\mathbf{G}_i - \mathbf{G}_j \right) S \left(\mathbf{G}_j + \mathbf{k} \right) \frac{\left(G_{xj} + k_x \right)}{\left| \mathbf{G}_j + \mathbf{k} \right|}, \tag{3.24}$$

$$M_{ij}^{zz} = \frac{1}{H_0} M_S \left(\mathbf{G}_i - \mathbf{G}_j \right) \frac{\left(G_{xj} + k_x \right)^2}{\left| \mathbf{G}_j + \mathbf{k} \right|^2} \left(1 - C \left(\mathbf{G}_j + \mathbf{k} \right) \right), \tag{3.25}$$

$$
\begin{aligned}
M_{ij}^{xz} = \; & -\frac{1}{H_0} M_S \left(\mathbf{G}_i - \mathbf{G}_j \right) C \left(\mathbf{G}_j + \mathbf{k} \right) - \delta_{ij} \\
& + \frac{1}{H_0} \sum_{\mathbf{G}_l} M_S \left(\mathbf{G}_i - \mathbf{G}_l \right) \lambda_{\text{ex}}^2 \left(\mathbf{G}_l - \mathbf{G}_j \right) \times \\
& \times \left[\left(\mathbf{G}_j + \mathbf{k} \right) \cdot \left(\mathbf{G}_l + \mathbf{k} \right) - \left(\mathbf{G}_i - \mathbf{G}_l \right) \cdot \left(\mathbf{G}_i - \mathbf{G}_j \right) \right],
\end{aligned}
\tag{3.26}
$$

$$
\begin{aligned}
M_{ij}^{zx} = \; & \frac{1}{H_0} M_S \left(\mathbf{G}_i - \mathbf{G}_j \right) \frac{\left(G_{xj} + k_x \right)^2}{\left| \mathbf{G}_j + \mathbf{k} \right|^2} \times \\
& \times \left(1 - C \left(\mathbf{G}_j + \mathbf{k} \right) \right) + \delta_{ij} + \\
& - \frac{1}{H_0} \sum_{\mathbf{G}_l} M_S \left(\mathbf{G}_i - \mathbf{G}_l \right) \lambda_{\text{ex}}^2 \left(\mathbf{G}_l - \mathbf{G}_j \right) \times \\
& \times \left[\left(\mathbf{G}_j + \mathbf{k} \right) \cdot \left(\mathbf{G}_l + \mathbf{k} \right) - \left(\mathbf{G}_i - \mathbf{G}_l \right) \cdot \left(\mathbf{G}_i - \mathbf{G}_j \right) \right].
\end{aligned}
\tag{3.27}
$$

At this stage, analytical work is done, and one needs to implement a problem in a specific programming language. The numerical part contains the definition of matrix, diagonalization, and postprocessing of the data. For this purpose, I used Python3 programming language[1]. This software is very efficient in doing research due to well-established libraries for numerical calculus and data visualization. PWEM requires rather basic matrix operations like multiplication, addition, and diagonalization, however computational time scales up parabolically with the amount of reciprocal vector, so there is a need for high optimization of code. The library NumPy, which I used heavily for this task, relies on the BLAS (Basic Linear Algebra Subprograms) which is a set of low-level routines greatly optimized for speed. Thus the code provides the reasonably fast implementation of PWEM that could effectively solve problems with dozens of thousands of reciprocal vectors.

---

[1]https://github.com/szymag/ZFN

The numerical studies encompasses also: data analysis and visualization. I implemented the codes in Python3 for postprocessing the outcomes of PWEM and included them in the package with the code of PWEM. There are two main outcomes of the PWEM: eigenfrequency and corresponding profiles of eigenmodes. This information can be presented visually as the plot of dispersion relation or IDOS (both are dependencies on frequency) and the plots of the spatial profiles of SWs (for selected frequencies). The profiles can be then processed further to obtain e.g., the spin wave–elastic wave cross section (work P1), logarithmic derivative (work P3), and localization measure (work P4). The codes for the calculation of these characteristics were also developed. Figure 3.1 present exemplary dispersion relation and SW modes obtained by PWEM.
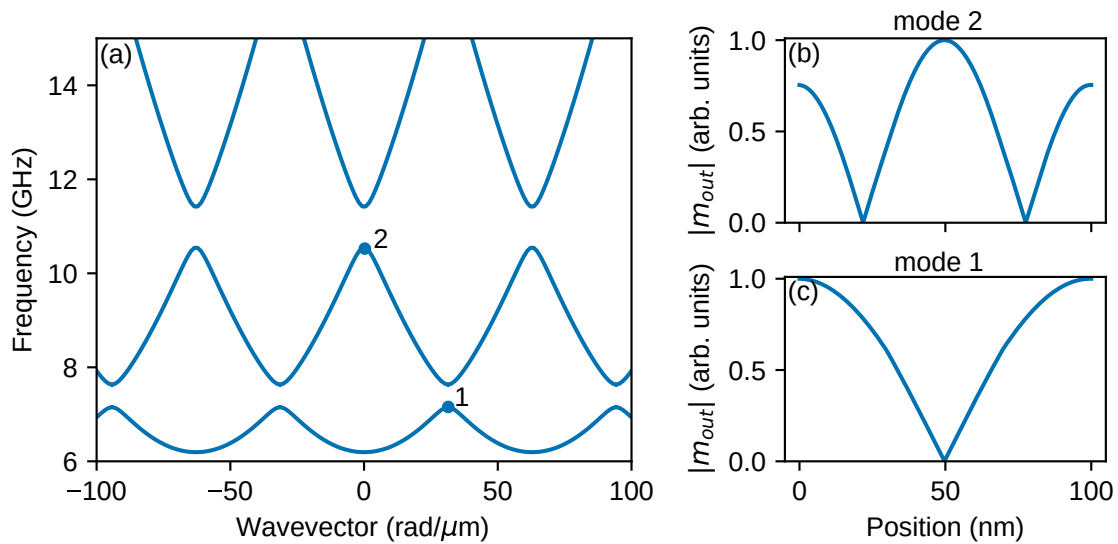
Fig. 3.1 (a) The dispersion relation obtained with plane wave expansion method for exchange spin waves in 1D magnonic crystal composed of two alternative repeating layers of thickness 20 nm and unit cell 100 nm. made of different materials: Co (60 nm width) and Py (40 nm width). (b) and (c) presents exemplary profiles of modes – the absolute value of dynamic comment of magnetization was plotted. Wavevector and frequency for which modes were obtained are marked on dispersion relation by blue dots.

Supercell approach

The PWEM can be used to calculate the spectrum of the system, that do have translational symmetry. The method still requires periodicity, however, the difference is in the definition of the unit cell. In this approach, we rather define a full system as a one unit cell, and periodicity is artificially assumed[69, 100]. In this manner, so-called the supercell approach was used

in work P3, where two semi-infinite one-dimensional crystals were defined within one unit cell, and in work P4, where the unit cell contained the finite approximate of the Fibonacci quasicrystal.

3.2   Micromagnetic simulations

The finite-difference method (FDM) and finite-elements methods (FEM) are the numerical techniques that are commonly used for solving differential equations[78], regardless of the geometry of the considered system. The implementation of these methods in the LLE creates a wide class of tools under the common name micromagnetic simulations (MS)[76]. Generally, they take the assumption of micromagnetism[16], where the system is treated as a continuum medium (i.e., the atomistic structure of the magnetic material is represented only by effective field, and the length scale is small enough to investigate nano- and micro-scaled effects), and then the LLE is solved on the discrete mesh. In my research, I used MuMax3[121] software that is based on FDM. Below, I shortly describe the assumptions and workflow that I develop to work with this software.

The first task in the computational scheme is to define the geometry of the considered system, which is then discretized. Since MumMx3 is FDM, the only way the system can be discretized is into cuboids with a regular grid. The field quantities (i.e., magnetization, effective fields) are discretized and integrated over the volume of the cuboid, while spatial derivatives are approximated by finite differences. This approach has two main drawbacks: it poorly convey the curved shapes, and since all elements have equal volume computational resources are used on the area that is not of particular interests. Fig. 3.2(a) presents an exemplary cuboid mesh of the sphere, with clearly visible stairs, where a curved edge should be expected. One can overcome this issue with finer cuboids, however, this approach is of course computationally costly. On the contrary, FEM can better represent complex geometries. Additionally, the mesh density can be adjusted on demand, i.e., in places where higher accuracy is required. An exemplary mesh suitable for FEM is presented in Fig. 3.2(b). It is visible, that edge of the sphere is well preserved. That freedom comes from the fact, that quantities are approximated by a set of interpolation functions. In general, implementation of the finite-element method is much more complex, and the software which provides this method is typically stand-alone. The specific physical problem can be then implemented. In such way community implemented Landau-Lifshitz equation for example in COMSOL[120] and FEniCSx[105]. In my research, I dealt with thin films and waveguides, which are perfectly suitable for MumMax3 software.

Definition of system properties in micromagnetic simulation

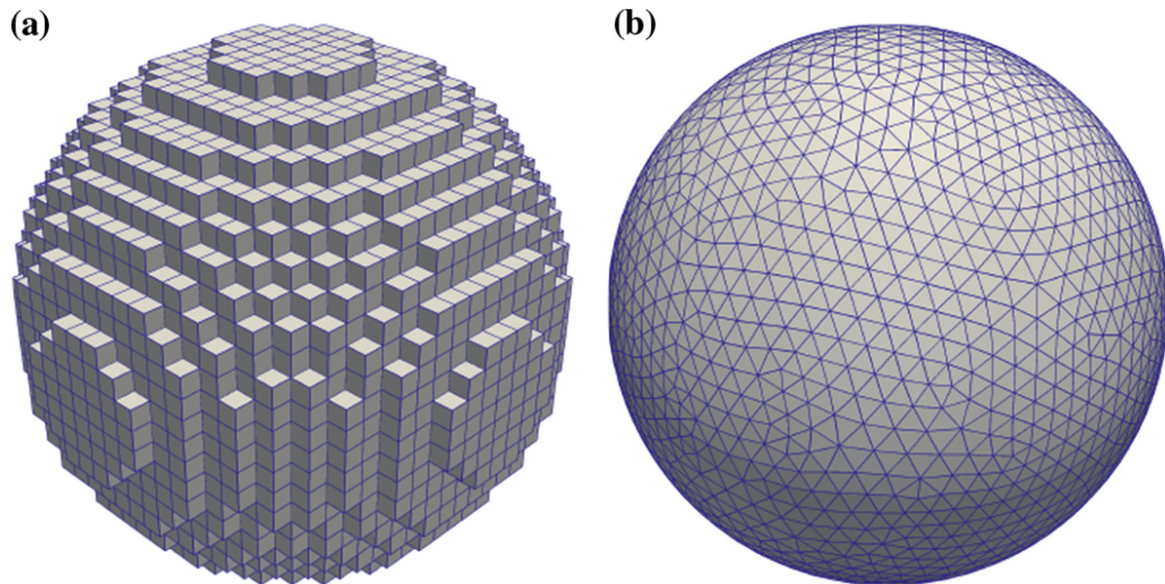**(a)**   **(b)**

Fig. 3.2 Mesh of the sphere. (a) presents mesh defined for finite difference method, where cell are cuboids and thus they badly represents the curvature of the body. (b) shows mesh constructed from tetrahedrons that can model the original shape. This mesh is suitable for the finite element method. Figure reprinted by permission from Springer Nature from Ref. [4], © 2015 Springer Nature Ltd..

The size of the mesh should fulfill several conditions. Firstly, it should be small enough to describe properly the dependence of magnetization in space, i.e., the direction of the magnetization vector should vary smoothly in space. The angle should be smaller than 0.4 rad. If one wants to investigate exchange spin waves, then cell size needs to be around the value of exchange length, which for typical magnetic material it varies from a few to dozen of nm. For larger waves, where dipolar interactions are dominant, cell size can be bigger than the value of exchange length, however, one should discretize in a way, to properly represent non-uniformity in the magnetization in the magnetic body. There are no typical values, that one can propose, and the proper grid size is selected by trial and error. Sometimes, assuming a cell too big is done on purpose, because it simplifies investigation since it will average variation of magnetization. For example, a common technique is to assume one cell through the thickness of a thin film. In this way, we neglect perpendicular standing spin waves.

In the next step, it is necessary to define on the already created grid, the magnetic body. It is called in MuMax3 geometry. There are several built-in functions like plane, ellipse, and ellipsoid. They can be modified later with a geometrical operation like intersection, addition,

etc. Magnetic properties are defined via a so-called region, where user define magnetic parameters like magnetization saturation, exchange length, and magnetization damping.

To investigate SW dynamics, one needs to achieve a stable magnetic configuration. This is a necessary condition for SW investigation because otherwise, all three components vary in time, and the assumption of precession with a small angle around equilibrium cannot be used. The MuMax3 has implemented a method to find the minima of the magnetic system by minimizing free energy. It is done with the steepest descent algorithm. There are many approaches for SW excitation, and any time-depended torque leads to SW excitation. It is worth mentioning, that in the real magnetic structures in room temperatures SW are present all time, they are excited thermally, and can be detected by ultra-sensitive tools, like Brillouin light scattering spectroscopy[118]. In a linear regime, the frequency of the source corresponds to the frequency of SW. Depending on the need, one can reproduce the experimental source into mumax3, by shaping effective field $h(\mathbf{r}, t)$. The most often used antenna design is coplanar waveguide[92], where microwave current flows in the central line, and is surrounded from both sides by ground lines. Knowing the analytical formula or numerical data for the spatial distribution of the magnetic field emitted by the antenna, the profile can be introduced into the simulations. This is done when one is interested specifically in the SW modes that are excited in the experiment, and the reproduction of the efficiency of SW excitation is crucial in the research. Otherwise, one can use an easier approach and define some arbitrary dynamic magnetic field. The simplest way is the excitation of harmonic signal with frequency f:

$$h(\mathbf{r}, t) = h_0(\mathbf{r}) \sin(2\pi f t), \tag{3.28}$$

where, $h_0(r)$ is the spatial amplitude of the signal, and can take the form of Heaviside step function, non-zero on several unit cells. SW frequency is given, and system response with wavenumber, thus the area of excitation, i.e., the width of fictitious antenna, should be smaller than half of SW wavelength to efficiently excite SW. Particular attention should be also put to the amplitude. The absolute value should be some fraction of the external field, to keep the system in the linear regime, and keep the cone of precession small enough. The direction of excitation needs to be applied perpendicularly to the direction of the external magnetic field. This kind of excitation is used in the work P2, where a harmonic wave is propagating in the magnonic waveguide. The objective is to observe SW spatial distribution.

Another common technique is broadband excitation, used e.g. for numerical calculations of system's dispersion relation. A wide range of frequencies and wavevectors needs to be excited, which means that in real spaces, i.e., time and space one needs to define a magnetic field by a function that after transformation to reciprocal spaces will have desired profile, ideally uniform distribution in some range of frequencies. These properties are fulfilled by

'sinc' function:

$$h(\mathbf{r},t) = h_0(\mathbf{r}) \operatorname{sinc}(kx) \operatorname{sinc}(2\pi f_{\text{cut}})(t - t_0), \qquad (3.29)$$

where f_{cut} is a frequency until which SWs are excited, and t_0 determines the shift of the signal in time. The profile of the sinc function is presented in Fig. 3.3 as well as its Fourier transform. Although the delay t_0 does not affect the distribution of the signal itself, it shifts the maximum of a function, and then all shape can be generated by the antenna. Otherwise, if one keeps $t_0 = 0$ only half of the signal will be generated and this can lead to artifacts in the spectrum of SWs. The FFT in Fig. 3.3(b) presents distribution of excited frequencies. f_{cut} was assumed to be 7 GHz, and as it can be seen till this value distribution is uniform almost across all ranges except the region of $f_{\text{cut}} = 7$ GHz. The oscillation around f_{cut} are so-called Gibbs phenomenon and it is the effect of discontinuity of squared function at f_{cut}. Another important factor to which one needs to pay attention is sampling in time. To fully reconstruct a continuous function by discrete sequence the sampling must be at least twice the highest frequency, i.e., f_{cut}.
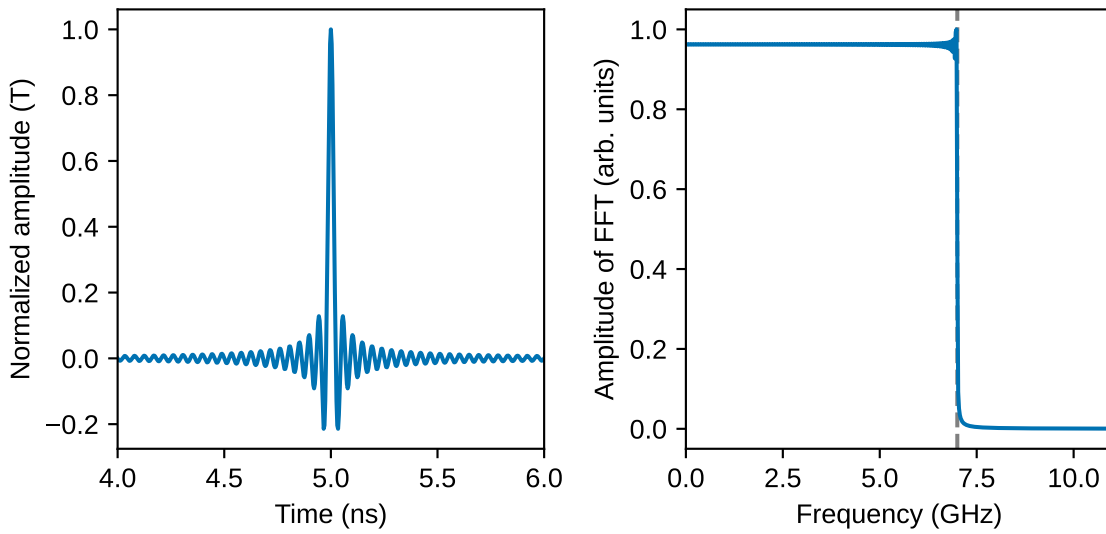
Fig. 3.3 (a) Profile of sinc function that can generate broadband spectrum of waves. The curve is defined with $f_{\text{cut}} = 7$ GHz and $t_0 = 5$ ns. (b) The FFT spectrum of sinc function. The jump at 7 GHz refer to f_{cut} frequency.

Postprocessing

The results from the micromagnetic solver are given in the form of three component magnetization vectors on the defined grid at the specific time frame. In other words, the software

returns a snapshot of magnetization in time at a defined sampling rate. In the next step, the task is to extract relevant information by means of numerical postprocessing of the data.

Raw data are obtained for real spaces, i.e., time and space. In these domains, one can investigate for example spatial profile of SW, and interference. For example, after reaching a steady state, integrating signals over time can provide information about the spatial distribution of SW in the system[102]. It is also possible for example to investigate SW characteristics like transmittance and phase shift that SW can get after propagating through some defined barrier. This kind of analysis was performed in the P2. The next technique to work with data provided by micromagnetic simulation is to transform them into reciprocal spaces, time into frequency, and/or space into a wavevector. This is done by applying a fast Fourier transform (FFT) to the data. Thanks to this, one can study the dispersion relation of SW and profiles of excitations.

Chapter 4

Research

In this chapter, I present my results published in four peer-reviewed journals. All these works are concentrated on the SW dynamics in magnonic structures, in particular, on the role of localization and propagation in the system. Each paper is presented in a separate section, named the same as the titles of the manuscript. For convenience, I will refer to these publications by the labels: P1-P4. Papers are included in the dissertation in order of their publication date:

- P1 - Driving magnetization dynamics in an on-demand magnonic crystal via the magnetoelastic interactions

- P2 - Anomalous refraction of spin waves as a way to guide signals in curved magnonic multimode waveguides

- P3 - Interface modes in planar one-dimensional magnonic crystals

- P4 - Spin-wave localization on phasonic defects in one-dimensional magnonic quasicrystal

P1 paper was published with experimentalists from the Netherlands ("University of Groningen"), Germany ("University of Greifswald"), and France ("Le Mans University"). We investigated the role of SW localization on magnetoelastic interaction. P2 treats the topic of SW in magnonic waveguides that have bent. With the theoretical team from Ukraine ("Igor Sikorsky Kyiv Polytechnic Institute" and "Institute of Magnetism of NAS of Ukraine"), We proposed a concept based on a graded refractive index, that allows passing SW through bent keeping the coherence of the signal. P3 concern the theoretical investigation of the interface modes between two joint one-dimensional magnonic crystals. We derive their bulk-to-edge correspondence for SW, which gives the condition for the existence of interface modes. In

P4 we investigate the role of defects in the one-dimensional quasiperiodic magnonic crystal. We discuss the evolution of the SW spectrum and mode localization under different levels of disorder.

Each section contains a short introduction to the paper and describes my contribution.The statements of other co-authors about their contributions are gathered in Appendix B. Publications are placed in the thesis with the publishers' permission (American Physical Society, Springer Nature).

4.1   P1 - Driving magnetization dynamics in an on-demand magnonic crystal via the magnetoelastic interactions

The research presented in the paper P1 was done in collaboration with an experimental group from "Zernike Insitute for Advanced Materials" at "the University of Groningen" in the Netherlands. The experiment was conducted by C.L. Chang under the supervision of R. I. Tobey. Support in conducting the experiment was given by a group from IMMM UMR CNRS in Le Mans in France and the Institute of Physics at the University of Greifswald in Germany.

The collaboration started from experimental measurements of magnetization dynamics in a 40 nm thick film, for the various configurations of ferromagnetic layer and substrate (Ni or $Co_{0.2}Fe_{0.6}B_{0.2}$ deposited on MgO or glass). The experiment relies on the optical excitation of elastic and magnetic dynamics by two interfering laser pulses shining onto the surface[52]. The goal was to suppress magnetization periodically in space, making the one-dimensional magnonic crystal created on-demand. In the system were excited thermoelastically the surface acoustic waves that could propagate along the magnetic film. Due to magnetoelastic interactions[129, 26], the spin waves could also be excited. The spin wave excitation was then probed by a normally incident probe pulse that can sample the temporal evolution magneto-optical Faraday effect with femtosecond resolution. This experiment collects a global, averaged signal of magnetization dynamics. The measurements were conducted for various magnetic field values and in-plane angles.

The experiment showed the angular dependence between the direction of propagation of the surface acoustic wave, being the direction of periodicity of magnonic crystal, and magnetic field: the null signals at 0 and 90 degrees were recorded, as was expected for magnetoelastic interactions of spin waves with Rayleigh surface acoustic wave. However, for Ni deposited on MgO additional suppression in amplitude was found around 30 degrees making two distinct lobes in this angular dependence. It was also reported that the shape of

the resonance differs in the two angular regimes, i.e., low angle and high angle regimes. After applying Fourier transformation to the time-resolved Faraday signals, data revealed that for high angles, the peak is well represented by two Lorentzians, while for low angles peak can be fitted with one Lorentzian. At the time of discovering these results that were at first glance not expected, prof. Tobey visited Poznań and gave a seminar describing his experiments and highlighting recent findings. At that moment, we did not have a tool that could solve magnetoelastic interactions. Therefore, we decided to use the plane wave expansion method and investigate the evolution of spin wave eigenmodes under magnetic field applied in-plane at different angles, and qualitatively estimate the Faraday signal. About that time Rodolfo Gallardo published, on arXiv, a paper [32] where he considered an in-plane magnetic field, applied at the oblique direction with respect to wavevector. I implemented this feature to the code of the plane wave expansion method and could calculate spin wave spectra in the experimentally considered system. The implementation was verified by Mateusz Zelent, who performed the micromagnetic simulations. We could observe that for low angles the frequency separation of modes was low, while for higher angles fundamental mode was distinctive from other quantized modes.

From the plane wave expansion method, we extracted the profile of spin wave modes. Thanks to this, we could analyze the evolution of spin wave localization in the one-dimensional magnonic crystal under angle variation. We introduced phenomenological formula describing the magnetoelastic interaction that takes into account spatial profile and frequency separation. We could qualitatively reproduce the measurements in the sense that two lobes were also observed in the angular dependence of the Faraday signal.

In work P1, I performed numerical calculations of spin wave spectra with the plane wave expansion method, analyzed data, wrote sections 'the model', and 'numerical simulations', and contributed to the manuscript preparation.

Driving Magnetization Dynamics in an On-Demand Magnonic Crystal via the Magnetoelastic Interactions

C. L. Chang,[1] S. Mieszczak,[2] M. Zelent,[2] V. Besse,[3] U. Martens,[4] R.R. Tamming,[1] J. Janusonis,[1]
P. Graczyk,[2] M. Münzenberg,[4] J.W. Kłos,[2,4] and R. I. Tobey[1,5,*]

[1] *Zernike Institute for Advanced Materials, University of Groningen, Groningen, Netherlands*
[2] *Faculty of Physics, Adam Mickiewicz University in Poznan, Poznań, Poland*
[3] *IMMM UMR CNRS 6283, Le Mans Université, Le Mans Cedex, France*
[4] *Institute of Physics, University of Greifswald, Greifswald, Germany*
[5] *LUMOS, Center for Integrated Nanotechnologies, Los Alamos National Laboratory, Los Alamos, USA*

Using spatial light interference of ultrafast laser pulses, we generate a lateral modulation in the magnetization profile of an otherwise uniformly magnetized film, whose magnetic excitation spectrum is monitored via the coherent and resonant interaction with elastic waves. We find an unusual dependence of the magnetoelastic coupling as the externally applied magnetic field is angle- and field-tuned relative to the wave vector of the magnetization modulation, which can be explained by the emergence of spatially inhomogeneous spin-wave modes. In this regard, the spatial light interference methodology can be seen as a user-configurable, temporally windowed, on-demand magnonic crystal, potentially of arbitrary two-dimensional shape, which allows control and selectivity of the spatial distribution of spin waves. Calculations of spin waves using a variety of methods, demonstrated here using the plane-wave method and micromagnetic simulation, can identify the spatial distribution and associated energy scales of each excitation, which opens the door to a number of excitation methodologies beyond our chosen elastic wave excitation.

I. INTRODUCTION

The magnetic excitation spectrum of a thin (tens of nanometers), uniformly magnetized film is well studied and understood [1,2]. The fundamental *spin-wave* mode, where the magnetization precesses in phase (i.e., with the wave vector $k = 0$) in the entire volume of the system, is called the Kittel mode and can be measured by experimental techniques such as ferromagnetic resonance or time-resolved magneto-optical Kerr (or Faraday) effects [3]. One can also observe spin-wave (SW) confinement (and quantization) along the film depth, whose energy depends on film thickness and pinning effects at the surfaces. These modes, called perpendicular standing SW modes (PSSW), are still laterally uniform in amplitude and phase [3] for in-plane wave vector $k = 0$.

Going beyond lateral phase homogeneity brings about the appearance of spin-wave modes of finite wave vector ($k > 0$). At low wave vectors, the spin-wave dispersion is highly anisotropic with respect to the direction of an externally applied magnetic field due to dominating dipolar interactions [4,5]. With increasing wave vector,

exchange interactions become more important and the SW modes are termed the isotropic exchange SW. Depending on the particulars of the dispersion relation (determined by magnetic field orientation and the relative strength of dipolar-to-exchange interactions), the SW modes can have positive, zero, or negative group velocity. The SW dispersion, in both dipolar and exchange regimes, can be found by optical means using Brillouin spectroscopy [6], while time-resolved magneto-optical imaging based on the Faraday effect can also be used to determine the dispersion of SW [7]. This latter technique is limited to purely dipolar SWs due to the spatial resolution limits associated with the particular probing wavelength that is used.

Structuring the lateral magnetic landscape further modifies the SW spectrum, while opening opportunities for spin-wave localization, control and manipulation. This is the scientific discipline of magnonics, where artificially engineered and spatially patterned magnetic materials such as arrays of magnetic dots [8], holes in magnetic films (antidots) [9,10], magnetic stripes [11–13], and bicomponent arrays [14], as well as more complex spatial patterns such as magnonic quasicrystals [15] or the inherent domain structure of multilayers of high perpendicular anisotropy [16], can be used to manipulate and localize

*[*]r.i.tobey@rug.nl

SW dynamics. The periodic magnetization profile forms a so-called "magnonic crystal."

For magnonic crystals (MCs) operating in a dipolar regime, the dispersion relation can be tuned by the change of the direction of the external field with respect to the periodically patterned structure [17,18]. This effect results from the presence of static and dynamic (de)magnetizing fields and is observed even for standing ($k = 0$) SW modes. The additional feature of MCs is a band structure of SW dispersion that is manifested by the presence of multiple modes for the same value of wave vector k (when k is reduced into the first Brillouin zone). Therefore, at $k = 0$, there exists a sequence of modes for which the spatial distribution of the amplitude and phase within an individual unit cell of MC is repeated periodically in the whole structure.

Shining light onto the surface of a magnetic material can modify the magnetization landscape due to heating, thereby opening the possibility of using the spatial patterning of light to induce magnonic behavior. In most ultrafast optical experiments on magnetic materials, a large-aperture optical beam is used to excite the sample surface, resulting in uniform suppression of the magnetization profile, impulsively modifying the effective field landscape, and generating the laterally homogeneous free precession of a Kittel-like mode, as well as PSSW excitation [3]. Attempts to laterally shape the excitation pattern have had success as evidenced in recent papers by Busse *et al.* [19] and Vogel *et al.* [20] utilizing continuous and pulsed laser sources, respectively. In the context of magnonics, spatially patterned optical excitation offers user-defined, reprogrammable arrangements of magnetic properties with the potential for unparalleled control of spin-wave generation and propagation [21]. These latter two aspects directly relate to the possibility of spin-wave signal processing [22,23], combining two required elements, namely, a spatially extended, or distributed, coherent source of SWs and the possibility to manipulate their respective phases. Both of these requirements can be fulfilled, in principle, by our optical interference methodology.

In this paper, we provide a unique view of the effects of a spatially periodic optical excitation of a uniform magnetic film, the emergence of a magnonic crystal, and finally the elastic excitation of spatially distributed SW modes [24,25]. We extend the interpretation and understanding of our previous results [26–28] by detailing the precessional response as a function of the angle of the applied magnetic field relative to the MC wave vector. In doing so, we augment our previous identification of elastically driven ferromagnetic resonance to include localized spin-wave modes that exist on the magnetically modulated magnetization background. The periodic and inhomogeneous pattern of spin-wave eigenmodes also allows us to change the magnetoelastic interaction. We show that this nonuniformity alters the anisotropy of the magnetoelastic coupling observed in homogeneous magnetic film [29,30]. This additional anisotropy of a magnetoelastic interaction can be explained only if the spatial modulation in the SW profiles is accounted for, in effect, an optically induced magnonic crystal.

The present paper contains experimental and modeling sections. In the first section, we perform the transient grating (TG) experiments on two materials, Ni and CoFeB thin films (40-nm films on transparent substrates such as glass or MgO), which show markedly different responses as a function of the angle of the applied field for a fixed acoustic wavelength of 1.1 μm. In the Ni films (low Curie temperature, T_C, low saturated magnetization, M_S), an unexpected and previously unwitnessed (binary) phase shift of π is evident as the magnetic field angle is scanned from zero to 90 degrees (relative to the TG wave vector); see Fig. 1. Accompanying this evolution in phase is a strong suppression in precessional amplitude in the intermediate region, indicative of interference between two (or more) distinct modes of precession in two different angular regimes. This interpretation is supported by the second set of measurements on $Co_{0.2}Fe_{0.6}B_{0.2}$ (high T_C, high M_S), which exhibit elastically driven precession in only one of the previously determined angular regimes and, amazingly, the near-complete suppression of precession in the second angular regime.

We claim that these findings can be reconciled by considering the interaction of elastic waves with the underlying modulated magnetization landscape induced by the spatially periodic heating. Using the plane-wave method (PWM) [31,32], we calculate the SW eigenfrequencies
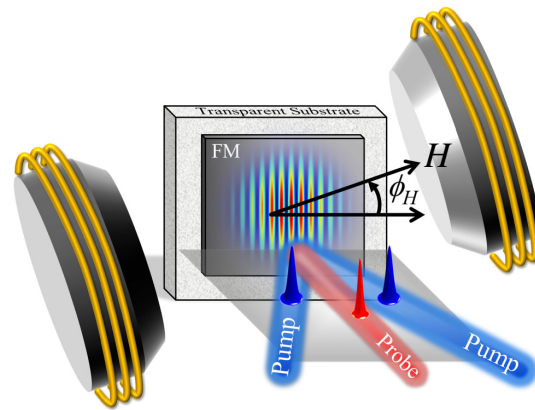

FIG. 1.   We excite the ferromagnetic thin film with two interfering ultrashort pulses, which simultaneously generates the surface propagating acoustic waves and laterally suppresses the magnetization profile to form the magnonic crystal. A magnetic field H can be fully rotated around the sample normal and the angle ϕ_H denotes its direction relative to the periodicity of a magnonic crystal.

and corresponding spatial profiles, taking into account the (de)magnetizing fields as a function of the angle between the applied magnetic field and the direction of modulation of magnetization (see Fig. 1). The calculations are performed for selected modulation depths of the time-dependent magnetization landscape, which are extracted from the two-temperature model (TTM) and two-dimensional thermal diffusion considerations [28]. The angular dependence of the eigenmode frequencies (at $k = 0$) is verified by micromagnetic simulations (MS) and excellent agreement is achieved between the more rigorous and semianalytical PWM and numerical micromagnetic results.

II. EXPERIMENTAL RESULTS

We begin with a brief recapitulation of the key features of our experimental approach. As shown in Fig. 1, the experiment relies on the impulsive optical excitation of elastic and magnetic dynamics at the surface of a thin metallic ferromagnetic film by impinging two interfering laser pulses onto its surface. In our experiments, we utilize the second harmonic of the Ti:sapphire amplified laser as the excitation source, whose primary action is to (1) impulsively suppress sample magnetization [33,34] in the form of a spatially periodic pattern and (2) thermoelastically excite acoustic waves that propagate along the surface of the film/substrate heterostructure [35,36]. We have previously identified the acoustic waves as both Rayleigh surface acoustic waves (SAW) and surface-skimming longitudinal waves (SSLW) [27]. The latter has also been shown recently by Sander *el al.* [37]. The ensemble of excitation processes is then probed by a normally incident probe pulse and can include time-resolved diffraction of probe light due to the spatial periodicity of strain and/or surface deformation and/or polarization analysis of the transmitted or specularly reflected probe light to extract magnetization dynamics. For magnetization dynamics, we also implement an electromagnet that can rotate around the sample normal. Further experimental details can be found in the work of Janusonis *et al.* [28].

The details of the magnetoelastic interaction depend on the material and substrate combination. However, we can make a few general statements. For a fixed grating periodicity, the observed frequencies are solely determined by the velocity of acoustic waves in the film/substrate heterostructure and may depend on the propagation direction, for example, in a crystalline material. The amplitude of strain will vary depending on which elastic mode is being driven and the film/substrate thermoelastic properties as well as the grating periodicity. With regard to magnetization dynamics, there will be an applied field condition wherein the natural precessional frequency of the ferromagnetic resonance or a particular spin-wave resonance will match that of the underlying elastic wave, at

which point elastic energy will drive precessional motion resonantly via magnetoelastic interactions, provided the spatial symmetries of the particular magnetic and elastic excitations are similar. The resonance condition can be visualized either in the frequency domain as an increase in precessional amplitude in the Fourier transform or in the time domain by an increase in the temporal range over which precession occurs and/or the amplitude of this precession (i.e., in the maximum polarization rotation in a Faraday geometry). Furthermore, in the time domain, a characteristic phase evolution is observed as the resonance is traversed. Finally, we mention that there are conditions under which parametric frequency-mixing effects have been observed [38], wherein magnetization precession is driven at the sum and difference frequencies of the underlying elastic wave(s). Until now, we have speculated that all resonance conditions were the result of the interaction of the elastic waves with the uniform precessional motion, i.e. the Ferromagnetic Resonance (FMR).

The first indication of nontrivial dynamics in our experiments is contained in Fig. 2, where we compare the (normalized) temporal evolution at the resonance condition for two representative magnetic field angles, 15° and 60° (we will continue to compare these two angles as representative angles for the general features of the experiments). The data shown here are for the Rayleigh SAW resonance for the Ni/MgO heterostructure at approximately 500 G. Both plots, being on resonance and driven by the same acoustic transient (the elastic frequency is independent of magnetic field angle), precess at the same frequency. However, there are clear differences. First and most notably, the plots show a difference in precessional phase—an unexpected feature for an elastically driven FMR in a uniformly magnetized film. Second, the shapes of the magnetization precession in time are drastically different for the two plots; particularly, the onset time at 60° is considerably faster than at 15°. Both features (delayed onset, opposite precessional phase)
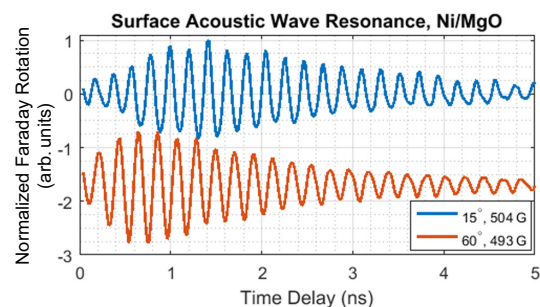

FIG. 2. Normalized time-resolved Faraday traces at the Rayleigh surface acoustic wave resonance for Ni/MgO at two representative angles. The linecuts exhibit opposite phases of precession and differences in their onset times.
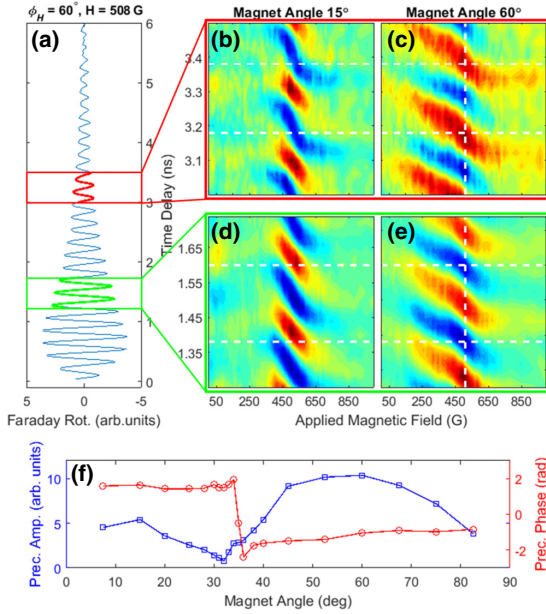
FIG. 3. The surface acoustic wave resonance for Ni(40 nm)/MgO. (a) A representative time-resolved Faraday response is taken for magnet angle $\phi = 60°$ and at resonance field $H \approx 504$ G [vertical dashed line in (c),(e)]. The time response (a) shows the oscillatory dynamics that persist for nearly 6 ns. The amplitude of the Faraday signal exhibits the resonance dependence on applied field H both for late times (b),(c) and early times (d),(e). This resonance can be attributed to the interaction between elastic and magnetic degrees of freedom. The backward S patterns in (b)–(e) show that the phase changes by π as the resonance condition is crossed with an increasing field. A comparison between (b),(d) and (c),(e) shows an additional change in the precessional phase between low and high angles, as indicated by the white horizontal lines (the key finding of this paper). Accompanying the changes in the precessional phase is a suppression of the precessional amplitude for intermediate values of the magnet angle. The change of precessional amplitude and phase in dependence on the angle at the peak resonance field is shown in (f).

are characteristic responses for any Ni/substrate configuration and any type of elastic wave resonance (SAW or SSLW). In the remainder of this report, we provide details of these unexpected results in order to support our picture of elastic excitation of a variety of spin-wave modes in the (optically induced) magnetically textured thin film.

In Fig. 3(a), we replicate the time-resolved Faraday plot shown in Fig. 2 to bring attention specifically to the flipping of the precessional phase for different angular regimes. A single time trace is extracted from our full field measurements, portions of which are shown in Figs. 3(b)–3(e) for representative magnet angles of 15°

and 60°. As indicated in the time trace [Fig. 3(a)] the full field scans are shown for both late time delays [red, panels (b) and (c)] and early time delays [green, panels (d) and (e)]. Each panel (b)–(e) is individually scaled in amplitude in order to show the shape of the resonance. We draw attention as well to the backward S shape in each of the panels. As mentioned previously, this shape reveals that a π phase shift occurs as the resonance is traversed and is the hallmark of a driven harmonic oscillator.

This representation brings into focus precessional phase differences between the angles 15° and 60° as can be seen by following the horizontal lines [compare panels (b) and (c), (d) and (e)]. In assessing the full angular range, we identify an intermediate angular regime where these two precessional features interfere, resulting in a suppression of measured precessional amplitude. This interference effect is shown in Fig. 3(f), which is extracted from Fourier transforming the time domain data and assessing the precessional amplitude at the peak resonance field. Accompanying this fitting procedure, the phase of precession is also extracted and overlaid in panel (f). For Ni/MgO, only angles between 7.5° and 82.5° are acquired, but supporting data in the Appendix Sec. 1 show full angular dependencies for Ni/glass heterostructures and null signals at 0° and 90°, as expected for the magnetoelastic interaction. The suppression in amplitude in an angular range around 30° separates two excitation "lobes." We find that all angles in the first lobe display the phase indicated in Figs. 3(b) and 3(d), while all angles in the second lobe display the precessional phase indicated in (c) and (e) [i.e., the extracted phase in (f) is binary]. The same phase-reversal and amplitude-suppression phenomena are present for all acoustic frequencies regardless of the acoustic mode (SAW or SSLW), all Ni/substrate combinations (Appendix Sec. 1), and are only a function of the relative angle between the excitation wave vector and applied field. The latter are verified by changing the absolute angle of the transient grating excitation (by rotating the phase mask angle) and finding the new magnet angle where suppression occurs.

It is also clear from the data displayed in Figs. 3(b)–3(e) that the shape of the resonance differs in the two angular regimes. To extract this behavior, we apply Fourier transforms to the time-resolved data for all magnetic field angles. Representative Fourier transforms for 15° and 60° are shown in Figs. 4(a) and 4(b) along with linecuts and associated two-Lorentzian fits in panels (c) and (d). We make two notes that hold generally for all excitation frequencies and substrate materials. (1) For angles in the second response lobe ($\theta > 40°$), the resonance line shape is well represented by a two-Lorentzian fit, with a main resonance (blue arrow) and a prominent low-field shoulder (red arrow). The field at which the shoulder resonance occurs strongly reduces as the magnetic field angle is increased. (2) In the low angle regime ($\theta < 20°$), the lineshape is not well represented by Lorentzians and always exhibits

a suppressed spectral weight on the low field side of the resonance. Intermediate angles (near the suppression) are difficult to assess due to low precessional amplitude and the onset of mixed-phase behavior.

The positions of the main resonance and shoulder are plotted in Fig. 4(e), where the error bars represent the widths of the resonances (the widths of the resonances do not change appreciably as a function of angle). Center positions and widths are extracted from the multi-peak fitting procedure. Regardless of the fitting function (Lorentzian or Gaussian), the peak positions are found consistently, while details of the lineshape can only be recovered by utilizing the appropriate function in the appropriate angular range. In Appendix 2, we show the resonance line shapes as the angle is increased to show the shoulder dispersion.
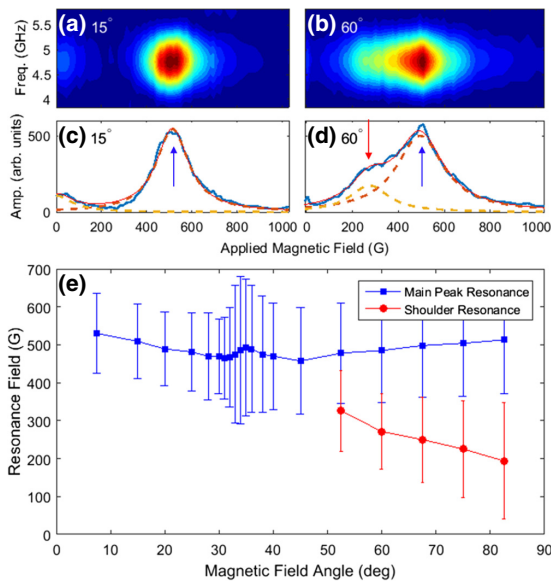
FIG. 4. (a),(b) The Fourier amplitude of the magnetization precession shows the driving frequency of approximately 4.8 GHz, which is dictated by the excitation grating period and acoustic velocity. Plots (c),(d) present the field-dependent line shapes of (a),(b) accompanied by two-Lorentzian fits to the data. At all angles above 40°, the resonance line shape is well represented by a two-Lorentzian fit incorporating a main resonance (blue arrow) and a shoulder (red arrow). At all angles below approximately 20°, the resonance line shape is not reproduced by a Lorentzian fit; specifically the low field side exhibits a reduced spectral intensity. For intermediate angles, the resonance amplitude is small and consequently the line shape is difficult to fit. The resonance fields of both the main response and high-angle shoulder are plotted in (e), where the error bars represent the widths of the resonances. The strongly dispersing shoulder is evident and can be seen explicitly (see Appendix 2 for detailed discussion).
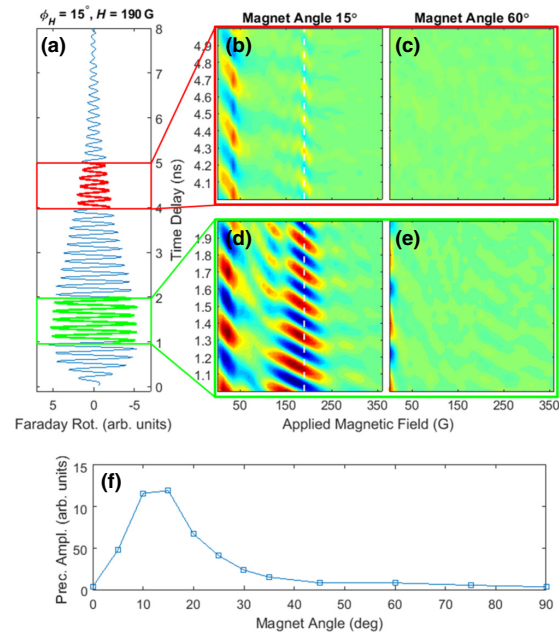
FIG. 5. The magnetoelastic response for $Co_{0.2}Fe_{0.6}B_{0.2}$(40 nm)/glass is observed at low magnet angles only. (a) A representative time-resolved Faraday signal is displayed for the higher elastic resonance (SSLW) at $H = 190$ G and $\phi_H = 15°$ [see the dashed vertical line in (b),(d)]. (b)–(e) $Co_{0.2}Fe_{0.6}B_{0.2}$ only exhibits at low magnet angles while the precessional motion at large magnet angles is strongly suppressed (f). Panels (b)–(e) are plotted on the same scale. In comparing this result to Ni samples, we recognize that only the first precessional lobe is active in $Co_{0.2}Fe_{0.6}B_{0.2}$, while two distinct precessional lobes are active in Ni.

We now turn to the response in the second test material, $Co_{0.2}Fe_{0.6}B_{0.2}$, which shows both similarities and differences in comparison to the Ni sample. First, it is clear that a similar resonance condition can be achieved [Figs. 5(a)–5(f)]. At a 15° magnet angle, we show the response for the SSLW (5.25 GHz) resonating at approximately 150 G, while the SAW response can be seen at much lower field values (< 50 G) (because of the larger M_S, all resonances are downshifted in the applied field relative to the low M_S materials for a fixed excitation frequency). The precessional motion persists for extended lengths of time, while the width of the resonance as a function of the applied field is narrow; both features are related to the low Gilbert damping in this material (precessional damping parameters for these films were previously measured by members of this collaboration [39]). Furthermore, owing to this narrow resonance, nearby resonance features are now apparent. This is especially the case on the

low-field side (approximately 100 G, 1.8 ns) and a suggestion of a resonance on the high-field side (> 250 G). Both additional resonances clearly have the same frequency as, but appear to be out of phase with, the main SSLW feature. However, perhaps the most striking deviation from the Ni data is the near-complete suppression of precessional motion at large angles. The integrated intensity at the SSLW resonance is shown in panel (f), indicating that this suppression is present over a large angular range. To summarize, a comparison between the two materials indicates that, for Ni, precession occurs in two distinct angular regimes, accompanied by an intermediate interference, while for $Co_{0.2}Fe_{0.6}B_{0.2}$ only the first precessional lobe can be accessed. In both materials, the first precessional lobe peaks at approximately $15°$. We mention in passing that our films of $Co_{0.2}Fe_{0.6}B_{0.2}$ on glass substrates do exhibit a uniaxial in-plane anisotropy (significantly weaker than reported in [40]); however this is determined not to be the cause of the suppression in high angle response.

It is our contention that these effects are accounted for if we consider the laterally varying (transient) magnetic texture, its associated spin-wave distribution, and finally their resonant interaction with phase-locked elastic waves. We are guided into this line of thinking based on two considerations. First, a recent paper by Langer *et al.* [41] showed both in calculation and experiment that a laterally varying demagnetization landscape (along one dimension) localizes SW distributions in different regions of the MC based on the angle of the applied magnetic field. Secondly, in comparison to other works in magnetoelastics, ours is the only one in which acoustic waves interact with a spatially modulated magnetization profile, as well as the only one that shows anomalous angular dependence. In experiments most similar to ours, the resonant interaction between surface propagating elastic waves and magnetization [30,42,43] exhibits coupling behavior roughly peaked at $45°$, with no indication of a suppression at intermediate angles. These studies occur on uniformly magnetized films, while the experimental technique (acoustic power transmission) precludes a direct measurement of the magnetization and the details of precessional phase, as we achieve here.

To incorporate the spatial periodicity in our understanding, we take cues from Langer *et al.* [41] and determine the SW eigenmodes in our laterally modulated magnetization profile. We calculate the temperature profile using the TTM until the electrons and lattice are in thermal equilibrium within the pump excitation volume and then propagate this temperature gradient in two dimensions using COMSOL's thermal diffusion capabilities. The simulation incorporates the thin film and substrate thermal conductivities as well as the thermal boundary resistance between the two dissimilar materials. Periodic and insulating boundary conditions are used where appropriate. From this temperature profile, a magnetization profile

$M_S(x)$ is calculated using a Curie-Weiss law for Ni and data measured on similar films of $Co_{0.2}Fe_{0.6}B_{0.2}$ [19]. For the timescales involved in our experiments (several nanoseconds), the temperature and magnetization profile are taken as constant throughout the depth of the film.

III. THE MODEL

We use two computational methods to simulate the experimental outcomes and to understand the physical mechanism behind them: the plane-wave method based on homemade code and micromagnetic simulations performed with the aid of the MUMAX3 package [44]. For PWM, we use M_S calculated numerically using TTM, whereas, for MS, we approximated this profile with a sinusoidal function. Both methods use the Landau-Lifshitz (LL) equation as an equation of motion:

$$\frac{\partial \mathbf{M}}{\partial t} = \mu_0 \gamma \mathbf{M} \times \mathbf{H}_{\text{eff}}, \quad (1)$$

where μ_0 is the permeability of vacuum, γ is the gyromagnetic ratio, and $\mathbf{M}$ is the magnetization vector. $\mathbf{H}_{\text{eff}}$ denotes the effective field, which is composed of the following terms:

$$\mathbf{H}_{\text{eff}} = \mathbf{H}_0 + \mathbf{H}_{\text{DM}}(\mathbf{r}, t) + \mathbf{H}_{\text{ex}}(\mathbf{r}, t). \quad (2)$$

The field $\mathbf{H}_0$ denotes the in-plane applied external magnetic field; $\mathbf{H}_{\text{DM}}(\mathbf{r}, t)$ is the demagnetizing field; and $\mathbf{H}_{\text{ex}}(\mathbf{r}, t)$ is the exchange field [45]. In our system, the external field can be rotated in-plane with respect to the one-dimensional (1D) spatial profile of magnetization saturation (Fig. 1). In both the PWM and MS calculations, we assume the following values of material parameters: $\gamma = 176$ GHz/T, $\mu_0 H_0 = 0.05$T (500 G), $M_{S,Ni} = 0.484 \times 10^6$ A/m, exchange length $\lambda_{\text{ex,Ni}} = 7.64$ nm, period of $M_S(x)$ $\Lambda = 1.1$ μm, and thickness of the Ni layer $d = 40$ nm. Since the magnetic landscape modulation is smooth, and therefore there are no abrupt changes of the static demagnetizing field, the static component of magnetization can be considered as saturated and parallel to the applied field, $\mathbf{H}_0$.

The PWM is used, in general, to solve linear differential equations with periodic coefficients where the solutions have the form of Bloch functions. To express the dynamical component of the magnetization m_i, as well as the dynamic demagnetizing field $h_{\text{DM},i}$, we use Bloch functions of the form

$$\begin{aligned} m_i(\mathbf{r}, \phi, t) &= m_i(\mathbf{r}, \phi) e^{i\omega t} e^{i\mathbf{k}\cdot\mathbf{r}}, \\ h_{\text{DM},i}(\mathbf{r}, \phi, t) &= h_{\text{DM},i}(\mathbf{r}, \phi) e^{i\omega t} e^{i\mathbf{k}\cdot\mathbf{r}}, \end{aligned} \quad (3)$$

where i denotes the in-plane or out-of-plane direction; $\mathbf{r} = (x, y, 0)$ is the in-plane position vector; $\mathbf{k}$ is the wave

vector; and ω is the angular frequency of SW's precession. Using the magnetostatic approximation [46], the demagnetizing fields in a planar magnonic crystal is calculated analytically [47] from Maxwell's equations. For convenience in further calculation, we introduce two coordinate systems: (xyz) connected to the periodic landscape and $(x'y'z')$ related to the direction of the external field (Fig. 6). We consider the x', y', z' components of magnetization **M** and effective field $\mathbf{H}_{\text{eff}}$ upon the spatial coordinates x, y, z and the angle of the applied field ϕ [48]. The angular dependence of the effective field $\mathbf{H}_{\text{eff}}(\phi)$ is included in the model only by the anisotropy of the demagnetizing field. Using the method presented by Kaczer [47], we can calculate the x' component of a static demagnetizing field $\mathbf{H}_{\text{DM}}$,

$$H_{\text{DM},x'}(\mathbf{r}, \phi) = -\sum_{\mathbf{G}} M_S(\mathbf{G}) \cos^2(\phi)$$
$$\times \left[1 - \cosh(|\mathbf{G}|z) e^{-|\mathbf{G}|d/4}\right] e^{i\mathbf{G}\cdot\mathbf{r}}, \quad (4)$$

and the y', z' components of the amplitude for a dynamic demagnetizing field $\mathbf{h}_{\text{DM}}$ for $\mathbf{k} = 0$:

$$h_{\text{DM},y'}(\mathbf{r}, \phi) = -\sum_{\mathbf{G}} \left\{ m_{y'}(\mathbf{G}) \sin^2(\phi) \left[1 - \cosh(|\mathbf{G}|z) e^{-|\mathbf{G}|d/4}\right] \right.$$
$$\left. - i m_{z'}(\mathbf{G}) \sin(\phi) \sinh(|\mathbf{G}|z) e^{-|\mathbf{G}|d/4} \right\} e^{i\mathbf{G}\cdot\mathbf{r}},$$

$$h_{\text{DM},z'}(\mathbf{r}, \phi) = -\sum_{\mathbf{G}} [m_{z'}(\mathbf{G}) \cosh(|\mathbf{G}|z) e^{-|\mathbf{G}|d/4}$$
$$- i m_{y'}(\mathbf{G}) \sin(\phi) \sinh(|\mathbf{G}|z) e^{-|\mathbf{G}|d/4}] e^{i\mathbf{G}\cdot\mathbf{r}},$$
$$(5)$$

where $\mathbf{G} = [G_x, 0, 0]$ is a reciprocal lattice vector. We use $M_S(\mathbf{G})$, $m_{z'}(\mathbf{G})$, $m_{y'}(\mathbf{G})$ to denote the coefficients of Fourier expansions for magnetization saturation $M_S(\mathbf{r})$ and the periodic factor of the dynamical component of magnetization $m_i(\mathbf{r})$. The symbol d stands for the thickness of the ferromagnetic layer.

The LL equation can be transformed (in the linear approximation) into the algebraic eigenvalue problem for eigenvalues (the frequencies of SW eigenmodes) and the eigenvectors [the sets of Fourier components for SW Bloch functions, $m_i(\mathbf{G})$]. As a result, we obtain the frequency spectrum with the corresponding set of the profiles of dynamical magnetization for SW eigenmodes for a selected value of the external field angle ϕ.

The MS are performed by solving numerically the LL equation in a real space and time domain [49]. For the excitation of the SW precession, we use a microwave external magnetic field in the form of the *sinc* function in the time domain and spatially homogeneous in the whole sample. After simulating the response for 30 ns, we perform a fast Fourier transform of the signal to arrive at the frequency spectra of SW excitation.
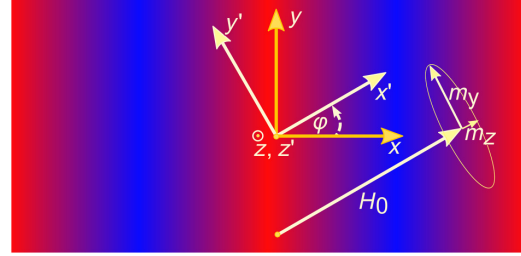

FIG. 6. The top view of the sample: a false-color representation of the sample temperature (red = hot, blue = cold) for two periods of the MC. The coordinates (x, y, z) are defined by the periodic structure, while (x', y', z') are oriented with respect to the direction of an external magnetic field. The in-plane (y') and out-of-plane (z') component of dynamic magnetization depends on x and y coordinates: $m_{y'}(x, y)$, $m_{z'}(x, y)$.

For a given spin-wave spatial profile, we consider (1) the efficiency of detection by Faraday rotation measurements, which relies solely on the spin-wave spatial symmetry, and (2) the elastic-to-magnetic excitation efficiency, which relies on both SW and elastic spatial symmetries. We deal with these aspects separately. With respect to detection efficiency, the largest Faraday signal (collected over many spatial periods) comes from any mode whose spatial profile exhibits a (relatively) homogeneous phase (a FMR mode [50] will possess a large Faraday signal [51], while a mode with an odd node number in Λ will sum to zero). To assess which of these modes exhibits the largest Faraday detection efficiency, we calculate the net out-of-plane magnetic moment over a period for the modes of $k = 0$ with the following formula:

$$I_n \propto \frac{\left| \int_0^{\Lambda} m_z^n(x) \, dx \right|}{\int_0^{\Lambda} \left| m_z^n(x) \right| dx}, \quad (6)$$

where $m_z^n(x)$ is the profile of the nth eigenmode for the out-of-plane component of dynamical magnetization.

With respect to the excitation cross section, we reiterate that the spatial period of the MC and that of the elastic waves are the same, both being derived from the same optical interference pattern. Furthermore, they are spatially phase locked in that the hot and cold regions of the MC experience opposite torques (through magnetoelastic coupling) on each half cycle of the acoustic wave. Therefore, the excitation efficiency σ of SW due to magnetoelastic interaction will depend on spatial profile of SW. To take into account the nonuniform distribution of the SW amplitude in one period of MC and the different signs of magnetoelastic torque in hot and cold regions, we integrate the dynamic component of magnetization $m_z^n(x)$ with the factor $\cos(2\pi x/\Lambda)$ to incorporate the magnetoelastic coupling and the opposite sense torque on both half cycles

of the elastic wave:

$$\sigma \propto \frac{1}{(f - f_0)^2 + (\Delta f /2)^2} \sin(2\phi)$$

$$\times \int_0^\Lambda \left[m_z^n(x) \cos(2\pi x/\Lambda) \right] dx. \qquad (7)$$

The factor $\sin(2\phi)$ reflects the angular dependence of the torque resulting from the magnetoelastic interaction of acoustic waves with the magnetization [30], while the Lorentzian factor $1/[(f - f_0)^2 + (\Delta f /2)^2]$ reduces significantly the excitation efficiency if the frequency of SW, $f = \omega/(2\pi)$, differs from the frequency of the acoustic wave, f_0, by more than the elastic bandwidth (approximately 0.5 GHz).

IV. NUMERICAL SIMULATIONS

The outcomes of the PWM and MS calculation are provided in Fig. 7. In Fig. 7(b), we plot the SW eigenfrequency dependence for all low-energy modes as the magnetic field angle is changed from parallel to the periodicity of the magnetic landscape ($\phi = 0°$) to the perpendicular direction ($\phi = 90°$) [52]. The results of both computational techniques are in agreement for the modes of the largest detection efficiency—the orange-yellow points (PWM) overlap with the black-gray lines (MS). The noticeable features of this result (and all such results for laterally modulated M_S) are the presence of a nearly constant frequency fundamental mode (characterized by the spatial distribution with zero nodes and homogeneous phase) and the appearance of a network of higher-order modes whose frequencies increase as the angle of the magnetic field is increased. At low angles, several modes dip in frequency below the fundamental mode upon anticrossing with the fundamental mode at an intermediate angle $\phi \approx 20°$. We find that the general shape presented in Fig. 7(b) is reproduced for a large number of modulation depths (i.e., time delays) and is shifted up vertically along the frequency axis as the applied field is increased (correspondingly down as the field is reduced). We did not attempt to perform this calculation for very deep modulations or modulations that deviate strongly from sinusoidal, since they are not relevant to the timescales associated with elastic dynamics.

The spatial profile of any mode can be assessed as a function of the magnetic field angle (and strength). At selected points in the angular dependence, and for the modes showing the largest detection efficiency (orange or dark yellow), we show [in Fig. 7(a)] the spatial profiles indicated as positions I through XII. In this case, the profiles are only shown for a fixed applied field strength of 500 G, at a fixed time delay (i.e., a fixed modulation depth). In particular, we note that the fundamental mode (I, II, III, X, XI, XII) shows zero nodes, while one of the higher-order modes labeled (VII, VIII, IX, IV, V, VI) is displayed with

both solid and dashed lines to delineate a change in phase for different portions of the SW profile [i.e., lateral node(s) in the precessional wave function]. A symbolic temperature scale is provided above the modal distributions (with blue and red regions corresponding to lower and higher temperature, respectively) to indicate where within the lateral dynamic magnetization profile the SW amplitude is maximized. For example, we find a general feature of our calculations to be that at low angles (curves I and II) the mode is strongly localized in the cold regions of the MC, which evolves into a uniform profile (curves X, XI, and
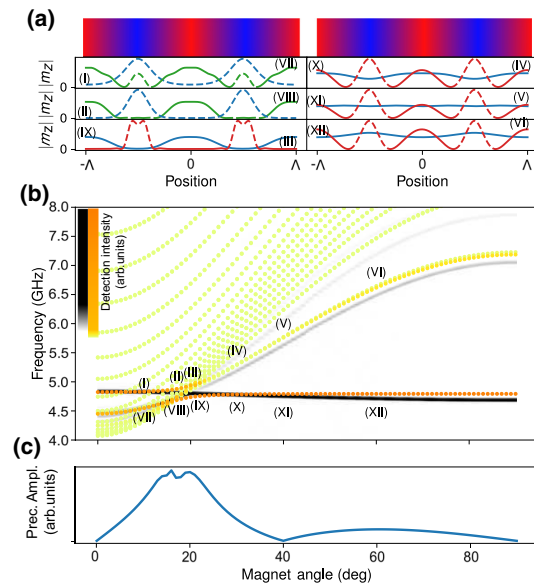
FIG. 7. Plane-wave method and micromagnetic calculation for angular dependence of the eigenfrequencies of spin-wave modes in a periodically modulated magnetic landscape. (a) The spatial distribution of the lowest-energy eignemodes (with the largest detection efficiency) is marked in the main plot by labels I–XII. The modes are plotted for two periods of the MC. The red (blue) color bars above symbolize the hotter (colder) regions of the magnonic crystal, respectively. The sections of solid and dashed lines distinguish the regions of opposite precession phase. Spatial profiles are color coded to indicate main resonance (blue) and dispersing modes, which we associated with the shoulder in Fig. 4 (orange/green). (b) Angular dependence of the eigenfrequencies of spin-wave modes. The color scales for orange-yellow (PWM) points or black-gray lines (MS) correspond to the simulated detection efficiency [the darker the line or symbol, the larger the value of Eq. (5)]. The plane-wave-method calculation is done for a simulated M_S profile (from two temperate models), whereas the micromagnetic simulations are performed for a sinusoidal approximation of the M_S profile. The bottom panel (c) presents the simulated procession amplitude of a spin wave pumped by an elastic wave inclusive of excitation efficiency [Eq. 6] and detection efficiency [Eq. (7)]. The outcome is two excitation lobes with a minimum around 40°.

XII) as the angle is increased. This latter profile we associate with a true FMR displaying a constant phase and (nearly) constant amplitude over the entire MC. We can now understand why higher-order modes dip in frequency below the fundamental at low angles; since a significant SW amplitude is present in the reduced M_S, hot regions of the sample (e.g., curve VII), the frequency of SW eigenmodes is therefore reduced. Finally, we note that at low angles the mode density is high, while at high angles the modes (at least the lowest two) are energetically well separated.

The bottom panel of Fig. 7 shows a qualitative estimation of the detected signal in a Faraday rotation measurement. In order to estimate the amplitude of Faraday signal from the spectrum and the profiles of SW eigenmodes, we use the phenomenological formula in Eq. (7) and the procedure described in the Sec. III. The frequency of $f = 4.8$ GHz driving the SW dynamics and the FWHM = 0.5 GHz (where Δf is the FWHM) of this resonance are taken from the experimental outcomes (see Fig. 4). By using this approach, we are able to reproduce qualitatively the angular dependence of the intensity of a Faraday signal. The simulated dependence shown at the bottom of Fig. 7 presents two lobes with a distinctive minimum around 30–40°, similar to those seen in the experiment (see Fig. 3). The relative heights of the two lobes (for lower and higher angles) are different for experimental and numerical outcomes.

V. DISCUSSION

We now discuss the connections between the experimental and calculation results, supporting our claim of the emergence of optically induced MC and our ability to control the band structure. We begin by considering the behavior at high magnetic field angles, where the eigenmode solution of the fundamental mode exhibits a FMR-like appearance (the SW amplitude is delocalized over the entire MC structure, homogeneous phase profile). We note that, while the detection efficiency of such a mode is large (dark orange in Fig. 7), the excitation efficiency by the elastic waves is actually quite small. In one period of the MC, the elastic wave has both compressional and dilational phases and, thus, cannot drive the fundamental mode as indicated. However, if we understand the fundamental mode to be driven locally, then at each region of the MC, hot and cold, a FMR can be driven. Such a locally driven FMR would be exactly the same as in the case of transducer-based measurements, where a unidirectional multicycle elastic wave drives the FMR precessional motion locally and out of phase on each half cycle of the wave [30,42,43,53]. In our experiments, optically probing the average magnetization precession via Faraday rotation results in the superposition of FMR responses in the hot and cold regions of the MC, which will add out of phase (because of the opposite sign of the strain in the two regions).

The picture of a locally driven FMR can explain one of the main observations of our data, namely, the difference in the high angle response between Ni and $Co_{0.2}Fe_{0.6}B_{0.2}$ films. The marked difference between these two materials is their Curie temperature; Ni has a low Curie temperature (600 K) while $Co_{0.2}Fe_{0.6}B_{0.2}$ has a high Curie temperature (1300 K). Assuming that the optical absorption and thermal diffusion are similar in the two materials (both lustrous metals deposited on similar silicate substrates), this large difference in T_C translates into a smaller magnetization modulation for the case of $Co_{0.2}Fe_{0.6}B_{0.2}$ and thus a smaller aggregate Faraday signal. In fact, the case for the locally driven FMR would result in a nearly suppressed high angle response (Fig. 7), which corresponds very well with the results found for $Co_{0.2}Fe_{0.6}B_{0.2}$ [Fig. 5(f)]. This suggests that, for high M_S materials, any spin-wave mode with odd spatial symmetry (whether it is a SW with odd spatial symmetry or a locally driven FMR) would be invisible in a Faraday measurement, while a mode that is strongly localized in one particular region of the MC (i.e., low angles) will be visible in the experiment. Applying the same considerations to Ni [Fig. 3(f)], we still need to explain the appearance and the increased signal detected at high angles. At the points where constructive optical interference occurs, the sample lattice temperature can easily reach T_C and remains at an elevated temperature for several nanoseconds. Nevertheless, as shown in Fig. 7, the modal profile at high angles should maintain its homogeneous phase and amplitude (i.e., the FMR) and, thus, we continue to expect a reduced second lobe detection, in effect a result like in $Co_{0.2}Fe_{0.6}B_{0.2}$. We suspect that the anomalous behavior in Ni, where in the second lobe we measure a large precessional amplitude, may be the result of a reduction in magnetoelastic coupling strength (not simply the reduction in M_S), which is prevalent as one approaches the Curie temperature [54,55]. We also mention that similar experiments on arrays of Ni wires, in this case excited by a uniform optical pulse, also excite magnetization and elastic dynamics, as well as the long-lived resonant magnetization precession. In this geometry, the wires themselves should be considered as a proxy for the hot regions of the TG signal (suppressed magnetization, initial dilational strain) and their physical structure, such as width, period, material, and substrate, are chosen to closely mimic the strain amplitude generated in the TG experiment. Nonetheless, an elastically driven magnetization precession as much as ten times smaller is witnessed for similar excitation fluences taken at the same magnetic field angle, 15° (portions of this work will be published at a future date). We suspect that this reduced signal level is a signature of hot Ni wires precessing under the action of the elastic waves, but with reduced magnetization and reduced magnetoelastic coupling. To fully vet this idea, additional
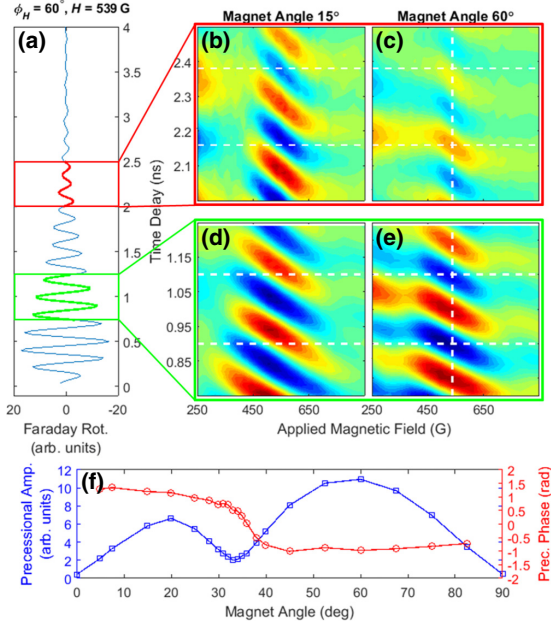
FIG. 8. (a)–(e) The surface-skimming longitudinal wave on glass substrates ($\Lambda = 1.1$ μm, $f = 5.15$ GHz) shows the same behavior as the Ni/MgO shown in Fig. 3. (f) A suppression in precessional amplitude at approximately 30° separates two excitation lobes with opposite precessional phases.
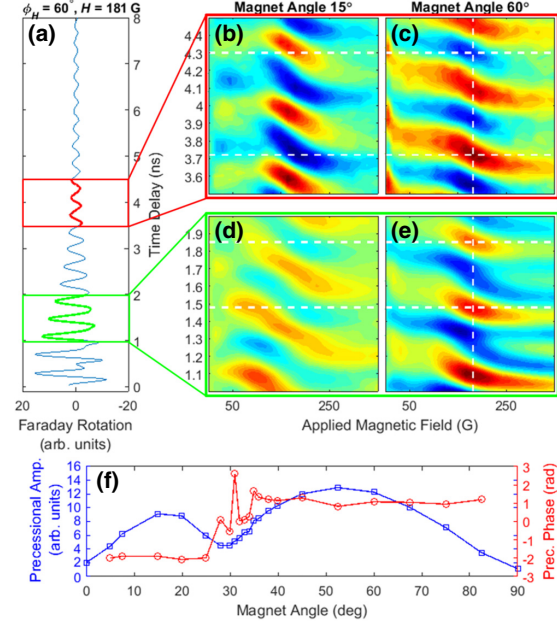
FIG. 9. (a)–(e) The Rayleigh surface acoustic wave on glass substrates ($\Lambda = 1.1$ μm, $f = 2.6$ GHz) shows the same behavior as both SSLW on Ni/glass and SAW on Ni/MgO shown in Fig. 3. (f) A suppression in precessional amplitude at approximately 30° separates two excitation lobes with opposite precessional phases.

fluence-dependent measurements would need to be done for a series of materials with varying M_S values.

Finally, in the same range of large magnetic field angles, one would also expect to measure the higher-lying precessional mode (IV–VI) when the field is reduced and this mode crosses the elastic excitation frequency. Based on the shape of the calculated angular dispersion, the larger the angle between the MC wave vector and the magnetic field, the lower in the field the resonance will occur. This is precisely the behavior that we witness for the high angle shoulder present in the case of Ni. Again, the visibility of this mode would rely on suppressed detection efficiency in the sample hot region, because of both the reduction in M_S and the reduced coupling strength. These same arguments indicate that a similar feature would not be present for $Co_{0.2}Fe_{0.6}B_{0.2}$, since the higher lying mode has an even number of nodes in one period.

At small angles of the magnetic field, the fundamental mode is concentrated in the cold region of the sample regardless of the material in question and, as indicated in Fig. 7, also exhibits a π phase flip in the precessional amplitude (plotted as a dotted, rather than a solid, line). To assess this absolute phase of precession, we follow the fundamental mode profile and precessional phase for sequential small angular steps from 90° to 0° (XII–IX,

VIII, VII). Assuming that the mode is well behaved and continuously evolves as a function of the angle, identifying the precessional properties of this fundamental branch can then be used to reveal the properties of all other modes of precession at low angles. Thus, the fundamental mode (XII–IX, I, II) can be identified as precessing with a π phase modulation on either side of the anticrossing point. This feature of the MC spin-wave distribution directly relates to the opposite precessional phase for Ni samples in the high and low magnetic field angles. In both cases, the predominant signal is derived from precession occurring in the cold regions of the sample, but the nature of the MC SW distribution dictates that these two must have opposite phases.

Furthermore, as indicated in the angular dispersion curve (Fig. 7), the MC at low angles of a magnetic field exhibits a network of modes at similar energy scales and within the excitation bandwidth of the acoustic wave. These additional modes can be seen explicitly in Fig. 5, where the low Gilbert damping of $Co_{0.2}Fe_{0.6}B_{0.2}$ results in narrow field resonances and the appearance of satellite resonance features [i.e., at early time delays [Fig. 7(d)], additional resonances can be seen on both sides of the main precessional mode]. In the high damping case of Ni, the field-tuned resonances are wide and individual modes
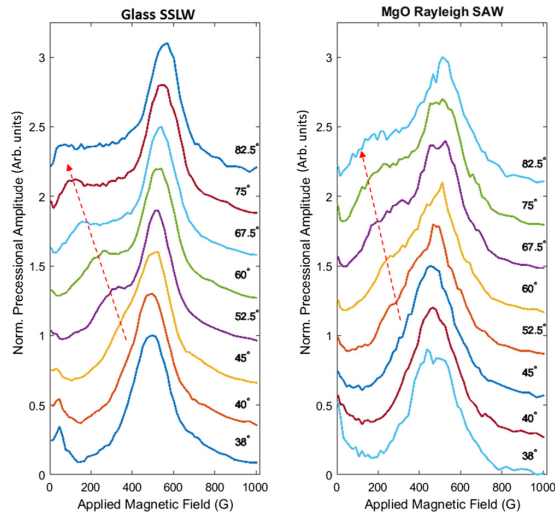
FIG. 10. Resonance response as a function of applied field angle for Ni/glass (left) and Ni/MgO (right), showing the main resonance and the strongly dispersing shoulder indicated by the arrow.

cannot be identified; however, the line shapes of the low angle resonance suggest that more than one mode may be active simultaneously. For example, the out-of-phase precession of two modes in proximate energy would suppress portions of the observed resonance and distort the line shape similar to the observed dynamics in Figs. 4(a) and 4(c), while simultaneously delaying or slowing the onset of precessional dynamics, for example, as seen in Fig. 2.

VI. CONCLUSION

In summary, we elucidate the magnetoelastic interaction for a range of magnetic field angles relative to the TG excitation wave vector. The key finding is the identification of distinct angular regimes where precessional motion can be driven elastically. In the low-T_C Ni sample, this is manifested as the precessional motion of an opposite phase in two angular regimes, along with their interference and suppression of precessional motion at intermediate angles. For high-T_C $Co_{0.2}Fe_{0.6}B_{0.2}$, this is manifested as driven precessional motion in only one of the previously determined angular regimes and the near-complete suppression in the other. To explain these findings, we calculate, using PWM and micromagnetic simulations, the SW amplitude distribution in a laterally (periodically) modulated magnetization profile as a function of modulation depth and magnetic field angle, which, in turn, allows us to infer that in different angular regimes the elastic waves couple to distinct spin-wave structures. At high angles (the second precessional lobe), the elastic wave excites a true FMR response, which we understand to be locally activated at each half period of the elastic wave. At low angles

(the first precessional lobe), we infer that a spin-wave mode, localized in the cold region of the sample, is elastically activated. Connected to these findings, we suggest that in low-T_C materials such as Ni, one must incorporate an understanding of the temperature dependence of the magnetoelastic constants to understand the observed dynamics, while this is less prevalent in high-T_C materials since, even in the hot regions of the sample, optical excitation increases the temperature by only a fraction of T_C. The ability to optically generate a transient magnetic landscape and control the spatial regions where the localized magnetic groundstates reside could impact a wide range of optomagnonics research that currently utilizes artificially textured materials.

APPENDIX

We include here additional data sets displaying the resonance effects in Ni on glass substrates at both SAW and SSLW resonances.

1. Angular dependence for Ni/glass at SAW and SSLW resonances

The change in precessional phase and the accompanying intermediate suppression of precessional amplitude are also witnessed for the Ni/glass heterostructure [here, soda-lime glass (SLG) or standard microscope slide glass]. For this material, a strong but rapidly damped SSLW drives precession at 5.15 GHz (Fig. 8) and the Rayleigh SAW resonance at 2.6 GHz (Fig. 9). For both elastic waves, a phase flip and concomitant intensity suppression occur at roughly $30°$, which is the same angle range that is witnessed in the main text for the Ni/MgO heterostructure. The suppression in amplitude is accompanied by the same binary phase reversal.

2. Dispersion of the shoulder with magnetic field angle

In Fig. 4 of the main text, we show the resonance field positions of the main and shoulder peaks as a function of

angle of the magnetic field. Here we show all the data sets to further enforce the notion of a strongly dispersing shoulder. For both glass and MgO substrates, we show the integrated Fourier transform of the resonance responses. For glass, this is the surface-skimming longitudinal wave response at 4.8 GHz, while for MgO this is the Rayleigh surface acoustic wave response at 5.15 GHz. The glass data are stronger in amplitude and, therefore, the signal to noise is better. However, in both cases, we see the main resonance peak change from an asymmetric response at $38°$ to develop a shoulder that disperses to lower field values as indicated by the arrows. The appearance of the shoulder in the Ni samples is thus independent of the type of acoustic wave driving the response, while its observation that we suggest in the main text is related to the next SW mode above the fundamental. The absence of this mode for $Co_{0.2}Fe_{0.6}B_{0.2}$ we attribute to the symmetry of the SW and the reduced detection efficiency due to the reduced modulation depth in a high-T_C material.

[1] A. G. Gurevich, and G. A. Melkov, *Magnetization Oscillations and Waves* (CRC Press, Boca Raton, FL, 1996).

[2] R. E. Arias, Spin-wave modes of ferromagnetic films, Phys. Rev. B **94**, 134408 (2016).

[3] M. van Kampen, C. Jozsa, J. Kohlhepp, P. LeClair, L. Lagae, W. de Jonge, and B. Koopmans, All-optical Probe of Coherent Spin Waves, Phys. Rev. Lett. **88**, 227201 (2002).

[4] M. J. Hurben, and C. E. Patton, Theory of Magnetostatic waves for inplane magnetized isotropic films, J. Magn. Magn. Mater. **139**, 263 (1995).

[5] B. A. Kalinikos, and A. N. Slavin, Theory of dipole-exchange spin wave spectrum for ferromagnetic films with mixed exchange boundary conditions, J. Phys. C: Solid State Phys. **19**, 7013 (1986).

[6] S. O. Demokritov, B. Hillebrands, and A. N. Slavin, Brillouin light scattering studies of confined spin waves: Linear and nonlinear confinement, Phys. Rep. **348**, 441 (2001).

[7] Y. Hashimoto, S. Daimon, R. Iguchi, Y. Oikawa, K. Shen, K. Sato, D. Bossini, Y. Tabuchi, T. Satoh, B. Hillebrands, G. E. W. Bauer, T. H. Johansen, A. Kirilyuk, T. Rasing, and E. Saitoh, All-optical observation and reconstruction of spin wave dispersion, Nat. Commun. **8**, 15859 (2017).

[8] S. Tacchi, F. Montoncello, M. Madami, G. Gubbiotti, G. Carlotti, L. Giovannini, R. Zivieri, F. Nizzoli, S. Jain, A. O. Adeyeye, and N. Singh, Band Diagram of Spin Waves in a Two-Dimensional Magnonic Crystal, Phys. Rev. Lett. **107**, 127204 (2011).

[9] R. Mandal, S. Saha, D. Kumar, S. Barman, S. Pal, K. Das, A. K. Raychaudhuri, Y. Fukuma, Y. Otani, and A. Barman, Optically induced tunable magnetization dynamics in nanoscale co antidot lattices, ACS Nano **6**, 3397 (2012).

[10] M. Zelent, N. Tahir, R. Gieniusz, J. W. Kłos, T. Wojciechowski, U. Guzowska, A. Maziewski, J. Ding, A. O. Adeyeye, and M. Krawczyk, Geometrical complexity of the antidots unit cell effect on the spin wave excitations spectra, J. Phys. D: Appl. Phys. **50**, 185003 (2017).

[11] M. Mruczkiewicz, P. Graczyk, P. Lupo, A. Adeyeye, G. Gubbiotti, and M. Krawczyk, Spin wave nonreciprocity and magnonic band structure in thin permalloy film induced by dynamical coupling with an array of Ni stripes, Phys. Rev. B **96**, 104411 (2017).

[12] A. V. Sadovnikov, E. N. Beginin, S. A. Odincov, S. E. Sheshukova, Y. P. Sharaevskii, A. I. Stognij, and S. A. Nikitov, Frequency selective tunable spin wave channeling in the magnonic network, Appl. Phys. Lett. **108**, 172411 (2016).

[13] J. Topp, D. Heitmann, M. P. Kostylev, and D. Grundler, Making a Reconfigurable Artificial Crystal by Ordering Bistable Magnetic Nanowires, Phys. Rev. Lett. **104**, 207205 (2010).

[14] M. Krawczyk, M. Mamica, M. Mruczkiewicz, J. W. Kłos, S. Tacchi, M. Madami, G. Gubbiotti, G. Duerr, and D. Grundler, Magnonic band structures in two-dimensional bicomponent magnonic crystals with in-plane magnetization, J. Phys. D: Appl. Phys. **46**, 495003 (2013).

[15] J. Rychły, J. W. Kłos, M. Mruczkiewicz, and M. Krawczyk, Spin waves in one-dimensional bicomponent magnonic quasicrystals, Phys. Rev. B **92**, 054414 (2015).

[16] C. Banerjee, P. Gruszecki, J. W. Klos, O. Hellwig, M. Krawczyk, and A. Barman, Magnonic band structure in a Co/Pd stripe domain system investigated by Brillouin light scattering and micromagnetic simulations, Phys. Rev. B **96**, 024421 (2017).

[17] R. A. Gallardo, A. Banholzer, K. Wagner, M. Koerner, K. Lenz, M. Farle, J. Lindner, J. Fassbender, and P. Landeros, Splitting of spin-wave modes in thin films with arrays of periodic perturbations: Theory and experiment, New J. Phys. **16**, 023015 (2014).

[18] C. Banerjee, S. Choudhury, J. Sinha, and A. Barman, Pseudo-One-Dimensional Magnonic Crystals for High-Frequency Nanoscale Devices, Phys. Rev. Appl. **8**, 014036 (2017).

[19] F. Busse, M. Mansurova, B. Lenk, M. von der Ehe, and M. Munzenberg, A scenario for magnonic spin-wave traps, Sci. Rep. **5**, 12824 (2015).

[20] M. Vogel, A. V. Chumak, E. H. Waller, T. Langner, V. I. Vasyuchka, B. Hillebrands, and G. von Freymann, Optically reconfigurable magnetic materials, Nat. Phys. **11**, 487 (2015).

[21] B. Lenk, H. Ulrichs, F. Garbs, and M. Munzenberg, The building blocks of magnonics, Phys. Rep. **507**, 107 (2011).

[22] G. Csaba, A. Papp, and W. Porod, Perspectives of using spin waves for computing and signal processing, Phys. Lett. A **381**, 1471 (2017).

[23] S. Klingler, P. Pirro, T. Br"acher, B. Leven, B. Hillebrands, and A. V. Chumak, Spin-wave logic devices based on isotropic forward volume magnetostatic waves, Appl. Phys. Lett. **106**, 212406 (2015).

[24] P. Graczyk, J. Kłos, and M. Krawczyk, Broadband magnetoelastic coupling in magnonic-phononic crystals for high-frequency nanoscale spin-wave generation, Phys. Rev. B **95**, 104425 (2017).

[25] P. Graczyk, and M. Krawczyk, Coupled mode theory for the acoustic wave and spin wave interaction in the magphonic crystals: Propagating magnetoelastic waves, Phys. Rev. B **96**, 024407 (2017).

[26] J. Janušonis, C. L. Chang, P. H. M. van Loosdrecht, and R. I. Tobey, Frequency tunable surface magneto elastic waves, Appl. Phys. Lett. **106**, 181601 (2015).

[27] J. Janušonis, C. L. Chang, T. Jansma, A. Gatilova, V. S. Vlasov, A. M. Lomonosov, V. V. Temnov, and R. I. Tobey, Ultrafast magnetoelastic probing of surface acoustic transients, Phys. Rev. B **94**, 024415 (2016).

[28] J. Janušonis, T. Jansma, C. L. Chang, Q. Liu, A. Gatilova, A. M. Lomonosov, V. Shalagatskyi, T. Pezeril, V. V. Temnov, and R. I. Tobey, Transient grating spectroscopy in magnetic thin films: Simultaneous detection of elastic and magnetic dynamics, Sci. Rep. **6**, 29143 (2016).

[29] M. Weiler, L. Dreher, C. Heeg, H. Huebl, R. Gross, K. Sato, M. S. Brandt, and S. T. B. Goennenwein, Elastically Driven Ferromagnetic Resonance in Nickel Thin Films, Phys. Rev. Lett. **106**, 117601 (2011).

[30] L. Dreher, M. Weiler, M. Pernpeintner, H. Huebl, R. Gross, M. S. Brandt, and S. T. B. Goennenwein, Surface acoustic wave driven ferromagnetic resonance in nickel thin films: Theory and experiment, Phys. Rev. B **86**, 134415 (2012).

[31] J. W. Kłos, and M. Krawczyk, *Magnetic Structures of 2d and 3d Nanoparticles: Properties and Applications* (Pan Stanford, Boca Raton, 2016).Chap. Magnonic crystals: From simple models toward applications.

[32] J. W. Kłos, D. Kumar, M. Krawczyk, and A. Barman, Omnidirectional spin-wave nanograting coupler, Phys. Rev. B **89**, 014406 (2014).

[33] E. Beaurepaire, J.-C. Merle, A. Daunois, and J.-Y. Bigot, Ultrafast Spin Dynamics in Ferromagnetic Nickel, Phys. Rev. Lett. **76**, 4250 (1996).

[34] T. Roth, A. J. Schellekens, S. Alebrand, O. Schmitt, D. Steil, B. Koopmans, M. Cinchetti, and M. Aeschlimann, Temperature Dependence of Laser-Induced Demagnetization in Ni: A Key for Identifying the Underlying Mechanism, Phys. Rev. X **2**, 021006 (2012).

[35] J. A. Rogers, A. Maznev, M. J. Banet, and K. A. Nelson, Optical generation and characterization of acoustic waves in thin films: Fundamentals and applications, Annu. Rev. Mater. Res. **30**, 117 (2000).

[36] T. F. Crimmins, A. A. Maznev, and K. A. Nelson, Transient grating measurements of picosecond acoustic pulses in metal films, Appl. Phys. Lett. **74**, 1344 (1999).

[37] M. Sander, M. Herzog, J. E. Pudell, M. Bargheer, N. Weinkauf, M. Pedersen, G. Newby, J. Sellmann, J. Schwarzkopf, V. Besse, V. V. Temnov, and P. Gaal, Spatiotemporal Coherent Control of Thermal Excitations in Solids, Phys. Rev. Lett. **119**, 075901 (2017).

[38] C. L. Chang, A. M. Lomonosov, J. J. Janušonis, V. S. Vlasov, V. V. Temnov, and R. I. Tobey, Parametric frequency mixing in a magnetoelastically driven linear ferromagnetic-resonance oscillator, Phys. Rev. B **95**, 060409(R) (2017).

[39] H. Ulrichs, B. Lenk, and M. Munzenberg, Magnonic spin-wave modes in CoFeB antidot lattices, Appl. Phys. Lett. **97**, 092506 (2010).

[40] U. Martens, T. Huebner, H. Ulrichs, O. Reimer, T. Kuschel, R. R. Tamming, C.-L. Chang, R. I. Tobey, A. Thomas, M. Munzenberg, and J. Walowski, Anomalous Nernst effect on the nanometer scale: Exploring three-dimensional temperature gradients in magnetic tunnel junctions, Commun. Phys. **1**, 65 (2018).

[41] M. Langer, F. Roder, T. Gallardo, S. Schneider, C. Steinen, R. Gatel, R. Hubner, L. Bischoff, K. Lenz, J. Lindner, P. Landeros, and J. Fassbender, The role of internal demagnetizing field for the dynamics of a magnonic crystal, Phys. Rev. B **95**, 184405 (2017).

[42] M. Weiler, L. Dreher, C. Heeg, H. Huebl, R. Gross, M. S. Brandt, and S. T. B. Goennenwein, Elastically Driven Ferromagnetic Resonance in Nickel Thin Films, Phys. Rev. Lett. **106**, 117601 (2011).

[43] P. G. Gowtham, T. Moriyama, D. C. Ralph, and R. A. Buhrman, Traveling surface spin-wave resonance spectroscopy using surface acoustic waves, J. Appl. Phys. **118**, 233910 (2015).

[44] A. Vansteenkiste, J. Leliaert, M. Dvornik, M. Helsen, F. Garcia-Sanchez, and B. Van Waeyenberge, The design and verification of MuMax3, AIP Adv. **4**, 107133 (2014).

[45] M. Krawczyk, M. L. Sokolovskyy, J. W. Kłos, and S. Mamica, On the formulation of the exchange field in the Landau-Lifshitz equation for spin-wave calculation in magnonic crystals, Adv. Condens. Matter Phys. **2012**, 764783 (2012).

[46] D. D. Stanciel, and A. Prabhakar, *Spin Waves: Theory and Applications* (Springer, New York, 2009).

[47] J. Kaczer, and L. Murtinova, On the demagnetizing energy of periodic magnetic distributions, Phys. Status Solidi **23**, 79 (1974).

[48] R. A. Gallardo, T. Schneider, A. Roldán-Molina, M. Langer, J. Fassbender, K. Lenz, J. Lindner, and P. Landeros, Dipolar interaction induced band gaps and flat modes in surface-modulated magnonic crystals, Phys. Rev. B **97**, 144405 (2018).

[49] J. Rychły, P. Gruszecki, M. Mruczkiewicz, J. Kłos, S. Mamica, and M. Krawczyk, Magnonic crystals-prospective structures for shaping spin waves in nanoscale, Low Temp. Phys. **41**, 745 (2015).

[50] J. C. Bihler, W. Schoch, W. Limmer, S. T. B. Goennenwein, and M. S. Brandt, and Spin-wave resonances and surface spin pinning in Ga1-xMnxAs thin films, Phys. Rev. B **79**, 045205 (2009).

[51] J. Hamrle, J. Pištora, B. Hillebrands, B. Lenk, and M. Munzenberg, Analytical expression of the magneto-optical Kerr effect and Brillouin light scattering intensity arising from dynamic magnetization, J. Phys. D: Appl. Phys. **43**, 325004 (2010).

[52] C. Gonzalez-Fuentes, C. Garcia, P. Landeros, and R. A. Gallardo, Theory of ferromagnetic resonance driven by the combined action of spin-transfer torque and voltage-controlled magnetic anisotropy, Phys. Rev. B **96**, 174440 (2017).

[53] L. Thevenard, C. Gourdon, J. Y. Prieur, H. J. von Bardeleben, S. Vincent, L. Becerra, L. Largeau, and J. Y. Duquesne, Surface-acoustic-wave-driven ferromagnetic resonance in (Ga,Mn)(As,P) epilayers, Phys. Rev. B **90**, 094401 (2014).

[54] E. du Tremolet de Lacheisserie, and J. Rouchy, The magnetoelastic coupling in nickel, J. Magn. Magn. Mater. **28**, 77 (1982).

[55] R. R. Birss, and E. W. Lee, The saturation magnetostriction constants of nickel within the temperature range – 196 to 365C, Proc. Phys. Soc. **76**, 502 (1960).

4.2   P2 - Anomalous refraction of spin waves as a way to guide signals in curved magnonic multimode waveguides

This research was done with collaborators from Ukraine. Oksana Busel from National Technical University of Ukraine "Igor Sikorsky Kyiv Polytechnic Institute" (KPI), and Andriy N. Kuchko from "Institute of Magnetism of NAS of Ukraine" and KPI.

In paper P2, we address the issue of guiding the spin wave in the curved multimode magnonic waveguide. In any circuit, a signal is directed not only in straight channels but needs to change direction. This is in particular issue for wave-based operations because bending leads to scattering to perpendicularly quantized modes and, in consequence, signal decoherence. One can overcome this by limiting the consideration to only a single-mode waveguide, where the only solution is a fundamental mode. In our paper, however, we propose a method for bending the wavefront correspondingly to the bending of the waveguide. Multimode waveguides are of great interest from an application's perspective due to their higher operating frequency and bandwidth.

Our research started with the analysis of the one-dimensional problem of spin wave scattering on a ferromagnetic layer embedded in a ferromagnetic matrix. By solving it analytically and numerically, we obtain the dependencies of the spin wave's amplitude and phase shift on the changes of magnetization saturation or anisotropy field in the ferromagnetic layer. We could observe that phase shift increases almost linearly across a given range while the transmission is kept high. It is worth noting that the resonance effect could be observed. Having the results in hand, we proposed a two-dimensional graded index slab that has modified magnetic parameters perpendicularly to the direction of propagation. This element works as a metasurface, where spin wave propagates through, gain phase shift that changes according to already investigated the one-dimensional case and can change the direction of the wavefront. We calculated the bending angle with generalized Snell's law[112, 89], where the bending angle is proportional to the gradient of the material modulation. This step was also supported by numerical calculations. Finally, we embedded the graded index slab into the bent of the waveguide and by simulation in time, we demonstrate that by defining properly the graded index element one can tilt the wavefront that corresponds to the bent of the waveguide and thus keep the phase of the signal.

We considered the nanoscale structure made of the alloy Co-Fe-B that would justify neglecting dipolar interactions in the analytical model. In the first stage of the consideration, we did not assume any thickness of the system or direction of the external magnetic field

since the exchange spin wave is insensitive to these parameters. However, we discuss also the impact of the dipolar interaction for spin wave guiding when the graded index element is defined by magnetization saturation gradient, and the external magnetic field is applied out-of-plane to avoid anisotropic propagation that appears in an in-plane magnetized system.

The research presented in the paper P2 was also included in the review paper "Roadmap on Spin-Wave Computing" published in IEEE Advances in Magnetics[19], where we present our method on top of the current stage of research. In work P2, I performed numerical simulations, implemented generalized Snell's law, prepared most of the graphics, analyzed data, and wrote a manuscript. I was also the corresponding author.

Anomalous Refraction of Spin Waves as a Way to Guide Signals in Curved Magnonic Multimode Waveguides

Szymon Mieszczak[1,*] Oksana Busel[2,†] Paweł Gruszecki[1,3] Andriy N. Kuchko[2,4]
Jarosław W. Kłos[1] and Maciej Krawczyk[1]

[1]*Faculty of Physics, Adam Mickiewicz University, Poznań, Uniwersytetu Poznanskiego 2, Poznań 61-614, Poland*
[2]*National Technical University of Ukraine "Igor Sikorsky Kyiv Polytechnic Institute", Peremohy Ave. 37,
Kyiv 03056, Ukraine*
[3]*Institute of Molecular Physics, Polish Academy of Sciences, Mariana Smoluchowskiego 17, 60-179 Poznań,
Poland*
[4]*Institute of Magnetism of NAS of Ukraine, Vernadskogo Ave. 36b , Kyiv 03142, Ukraine*

We present a method for efficient spin-wave guiding within the magnonic nanostructures. Our technique is based on the anomalous refraction in the metamaterial flat slab. The gradual change of the material parameters (saturation magnetization or magnetic anisotropy) across the slab allows tilting the wavefronts of the transmitted spin waves and controlling the refraction. Numerical studies of the spin-wave refraction are preceded by the analytical calculations of the phase shift acquired by the spin wave due to the change of material parameters in a confined area. We demonstrate that our findings can be used to guide the spin waves smoothly in curved waveguides, even through sharp bends, without reflection and scattering between different waveguide's modes, preserving the phase, the quantity essential for wave computing.

I. INTRODUCTION

Phase and amplitude are the fundamental characteristics of waves. The processing of any kind of wave relies on the interference effects, which depend on these characteristics. Thus, the control of spin waves' (SWs') phase and amplitude is essential in magnonics [1] to perform both analog [2,3] and digital [4] SW-based computing [5].

One of the significant challenges limiting the application of SWs relates to the capability of coherent and weakly damped signal transmission. Fulfilling this condition is necessary to transmit the information, encoded in SW phase or amplitude, between particular parts of a magnonic circuit, sometimes in a grid of interconnected and crossed waveguides, enabling a flow of SWs in different directions [4,6]. Typically, the interconnections are realized by waveguides being narrow and flat ferromagnetic stripes. Here arises the problem of the SW scattering on bends of waveguides. If the static magnetization is saturated and oriented along the direction of the external magnetic field [7], then the (static and dynamic) magnetic surface charges, generated by the normal to the surface component of the magnetization, changes at the bends of the waveguide. On the

other hand, if the external magnetic field is low [8] or the waveguide is properly patterned [9], the static magnetization follows the shape of the curved waveguide due to the shape anisotropy, which minimizes the changes of magnetic charges at bends. Nevertheless, the magnetic volume charges are generated due to curvilinear magnetic configuration in this system. In addition, the exchange interaction is modified, which induces the effects equivalent to the presence of the anisotropy field or the field of Dzyaloshinskii-Moriya interaction [10–12].

The SWs' wavelength is a few orders of magnitude shorter than the electromagnetic waves of corresponding frequencies [2]. Therefore, typical magnonic waveguides of the width accessible in photolithographic fabrication techniques are multimodal waveguides even in the GHz-frequency range. The fabrication of a single-mode waveguide for SWs is difficult since their widths need to be narrow, especially for high-frequency SWs [13]. Also, the generation of high-frequency harmonic SWs is challenging and requires the modification of the standard methods, based on the SW excitation by radiofrequency field. The different approaches use the effects of SW confinement, interference in periodic gratings, coupling between the materials of high and low ferromagnetic resonance frequency or spin vortex core [14–17]. The phase-sensitive mapping of SW profiles can be achieved using the

*szymon.mieszczak@amu.edu.pl
†opbusel@gmail.com

micro-Brillouin light scattering [18,19], which is however limited in resolution to 200 nm. Only with a sophisticated extension, is it possible to detect SWs with Brillouin light scattering with a resolution below 100 nm [20]. The finer resolution can be gained using x-ray microscopy [21] where the x-ray magnetic circular dichroism is used to find the spatial map of the phase [22].

To date, the single-mode waveguides for short SWs can be realized in the systems utilizing domain walls as magnonic waveguides since they can create narrow potential wells where SW modes can be localized and propagate lengthwise [23–29]. Difficulties associated with SW wavelengths' dependence on the direction of propagation (anisotropic dispersion relation) are negligible for short-wavelength SWs where exchange interactions of isotropic nature dominate over the anisotropic dipolar interactions. Also, for the magnetic configuration where the magnetic field is applied perpendicularly to the film's surface, the SW dynamics is naturally isotropic, independently on the frequency of SW. The only obstacle related to that geometry is a high bias field demanded to magnetize the sample uniformly. It can be overcome in materials with strong out-of-plane anisotropy, but these are usually characterized by high SW damping.

In multimode waveguides, the mechanism, which leads to the decoherence of the propagating SWs is scattering to other, perpendicularly quantized modes. Therefore, the signal loses the information encoded in the phase. Another consequence is that the SW propagates along a longer zigzag–shaped path [30], which can also be interpreted as a redistribution of the momentum (wave vector) between the components, that are transferal and longitudinal to the waveguide's axis. It is worthwhile to note, that the transverse quantization of the modes in the planar waveguide is related not only to the width of the structure but can also be introduced additionally by the periodic patterning along the waveguide [31–34].

We point out that the scattering between the modes is one of the most important factors for the SW decoherence at the bends of the magnonic waveguide. Therefore, the question arises: can we modify the properties of the bending region to block the redistribution of incoming mode into the different outgoing modes, keeping the transmission as high as possible? One possible solution is to fill the bending region by the material of spatially tailored properties, which refract the SW and redirect its propagation strictly along the outgoing section of the waveguide. In other words, we should look for the particular kind of so-called graded index (GRIN) element for SWs [35–43]. Recently GRIN elements have been used to bend SWs for in-plane [37] and out-of-plane [40] magnetized films. Another exciting idea is an application of SW lenses, in particular flat metalenses [44], i.e., lenses of fixed width introducing different phase delay of transmitted waves alongside the interface. Except for the changes

in the phases of refracted waves, the GRIN element should not introduce significant changes to their amplitudes. The interplay between the material parameters of the slab and its sizes determines the conditions for the resonant transmission [45,46]. Therefore, we need to design a system to work in the conditions close to the resonant transmission.

In this paper, we employ the anomalous refraction [47] achieved in the GRIN slab to change the direction of coherently propagating SWs at the bend of the waveguide. For anomalous refraction, the wavefronts of refracted waves are tilted at a desirable angle with respect to wavefronts of the incident waves, even at normal incidence. This phenomenon requires a linear change of the phase of the transmitted waves alongside the interface, where the refraction takes place. Its description requires the generalization of Snell's law [47,48]. We develop the analytical theory for the scattering of exchange SWs on the homogeneous ferromagnetic slab of finite width embedded in a ferromagnetic layer. Minimizing the total energy, we derive the boundary conditions on the interfaces between the slab and its surroundings. We obtain the complete relations between the phases and amplitudes of the incident and scattered SWs. These calculations are successfully compared to micromagnetic simulations. Then, we use our findings to demonstrate both analytically and numerically an anomalous refraction for the purely exchange SWs incident from a waveguide to a semi-infinite film through a flat magnonic GRIN slab. We treat the GRIN element as an inhomogeneous slab linking the input and output branches of the waveguide at the bend.

The paper is organized as follows. In the next section, we describe the analytical model. In Sec. III we show and discuss the results of the analytical and numerical studies, which are summarized in Sec. IV. In Appendix A we present details of analytical calculation, while in Appendix B details of micromagnetic simulations.

II. MODEL AND METHODS

A. Boundary-condition problem

Let us consider SWs propagating (along the x axis) through a ferromagnetic layer B ($0 < x < d$) embedded as a slab between two half-spaces of the ferromagnetic matrix A ($x \leq 0$ and $x \geq d$), as shown in Fig. 1. The slab B is exchange coupled by thin interfaces of thickness δ to the matrix A. For simplicity's sake, we assume that the system is uniform and infinitely extended in the x-z plane. We consider the case when the static magnetizations $\mathbf{M}_A$ and $\mathbf{M}_B$ are oriented along the z axis (see Fig. 1) and are parallel to each other everywhere in the system: $\mathbf{M}_{A(B)} = [0, 0, M_{S,A(B)}]$, where $M_{S,A(B)}$ denotes the saturation magnetization. The indexes A and B denote materials of the matrix and the slab, respectively.

The dynamics of magnetization in an effective magnetic field can be described by the Landau-Lifshitz equation
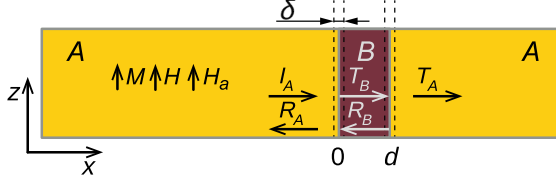
FIG. 1. Scattering of the SWs on a ferromagnetic layer (dark area) embedded in a ferromagnetic matrix (light area). The uniaxial anisotropy field H_a and the static magnetization M for ferromagnetic matrix (A) and layer (B) are parallel to each other and tangential to the plane of the layer. The layer B of thickness d is exchange coupled to the matrix A by the interfaces of thickness δ.

(LLE):

$$\frac{\partial \mathbf{M}_{A(B)}}{\partial t} = -\mu_0 |\gamma| \left[\mathbf{M}_{A(B)} \times \mathbf{H}_{\text{eff},A(B)} \right], \qquad (1)$$

where the effective field is a variational derivative of the energy W with respect to the magnetization vector: $\mathbf{H}_{\text{eff},A(B)} = -(1/\mu_0)\delta W/\delta \mathbf{M}_{A(B)}$. The parameter γ is the gyromagnetic ratio and μ_0 is the permeability of the vacuum. The total magnetic energy density of the system w includes the following: the density of the Zeeman energy $\left(-\mu_0 \mathbf{H} \cdot \mathbf{M}_{A(B)} \right)$, with the external magnetic field $\mathbf{H}$; the exchange energy density $\left[1/2\alpha_{A(B)} \left(\partial \mathbf{M}_{A(B)}/\partial x_i \right)^2 \right]$, with the exchange interaction parameter $\alpha_{A(B)} = 2A_{\text{ex},A(B)}/M_{S,A(B)}^2$, where $A_{\text{ex},A(B)}$ is the exchange stiffness constant in the material A or B, respectively; the density of anisotropy energy $\left[-1/2\beta_{A(B)} \left(\mathbf{M}_{A(B)} \cdot \mathbf{n}_a \right)^2 \right]$, where $\beta_{A(B)} = 2K_{A(B)}/M_{S,A(B)}^2$ and $\mathbf{n}_a$ is the unit vector of the easy axis. Anisotropy energy density is expressed by the uniaxial anisotropy constant $K_{A(B)}$. Assuming that the thickness of the interface δ is smaller than the exchange length $\lambda_{\text{ex}} = \sqrt{2A_{\text{ex}}/\mu_0 M_S^2}$, we can neglect the structure of the interfaces (roughness, material mixing) and introduce the coupling parameter A, which is the parameter of the interlayer exchange and can be expressed via the interface thickness δ [49,50]. We postulate the exchange type of coupling characterized by the energy density at the interfaces: $x = 0, d$ (i.e., the energy per unit area): $-A\mathbf{M}_A \cdot \mathbf{M}_B$, where $A = \left(A_{\text{ex},A} + A_{\text{ex},B} \right)/(2M_{S,A}M_{S,B}\delta)$ is coupling parameter.

Minimizing the total energy, we can derive boundary conditions:

$$\begin{cases} \left(\alpha_A \dfrac{\partial}{\partial x} + A \dfrac{M_{S,B}}{M_{S,A}} \right) m_A - A m_B = 0 \\ \left(\alpha_B \dfrac{\partial}{\partial x} - A \dfrac{M_{S,A}}{M_{S,B}} \right) m_B + A m_A = 0 \end{cases}, \quad x = 0, \quad (2)$$

$$\begin{cases} \left(\alpha_B \dfrac{\partial}{\partial x} + A \dfrac{M_{S,A}}{M_{S,B}} \right) m_B - A m_A = 0 \\ \left(\alpha_A \dfrac{\partial}{\partial x} - A \dfrac{M_{S,B}}{M_{S,A}} \right) m_A + A m_B = 0 \end{cases}, \quad x = d. \quad (3)$$

At each interface between matrix and slab, the solutions of the LLE satisfy the boundary conditions for the amplitudes of the dynamical components of magnetization $\mathbf{m}_{A(B)} = \left[m_{A(B),x}, m_{A(B),y}, 0 \right]$ [for convenience, in Eqs. (2) and (3) they are expressed via the cyclic variables $m_{A(B)} = m_{A(B),x} \pm i m_{A(B),y}$, where i is the imaginary unit] for every interface, namely at $x = 0$ and $x = d$.

We are looking for a solution in linear regime, i.e., describing the harmonic precession with the angular frequency ω: $\mathbf{m}(\mathbf{r}, t) = \mathbf{m}(\mathbf{r}) \exp(i\omega t)$.

For the general stationary solution $\mathbf{m}(\mathbf{r})$, we have to include the waves propagating both to the left and to the right. This can be mathematically expressed as

$$m_A = I_A e^{ik_A x} + r_A e^{-ik_A x}, \quad x \leq 0, \quad (4)$$

$$m_B = t_B e^{ik_B x} + r_B e^{-ik_B x}, \quad 0 < x < d, \quad (5)$$

$$m_A = t_A e^{ik_A x}, \quad x \geq d. \quad (6)$$

The parameters k_A and k_B stand for the wave numbers in the matrix and the slab, respectively. The wave numbers k_A and k_B depend on the external magnetic field H and material parameters: saturation magnetization $M_{S,A(B)}$ and anisotropy field $H_{a,A(B)} = 2K_{A(B)}/(\mu_0 M_{S,A(B)})$. The amplitude of incoming wave is normalized to 1: $I_A = 1$. All the remaining amplitudes r_A, t_B, r_B, t_A are, in general, complex valued: $R_A e^{i\varphi_{R_A}}$, $T_A e^{i\varphi_{T_A}}$, $T_B e^{i\varphi_{T_B}}$, $R_B e^{i\varphi_{R_B}}$ and contain the information about the real amplitudes R_A, T_B, R_B, T_A and phases φ_{R_A}, φ_{T_A}, φ_{T_B}, φ_{R_B}.

For calculating the complex amplitudes of SWs, namely r_A, t_B, r_B, and t_A [presented in Appendix A, Eqs. (A1)–(A4)], we use the boundary conditions Eqs. (2) and (3).

B. Huygens-Fresnel principle and generalized Snell's law

Let us discuss the design of a GRIN slab in the form of the rectangular region with a gradual change of the magnetic parameters enabling the direction of the transmitted waves to be steered. To describe the wave refraction in this system, we use the Huygens-Fresnel principle [51]. This concept was developed for optics but can be adapted to other types of waves [52]. The postulation states that every point on a wavefront is itself the source of the cylindrical wavelets, and the sum of these cylindrical wavelets forms the new wavefront. In the considered case, we assume that

the source points are located at the right interface of the GRIN slab (at $x = d$) and are aligned along the y axis. We can calculate the complex amplitude at any position on the right side of the GRIN slab using the amplitude and phase shift obtained from the solution of the boundary problem. Postulation given by Huygens-Fresnel can be mathematically expressed as

$$\mathcal{T}(\mathbf{r}) = \sum_j \frac{T_j e^{i[\mathbf{k} \cdot (\mathbf{r} - \mathbf{r}_j) + \phi_j]}}{|\mathbf{r} - \mathbf{r}_j|}. \qquad (7)$$

The summation is done over the interface of the GRIN slab (at the position $x = d$) at a large number of locations $\mathbf{r}_j = [d, y_j]$. The phase ϕ_j is tailored by changing the saturation magnetization or anisotropy field in the GRIN slab. The partial amplitude T_j indicates the transmittance of the SW through the GRIN slab into the semi-infinite medium A defined as $\mathrm{abs}(t_A)^2$ and the phase ϕ_j defined as $\arg(t_A)$ [Eq. (A1) in Appendix A].

Another approach for calculating the angle of the refracted wave is to use the generalized Snell law [47,53]. It states that a nonzero gradient of phase along the interface induces an additional perpendicular to the interface component of the wave vector. Mathematically it can be expressed by the following formula:

$$k_{\mathrm{incident},y} = k_{\mathrm{refracted},y} + \frac{d\phi}{dy}, \qquad (8)$$

where ϕ is induced phase along the y axis and k_{incident} and $k_{\mathrm{refracted}}$ are the wave numbers of the incident and refracted wave, respectively. In the case with known $\phi(y)$ dependence along the y axis, the generalized Snell law together with SW dispersion relation, can be used to predict the overall direction of the wave vector of the outgoing SWs from the GRIN slab. In our case, for normal incident waves, $k_{\mathrm{incident},y} = 0$, therefore, $k_{\mathrm{refracted},y} = -d\phi/dy$. The missing component of wave vector, perpendicular to the interface, can be calculated with the use of SW dispersion relation $k(\omega)$: $k_{\mathrm{refracted},x}^2 = k^2(\omega) - k_{\mathrm{refracted},y}^2$. Overall, the GRIN slab acts here as a metasurface. Note, that in photonics, metasurfaces can also have widths comparable to the wavelength [54].

III. RESULTS

In order to design the GRIN slab, that is schematically shown in Fig. 2, we propose to use Co-Fe-B layer as a base material due to high saturation magnetization, relatively low SW damping [55,56], which is crucial for SW processing, [57] and because of the possibility of tailoring the material parameters, required to obtain anomalous refraction.

By implantation of Ga ions, we can locally reduce the magnetization and create the distribution of saturation magnetization of high spatial resolution [46,58,59].
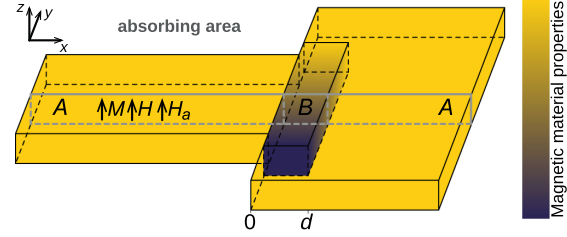

FIG. 2. Geometry of the simulation system with the GRIN element. The system consists of the ferromagnetic slab (B) characterized by the gradient of magnetic parameters (e.g., saturation magnetization M_S or anisotropy field H_a), which links the straight section of the waveguide and the semi-infinite plane made of the homogeneous material A. The magnetic parameters in the slab B are changing in the y direction. At each x-z cross section (see Fig. 1), the phase shift of transmitted wave is different, which allows refracting the plane wave propagating initially in the x direction. The absorbing material is placed at the sides of the simulated system, in order to avoid the impact of boundaries. The external magnetic field **H** is applied along the z direction; the static magnetization and the anisotropy field are aligned with the external field.

From the other side, when the sufficiently thin layer of Co-Fe-B is deposited on MgO, the surface-induced out-of-plane anisotropy can force the perpendicular orientation of the magnetization [45,60]. The effective anisotropy field (including both the shape and surface, magnetocrystalline anisotropy) can be controlled by the annealing in the fabrication process or by the application of the electric field [61–63]. The perpendicular orientation of the magnetization ensures the isotropic SW dispersion, which simplifies the design of refraction effects. The effect of continuous change of saturation magnetization can be achieved also in a magnetic insulator, like yttrium iron garnet (YIG) by temperature [64] or strain [65].

At the initial stage, we perform the analytical studies of the SWs' transmission through the slab formed in a Co-Fe-B matrix by the modification of the saturation magnetization or the anisotropy field.

Particular attention is paid to the identification of the resonances of the slab, where the amplitude of transmitted SWs is the highest. The results are cross checked by micromagnetic simulations. Then, we present the outcomes of micromagnetic simulations for the guiding of the SWs in the waveguide with the GRIN slab at the bend. The GRIN slab is designed using the results from the initial stage and used to guide the SWs coherently through the bend of the magnonic waveguide.

A. Spin-wave propagation through the slab—one-dimensional scenario

Let us analyze the SW transmission through a uniform slab of finite width with modified either saturation

magnetization or uniaxial anisotropy field. Equations (4)–(6), with Eqs. (A1)–(A5) are taken into account to determine the phase shift $\arg(t_A)$ and the transmittance $\text{abs}(t_A)^2$ of the transmitted SWs in dependence on frequency or other considered magnetic parameters (e.g., the saturation magnetization or the anisotropy field).

To demonstrate various aspects of the system, as well as to check the validity of the model, we show the results of the analytical calculations and their comparison with the results of the micromagnetic simulations for four scenarios: (i) $M_{S,B} = 800$ kA/m in the slab is fixed, the exchange constant $A_{\text{ex},B}$ is equal to 20 pJ/m, the frequency of SWs varies in the range of 14–40 GHz and the uniaxial anisotropy is neglected, (ii) $M_{S,B} = 1200$ kA/m, $A_{\text{ex},B} = 27$ pJ/m, frequency of SWs varies in the range of 14–40 GHz and the uniaxial anisotropy $K_B = 50$ kJ/m³ is included, (iii) $M_{S,B}$ varies in the slab in the range of 300–800 kA/m, $A_{\text{ex},B} = 20$ pJ/m, frequency of SWs is 25 GHz and the uniaxial anisotropy is neglected, (iv) $M_{S,B} = 1200$ kA/m, $A_{\text{ex},B} = 27$ pJ/m, SWs frequency is 25 GHz and the uniaxial anisotropy K_B changes in the range of 0–490 kJ/m³. In all cases, the slab is 150 nm wide. Surrounding material A is assumed to be made from Co-Fe-B with $M_{S,A} = 1200$ kA/m, $A_{\text{ex},A} = 27$ pJ/m and $K_A = 0$. The external magnetic field $\mu_0 H = 0.5$ T is aligned along the z axis. Details of the micromagnetic simulations are presented in Appendix B.

We now analyze the dependence of the transmittance and phase shift of transmitted SWs on the frequency for the slab formed by the modification of saturation magnetization and uniaxial anisotropy, cases (i) and (ii). The results for these two cases are presented in Figs. 3 and 4, respectively. To explain these frequency dependencies, we should discuss the role of the transmission of exchange SWs in the SWs' dispersion relation

$$k(\omega) = \sqrt{a\left(\frac{\omega}{\omega_0} - b\right)}, \qquad (9)$$

where $\omega_0 = \gamma \mu_0 H$ is proportional to the value of external field H and is expressed in the angular frequency unit, the factor $a = M_S \mu_0 H/(2A_{\text{ex}})$ is proportional to the saturation magnetization, and the term $b = 1 + H_a/H$ changes linearly with the anisotropy field $H_a = 2K/(\mu_0 M_S)$. By the change of M_S, the wave vector is scaled, regardless of the range of frequencies. However, the impact of H_a on the wave vector is significant only for low frequencies (ω is similar to ω_0) when the additive term b cannot be neglected. Moreover, for lower frequencies and sufficiently large positive value of the uniaxial anisotropy ($b > \omega/\omega_0$), the wave vector becomes imaginary and the SWs can only tunnel.

The decrease of M_S in the slab B (for A_{ex}, H, K kept constant in the system) results in the decrease of k and the reduction of the phase acquired by the transmitted
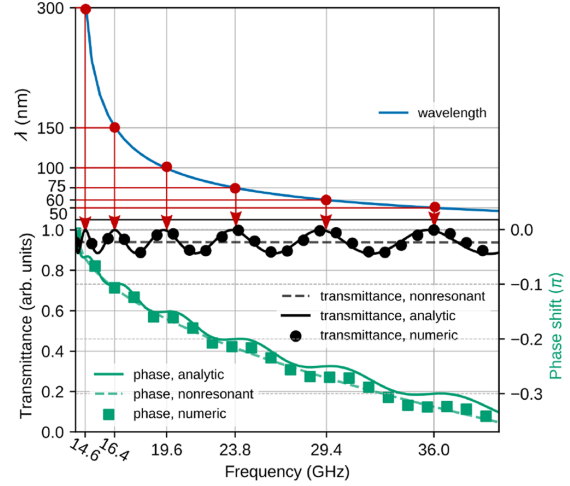

FIG. 3. SWs' wavelength (blue color) as a function of frequency. Red dots indicate fulfilled resonant conditions by Eq. (10). Enhancement of transmittance at these frequencies can be observed. Values on the horizontal axis represent the resonant frequencies. The transmittance (black color) and the phase shift (green color) for SWs traveling through the 150-nm-wide slab with respect to the frequency. Dots and squares represent the values obtained in the numerical simulations, while the solid lines represent the analytical results. Dashed lines represent the case when the reflection in the system is neglected. The value of the external field is equal to 0.5 T, reduced M_S in the slab is equal to 800 kA/m and reduced A_{ex} to 20 pJ/m.

SW. As a result, the phase shift is negative (referring to the SWs propagating at the same distance d in the matrix A where M_S is not reduced). This negative phase shift is growing with the increasing frequency $\Delta\varphi(\omega) = d\left[k(\omega, M_{S,B}) - k(\omega, M_{S,A})\right]$—see green lines and points in Fig. 3, because $k(\omega)$ is an increasing function of the frequency. The increase of the anisotropy field H_a in the slab B reduces the value of k. Therefore, the SWs gain additional phase during the transmission through the slab (referring to the SWs propagating at the same distance in the matrix A where H_a are not added). This positive phase shift is growing (see green lines and points in Fig. 4) for the same reasons as in the case of the slab formed by the change of M_S.

It is visible that the value of transmittance oscillates. It is especially noticeable in the case of the slab induced by the M_S reduction, Fig. 3. To explain this behavior, the dispersion relations of SWs as the dependencies of wavelength on frequency $\lambda(\omega) = 2\pi/k(\omega)$ are plotted in Figs. 3 and 4 [cf. Eq. (9)]. The resonance condition for wave transmitted through the slab of the width d reads

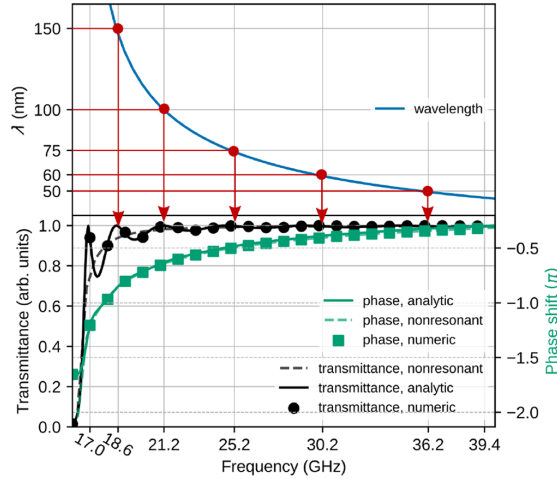$$2d = N\lambda(\omega), \qquad (10)$$

FIG. 4. SWs' wavelength (blue color) as a function of frequency. Red dots indicate fulfilled resonant conditions, Eq. (10), where we observe an enhancement of the transmittance. Values on the horizontal axis represent the resonant conditions. Transmittance (black color) and phase shift (green color) for SWs propagating through the 150-nm-wide slab with respect to the frequency. Dots and squares represent the values obtained in numerical simulation, while the solid lines represent the analytical results. Dashed lines represent the case when the reflection in the system is neglected. The value of the external field is equal to 0.5 T and the uniaxial anisotropy constant $K = 5$ kJ/m^3 within the slab.

where N is the natural number. The condition Eq. (10) corresponds to the constructive interference of the wave after the round trip at a distance of $2d$. The frequencies for these resonances are marked in Figs. 3 and 4 by the red arrows. They match the locations of the maxima of the transmittance. In order to confirm the presence of standing resonance modes within the slab, we perform both the analytical calculations and micromagnetic simulations. We calculate the squared dynamical magnetization, averaged in time, at the frequencies corresponding to the maxima of the transmission. It can be observed that the slab works as a resonator (see the results in Appendix A), similar to Fabry-Perot resonators known in optics [51]. It is worthwhile to note, that the fabrication of the sharp interfaces between the GRIN slab and its surrounding might be problematic, especially when one would like to use the ion implantation to shape the distribution of saturation magnetization within the sample. The effect of a smooth transition between the slab and surrounding is important for the sharpness of resonances, but it does not affect significantly the phase shift acquired by the SW.

One can predict the phase shift, which SWs gain during the transmission through the slab, by defining a magnonic

refractive index [37,66]. However, this approach takes into account only the refractive properties of the bulk material expressed in the dispersion relation. By solving the LLE [Eq. (1)] with clearly defined boundary conditions [Eqs. (2) and (3)], we can obtain full information about the SWs' refraction in the system. Hence, we can see in Figs. 3 and 4 the corrections, which come from taking into account the reflection from boundaries. The dashed lines with a lighter color indicate the cases when no reflection is considered in the system. As we can see, even for strong exchange coupling (when the majority of energy is transmitted for any condition) at the interface, A, the difference is noticeable. For weaker coupling, where a more significant fraction of energy is turned back, the impact on the phase shift and the transmittance could be even more significant [45]. This points out that the design of the GRIN slab has to take into account the presence of the resonances.

Numerical calculations fully support the analytical approach presented in this part, and thus the validated model is used for further stages of this study.

Let us now discuss cases (iii) and (iv), described at the beginning of the section. Here, we aim to control the SW guiding in the confined structures like waveguides using the GRIN slab, so in the following we introduce the change of the material parameters, saturation magnetization M_S and the anisotropy field H_a. According to Fig. 2, we change the material parameters of the slab at fixed frequency of SWs $f = \omega/(2\pi) = 25$ GHz.

In Fig. 5(a), the transmittance and the phase shift with respect to M_S in the slab are presented. The resonant phenomenon is visible, like in the previous cases. The modulation of the transmittance is around 20%. The dashed black line represents the transmittance of SWs through the slab when the reflection is neglected. The impact of the resonances is visible, and taking into account the resonant effect is well based. The phase shift changes rather smoothly in the considered range of M_S, and in total, the difference is around 1.75π. Deviations of the green solid and squared lines (analytical and numerical results, respectively) from the dashed line are minor and visible mainly near the resonances. Fig. 5(b) shows the results for the transmittance and phase shift as a function of the anisotropy constant K in the slab in the range of 0–490 kJ/m^3, which is equivalent to the presence of the anisotropy field $\mu_0 H_a$ in the range 0–0.8 T.

We can see that for the anisotropy field larger than 0.4 T, the transmittance drops dramatically, and the resonance peaks are not observed anymore. This feature is attributed to the lack of oscillating solution within the slab. The SWs need to tunnel through the slab with a significant reduction of the amplitude. Just below this value [$H_a = 2\pi/(\gamma\mu_0)f - H$], the resonant behavior of the transmittance is observed with a high variation of the transmittance.
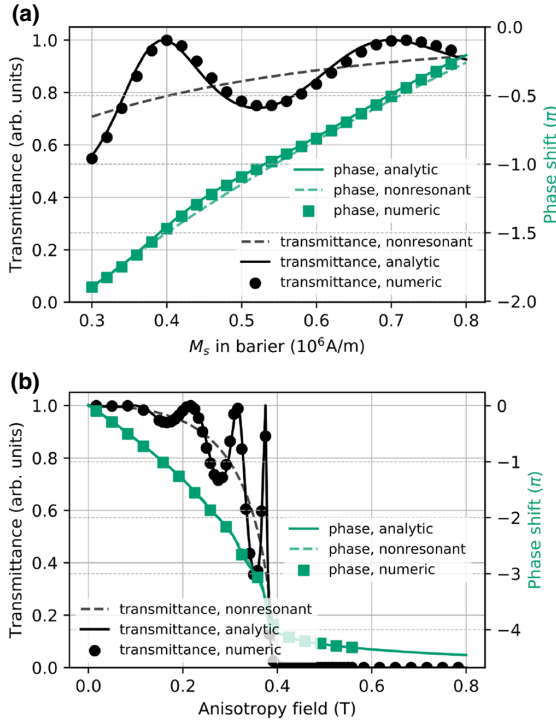
FIG. 5. Transmittance (black color) and phase shift (green color) for SWs traveling through the 150-nm-wide slab with respect to (a) M_S and (b) the anisotropy field in the slab. Dots and squares represent the values obtained in numerical simulation, while the solid lines represent the analytical results. Dashed lines represent the nonresonant case. The constant frequency equal to 25 GHz and external field equal to 0.5 T are considered. (a) The reduced exchange A_{ex} is equal to 20 pJ/m. Resonant peaks are visible for the specific values of M_S. (b) M_S and A_{ex} remain the same as in the matrix, i.e., 1200 kA/m and 27 pJ/m, respectively.

B. Anomalous refraction of spin waves

Based on the model developed in Sec. II, we design a GRIN slab that bends wavefronts of the incident waves in the desired way. The slab is an element that modifies the phase of the incoming plane waves (at the interface located in $x = 0$) to gain the linear change of the phase of the transmitted waves alongside the interface (at $x = d$). This idea is based on the general concept of tailoring the phase changes alongside the interface and provide the desired functionality, like focusing [44], beam steering or delay [67]. In the present case, we want to design an element suitable for the change of the direction of SWs' propagation. Let us study numerically the case of the two-dimensional slab with the gradient of M_S, like it is schematically presented in Fig. 2. In the section of the straight and flat waveguide of the width 100 nm, we excite
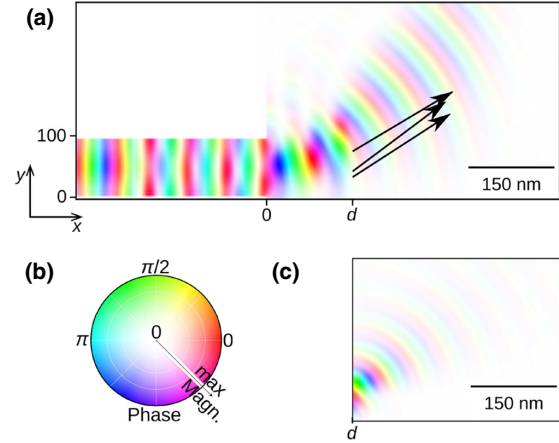

FIG. 6. The squared amplitude of SWs propagating in the system shown in Fig. 2, at the frequency 25 GHz. (a) When SWs reach the semi-infinite medium after the slab, the new wavefront starts to form due to the gradient of magnetic parameters. The bending of SWs reaches the angle of ca. 36°. (b) The color palette of SW. The color indicates the phase, while the intensity indicates the amplitude. (c) The bending of SWs ca. 36° obtained according to the Huygens-Fresnel formula [Eq. (7)]. Source points of cylindrical SWs are located on the right border of the slab—at the position d. The amplitude of the transmittance and the phase shift are obtained from the boundary-condition problem, like in Fig. 5(a).

the plane wave, which propagates along the x axis. The waveguide is attached to the large plate of the same thickness and made of the same material. At the front of the plate, we defined the 150-nm-wide slab—see Fig. 2. In the slab, we take the reduced value of M_S, which is increasing from 300 kA/m up to 800 kA/m on the distance 100 nm, in direct contact with the waveguide. Above M_S goes to the value of a semi-infinite plane, it is $M_S = 1200$ kA/m.

The results of the numerical simulations are presented in Fig. 6(a). The wavefront changes the direction, and the outgoing SWs are bent. The arrows in Fig. 6(a) indicate the direction of the refracted waves estimated with Eq. (8). Although the gradient of the phase shift is not perfectly linear, this estimation seems to be very good.

The results of the numerical simulations are also compared to the results of the analytical consideration using the Huygens-Fresnel principle. Complex amplitudes at every position are calculated according to the postulation given by Eq. (7). We assume that at the position d [as it is shown in Fig. 6(c)], we have a line of sources of cylindrical waves. Figure 5(a) presents the transmittance and phase shift of the SW that we need to put into Eq. (7). The application of this equation is shown in Fig. 6(c). Since the phase shift changes smoothly along the y axis, the wavefront of the SWs transmitted through the slab is reconstructed in a

way so that we observe the bending of SWs of approximately 36°. We can conclude that the procedure based on the Huygens-Fresnel principle and the approach based on the generalized Snell law are suitable for the estimation of the results of the numerical simulation, and these analytical approaches can describe the system.

C. Graded index slab at the bend of the magnonic waveguide

We use the GRIN slab, designed in the previous section, to guide the SWs through the bend of the waveguide. The numerical study is performed with the aid of micromagnetic simulations (see Appendix B).

Let us consider two straight sections of the flat waveguides of the width 100 nm, made of Co-Fe-B, and connected at the angle 36°. At this angle, we observe the refraction of the SWs by the GRIN slab with the assumed gradient of the saturation magnetization (Fig. 6). In Fig. 7(a), we present this curved waveguide with such a GRIN slab placed at the bend, whereas the results for SWs' propagation through the same structure without the GRIN element are presented in Fig. 7(b). These two systems guide the SWs differently. We can see the SWs' interference pattern in the outgoing section of the bent waveguide without the GRIN slab. Such behavior results from the scattering of the incident fundamental mode (not quantized across the waveguide's width) to the higher modes (quantized across the waveguide's width). As a consequence, the information encoded into the phase of the incident fundamental mode is lost. On the other hand, the application of the GRIN slab introduces the anomalous refraction at waveguide's bend causing that the outgoing waves to propagate along the waveguide in the form of the fundamental mode with nondisturbed wavefronts and well-defined phase. The details of the shape of the bend are irrelevant as long as its geometry follows the rotation of the SW's wavefront in graded index material.

In the previous calculations, the dipolar interactions are neglected, since their full consideration in the boundary-condition problem is a complicated task. Therefore, all investigations are limited to the exchange SWs, including the micromagnetic simulations. Such an approach is justified because the exchange interactions dominate over the dipolar ones for short-wavelength SWs. However, in order to verify the applicability of the GRIN slab, we perform simulations that also include dipolar interactions.

Let us discuss the waveguide with a GRIN slab in which the gradient of the anisotropy field is introduced. In this scenario, the static dipolar magnetic field is uniform throughout the whole system, i.e., if $H > M_S$, like in our system, $\mathbf{H}_{\mathrm{dem},0} = -\hat{\mathbf{z}}M_S$, since the saturation magnetization is uniform, which makes the system easier to model. Following Fig. 5(b), we choose the range of anisotropy, which needs to be applied to have the same bending of
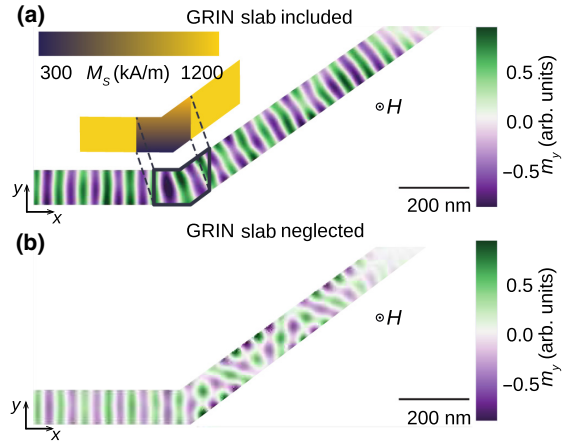

FIG. 7. (a) Propagation of SWs in the Co-Fe-B waveguide, where the GRIN slab is placed at the bend, releases the anomalous refraction. The GRIN slab has the same gradient of M_S as used in Fig. 6. The color map represents a dynamical component of the magnetization in the y direction. A snapshot is taken at the moment when a steady state is reached. At the beginning of the horizontal branch of the waveguide, the microwave antenna excites the SWs and at the end of the tilted branch, the SWs are damped to avoid any reflection. After taking a turn, the SWs propagate smoothly. (b) SWs' propagation in the waveguide without a gradient of magnetic parameters. After taking a turn, the SWs show a complex behavior due to interference between different modes of the waveguide. The width of the waveguide is 100 nm. The material parameters are the same as for the system presented in Fig. 6.

SWs, as for the studies presented in Fig. 7. Keeping the same shape of the GRIN slab, we choose the gradient of the uniaxial anisotropy field in the range from 0.27 to 0 T. The results are compared with the case when the dipolar interactions are included in the micromagnetic simulations, for the same geometry and the values of magnetic parameters. For the 100-nm-wide and 5-nm-thick waveguide, the static demagnetizing field shifts down the dispersion relation, so in order to keep the same wave vector for the considered frequency (25 GHz), it is necessary to apply the external magnetic field of increased value with respect to simulations without the dipolar interactions. We analyze the dispersion relations and find that an additional field $\mu_0 H = 1.35$ T compensates the effect of the static demagnetizing field. The cases when the dipolar interaction is taken into account or neglected, are compared in Fig. 8. Only a small difference is visible, which means that the impact of the dipolar field is not significant. The difference results from different boundary conditions at the edges of waveguides, where spins are partially pinned [68].

It is necessary to note, that in the case of the GRIN slab with the gradient of saturation magnetization in the
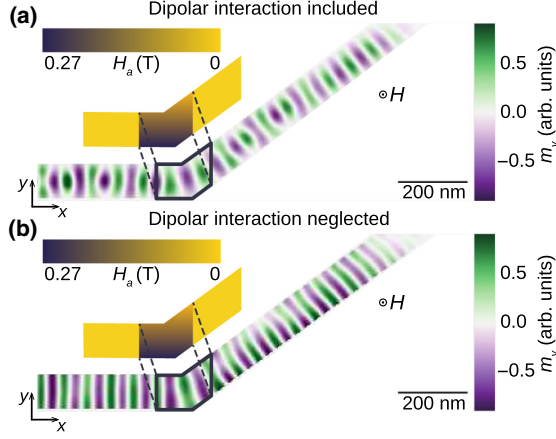
FIG. 8. SW propagation in the bent waveguide of the same geometry, as in Fig. 7. The GRIN slab placed at the bend is characterized by the gradient of anisotropy field H_a. The gradient of H_a is chosen to obtain refraction at the same angle, as in Fig. 7. In(a) the dipolar interaction is included and in(b) it is neglected in the micromagnetic simulations.

out-of-plane magnetized thin film, the static demagnetizing field is not uniform. As a result, both the saturation magnetization and static effective magnetic field are changed in parallel, and it also needs to be taken into account in the design of the GRIN slab for SW steering, which is out of the scope of this paper.

IV. SUMMARY

We present a comprehensive study of the SWs' propagation through the GRIN slab with spatially modulated saturation magnetization or uniaxial anisotropy. Using the analytical model, cross checked by numerical simulations, we are able to relate the phase acquired by SWs during the transmission through the GRIN slab at different locations to the values of the spatially dependent magnetic parameters. With this knowledge, we design the GRIN slab, ensuring the phase-coherent refraction of SWs at a desirable angle, determined by the gradient of saturation magnetization or the gradient of the anisotropy field. Notably, the presented GRIN slab enabled a wide range of phase changes (ca. 1.75π) for high and uniform transmission of SWs (transmittance in the range of 80%–100%) enhanced by utilizing the Fabry-Perot resonances. The analytical model and the main numerical demonstrations are performed for the exchange SWs, later validated with micromagnetic simulations for selected cases with included dipolar interactions.

As an application, we demonstrate the GRIN slab used to guide the SWs coherently in fundamental mode

along the bend in a magnonic waveguide. The micromagnetic simulations are performed for realistic structure and showed the possibility for experimental realization of this idea.

The GRIN slab considered in this paper can be activated on demand by the voltage-induced anisotropy [63]. The spatial changes of the perpendicular anisotropy can be introduced by the variation of the thickness of an insulating spacer separating one of the electrodes. This can open the route for voltage-controlled routing of SWs.

The proposed approach can be verified experimentally by state-of-the-art techniques, like x-ray magnetic circular dichroism [22,69], phase-resolved Brillouin-light-scattering [70], or broadband-microwave spectroscopy [46,71]. We believe that our findings are substantial for further development of the circuits for analog and digital computing based on SWs and contribute to the field of magnonics.

APPENDIX A: SPATIAL PROFILES OF THE SPIN WAVES, RESONANTLY SCATTERED AT THE MAGNETIC SLAB

Solution of the LLE, Eq. (1), provides information about the complex amplitudes of SWs, which propagate in the system. The one-dimensional model presented in this paper has the following solutions:

$$t_A = \frac{4e^{id(k_B - k_A)}}{\alpha_A \alpha_B k_A k_B \left[(f^+)^2 - e^{2idk_B}(f^-)^2 \right]}, \qquad \text{(A1)}$$

$$r_A = \frac{-(f^-)^* f^+ + e^{2idk_B}(f^+)^* f^-}{\left[(f^+)^2 - e^{2idk_B}(f^-)^2 \right]}, \qquad \text{(A2)}$$

$$t_B = \frac{2f^+}{\alpha_B k_B \left[(f^+)^2 - e^{2idk_B}(f^-)^2 \right]}, \qquad \text{(A3)}$$

$$r_B = \frac{2e^{2idk_B} f^-}{\alpha_B k_B \left[(f^+)^2 - e^{2idk_B}(f^-)^2 \right]}, \qquad \text{(A4)}$$

where $f^{\pm}$ is an auxiliary function, namely

$$f^{\pm} = \frac{M_B}{\alpha_A M_A k_A} \pm \frac{M_A}{\alpha_B M_B k_B} - \frac{i}{A},$$

and $(f^{\pm})^*$ is its complex conjugate. The dependence of the wave number on angular frequency $k_{A(B)}(\omega)$ expresses the dispersion relation:

$$k_{A(B)} = \frac{1}{\sqrt{\alpha_{A(B)}M_{S,A(B)}}}\sqrt{\frac{\omega}{\gamma} - \mu_0\left[H + H_{a,A(B)}\right]}, \quad (A5)$$

where H and $H_{a,A(B)}$ are external and anisotropy fields, respectively.

Parameter δ is the thickness of the interfaces and it is a fitting parameter. We find that the best match between analytical and numerical results is achieved for the value of $\delta = 0.5$ nm. It is a reasonable value since the size of the unit cell in micromagnetic simulations is 1 nm.

Information about the energy flow (the amplitude of SWs) and phase shifts can be extracted from Eqs. (A1)–(A4), and as we can see in Figs. 3–5, both quantities fit perfectly to micromagnetic simulations.

Let us present the spatial profile of dynamical components of the magnetization vector. Set of Eqs. (4)–(6), with coefficients defined in Eqs. (A1)–(A4), describe the analytical solution of SW in complex form. To visualize these spatial profiles, the magnetization should be presented in the real form:

$$m = \text{Re}\left[\tilde{m}e^{i(kx-\omega t)}\right] = |\tilde{m}|\cos\left(kx - \omega t + \arg\tilde{m}\right), \quad (A6)$$

where $\tilde{m}$ is a complex coefficient defined for a specific region. It can be incidence, reflection, or transmission coefficient, as defined in Eqs. (A1)–(A4).

In order to compare the results of the analytical model with the ones from numerical simulations, we need to get rid of the explicit dependence on time, because we are not able to compare some exact moments in time. Hence, we average the squared magnetization component in time. The same as we did with the output from simulation after reaching a steady state. The comparison is shown in Fig. 9. We plot the spatial profile of SW for five specific frequencies (see Fig. 3), Figs. 9(a)–9(e), where transmittance is equal to 1 (see Fig. 3). Dark background represents the slab B. Standing wave is visible, which indicates the existence of resonant effect in accordance with Eq. (10). The slab is coupled to the surrounding, and the transmission is relatively high. Therefore, the nodes are not located at zero level, because the amplitude of the reflected wave is always lower than the amplitude of the incident wave. On the right areas (light background), SWs are propagating with a constant amplitude, so after averaging, we get a straight line. Its level indicates the energy flow.

Figure 9 is another remarkable confirmation of the validity of our analytical model.
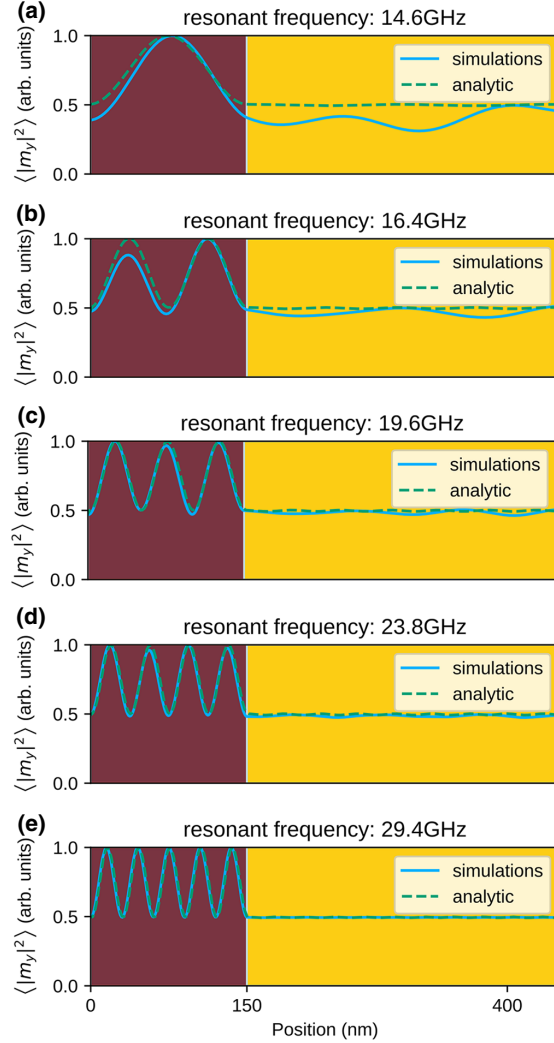

FIG. 9. Normalized spatial profile of dynamical component of the magnetization for the five lowest resonances (a) 14.6 GHz, (b) 16.4 GHz, (c) 19.6 GHz, (d) 23.8 GHz, and (e) 29.4 GHz. Width of the slab is 150 nm, M_S in the matrix is 1200 kA/m and $A_{ex} = 28$ pJ/m. External field is 0.5 T, reduced M_S within the slab is 800 kA/m and reduced exchange stiffness constant A_{ex} is 20 pJ/m. The presented resonances correspond to Fig. 3.

APPENDIX B: MICROMAGNETIC SIMULATIONS

The micromagnetic simulations are performed with the use of the mumax3 package [72], which is the finite-difference time-domain solver of the full Landau-Lifshitz equation. The simulations are conducted to (i) calculate the transmittance and the phase shift of the waves transmitted through the one-dimensional slab, (ii) demonstrate anomalous refraction in thin film, and finally, (iii) to demonstrate

a slab suitable for SW bending in magnonic waveguides. In all these cases, the steady state is simulated, i.e., the response of the system after long, continuous excitation of SWs at a single frequency enabling SWs to travel to the sides of the simulated system.

In order to neglect the influence of the reflections from the borders of the simulated system and, therefore, simplify interpretation of the results, the absorbing boundary conditions are implemented around the sides of the simulated domain (see Fig. 2). In all the simulations we consider SW propagation in 5-nm-thick Co-Fe-B film ($M_S = 1200$ kA/m, $A_{ex} = 27$ pJ/m and reduced damping to 0.0001) in the presence of the out-of-plane magnetic field (applied along the z axis) of value $\mu_0 H = 0.5$ T and discretized with cuboid elements of dimensions ($1 \times 1 \times 5$ nm^3). These values are comparable to the exchange length. Magnetic parameters are modulated only in the region of the slab described in the main part of the paper. In order to be consistent with the analytical theory, which neglects the dipolar interactions, most of the simulations are performed with neglected dipolar interactions as well. Nevertheless, in order to further validate this model, a set of micromagnetic simulations with included dipolar interaction is performed to demonstrate the applicability of the considered slabs to bend SW in a curved waveguide (see Fig. 8).

To calculate the transmittance and the phase shift of the transmitted SW through the slab with respect to frequency or various magnetic parameters, we define a one-dimensional geometry, i.e., discretized by $L_x \times L_y \times L_z$ (4096 $\times$ 1 $\times$ 1) unit cells. These values are obtained by running two separate simulations, i.e., a reference simulation without the slab, and the additional one with the slab. Then, the results of these simulations are compared in order to extract the values of transmittance and phase shift. The transmittance was calculated as a ratio of squared amplitude and the phase shift—as a difference of the SW phases. SWs are excited by an rf magnetic field of frequencies in the range of 14–40 GHz for fixed material parameters or 25 GHz for various material parameters of the slab. rf field is applied locally in a 6-nm narrow region, located on the left side of the slab at a distance of 1548 nm from the slab.

To demonstrate an anomalous refraction in action, we define a two-dimensional system discretized by $L_x \times L_y \times L_z$ (1024 $\times$ 1024 $\times$ 1) unit cells. The scheme of the system is presented in Fig. 2. SWs are excited by an rf field of frequency 25 GHz applied locally in a 6-nm narrow region located on the left side of the slab in the distance of 232 nm. Three different areas can be distinguished there. On the left is the narrow part, 100-nm-wide waveguide, which introduces SWs into the system. In the middle is a 100-nm-wide and 150-nm-long slab with a gradient of the magnetic parameters. The gradient of the magnetic parameters is induced along the y axis.

Saturation magnetization changes in the range of 300–800 kA/m on the distance 100 nm, with direct contact with waveguide. Above is smoothly changed in the range of 800–1200 kA/m to avoid sharp edges. Below, a constant value of 300 kA/m is assumed. On the right-hand side is the semi-infinite medium, which allows the propagation of SWs in any direction freely.

Finally, using the knowledge from the previous step, we design a curved waveguide, which supports coherent SW propagation alongside the waveguide. To create such a curved waveguide, we cut the finite two-dimensional system following the newly created wavefront. The system is discretized by $L_x \times L_y \times L_z$ (2048 $\times$ 512 $\times$ 1) unit cells. SWs are excited by an rf magnetic field of frequency 25 GHz applied locally in 6-nm narrow region located at the distance of 224 nm to the corner from the left side.

[1] S. O. Demokritov and A. N. Slavin, *Magnonics – From Fundamentals to Applications* (Springer-Verlag, Berlin, Heidelberg, 2013).

[2] G. Csaba, Ádám Papp, and W. Porod, Perspectives of using spin waves for computing and signal processing, Phys. Lett. A **381**, 1471 (2017).

[3] A. Khitun, Magnonic holographic devices for special type data processing, J. Appl. Phys. **113**, 164503 (2013).

[4] A. Khitun, M. Bao, and K. L. Wang, Magnonic logic circuits, J. Phys. D: Appl. Phys. **43**, 264005 (2010).

[5] A. V. Chumak, in *Spintronics Handbook: Spin Transport and Magnetism* (CRC Press, 2019), 2nd ed.

[6] K. Vogt, F. Fradin, J. Pearson, T. Sebastian, S. Bader, B. Hillebrands, A. Hoffmann, and H. Schultheiss, Realization of a spin-wave multiplexer, Nat. Commun. **5**, 3727 (2014).

[7] A. V. Sadovnikov, C. S. Davies, V. V. Kruglyak, D. V. Romanenko, S. V. Grishin, E. N. Beginin, Y. P. Sharaevskii, and S. A. Nikitov, Spin wave propagation in a uniformly biased curved magnonic waveguide, Phys. Rev. B **96**, 060401 (2017).

[8] K. Vogt, H. Schultheiss, S. Jain, J. Pearson, A. Hoffmann, S. Bader, and B. Hillebrands, Spin waves turning a corner, Appl. Phys. Lett. **101**, 042410 (2012).

[9] A. Haldar, D. Kumar, and A. O. Adeyeye, A reconfigurable waveguide for energy-efficient transmission and local manipulation of information in a nanomagnetic device, Nat. Nanotechnol. **11**, 437 (2016).

[10] D. D. Sheka, O. V. Pylypovsky, P. Landeros, Y. Gaididei, A. Kakay, and D. Makarov, Micromagnetic theory of curvilinear ferromagnetic shells, arXiv:1904.02641v1 (2019).

[11] Y. Gaididei, A. Goussev, V. P. Kravchuk, O. V. Pylypovskyi, J. M. Robbins, D. D. Sheka, V. Slastikov, and S. Vasylkevych, Magnetization in narrow ribbons: curvature effects, J. Phys. A **50**, 385401 (2017).

[12] V. S. Tkachenko, A. N. Kuchko, M. Dvornik, and V. V. Kruglyak, Propagation and scattering of spin waves in curved magnonic waveguides, Appl. Phys. Lett. **101**, 152402 (2012).

[13] Q. Wang, B. Heinz, R. Verba, M. Kewenig, P. Pirro, M. Schneider, T. Meyer, B. Lägel, C. Dubs, T. Brächer, and A. V. Chumak, Spin Pinning and Spin-Wave Dispersion in Nanoscopic Ferromagnetic Waveguides, Phys. Rev. Lett. **122,** 247202 (2019).

[14] V. E. Demidov, M. P. Kostylev, K. Rott, J. Münchenberger, G. Reiss, and S. O. Demokritov, Excitation of short-wavelength spin waves in magnonic waveguides, Appl. Phys. Lett. **99,** 082507 (2011).

[15] C. Liu, J. Chen, T. Liu, F. Heimbach, H. Yu, Y. Xiao, J. Hu, M. Liu, H. Chang, T. Stueckler, S. Tu, Y. Zhang, Y. Zhang, P. Gao, Z. Liao, D. Yu, K. Xia, Na Lei, W. Zhao, and M. Wu, Exchange-torque-induced excitation of perpendicular standing spin waves in nanometer-thick YIG films, Nat. Commun. **4,** 2702 (2018).

[16] S. J. Hämäläinen, F. Brandl, K. J. A. Franke, D. Grundler, and S. van Dijken, Tunable Short-Wavelength Spin-Wave Emission and Confinement in Anisotropy-Modulated Multiferroic Heterostructures, Phys. Rev. Appl. **8,** 014020 (2017).

[17] J. Chen, T. Yu, C. Liu, T. Liu, M. Madami, K. Shen, J. Zhang, S. Tu, M. S. Alam, K. Xia, M. Wu, G. Gubbiotti, Y. M. Blanter, G. E. W. Bauer, and H. Yu, Excitation of unidirectional exchange spin waves by a nanoscale magnetic grating, Phys. Rev. B **100,** 104427 (2019).

[18] F. Fohr, A. A. Serga, T. Schneider, J. Hamrle, and B. Hillebrands, Phase sensitive Brillouin scattering measurements with a novel magneto-optic modulator, Rev. Sci. Instrum. **80,** 043903 (2009).

[19] S. J. Hämäläinen, M. Madami, Q. Huajun, G. Gubbiotti, and S. van Dijken, Control of spin-wave transmission by a programmable domain wall, Nat. Commun. **9,** 4853 (2018).

[20] J. Jersch, V. E. Demidov, H. Fuchs, K. Rott, P. Krzysteczko, J. Münchenberger, G. Reiss, and S. O. Demokritov, Mapping of localized spin-wave excitations by near-field Brillouin light scattering, Appl. Phys. Lett. **97,** 152502 (2010).

[21] G. Dieterle, J. Förster, H. Stoll, A. S. Semisalova, S. Finizio, A. Gangwar, M. Weigand, M. Noske, M. Fähnle, I. Bykova, J. Gräfe, D. A. Bozhko, H. Y. Musiienko-Shmarova, V. Tiberkevich, A. N. Slavin, C. H. Back, J. Raabe, G. Schütz, and S. Wintz, Coherent Excitation of Heterosymmetric Spin Waves with Ultrashort Wavelengths, Phys. Rev. Lett. **122,** 117202 (2019).

[22] J. Gräfe, M. Weigand, B. V. Waeyenberge, A. Gangwar, F. Groß, F. Lisiecki, J. Rychły, H. Stoll, N. Träger, J. Förster, F. Stobiecki, J. Dubowik, J. Kłos, M. Krawczyk, C. H. Back, E. J. Goering, and G. Schütz, in *Spintronics XII*, edited by H.-J. M. Drouhin, J.-E. Wegrowe, and M. Razeghi, Visualizing nanoscale spin waves using MAXYMUS, Proc. SPIE **11090,** 1109025 (2019).

[23] F. Garcia-Sanchez, P. Borys, R. Soucaille, J.-P. Adam, R. L. Stamps, and J.-V. Kim, Narrow Magnonic Waveguides Based on Domain Walls, Phys. Rev. Lett. **114,** 247206 (2015).

[24] K. Wagner, A. Kákay, K. Schultheiss, A. Henschke, T. Sebastian, and H. Schultheiss, Magnetic domain walls as reconfigurable spin-wave nanochannels, Nat. Nanotechnol. **11,** 432 (2016).

[25] C. Banerjee, P. Gruszecki, J. W. Klos, O. Hellwig, M. Krawczyk, and A. Barman, Magnonic band structure in a Co/Pd stripe domain system investigate by Brillouin light scattering and micromagnetic simulations, Phys. Rev. B **96,** 024421 (2017).

[26] J. Lan, W. Yu, R. Wu, and J. Xiao, Spin-Wave Diode, Phys. Rev. X **5,** 041049 (2015).

[27] Y. Henry, D. Stoeffler, J.-V. Kim, and M. Bailleul, Unidirectional spin-wave channeling along magnetic domain walls of Bloch type, Phys. Rev. B **100,** 024416 (2019).

[28] P. Gruszecki, C. Banerjee, M. Mruczkiewicz, O. Hellwig, A. Barman, and M. Krawczyk, in *Solid State Physics* (Elsevier, 2019), Vol. 70, p. 79.

[29] E. Albisetti, D. Petti, G. Sala, R. Silvani, S. Tacchi, S. Finizio, S. Wintz, A. Calò, X. Zheng, J. Raabe, E. Riedo, and R. Bertacco, Nanoscale spin-wave circuits based on engineered reconfigurable spin-textures, Comm. Phys. **1,** 56 (2018).

[30] P. Clausen, K. Vogt, H. Schultheiss, S. Schäfer, B. Obry, G. Wolf, P. Pirro, B. Leven, and B. Hillebrands, Mode conversion by symmetry breaking of propagating spin waves, Appl. Phys. Lett. **99,** 162505 (2011).

[31] J. W. Kłos, D. Kumar, M. Krawczyk, and A. Barman, Influence of structural changes in a periodic antidot waveguide on the spin-wave spectra, Phys. Rev. B **89,** 014406 (2014).

[32] S. Pan, J. W. Kłos, S. Mieszczak, A. Barman, and M. Krawczyk, Spin waves in periodic antidot waveguide of complex base, J. Phys. D: Appl. Phys. **50,** 275003 (2017).

[33] K.-S. Lee, D.-S. Han, and S.-K. Kim, Physical Origin and Generic Control of Magnonic Band Gaps of Dipole-Exchange Spin Waves in Width-Modulated Nanostrip Waveguides, Phys. Rev. Lett. **102,** 127202 (2009).

[34] F. Ciubotaru, A. V. Chumak, N. Y. Grigoryeva, A. A. Serga, and B. Hillebrands, Magnonic band gap design by the edge modulation of micro-sized waveguides, J. Phys. D: Appl. Phys. **45,** 255002 (2012).

[35] J.-N. Toedt, M. Mundkowski, D. Heitmann, S. Mendach, and W. Hansen, Design and construction of a spin-wave lens, Sci. Rep. **6,** 33169 (2016).

[36] C. S. Davies, A. Francis, A. V. Sadovnikov, S. V. Chertopalov, M. T. Bryan, S. V. Grishin, D. A. Allwood, Y. P. Sharaevskii, S. A. Nikitov, and V. V. Kruglyak, Towards graded-index magnonics: Steering spin waves in magnonic networks, Phys. Rev. B **92,** 020408 (2015).

[37] M. Vogel, B. Hillebrands, and G. Freymann, Spin-Wave Optical Elements: Towards Spin-Wave Fourier Optics, arXiv:1906.02301 (2019).

[38] P. Gruszecki and M. Krawczyk, Spin-wave beam propagation in ferromagnetic thin films with graded refractive index: Mirage effect and prospective applications, Phys. Rev. B **97,** 094424 (2018).

[39] N. J. Whitehead, S. A. R. Horsley, T. G. Philbin, and V. V. Kruglyak, A Luneburg lens for spin waves Appl. Phys. Lett. **113,** 212404 (2018).

[40] N. J. Whitehead, S. A. R. Horsley, T. G. Philbin, and V. V. Kruglyak, Graded index lenses for spin wave steering, Phys. Rev. B **100,** 094404 (2019).

[41] R. Gieniusz, P. Gruszecki, M. Krawczyk, U. Guzowska, A. Stognij, and A. Maziewski, The switching of strong spin wave beams in patterned garnet films, Sci. Rep. **7,** 8771 (2017).

[42] O. Dzyapko, I. Borisenko, V. Demidov, W. Pernice, and S. Demokritov, Reconfigurable heat-induced spin wave lenses, Appl. Phys. Lett. **109,** 232407 (2016).

[43] M. Vogel, R. Aßmann, P. Pirro, A. V. Chumak, B. Hillebrands, and G. von Freymann, Control of Spin-Wave Propagation using Magnetisation Gradients, Sci. Rep. **8**, 1 (2018).

[44] M. Zelent, M. Mailyan, V. Vashistha, P. Gruszecki, O. Gorobets, Y. Gorobets, and M. Krawczyk, Spin wave collimation using a flat metasurface, Nanoscale **11**, 9743 (2019).

[45] J. W. Kłos, Y. S. Dadoenkova, J. Rychły, N. N. Dadoenkova, I. L. Lyubchanskii, and J. Barnaś, Hartman effect for spin waves in exchange regime, Sci. Rep. **8**, 17944 (2018).

[46] O. V. Dobrovolskiy, R. Sachser, S. A. Bunyaev, D. Navas, V. M. Bevz, M. Zelent, W. Śmigaj, J. Rychły, M. Krawczyk, R. V. Vovk, M. Huth, and G. N. Kakazei, Spin-Wave Phase Inverter upon a Single Nanodefect, ACS Appl. Mater. Inter. **11**, 17654 (2019).

[47] N. Yu, P. Genevet, M. A. Kats, F. Aieta, J.-P. Tetienne, F. Capasso, and Z. Gaburro, Light Propagation with Phase Discontinuities: Generalized Laws of Reflection and Refraction, Science **334**, 333 (2011).

[48] J. Mulkers, B. Waeyenberge, and M. V. Milosevic, Tunable Snell's law for spin waves in heterochiral magnetic films, Phys. Rev. B **97**, 104422 (2018).

[49] J. F. Cochran and B. Heinrich, Boundary conditions for exchange-coupled magnetic slabs, Phys. Rev. B **45**, 13096 (1992).

[50] V. V. Kruglyak, O. Y. Gorobets, Y. I. Gorobets, and A. N. Kuchko, Magnetization boundary conditions at a ferromagnetic interface of finite thickness, J. Phys. Condens. Matter **26**, 406001 (2014).

[51] E. Hecht, , *Optics* (Pearson Education Limited, Essex, 2017).

[52] K. Tang, C. Qiu, J. Lu, M. Ke, and Z. Liu, Focusing and directional beaming effects of airborne sound through a planar lens with zigzag slits, J. Appl. Phys. **117**, 024503 (2015).

[53] N. Yu and F. Capasso, Flat optics with designer metasurfaces, Nat. Mat. **13**, 139 (2014).

[54] M. Jang, Y. Horie, A. Shibukawa, J. Brake, Y. Liu, S. M. Kamali, A. Arbabi, H. Ruan, A. Faraon, and C. Yang, Wavefront shaping with disorder-engineered metasurfaces, Nat. Photonics **12**, 84 (2018).

[55] A. Conca, J. Greser, T. Sebastian, S. Klingler, B. Obry, B. Leven, and B. Hillebrands, Low spin-wave damping in amorphous $Co_{40}Fe_{40}B_{20}$ thin films, J. Appl. Phys. **113**, 213909 (2013).

[56] P. Kuświk, H. Głowiński, E. Coy, J. Dubowik, and F. Stobiecki, Perpendicularly magnetized $Co_{20}Fe_{60}B_{20}$ layer sandwiched between Au with low Gilbert damping, J. Phys. Condens. Matter **29**, 435803 (2017).

[57] A. V. Chumak, A. A. Serga, and B. Hillebrands, Magnonic crystals for data processing, J. Phys. D: Appl. Phys. **50**, 244001 (2017).

[58] A. Maziewski, P. Mazalski, Z. Kurant, M. O. Liedke, J. McCord, J. Fassbender, J. Ferré, A. Mougin, A. Wawro, L. T. Baczewski, A. Rogalev, F. Wilhelm, and T. Gemming, Tailoring of magnetism in Pt/Co/Pt ultrathin films by ion irradiation, Phys. Rev. B **85**, 054427 (2012).

[59] A. Wawro, Z. Kurant, M. Jakubowski, M. Tekielak, A. Pietruczik, R. Böttger, and A. Maziewski, Magnetic Prop-

erties of Coupled Co/Mo/Co Structures Tailored by Ion Irradiation, Phys. Rev. Appl. **9**, 014029 (2018).

[60] S. Ikeda, K. Miura, H. Yamamoto, K. Mizunuma, H. D. Gan, M. Endo, S. Kanai, J. Hayakawa, F. Matsukura, and H. Ohno, A perpendicular-anisotropy CoFeB–MgO magnetic tunnel junction, Nat. Mater. **9**, 721 (2010).

[61] V. B. Naik, H. Meng, J. X. Xiao, R. S. Liu, A. Kumar, K. Y. Zeng, P. Luo, and S. Yap, Effect of electric-field on the perpendicular magnetic anisotropy and strain properties in CoFeB/MgO magnetic tunnel junctions, Appl. Phys. Lett. **105**, 052403 (2014).

[62] S. Miwa, M. Suzuki, M. Tsujikawa, T. Nozaki, T. Nakamura, M. Shirai, S. Yuasa, and Y. Suzuki, Perpendicular magnetic anisotropy and its electric-field-induced change a metal-dielectric interfaces, J. Phys. D: Appl. Phys. **52**, 063001 (2018).

[63] B. Rana, S. Choudhury, K. Miura, H. Takahashi, A. Barman, and Y. Otani, Electric field control of spin waves in ultrathin CoFeB films, Phys. Rev. B **100**, 224412 (2019).

[64] M. Vogel, A. V. Chumak, E. H. Waller, T. Langner, V. I. Vasyuchka, B. Hillebrands, and G. von Freymann, Optically reconfigurable magnetic materials, Nat. Phys. **11**, 487 (2015).

[65] A. V. Sadovnikov, A. A. Grachev, S. E. Sheshukova, Y. P. Sharaevskii, A. A. Serdobintsev, D. M. Mitin, and S. A. Nikitov, Magnon Straintronics: Reconfigurable Spin-Wave Routing in Strain-Controlled Bilateral Magnetic Stripes, Phys. Rev. Lett. **120**, 257203 (2018).

[66] J. Stigloher, M. Decker, H. S. Körner, K. Tanabe, T. Moriyama, T. Taniguchi, H. Hata, M. Madami, G. Gubbiotti, K. Kobayashi, T. Ono, and C. H. Back, Snell's Law for Spin Waves, Phys. Rev. Lett. **117**, 037204 (2016).

[67] Z. Tian, C. Shen, J. Li, E. Reit, Y. Gu, H. Fu, S. A. Cummer, and T. J. Huang, Programmable Acoustic Metasurfaces, Adv. Funct. Mater. **29**, 1808489 (2019).

[68] K. Y. Guslienko, S. O. Demokritov, B. Hillebrands, and A. N. Slavin, Effective dipolar boundary conditions for dynamic magnetization in thin magnetic stripes, Phys. Rev. B **66**, 132402 (2002).

[69] F. Lisiecki, J. Rychły, P. Kuświk, H. Głowiński, J. W. Kłos, F. Groß, N. Träger, I. Bykova, M. Weigand, M. Zelent, E. J. Goering, G. Schütz, M. Krawczyk, F. Stobiecki, J. Dubowik, and J. Gräfe, Magnons in a Quasicrystal: Propagation, Extinction, and Localization of Spin Waves in Fibonacci Structures, Phys. Rev. Appl. **11**, 054061 (2019).

[70] K. Vogt, H. Schultheiss, S. J. Hermsdoerfer, P. Pirro, A. A. Serga, and B. Hillebrands, All-optical detection of phase fronts of propagating spin waves in a $Ni_{81}Fe_{19}$ microstripe, Appl. Phys. Lett. **95**, 182508 (2009).

[71] K. Baumgaertl, S. Watanabe, and D. Grundler, Phase control of spin waves based on a magnetic defect in a one-dimensional magnonic crystal, Appl. Phys. Lett. **112**, 142405 (2018).

[72] A. Vansteenkiste, J. Leliaert, M. Dvornik, M. Helsen, F. Garcia-Sanchez, and B. V. Waeyenberge, The design and verification of MuMax3, AIP Adv. **4**, 107133 (2014).

Correction: An outdated manuscript file was inadvertently used for publication. The correct file has been processed, with changes to text in Sec. II A and to equations in Appendix A.

4.3 P3 - Interface modes in planar one-dimensional magnonic crystals

The paper P3 is a continuation of the studies concerning the magnonic surface/interface states conducted in the Department of Physics of Nanomaterials[70, 97]. The work started from a semester project that I prepared on the subject "Transport and topological states in 2D systems" conducted by prof. Anna Dyrdał. The goal was to calculate the Zak phase[136, 138] of the spin wave in centrosymmetric crystal from the symmetry criterion[137]. Joshua Zak demonstrated that it is enough to check the parity of eigenmodes at the edges of a given band to determine its Berry phase[12]. For the project, I calculated the Zak phase for exchange spin waves, taking for granted the formula provided by Zak, relying on the fact that one can draw a full analogy between exchange spin waves and electronic states in crystal.

In our group, we decided to continue the research, and as an ultimate goal, we wanted to demonstrate bulk-to-edge correspondence that could be used to determine the condition for the existence of the interface states, localized at the junction of two, semi-infinite, one-dimensional magnonic crystals.

I started the numerical studies for paper P3 by calculating spin wave spectra of one-dimensional magnonic crystal in the function of the bulk parameter, i.e., filling fraction, that is varying from zero to one. In this manner system transit from the uniform film made of one type of material, through the magnonic crystal to again uniform, but made of the second type of material. While the bulk parameter is changing, band gaps are closing and opening, and the Zak phase is changing. We selected two pairs of magnonic crystals with different filling fractions, and partially overlapping frequency gaps, to observe the interface modes.

Then, we derived the general formula for the Zak phase for the bands of magnonic crystals. The formula was derived both in exchange and exchange-dipolar regimes. This allowed us to formulate the existence condition for interface states in 1D planar magnonic crystals. We could predict in which common frequency gaps the interface modes will be induced and numerically confirm our theoretical predictions. We extended our consideration to the case when magnonic crystals are not faced on the high symmetry point, i.e., when the symmetry criterion for the Zak phase cannot be applied.

In the last part of work P3, we investigated the exchange-dipolar spin waves since such a system is not a close analog to the electronic system, and can be related to experimentally achievable structures. The system here possesses more complex behavior due to the sensitivity of dipolar interaction on interfaces. The complexity comes also from the fact that ferromagnetic resonance frequencies of both constituent materials are different. In the considered system: (i) the matching of the frequency gaps of two semi-infinite magnonic

crystals to the same frequency range is more complex; (ii) we can observe both the oscillatory and the evanescent solution in constituent elements of the structure (i.e., in different strips). Nevertheless, the numerical calculations confirmed also the theoretical prediction for the existence of the interface states in the band gap.

In work P3, I performed calculations of spin wave spectra by plane expansion wave method, determined the Zak phase, prepared graphics, and worked on the manuscript. I was the corresponding author of this manuscript.

scientific reports

OPEN

Interface modes in planar one-dimensional magnonic crystals

Szymon Mieszczak✉ & Jarosław W. Kłos

We present the concept of Zak phase for spin waves in planar magnonic crystals and discuss the existence condition of interface modes localized on the boundary between two magnonic crystals with centrosymmetric unit cells. Using the symmetry criterion and analyzing the logarithmic derivative of the Bloch function, we study the interface modes and demonstrate the bulk-to-edge correspondence. Our theoretical results are verified numerically and extended to the case in which one of the magnonic crystals has a non-centrosymmetric unit cells. We show that by shifting the unit cell, the interface modes can traverse between the band gap edges. Our work also investigate the role of the dipolar interaction, by comparison the systems both with exchange interaction only and combined dipolar-exchange interactions.

Band structure is a distinctive feature of wave excitations in periodic structures. Solutions of the wave equations in a periodic medium, Bloch waves are characterized by the quasimomentum $\hbar k$, related to the wavevector k. Adiabatic changes of the wavevector in the momentum space lead to the acquisition of a geometrical phase. Introduced by M. Berry[1], this phase is related to the topological invariants that distinguish the topological classes of the system. For Bloch waves $\Phi_k(x)$ propagating in a periodic 2D or 3D medium this role is played by Chern numbers[2–4], which are determined for successive bands from the Berry phases calculated along a closed loop in the momentum space - i.e., along the edge of 1st Brillouin zone. In a 1D system a loop for the Berry phase can be realized by sweeping the wavenumber k across the 1st Brillouin zone (i.e., in the range $[-\pi/a, \pi/a]$, where a is the period of the structure). Then, we take advantage of the periodicity of the Bloch function in the reciprocal space: $\Phi_k(x) = \Phi_{k+2\pi/a}(x)$. Referred to as the Zak phase[5,6], this phase characterizes each band of a 1D crystal due to the lack of degeneration in 1D systems. The Zak phase can be altered by changing other parameters of the system (e.g., by tuning its structural and material parameters) significantly enough to disturb the band structure resulting in band gap closing and reopening.

The Zak phase has an ambiguity related to the selection of the unit cell[7]. However, for a centrosymmetric unit cell it only takes on two well-defined values, which are 0 and π. These values classify the bands in two categories and distinguish the types of band gaps[6,8,9]. The classification can be based on the symmetry of the Bloch functions on the edges of the bands/gaps[8,10]. This can help establish the criteria for the existence of edge or interface modes[8] in terminated periodic structures, where bulk characteristics (symmetry of the bands and their Zak phases) correlate with surface parameters determining the existence of edge modes in the band gaps.

Zak phase and edge modes have been the subject of investigation in 1D continuous systems in the form of layered media or periodically corrugated waveguides. Various kinds of systems have been studied, including photonic crystals[11,12], microwave systems[13,14], plasmonic crystals[15] and phononic crystals[16]. It is worthy of notice that the definition and interpretation of surface parameters can vary with system. Examples include the rate of decay of electron waves outside the crystal (e.g., in vacuum[8]), surface impedance for electromagnetic waves[12], or pinning parameter for spin waves[17]. The Zak phase is measurable quantity[7] and is a powerful tool to predict the existence and to describe properties of surface/edge modes.

The studies on spin waves in magnonic crystals[18–20] reported to date, mostly address lattice models based on the Heisenberg Hamiltonian[21–23] or the Landau-Lifshitz equation, but discretized in the second-quantization approach to the Bogliubov-de Gennes Hamiltonian[24]. They strongly indicate the importance of the Dzyaloshinskii-Moriya interaction and dipolar interaction for the occurrence of non-zero Chern numbers. A general discussion of the topological origin of magnetostatic surface spin waves has been provided recently in Refs.[25–27]. Topological concepts can be used to reinterpret those studies of spin-wave defect and edge states in magnonic crystals[28–34] which discuss the existence of localized states in terms of symmetry criteria[8].

In this paper we demonstrate that (i) the same standard formula for the Zak phase as used for electronic states[1] applies to both exchange and exchange-dipolar spin waves in 1D planar magnonic crystals; (ii) in magnonic crystals with centrosymmetric unit cell the Zak phase can be determined by a symmetry-related criterion, and

Institute of Spintronics and Quantum Information, Faculty of Physics, Adam Mickiewicz University, Poznań, Poland. ✉email: szymon.mieszczak@amu.edu.pl
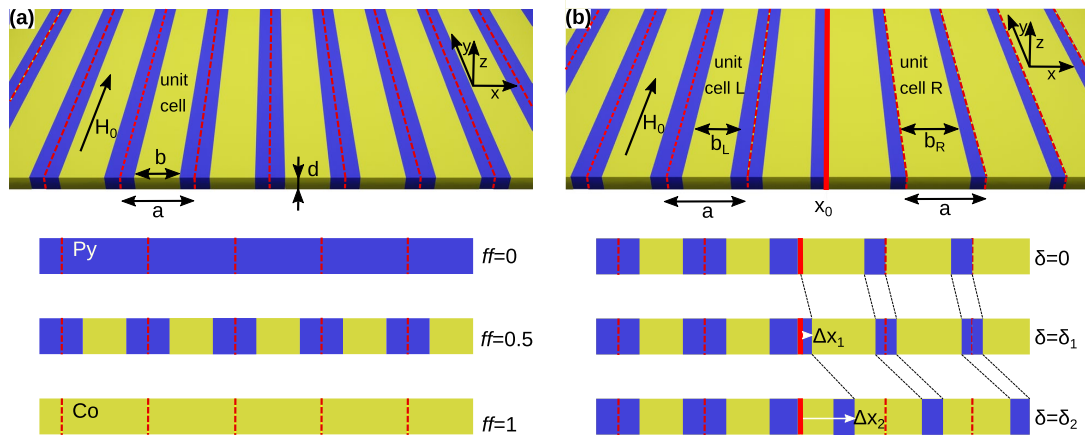
Figure 1. (**a**) The geometry of the one-dimensional magnonic crystal. Red dashed lines mark the edges of centrosymmetric unit cells of the size a (lattice constant). Yellow and blue colors distinguish the strips made of Co and Py of the width: b and $a - b$, respectively. The strips are thin $d \ll a$, and the magnetic field H_0 is applied along the strips (static demagnetizing effects are absent). In our studies, we changed the width of both strips, keeping the lattice constant fixed (see the inset below **a**). By sweeping the bulk parameter (i.e., the filling fraction) $ff = b/a$ in the range $[0, 1]$, we can tune the SW spectrum between the limits corresponding to the uniform layer of Py ($ff = 0$) and Co ($ff = 1$). (**b**) Two semi-infinite magnonic crystals differing in filling fractions ($ff_L \neq ff_R$), interfaced at the edges of units cells (solid red line). For the magnonic crystal on the left (right) side, we chose a centrosymmetric (non-centrosymmetric) unit cell. The selection of the unit cell does not affect the spectrum of the infinite magnonic crystal but is important for the formation of interface states. The parameter $\delta = \Delta x / a = [0, 1)$, describing the selection (i.e., the shift) of the unit cell, can then be treated as an interface parameter (see the inset below **b**). The values δ_1, δ_2 (and Δx_1, Δx_2) correspond to two possible selections of centrosymmetric unit cell.

the values of the Zak phase for successive bands can be used to investigate the existence of interface states on the boundary between two semi-infinite magnonic crystals; (iii) the calculations done for the fictitious model, where the dipolar interactions were switched off, shows a close analogy to the electronic system; (iv) the numerical calculations performed for a realistic, dipolar-exchange system confirm the theoretical predictions regarding the existence of interface spin-wave modes.

Structure and model

Structure. We investigate the spin-waves (SWs) localized on the interface between two one-dimensional magnonic crystals (1D MCs). Each 1D MC is built from two kinds of strips, differing in magnetic parameters, that are arranged periodically in the plane, being in direct contact with each other. The structure of a single 1D MC is schematically presented in Fig. 1a. Such a system can be fabricated by lithographic techniques[35–37], where two different materials can be deposited in separate areas, by the ion implantation, where magnetic anisotropy, magnetization saturation, or exchange length can be changed in initially homogeneous magnetic layer[38,39], or by inducing a thermal gradient that suppress locally the magnetization saturation[40]. In our model, we consider two sets of parameters corresponding to widely used materials, namely cobalt (Co) and permalloy (Py). The properties that are important for SW propagation are saturation magnetization M_S and exchange length λ_{ex}. These parameters are equal to $M_{S,Co} = 1445 \, kA/m$, $\lambda_{ex,Co} = 4.78 \, nm$, $M_{S,Py} = 860 \, kA/m$, $\lambda_{ex,Co} = 5.29 \, nm$. We assumed that both materials are amorphous, and there is no magnetocrystalline or surface magnetic anisotropy in our system. The strips are flat, i.e., their thickness d is much smaller than their width. This assumption allows restricting our consideration to the SW fundamental mode, that is not quantized across the thickness. Additionally, we assume that our sample is saturated by an external magnetic field of the magnitude $\mu_0 H_0 = 0.2 \, T$ oriented along the strips. For this magnetic configuration, the static demagnetizing field is equal to zero.

Two semi-infinite 1D MCs are jointed as it is presented in Fig. 1b. They are interfaced on the edges of their unit cells. The strips in both MCs are made of the same materials (Py and Co), and have the same period a and thickness d. The structures on both sides of the interface differ only by: (i) the filling fractions ff—the ratio between the width of Co strip b and the period a ($ff = b/a$) and (ii) the selection of the unit cell—described by the parameter δ. In the 1D crystal, the unit cell of the width a can be shifted by arbitrary distance in the range $\Delta x = [0, a)$ ($\Delta x = 0$ denotes unit cell with the whole Co(Py) strip on the left(right) side of unit cell). This selection does not affect the spectrum of infinite crystal (i.e., the band structure of propagating modes) but is important for the existence of surface/interface modes in the structures terminated at the edge of the unit cell. The parameter $\delta = \Delta x / a$ has two distinguished values equal to: $\delta_1 = 1/2 - ff/2$, $\delta_2 = 1 - ff/2$. For these values unit cell becomes centrosymmetric. We calculated the Zak phase and logarithmic derivative of Bloch function for δ_1, where both 1D MCs have the same type of symmetry, i.e., Co strip is placed in the middle of the unit cell.

Please also note that the cells for $\delta = 0$ and $\delta = 1$ are equivalent. In our studies, we are investigating the existence of SW modes localized on the interface between two 1D MC in the function of bulk parameter ff and interface parameter δ. One can imagine the system design based on modulation of some other bulk parameter, like value of external magnetic field[41,42], thickness modulation[43-45], or interface/surface parameters, like the modifications of the structures close to the interface/surface[29,31].

Model for magnetization dynamics. We describe the SW modes in 1D MCs using the classical approach, based on the Landau-Lifshitz equation (LLE), which is an equation of motion for spatially dependent magnetization vector $\boldsymbol{M}(\boldsymbol{r}, t)$ in the effective magnetic field $\boldsymbol{H}_{\text{eff}}(\boldsymbol{r}, t)$:

$$\partial_t \boldsymbol{M} = -\mu_0 |\gamma| \boldsymbol{M} \times \boldsymbol{H}_{\text{eff}}, \tag{1}$$

where $\mu_0 = 4\pi \times 10^{-7}$H/m is the permeability of vacuum and $|\gamma| = 194.6$ GHz/T gyromagnetic ratio. In our case $\boldsymbol{H}_{\text{eff}}$ is composed of the following terms:

$$\boldsymbol{H}_{\text{eff}}(\boldsymbol{r}, t) = \boldsymbol{H}_0(\boldsymbol{r}) + \boldsymbol{H}_{\text{dm}}(\boldsymbol{r}, t) + \boldsymbol{H}_{\text{ex}}(\boldsymbol{r}, t). \tag{2}$$

The symbols: $\boldsymbol{H}_0$, $\boldsymbol{H}_{\text{dm}}(\boldsymbol{r}, t)$ and $\boldsymbol{H}_{\text{ex}}(\boldsymbol{r}, t)$ stand for external field, demagnetizing field and exchange field, respectively. The last two terms are both spatially and temporally dependent since they are related to dynamic exchange and dynamic dipolar interaction. The SWs are calculated in linear approximation, where the magnetization dynamics can be considered as precession motion around the static magnetic configuration $\boldsymbol{M}(\boldsymbol{r}) \approx M_S \hat{\boldsymbol{y}}$ with dynamic component $\boldsymbol{m}(\boldsymbol{r}, t) = \boldsymbol{m}(\boldsymbol{r}) e^{i\omega t}$ circulating harmonically in time, with the frequency ω: $\boldsymbol{M}(\boldsymbol{r}, t) = \boldsymbol{M}(\boldsymbol{r}) + \boldsymbol{m}(\boldsymbol{r}) e^{i\omega t}$. We consider only the case where SWs propagate along the direction of periodicity $\hat{\boldsymbol{x}}$. Therefore, the SW amplitude $\boldsymbol{m}(x) = m_\parallel(x)\hat{\boldsymbol{x}} + m_\perp(x)\hat{\boldsymbol{z}}$ depends only on $x-$coordinate only. In linear approximation the LLE (1) has a form of the set of two ordinary linear differential equations with periodic coefficients (see Supplementary Information, Section 1). Therefore, according to the Floquet's theorem[46], their solutions can be presented as Bloch function $\boldsymbol{m}_k(x) = \boldsymbol{u}_k(x) e^{ikx}$ with two complex components $m_{k,\parallel}, m_{k,\perp}$ related to in-plane and out-of plane magnetization dynamics, respectively. The symbol k stands for the wavenumber and $\boldsymbol{u}_k(x) = u_{k,\parallel}(x)\hat{\boldsymbol{x}} + u_{k,\perp}(x)\hat{\boldsymbol{z}}$ is periodic component of the Bloch function: $\boldsymbol{u}_k(x) = \boldsymbol{u}_k(x + a)$.

In this study, we consider SW spectra for two kind of effective field: (i) dipolar interaction are neglected; (ii) dipolar interactions are included. In the first case, we assumed that the unit cell has a size equal to $a = 100$ nm, while in the second, $a = 1000$ nm. In both cases, the thickness $d = 20$ nm $\ll a$ and in the model, we assume an infinite length of strips that gives us an effectively 1D system.

Interface states. We followed the work[6] to determinate the Zak phase as a topological characteristic of every (nth) band of the dispersion relation:

$$\theta_n = \Im \int_{-\pi/a}^{\pi/a} \frac{\int_{-a/2}^{a/2} \boldsymbol{u}_{n,k}^* \cdot \partial_k \boldsymbol{u}_{n,k} dx}{\int_{-a/2}^{a/2} \boldsymbol{u}_{n,k}^* \cdot \boldsymbol{u}_{n,k} dx} dk, \tag{3}$$

for two 1D MCs which were then joined at the common interface. In supplementary Information, Section 1, we present a detailed discussion of the applicability of formula (3) to SW. The value of the Zak phase depends on the selection of the unit cell[7]. For the centrosymmetric unit cell, the Zak phase takes two quantized values, either 0 or π and can be deduced from symmetry criterion of modes (see Supplementary Information, Section 2 for details).

The necessary condition to observe the SW modes localized on the interface of two 1D MCs (Fig. 1b) is an overlapping some frequency gaps in the spectra of both 1D MCs. This fact ensures the exponential decaying of the mode on both sides of the interface, with the rate $\pm k_i$. For centrosymmetric unit cell, the logarithmic derivative is real and has a constant sign within the gap[8] (see Supplementary Information, Section 2). Therefore, the matching of the signs of logarithmic derivatives of Bloch function:

$$\rho(k) = \left. \partial_x \ln \left(m_{k,\alpha}(x) \right) \right|_{x=x_{0\pm}} = \left. \frac{\partial_x m_{k,\alpha}(x)}{m_{k,\alpha}(x)} \right|_{x=x_{0\pm}}, \tag{4}$$

on both sides of the interface between two 1D MCs ($x = x_{0\pm}$) is equivalent to the fulfillment the boundary conditions for $m_{k,\alpha}$ (for each component ($\alpha = \{\perp, \parallel\}$). These conditions allow finding the SW interface modes. It is worth noting that that we can limit our consideration only to one complex component of the Bloch function because $m_{k,\perp}/m_{k,\parallel} = Ce^{-i\pi/2}$, where C is real and has a constant sign, determined by the direction of precession ($C = 1$ for purely exchange waves).

The relation between the sign of logarithmic derivative ρ in the gap above nth band and Zak phases θ_m can be written for 1D MC of centrosymmetric unit cells as[12] (see Supplementary Information, Section 2):

$$\text{sgn}(\rho) = \pm(-1)^{n-1} \exp \sum_{m=1}^{n} i\theta_m, \tag{5}$$

where $m = 1, \ldots, n$ indexes all bands below the gap. The signs '+' and '-' in the formula (5) refers to two possible selection of the complex wavevector in the gap, which describes the mode decaying to the right ($k = k_r + ik_i$) and to the left ($k = k_r - ik_i$) in the crystal, respectively[10] ($k_i > 0$). The Eq. (5) relates the topological parameter (Zak phases) characterizing the bands of 1D MC(s) with the boundary condition at the interface (expressed by

the logarithmic derivative of the SW amplitude). The modes localized on the interface between two 1D MCs can (cannot) exist when the signs of logarithmic derivative are the same (different) on both side of the interface (see the plots of ρ for both 1D MC in Supplementary Information, Section 2). It means that the expression $(-1)^{n-1} \exp \sum_{m=1}^{n} i\theta_n$ must have opposite signs on both side of the interface to compensate the change of the sign related to different direction of decaying of interface modes for $x \rightarrow \pm\infty$ (i.e., the signs '±' at the beginning of the formula for $\text{sgn}(\rho)$ - see Supplementary Information, Section 2 for details).

The logarithmic derivative taken at the symmetry points of centrosymmetric unit cells has zeros and poles only at the edges of frequency gaps and ρ is real inside the gaps (see Supplementary Information, Section 2). It means that ρ cannot change its sign inside the gap. Therefore, the agreement of the signs of ρ in common frequency gaps, and eventually the existence of interface modes, depends on qualitative features of both 1D MCs spectra. More precisely, depends on the sequences of zeros and poles of ρ at gaps/bands boundaries and its signs in successive gaps. We show in the Supplementary Information, Section 2 that mentioned qualitative changes in the spectrum can be expresses as a $0 \leftrightarrow \pi$ flips of Zak phase θ.

It is worth noting that there are always two ways to select the centrosymmetric unit cell (i.e, there are two symmetry centers shifted by half of the period $\Delta x = a/2$) which are not equivalent for ρ and θ. When we shift the centrosymmetric unit cell by $a/2$ then θ flips $0 \leftrightarrow \pi$ in every band and ρ is negated in every second gap (see the Supplementary Information, Section 2 for explanations).

The more general case is when the unit cells are not selected as centrosymmetric. Then, the symmetry-related criteria for the existence of interface modes cannot be used. However, we can test the continuous transition between two different centrosymmetric selections of the unit cell. We investigate numerically how the shift of the unit cell Δx, described by the parameter $\delta = \Delta x/a$, influences the existence of SW interface modes. We will keep the centrosymmetric unit cell for the 1D MC on the left side (see Fig. 1b) and change the selection of the unit cell for 1D MC on the right by swapping the parameter δ in the whole range [0, 1). For the gradual change of δ, we should observe the continuous transition of the frequencies of the SW interface modes between the boundaries of the gap. The SW interface modes for the values δ_1 and δ_2 correspond to the selection of centrosymmetric cell for the 1D MC on the right side of the interface. In this case, the observation of interface states must be consistent with the symmetry-related existence conditions for these states.

Numerical calculations.   The LLE is solved by Plane Wave Method (PWM), which is suitable for periodic structures. Detailed discussion of the application of this computational method for planar magnonic crystals is presented in the paper by Krawczyk et al.[47]. Solving LLE with PWM gives us the information of dispersion relation and SW's eigenmodes. The bulk properties of SW in single unit cell (infinite 1D MC) are investigated for the one-dimensional unit cell with periodic boundary conditions. The calculations are done independence on the bulk parameter: filling fraction (ff).

To calculate the SW interface modes, we use a supercell approach[48]. We mimic two semi-infinite 1D MC, joined at the interface, by the supercell composed by finite 1D MC of two kinds, each consisting of $N = 100$ unit cells. Inevitable artifact of this approach is existence of second (complementary) interface, due to periodic boundary conditions, which can also bound the SW interface modes. Therefore, in our calculation, we will see two modes localized on different interfaces. This modes will be degenerated (and will occupy both interfaces at the same frequency) for $\delta = \delta_1$ or $\delta = \delta_2$, where unit cells are centrosymmetric and both interfaces are structurally identical.

For the geometry presented in Fig. 1b, the number of unit cells within each 1D MC should diverge to infinity. However, due to computational power limitations, we are constantly forced to perform the computations on the finite domain. To reproduce the spectrum of SW interface modes satisfactorily, we must consider the large supercell, where the distance between two interfaces is enough to avoid overlapping decaying exponentially "tails" of interface modes. For considered structures, this condition is fulfilled even for the smallest gap (characterized by small decay rates k_i) when taking about 100 unit cells of each MCs. Thus the length of each 1D MC is $D = Na$, where N is the number of unit cells and a unit cell's width. Such systems can be easily investigated on a desktop computers.

Results

Firstly, we consider the fictitious planar 1D MC with neglected dipolar interaction. This step allows us later to isolate the impact of dipolar interaction on the existence conditions of interface modes. We assumed a small lattice constant, $a = 100$ nm, where dipolar interaction would be negligible anyway. Nevertheless it is important to note, that even for small unit cell, system with dipolar interaction would vary in the following aspect: (i) dispersion relation is shifted up; (ii) dispersion relation is dependent on the direction of the external magnetic field; (iii) for k close to 0 group velocity is nonzero; (iv) for k close to 0 precession of magnetization vector is not perfectly circular.

Secondly, we consider the planar 1D MC with included dipolar interaction. To make them meaningful and propose a structure that is accessible experimentally, we assumed lattice constant, $a = 1000$ nm. In Supplementary Information, we show that the Zak phase for dipolar-exchange system (i.e., the system where the elliptical precession must be taken into account) is defined in the same way as for exchange systems. Therefore, the calculation of the Zak phase and logarithmic derivative can be performed in the same manner.

Exchange spin waves.   For the system of the small lattice constant $a = 100$ nm, we neglected the dipolar interactions. We start the discussion by analyzing the dependence of the band structure of infinite MC on the bulk parameter—ff. In Fig. 2, the gray and white areas mark the frequency bands and gaps, respectively. For exchange spin waves, the gaps in 1D MC are opened alternatively in the center of the 1st Brillouin zone (BZ),
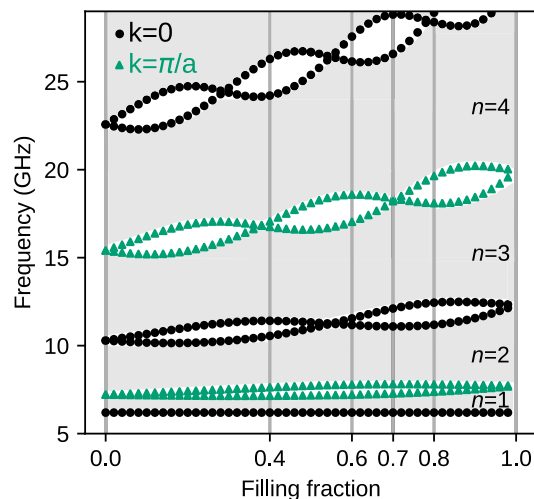
Figure 2. The evolution of SW spectra in dependence of the bulk parameter: filling fraction *ff* for exchange dominated 1D MC ($a = 100$ nm). White areas represents frequency gaps, while gray regions correspond to the successive frequency bands: $n = 1, 2, 3 \ldots$. The edges of the bands: $k = 0$ and $k = \pi/a$ are marked by black dots and green triangles, respectively. The vertical lines at $ff = 0.4, 0.7$ and $ff = 0.6, 0.8$ denote the pairs which were interfaced to look for the SW interface modes in common frequency gaps.

i.e., for $k = 0$, and edge of the 1st BZ, i.e., for $k = \pi/a$ (see also Fig.3). These values determine the edges of gaps: black dotted line for $k = 0$ and green dotted line for $k = \pi/a$. In the absence of magnetocrystalline anisotropy, the lowest black line is independent of the material or structural parameters, including *ff*. Its position reflects the Larmor frequency and is determined only by the external magnetic field. The edges of higher gaps (i.e., located above successive bands $n = 1, 2, 3, \ldots$) are interwoven and cross each other at specific values of filling fraction *ff* (see also Fig.3(b)). The values of *ff* at which the gaps are closed correspond to the cases when both the Co and Py layer contains the integer number of the half-wavelengths. It is equivalent to the appearance of standing SWs. The resulting fact is that SW does not scatter on Co|Py interfaces for this particular frequency. It is worth noting that for $ff = 0$ or 1, the system is composed of homogeneous Py or Co where the periodicity and the folding of dispersion relation are introduced artificially. The points at which the folded dispersion self-crosses, mark the frequencies for which the (Bragg) gaps start to open when we introduce thin layers of other material. For $ff \approx 0$ (for Py matrix with thin Co layer), the gaps are opened at smaller frequencies than the corresponding gaps for $ff \approx 1$. Co has larger exchange length of Co, so the slope of its (parabolic) dispersion relation increases faster with the wavenumber and the sections of dispersion relations (bands) folded into the 1st BZ are wider in frequency domain. Therefore, the gaps not only interwove their edge with increasing *ff* but also push towards higher frequencies. Relatively narrow band gaps make designing the magnonic system with neglected dipolar interactions difficult, and proper selection of the system's properties become crucial.

Due to the reversing of the order of the gap's edges, the Zak phases (3) of two surrounding bands are flipped, and the sign of logarithmic derivative (4) inside the gap is negated. This observation concludes that by adjusting the bulk parameters (i.e., filling fractions *ff*) for two 1D MCs joined at the interface, we can adjust the topological parameters of their spectra to obtain a common frequency gap. The matching of boundary conditions expressed by agreement of logarithmic derivatives of the Bloch functions, exponentially decaying in the interior of corresponding 1D MC, can be achieved (see Supplementary Information, Section 2).

In the numerical studies of interface modes, we will also investigate the more general case, when the unit cell for one 1D MC is not centrosymmetric and thus it is not interfaced with other 1D MC at its symmetry point.

Interface modes for $ff_L = 0.4$ and $ff_R = 0.7$. Figure 3a–c presents the dispersion relation within the 1st BZ for three selected filling fractions $ff = 0.4, 0.54, 0.7$. The dispersion branches in Fig. 3a–c are labeled with Zak phase, as well as edges of band gaps with the value of the logarithmic derivative ρ (see Supplementary Information, Section 2)—the marked values are valid for centrosymmetric unit cell, where $\delta = \delta_1$. For the value $ff \approx 0.54$ (Fig.3b), we observe the crossing of second ($n = 2$) and third ($n = 3$) band and closing the gap between these bands. Due to the band crossing, the Zak phases for $n = 2$ and $n = 3$ are flipped, where the change of the symmetry of the Bloch mode at the bands' edges are related to the change of Zak phase (modes profiles are presented in Supplementary Information, Section 4). Now, when we join two semi-infinite MCs of the filling fractions (with centrosymmetric unit cell: $\delta = \delta_1$) $ff_L = 0.4 < 0.54$ and $ff_R = 0.7 > 0.54$ (Fig. 3a, c), then we can agree with the sign of the logarithmic derivatives of Bloch function on both sides of the interface in the common frequency gap (see Supplementary Information, Section 3). Please note that, for the same sequence of the Zak phases for
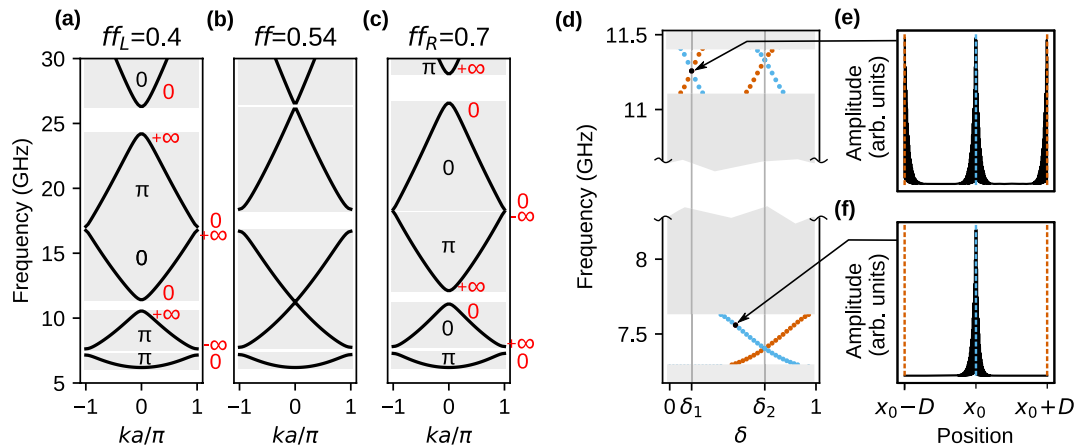
Figure 3. (**a–c**) Closing and reopening of the frequency gap (above the 2nd band, in the center of 1st Brillouin zone: $k = 0$) with the changes of filling fraction ff for exchange waves. The successive dispersion relations were plotted when the gap is (**a**) opened, $ff_L = 0.4$, (**b**) just closed, $ff = 0.54$, and (**c**) opened again, $ff_R = 0.7$. The labels: 0 and π stand for the Zak phases of the bands, 0 and ∞ (red color) - for logarithmic derivative on the edges of band gaps. The values of Zak phases and logarithmic derivatives were determined for the case $\delta = \delta_1$ (i.e., for Co strip in the center of the unit cell). The SW interface modes localized on the interface of two 1D MCs of $ff_L = 0.4$ and $ff_R = 0.7$. (**d**) The spectrum in the function of the surface parameter δ, defining the selection of the unit cells for 1D MC on the right. The values δ_1 and δ_2 correspond to the centrosymmetric unit cell with Co and Py strip in the middle. The calculations were performed for supercell approximation, where we considered the final sections of the 1D MCs, each of the size $D = Na$ and composed of $N = 100$ unit cells. Due to the application of periodic boundary conditions, we obtain an additional interface between 1D MCs. The frequency of interface mode localized in the center $x = x_0$ (on edge $x = x_0 \pm D$) of a supercell is marked by a blue dotted (orange dotted) line. (**e**, **f**) The profiles of the SW interface modes in the gaps above 1st and 2nd bands. The frequency and δ positions, for which modes are calculated, are indicated by arrows. The interfaces $x = x_0$ and $x = x_0 \pm D$ are pointed by blue dashed and orange dashed lines, respectively. For centrosymmetric case, the mode occupy both interface (**e**), while for non-centrosymmetric only one (**f**).

successive bands, the signs of logarithmic derivatives of Bloch functions decaying to the left or right (i.e., for the left and right 1D MC, respectively) are opposite in corresponding gaps (i.e., in the gaps between the same bands). Therefore, the band crossing is required to negate the sign of logarithmic derivatives $\text{sign}(\rho)$ in the reopened gap between the crossed bands (see the Supplementary Information 2 and 3 for more explanations) and ensure the matching of ρ on both sides of the interface.

Let us confirm the existence of interface states directly. For the two jointed semi-infinite 1D MCs (system presented in Fig. 1b), we ran PWM calculation (using the supercell approach) and collected SW spectra for wavenumber $k = 0$ (i.e., for periodic boundary conditions applied to the supercell). The change of parameter δ, determining the selection of the unit cell in the 1D MC on the right side of the interface, does not influence on the band structure but affect on the geometry of the interface between two 1D MCs. Therefore, by changing δ, we influence on the interface modes' frequency without perturbing the band structure. Results are presented in Fig. 3d. Gray strips indicate the frequency ranges where a continuum of states is observed, while white regions represent common frequency gaps. Due to narrow gaps, we broke the frequency axis to extend region of band gaps. During the evolution of δ, the values: $\delta = \delta_1 = 0.15$, $\delta = \delta_2 = 0.65$, correspond to the scenario, when right 1D MC is build of centrosymmetric unit cell (see inset Fig. 1b).

In the common frequency gaps, we find the pairs of interface modes localized on complementary interfaces between both 1D MCs. By blue color are marked states occupying central interface and by red color are marked states originating from periodic boundary conditions. For the centrosymmetric cases: $\delta = \delta_1, \delta_2$ (marked by vertical gray lines), both interfaces are equivalent, and the interface states are degenerated and localized on both interfaces at once. By changing the δ we can tune the frequency of interface modes and traverse the whole range of the frequency gap. For the whole range of $\delta = [0, 1)$ (note that $\delta = 0$ is equivalent to $\delta = 1$) the interface mode traverse the gap even few time, depending on the number of the decaying oscillation of Bloch function in the unit cell. These numbers increases for successive gaps.

It is worth noting that by the gradual changes of δ, we are continuously transiting between two different selection of centrosymmetric unit cell for the 1D MC on the right side of the interface (corresponding to δ_1 and δ_2). Such change will result in the flipping of the Zak phase for each band ($0 \leftrightarrow \pi$) and the negation of logarithmic derivative of Bloch function in every second gap, i.e., for the gaps opened at the edges of 1st BZ. This effect allows relating the (non)existence of interface modes for the cases: $\delta = \delta_1$ and $\delta = \delta_2$[6,8] (see Supplementary Information, Section 2). The gap around 7.5 GHz (presented in Fig.3d) is opened at edge of the 1st BZ (between the bands $n = 1$ and $n = 2$), so the interface modes can exist either for $\delta = \delta_1$ or $\delta = \delta_2$—we observe here only for $\delta = \delta_2$.
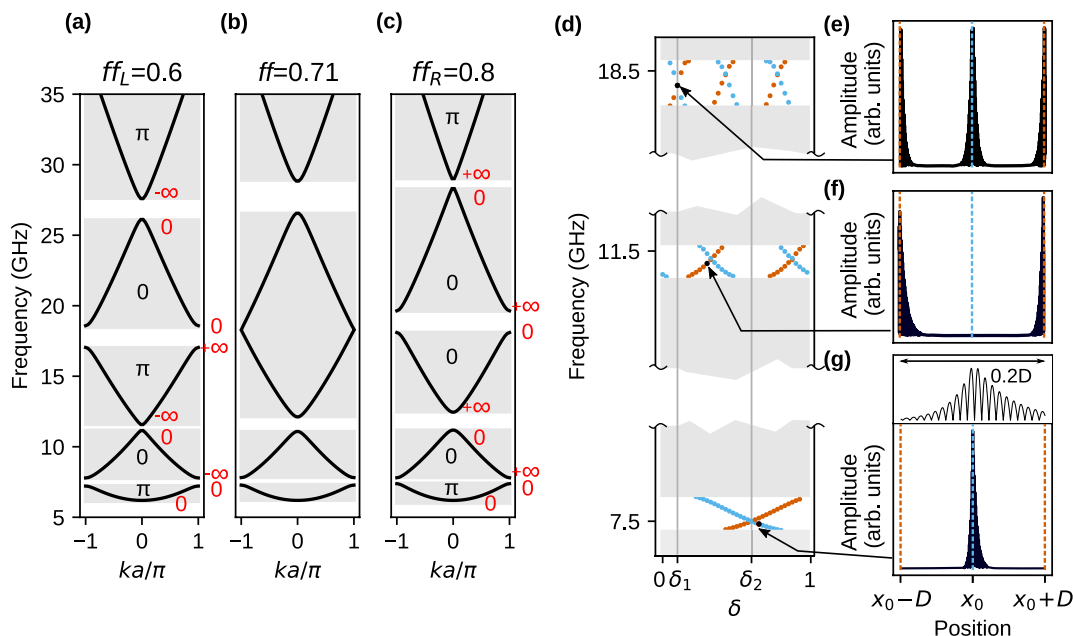
Figure 4. (**a–c**) Closing and reopening of the frequency gap (above the 1st band, at the edge of 1st Brillouin zone: $k = \pm \pi/a$) with the changes of filling fraction ff for exchange waves. The successive dispersion relations were plotted when the gap is (**a**) opened, $ff_L = 0.6$, (**b**) just closed, $ff = 0.71$ and (**c**) opened again, $ff_R = 0.8$. The values 0 and π are the Zak phases of the bands, 0 and ∞ (red color) stand for logarithmic derivative on the edges of band gaps. The values of Zak phases and logarithmic derivatives were determined for the case $\delta = \delta_1$ (i.e., for Co strip in the center of the unit cell). The SW interface modes localized on the interface of two MCs of $ff_L = 0.6$ and $ff_R = 0.8$. (**d**) The SW spectrum in the function of the surface parameter δ, defining the selection of the unit cells for 1D MC on the right. (**e–g**) The profiles of the SW interface modes in the gaps above 1st, 2nd and 3rd bands. We use the same conventions to mark the frequencies and localization of the SW interface modes as in Fig. 3e, f. Inset above (**g**) presents a close-up of the SW profile near the interface. It can be seen that despite the fact of decaying, the character of the mode is oscillating.

Whereas, the gap just above 11 GHz (Fig.3d) is opened at the center of the 1st BZ (between the bands $n = 2$ and $n = 3$), which means that the existence conditions of interface modes are the same in both cases ($\delta = \delta_1, \delta = \delta_2$)—here we observe that they exist for both selections of centrosymmetric unit cell.

Interface modes for $ff_L = 0.6$ and $ff_R = 0.8$. The interface modes can also be found when we select different values of filling fractions for 1D MCs on the left and right side of the interface: $ff_L = 0.6$ and $ff_R = 0.8$ (Fig. 4a and c, respectively). For the intermediate value of the filling fraction $ff = 0.71$ (Fig. 4b), we observe the crossing of the gap's edges between third ($n = 3$) and forth ($n = 4$) band—see Fig. 2. The crossing of the bands allows matching the signs of the logarithmic derivatives in the third gap on both sides of the interface between two MCs (see also Supplementary Information, Section 2). However in Fig. 4c we can notice that Zak phase of third ($n = 3$) and fourth ($n = 4$) band is 0. The reason for this is the additional swap of the Zak phase between the fourth and fifth band gap that is visible in Fig. 2. Regarding the Eq. (5), the sign of the logarithmic derivative is determined by the Zak phases of all bands below it, so the Zak phase of the band over the gap is irrelevant. The values of the logarithmic derivative at the edges of the gaps and the Zak phases superimposed on Fig. 4a–c was determined for centrosymmetric unit cell, i.e., for $\delta = \delta_1$—see also Fig. 2 in Supplementary Information, where the Zak phase was determined from the profiles of the Bloch functions at the edges of the bands.

The results of the SW spectra calculations ($k = 0$) of supercell with two jointed 1D MCs for $ff_L = 0.6$ and $ff_R = 0.8$ are presented in Fig. 4d–g. Figure 4d shows the SW spectra in the function of δ. In the considered frequency range, we can see three band gaps between the bands $n = 1, 2, 3, 4$. The interface states traverse between the edges of gaps, and the number of times increase with the number of band gaps. Similarly to the previous case ($ff_L = 0.4, ff_R = 0.7$), the interface modes appear in pairs and are localized in the middle of the supercell (Fig. 4g), at the edge of supercell (Fig. 4f) or at both locations (Fig. 4e)—due to degeneracy. The spatial oscillation of the interface modes are not visible because of the large number unit cells of each 1D MC ($N = 100$) within the supercell. The inset in top part of Fig. 4g shows the zoomed profile of interface mode in the vicinity of the interface. The modes has one oscillations per unit cell, therefore logarithmic derivative flips its sign once. As a results, this mode traverses once across the gap in the whole range of δ.
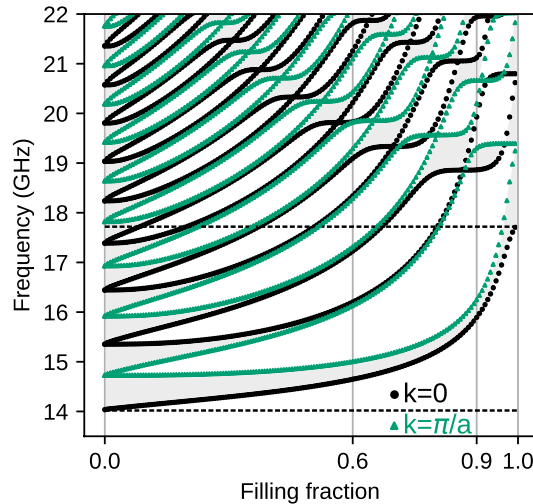
Figure 5. The evolution of dipolar-exchange SW spectra in dependence on the bulk parameter: filling fraction ff ($a = 1000$ nm). The vertical lines at $ff = 0.6, 0.9$ denote the pair of 1D MCs, that were interfaced. We used the same convention to mark frequency bands, gaps and their edges as in Fig. 2. The higher (lower) horizontal dashed line marks the FMR frequency for uniform Co (Py) layer.

We can analyze the existence of interface modes for two centrosymmetric cases $\delta = \delta_1$ and $\delta = \delta_2$ in similar way as for the structure $ff_L = 0.4$ and $ff_R = 0.7$. The gaps around 7.5 and 18.5 GHz open at the edge of the 1st BZ, therefore the interface state can be observed only for one selection of centrosymmetric unit cell. For the gap opened around 11.5 GHz, the absence of interface modes for $\delta = \delta_1$ implies the nonexistence of these states at $\delta = \delta_2$.

Dipolar-exchange spin waves. Let us now present the results for the system with included dipolar interactions. To observe the impact of dipolar interactions, we expanded the sizes of the system. The lattice constant is now larger by one order of magnitude: $a = 1000$ nm, referring to discussed case with exchange waves. Like in the previous section, we start from the analysis of SW spectra. Its dependence on the filling fraction ff is presented in Fig. 5. The first observation is that the fundamental mode is sensitive to magnetic parameters, contrary to spectrum with active only exchange interactions. The bottom of the 1st band ($k = 0$) is strongly dependent on ff. Starting from $ff = 0$, the frequency slowly increases from 14 GHz, while around $ff = 0.8$ it rises quickly, reaching ultimately about 17.5 GHz for $ff = 1$. The frequencies of the lowest SW modes (for $k = 0$) are just the frequencies of the ferromagnetic resonance (FMR), which is expressed as $f = \frac{|\gamma|\mu_0}{2\pi}\sqrt{H_0(H_0 + M_S)}$ for homogeneous layer of Py ($ff = 0$) or Co ($ff = 1$), differing significantly in saturation magnetization $M_{S,Py} < M_{S,Co}$. Therefore, the FMR frequency increases with the increase of filling fraction: $0 < ff < 1$. We marked the FMR frequencies of uniform Py and Co films by dashed lines.

The frequencies for other edges of the bands/gaps quickly increase with the ff too. However, their interweaving is not observed for low values of ff and low frequencies. It can be understood when we notice that the band crossing in 1D bi-component magnonic crystal requires the oscillatory solution in both components (strips, layers). In our system, the evanescent waves exist in Co strips for the frequencies below the FMR frequency of uniform Co. Additionally, due to confinement effect the frequencies of oscillatory modes in Co are increased for smaller ff where the Co strips are narrow. Therefore, to find the interface states, we selected a pair of MCs of relatively high filling fractions ff: 0.6|0.9 for which the edges of gaps can have different number of crossing points, that is related to different topological properties of their band structures.

The dispersion relations for these 1D MCs are presented in Fig. 6a, b. For reference, we showed the dispersion relations of the uniform film made of Co and Py in the range of $(-\pi/a, \pi/a)$. They are marked with dashed lines. Thanks to this comparison, we can attribute the first branch of MC in Fig. 6a as excitation in Py, while the fifth in Co. In Fig. 6b, the first branch of 1D MC is an excitation in Py, while the third one is an excitation in Co. The character of SW's profile is implicitly presented in Supplementary Information, Section 4. These bands are shifted up with respect to fundamental excitation in the uniform film due to the confinement and dipolar pinning in the strips[49]. The SW is forced to be quantized within the strip, and due to this, its frequency increase. For $ff = 0.9$ and the Py strip, this effect is the most significant because the Py strip is the narrowest—it has there only 100 nm. For $ff_R = 0.9$, two first bands have a minimum at the center of BZ, and a maximum at the edge of BZ. It violates the typical scenario when the maximum and minimum of two successive bands appear at the same position in BZ, i.e., the case when we observe only the direct gaps. This peculiarity of the system can be explained when we notice that the second band is not a result of folding the first band into the 1st BZ, but is related to the
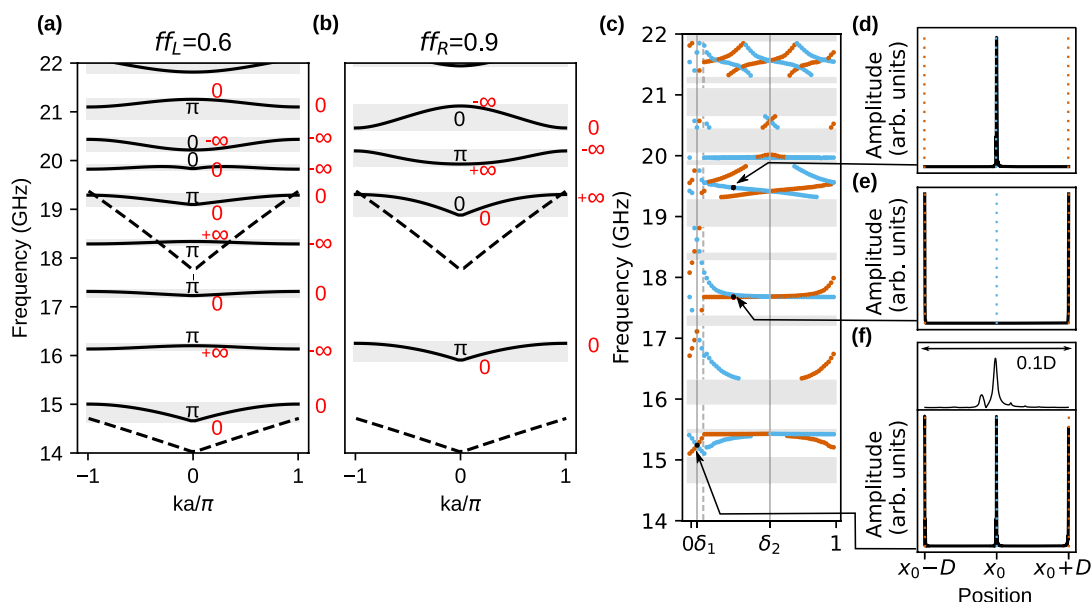
Figure 6. (**a**, **b**) The dipolar-exchange SW dispersion relations for two MCs which differ only in filing fractions: (**a**) $ff_L = 0.6$, (**b**) $ff_R = 0.9$. The spectrum for $ff = 0.9$ is shifted up in the frequency scale due to dipolar interaction, and the successive gaps in both spectra do not match each other. The forbidden ranges for interfaced MCs ($ff_L = 0.6$ and $ff_R = 0.9$) can originate from overlapping of various frequency gaps in both 1D MCs—see Fig. 5. The values: 0 and π are the Zak phases of the bands, whereas: 0 and ∞ (red color) stand for logarithmic derivatives on the edges of bad gaps. Dashed lines represent dispersion relation for a uniform system made from Py (branch starts at 14GHz) and made from Co (branch starts at 17.5 GHz). (**c**) The dipolar-exchange SW interface modes localized on the interface of two 1D MCs of $ff_L = 0.6$ and $ff_R = 0.9$. The spectrum of SW interface modes is shown in dependence on the surface parameter δ. We use the same conventions to mark the frequencies and localization of the SW interface modes as in Fig. 3d. The gray dashed line denotes $\delta = 1 - ff$ where the Py|Co interface is on the left edge of the unit cell. (**d**–**f**) The profiles of the SW interface modes in common (from both 1D MCs) forbidden frequency ranges. The close-up at the $x = x_0$ is presented above (**f**). The SWs decay exponentially in Co strips and have one oscillation per Py strip.

lowest oscillatory solution in the Co strips. In the first band, we observe in Co the evanescent excitation forced by the magnetization dynamics in Py. This consideration is supported by spatial profiles of the modes presented in Supplementary Information, Section 4. It is worth noting that the lowest mode in Co can be also identified by the non-zero group velocity, characteristic of dipolar dynamical coupling in the limit $k \rightarrow 0$.

The spectrum of considered 1D MC's is very rich and is dramatically modified with the change of the filling fraction—the bands' positions and their separations (width of the gaps) vary significantly with ff. Unlike the system with exchange interaction only, the positions of corresponding band gaps (i.e., the band of the same index n) are different. For example, the first band gap for $ff_R = 0.9$ is located in the frequency range corresponding to second and third band gaps for $ff_L = 0.6$. The bands are relatively narrow which proves that we are operating in crossover dipolar-exchange regime. The flat dispersion branches in Fig. 6a–c means the low value of the group velocity for SW.

In Fig. 6a, b, we marked the Zak phases for centrosymmetric unit cells ($\delta = \delta_1$). The values were determined by the inspection of the profiles of the Bloch functions at the edges of the bands (see Fig. 2e, f in Supplementary Information). The sequences of Zak phases allows determining the sign of logarithmic derivatives of Bloch function, ρ, in frequency gaps for MCs at left and right side of the interface. The values of ρ at edges of bands are marked in Fig. 6a, b with red color.

The careful inspection of the sign of ρ in common frequency gaps of both MCs (marked as white areas in Fig. 6a, b) allows indicating three common gaps in which the signs of ρ are opposite: gap below 1st band, gap around 18.5 GHz and tiny gap, slightly above 21 GHz. In these gaps, we did not find numerically any interface modes: Figure 6c does not present solution at these frequencies for $\delta = \delta_1$. Concluding, analysis of logarithmic derivative for dipolar-exchange waves is also valid tool to describe the existence criteria for interface modes.

This system posses some peculiarities. Due to disturbing the typical sequence of dispersion branches, logarithmic derivative can take the same values on the edges of band gaps. For $ff_R = 0.9$ first band gap ρ is equal to 0 on both of the edges, and in second gap is equal to $-\infty$. We were also not able to plot the logarithmic derivatives of Bloch functions, as we did for exchange waves in Supplementary Information, Section 2. It is related to the

difficulties with the determination of the complex wavenumber in the indirect gaps, needed to be specified to run the PWM calculations.

For selected pair of the filling fractions ($ff_L = 0.6$, $ff_R = 0.9$) of two 1D MCs, we performed the numerical studies of the modes localized at interface between 1D MCs. Using the PWM and supercell approach, we calculated the frequencies and profiles of interface modes localized on two complementary interfaces. The frequencies were plotted in dependence on the parameter δ which describes the selection of the unit cell in the MC on the right side of the interface. Figure 6d presents the evolution of interface states in the function of δ. The first observation is that the dependencies of the frequencies of interface modes on the unit cell shift δ can change their slopes abruptly. This effect is related to the sensitivity of dipolar interaction on the interfaces. With an increasing value of δ, the narrow Py strip ($ff = 0.9$) moves into the center of the unit cell (see the inset below Fig. 1b for graphical illustration). Till the δ reach the value marked by the gray dashed line $\delta = 1 - ff$, the Py strip on the interface is widening. After that, the Co strip starts to be located on the interface, so the MC on the left starts to be interfaced with different material on the right side.

The another interesting finding is the absence of multiple traverses of the interface modes across the common gap for the swap of parameter δ, observed for small frequencies (below 19.5 GHz, where the modes start spatially oscillate in Co) and for the larger values of the δ ($1 - ff < \delta < 1$, where the left edge of the unit cell of the right MC appears in Co strip). In this range of the δ, the solution at the edge of unit cell (which is the right side on interface between 1D MCs, as well) cannot change the sign. It is because of the evanescent profile of the mode in Co. This excludes multiple flips of the sign of the mode at the interface while δ is changed.

Figure 6d–f shows the profile of the interface states for selected values of δ and frequency. They are strongly localized on the interface. Inset above (d) presents a close-up of the interface region. The oscillatory character is only in the Py strips, while in Co, the amplitude decay exponentially. The strong localization is a consequence of wide gaps in which the imaginary parts of wavevector (describing the exponential rate of localization) can reach large values.

Summary

We have presented a comprehensive study on the existence of interface SW states in 1D planar magnonic crystals, using a continuous model of magnetization dynamics for the exchange and dipolar-exchange spin waves.

We have related bulk parameter in magnonic crystal to the symmetry-related conditions of existence of interface states: (i) the concept of Zak phase, which is a topological characteristic of individual bands in the frequency spectrum was connected to (ii) the logarithmic derivative of the Bloch function on both sides of the interface, expressing the boundary conditions for interface modes in the band gaps. We have also performed numerical results that allowed us to consider the behavior of the interface modes for non-centrosymmetric unit cells. We have shown that this degree of freedom can be used to induce or vanish the interface state in desired band gap.

Full analogy to the already investigated electronic and photonic systems is observed in the magnonic system where the dipolar interactions are neglected. For the dipolar-exchange waves, however, the analysis becomes more complex. We have observed new effects specific to dipolar interaction: (i) rarer crossings of band gap edges—the band gaps do not close in a wide range of the filling fraction and the selection of pair of MCs with band structures supporting interface modes is challenging; (ii) in the lower-frequency range (i.e., in lower band gaps) the observed interface modes do not traverse the band gap edges with shifting MC unit cell. Nevertheless, we have found numerous interface modes, and their existence (for centrosymmetric unit cell) was determined from the symmetry criterion of the Bloch function on the band edges.

Data availability

The datasets used and analyzed during the current study available from the corresponding author on reasonable request.

References

1. Berry, M. V. Quantal phase factors accompanying adiabatic changes. *Proc. R. Soc. Lond. A Math. Phys. Sci.* **392**, 45–57. https://doi.org/10.1098/rspa.1984.0023 (1984).
2. Chern, S.-S. Characteristic classes of Hermitian manifolds. *Ann. Math.* **47**, 85–121. https://doi.org/10.2307/1969037 (1946).
3. Kane, C. Topological band theory and the $\mathbb{Z}_2$ invariant. In *Topological Insulators Contemporary Concepts of Condensed Matter Science*, Vol. 6 (eds Franz, M. & Molenkamp, L.) 3–34 (Elsevier, 2013).
4. Silveirinha, M. G. Chern invariants for continuous media. *Phys. Rev. B* **92**, 125153. https://doi.org/10.1103/PhysRevB.92.125153 (2015).
5. Zak, J. Band center–a conserved quantity in solids. *Phys. Rev. Lett.* **48**, 359–362. https://doi.org/10.1103/PhysRevLett.48.359 (1982).
6. Zak, J. B̈errys phase for energy bands in solids. *Phys. Rev. Lett.* **62**, 2747–2750. https://doi.org/10.1103/PhysRevLett.62.2747 (1989).
7. Atala, M. *et al.* Direct measurement of the Zak phase in topological Bloch bands. *Nat. Phys.* **9**, 795–800. https://doi.org/10.1038/nphys2790 (2013).
8. Zak, J. Symmetry criterion for surface states in solids. *Phys. Rev. B* **32**, 2218–2226. https://doi.org/10.1103/PhysRevB.32.2218 (1985).
9. Rhim, J.-W., Behrends, J. & Bardarson, J. H. Bulk-boundary correspondence from the intercellular Zak phase. *Phys. Rev. B* **95**, 035421. https://doi.org/10.1103/PhysRevB.95.035421 (2017).
10. Kohn, W. Analytic properties of Bloch waves and Wannier functions. *Phys. Rev.* **115**, 809–821. https://doi.org/10.1103/PhysRev.115.809 (1959).
11. Wang, H.-X., Guo, G.-Y. & Jiang, J.-H. Band topology in classical waves: Wilson-loop approach to topological numbers and fragile topology. *New J. Phys.* **21**, 093029. https://doi.org/10.1088/1367-2630/ab3f71 (2019).

12. Xiao, M., Zhang, Z. Q. & Chan, C. T. Surface impedance and bulk band geometric phases in one-dimensional systems. *Phys. Rev. X* **4**, 021017. https://doi.org/10.1103/PhysRevX.4.021017 (2014).

13. Nakata, Y., Ito, Y., Nakamura, Y. & Shindou, R. Topological boundary modes from translational deformations. *Phys. Rev. Lett.* **124**, 073901. https://doi.org/10.1103/PhysRevLett.124.073901 (2020).

14. Chen, W.-J. *et al.* Experimental realization of photonic topological insulator in a uniaxial metacrystal waveguide. *Nat. Commun.* **5**, 5782. https://doi.org/10.1038/ncomms6782 (2014).

15. Wang, L., Cai, W., Bie, M., Zhang, X. & Xu, J. Zak phase and topological plasmonic Tamm states in one-dimensional plasmonic crystals. *Opt. Express* **26**, 28963–28975. https://doi.org/10.1364/OE.26.028963 (2018).

16. Li, Z.-W., Fang, X.-S., Liang, B., Li, Y. & Cheng, J.-C. Topological interface states in the low-frequency band gap of one-dimensional phononic crystals. *Phys. Rev. Appl.* **14**, 054028. https://doi.org/10.1103/PhysRevApplied.14.054028 (2020).

17. Rychły, J., Kłos, J. W., Mruczkiewicz, M. & Krawczyk, M. Spin waves in one-dimensional bicomponent magnonic quasicrystals. *Phys. Rev. B* **92**, 054414. https://doi.org/10.1103/PhysRevB.92.054414 (2015).

18. Kruglyak, V. V., Demokritov, S. O. & Grundler, D. Magnonics. *J. Phys. D Appl. Phys.* **43**, 264001. https://doi.org/10.1088/0022-3727/43/26/264001 (2010).

19. Krawczyk, M. & Grundler, D. Review and prospects of magnonic crystals and devices with reprogrammable band structure. *J. Phys. Condens. Matter* **26**, 123202. https://doi.org/10.1088/0953-8984/26/12/123202 (2014).

20. Kłos, J. W. *et al.* Magnonics and confinement of light in Photonic–Magnonic crystals. In *Optomagnonic Structures: Novel Architectures for Simultaneous Control of Light and Spin Waves* 79–134 (World Scientific, Singapore, 2021).

21. Owerre, S. A. Floquet topological magnons. *J. Phys. Commun.* **1**, 021002. https://doi.org/10.1088/2399-6528/aa8843 (2017).

22. Pershoguba, S. S. *et al.* Dirac magnons in honeycomb ferromagnets. *Phys. Rev. X* **8**, 011010. https://doi.org/10.1103/PhysRevX.8.011010 (2018).

23. Mook, A., Henk, J. & Mertig, I. Edge states in topological magnon insulators. *Phys. Rev. B* **90**, 024412. https://doi.org/10.1103/PhysRevB.90.024412 (2014).

24. Shindou, R., Matsumoto, R., Murakami, S. & Ohe, J.-I. Topological chiral magnonic edge mode in a magnonic crystal. *Phys. Rev. B* **87**, 174427. https://doi.org/10.1103/PhysRevB.87.174427 (2013).

25. Mohseni, M. *et al.* Backscattering immunity of dipole-exchange magnetostatic surface spin waves. *Phys. Rev. Lett.* **122**, 197201. https://doi.org/10.1103/PhysRevLett.122.197201 (2019).

26. Yamamoto, K. *et al.* Topological characterization of classical waves: The topological origin of magnetostatic surface spin waves. *Phys. Rev. Lett.* **122**, 217201. https://doi.org/10.1103/PhysRevLett.122.217201 (2019).

27. Liu, J., Wang, L. & Shen, K. Dipolar spin waves in uniaxial easy-axis antiferromagnets: A natural topological nodal-line semimetal. *Phys. Rev. Res.* **2**, 023282. https://doi.org/10.1103/PhysRevResearch.2.023282 (2020).

28. Kruglyak, V. V., Sokolovskii, M. L., Tkachenko, V. S. & Kuchko, A. N. Spin-wave spectrum of a magnonic crystal with an isolated defect. *J. Appl. Phys* **99**, 08C906. https://doi.org/10.1063/1.2164419 (2006).

29. Kłos, J. W. & Tkachenko, V. S. Symmetry-related criteria for the occurrence of defect states in magnonic superlattices. *J. Appl. Phys.* **113**, 133907. https://doi.org/10.1063/1.4798607 (2013).

30. Lisenkov, I. *et al.* Spin-wave edge modes in finite arrays of dipolarly coupled magnetic nanopillars. *Phys. Rev. B* **90**, 104417. https://doi.org/10.1103/PhysRevB.90.104417 (2014).

31. Rychły, J. & Kłos, J. W. Spin wave surface states in 1d planar magnonic crystals. *J. Phys. D Appl. Phys.* **50**, 164004. https://doi.org/10.1088/1361-6463/aa5ae1 (2017).

32. Gallardo, R. A. *et al.* Symmetry and localization properties of defect modes in magnonic superlattices. *Phys. Rev. B* **97**, 174404. https://doi.org/10.1103/PhysRevB.97.174404 (2018).

33. Osokin, S., Safin, A., Barabanenkov, Y. & Nikitov, S. Spin waves in finite chain of dipolarly coupled ferromagnetic pillars. *J. Magn. Magn. Mater.* **465**, 519–523. https://doi.org/10.1016/j.jmmm.2018.06.041 (2018).

34. Zhou, J. *et al.* Precessional dynamics of geometrically scaled magnetostatic spin waves in two-dimensional magnonic fractals. *Phys. Rev. B* **105**, 174415. https://doi.org/10.1103/PhysRevB.105.174415 (2022).

35. Wang, Z. K. *et al.* Observation of frequency band gaps in a one-dimensional nanostructured magnonic crystal. *Appl. Phys. Lett.* **94**, 083112. https://doi.org/10.1063/1.3089839 (2009).

36. Tacchi, S. *et al.* Forbidden band gaps in the spin-wave spectrum of a two-dimensional bicomponent magnonic crystal. *Phys. Rev. Lett.* **109**, 137202. https://doi.org/10.1103/PhysRevLett.109.137202 (2012).

37. Choudhury, S. *et al.* Shape- and interface-induced control of spin dynamics of two-dimensional bicomponent magnonic crystals. *ACS Appl. Mater. Interfaces* **8**, 18339–18346. https://doi.org/10.1021/acsami.6b04011 (2016).

38. Wawro, A. *et al.* Magnetic properties of coupled Co/Mo/Co structures tailored by ion irradiation. *Phys. Rev. Appl.* **9**, 014029. https://doi.org/10.1103/PhysRevApplied.9.014029 (2018).

39. Frackowiak, L. *et al.* Magnetic domains without domain walls: A unique effect of he+ ion bombardment in ferrimagnetic Tb/Co films. *Phys. Rev. Lett.* **124**, 047203. https://doi.org/10.1103/PhysRevLett.124.047203 (2020).

40. Chang, C. L. *et al.* Driving magnetization dynamics in an on-demand magnonic crystal via the magnetoelastic interactions. *Phys. Rev. Appl.* **10**, 064051. https://doi.org/10.1103/PhysRevApplied.10.064051 (2018).

41. Topp, J., Heitmann, D., Kostylev, M. P. & Grundler, D. Making a reconfigurable artificial crystal by ordering bistable magnetic nanowires. *Phys. Rev. Lett.* **104**, 207205. https://doi.org/10.1103/PhysRevLett.104.207205 (2010).

42. Mamica, S., Krawczyk, M. & Grundler, D. Nonuniform spin-wave softening in two-dimensional magnonic crystals as a tool for opening omnidirectional magnonic band gaps. *Phys. Rev. Appl.* **11**, 054011. https://doi.org/10.1103/PhysRevApplied.11.054011 (2019).

43. Mruczkiewicz, M. & Krawczyk, M. Nonreciprocal dispersion of spin waves in ferromagnetic thin films covered with a finite-conductivity metal. *J. Appl. Phys.* **115**, 113909. https://doi.org/10.1063/1.4868905 (2014).

44. Bessonov, V. D. *et al.* Magnonic band gaps in yig-based one-dimensional magnonic crystals: An array of grooves versus an array of metallic stripes. *Phys. Rev. B* **91**, 104421. https://doi.org/10.1103/PhysRevB.91.104421 (2015).

45. Langer, M. *et al.* Spin-wave modes in transition from a thin film to a full magnonic crystal. *Phys. Rev. B* **99**, 024426. https://doi.org/10.1103/PhysRevB.99.024426 (2019).

46. Teschl, G. *Ordinary Differential Equations and Dynamical Systems* (The American Mathematical Society, Rhode Island, 2012).

47. Krawczyk, M., Sokolovskyy, M. L., Kłos, J. W. & Mamica, S. On the formulation of the exchange field in the Landau-Lifshitz equation for spin-wave calculation in magnonic crystals. *Adv. Condens. Matter Phys.* **2012**, 14. https://doi.org/10.1155/2012/764783 (2012).

48. Rychły, J., Mieszczak, S. & Kłos, J. Spin waves in planar quasicrystal of penrose tiling. *J. Magn. Magn. Mater.* **450**, 18–23. https://doi.org/10.1016/j.jmmm.2017.03.029 (2018).

49. Centała, G. *et al.* Influence of nonmagnetic dielectric spacers on the spin-wave response of one-dimensional planar magnonic crystals. *Phys. Rev. B* **100**, 224428. https://doi.org/10.1103/PhysRevB.100.224428 (2019).

Acknowledgements

Author contributions

Competing interests
The authors declare no competing interests.

Additional information
Supplementary Information The online version contains supplementary material available at https://doi.org/10.1038/s41598-022-15328-x.

Correspondence and requests for materials should be addressed to S.M.

Reprints and permissions information is available at www.nature.com/reprints.

Publisher's note Springer Nature remains neutral with regard to jurisdictional claims in published maps and institutional affiliations.

Interface modes in planar one-dimensional magnonic crystals: Supplementary information

Szymon Mieszczak[1,*] and Jarosław W. Kłos[1,+]

[1]Institute of Spintronics and Quantum Information, Faculty of Physics, Adam Mickiewicz University, Poznań, Poland
*szymon.mieszczak@amu.edu.pl

ABSTRACT

We present the concept of Zak phase for spin waves in planar magnonic crystals and discuss the existence condition of interface modes localized on the boundary between two magnonic crystals with centrosymmetric unit cells. Using the symmetry criterion and analyzing the logarithmic derivative of the Bloch function, we study the interface modes and demonstrate the bulk-to-edge correspondence. Our theoretical results are verified numerically and extended to the case in which one of the magnonic crystals has a non-centrosymmetric unit cells. We show that by shifting the unit cell, the interface modes can traverse between the band gap edges. Our work also investigate the role of the dipolar interaction, by comparison the systems both with exchange interaction only and combined dipolar-exchange interactions.

1 Zak phase for spin waves in planar magnonic crystals

Exchange spin waves

The linearized Landau-Lifshitz-Gilbert equation can be written in the following form when the dipolar interactions are neglected $\boldsymbol{H}_{\mathrm{dm}} = 0$:

$$\begin{cases} \partial_t m_\parallel(x,t) = |\gamma|\mu_0\left(\hat{L}(x)m_\perp(x,t) - Vm_\perp(x,t)\right) \\ \partial_t m_\perp(x,t) = |\gamma|\mu_0\left(-\hat{L}(x)m_\parallel(x,t) + Vm_\parallel(x,t)\right), \end{cases} \tag{1}$$

where the function $V(x)$ and operator $\hat{L}(x)$ are defined as:

$$\begin{cases} V(x) = \left(\partial_x \lambda^2 \partial_x M_{\mathrm{S}}(x)\right) + H_0 \approx H_0 \\ \hat{L}(x) = M_{\mathrm{S}}(x)\partial_x \lambda^2(x)\partial_x \end{cases} \tag{2}$$

and λ is exchange length. We neglect the static term $\partial_x \lambda^2 \partial_x M_{\mathrm{S}}(x)$ because it is nonzero only at the interface between strips and can be neglected in numerical computations[1]. To find the eigenmodes, we are considering the harmonic dynamics in time: $\boldsymbol{m}(x,t) = \boldsymbol{m}(x)e^{i\omega t}$. The equation (1) is a Sturm-Liouville problem, can be written in the form analogous to Schrödinger equation:

$$\partial_t |m\rangle = \Lambda|m\rangle, \tag{3}$$

where we used the notation $|m\rangle := [m_\parallel(x), m_\perp(x)]^T e^{i\omega t}$ and the matrix Λ is defined as following:

$$\Lambda = |\gamma|\mu_0 \begin{pmatrix} 0 & -V + \hat{L} \\ V - \hat{L} & 0 \end{pmatrix}. \tag{4}$$

Let us consider the continuous transition of the vector $|m\rangle$ in the momentum space of the wavenumber k, after which it acquires the phase $\varphi(t)$:

$$|m'\rangle = e^{i\varphi}|m\rangle. \tag{5}$$

Eq. (3) is satisfied for $|m'\rangle$ as well. We can write the following relation resulting from (3):

$$\langle m|\partial_t|m'\rangle = \langle m|\Lambda|m'\rangle, \tag{6}$$

where we defined the inner product $\langle f_1 \mid f_2 \rangle := \int_{-a/2}^{a/2} \left(f_{1,\parallel}^*(x)f_{2,\parallel}(x) + f_{1,\perp}^*(x)f_{2,\perp}(x) \right) dx$. By differentiating $|m'\rangle$ in time and using the identity: $\partial_k = \dot{k}\partial_t$, we can write (6) in the form:

$$i\dot{\varphi} \langle m|m \rangle + \langle m|\partial_k|m \rangle \dot{k} = i\omega \langle m|m \rangle. \tag{7}$$

Taking into account that $|u\rangle = |m\rangle e^{-ikx}e^{-i\omega t}$, we obtain form (7):

$$\varphi = \underbrace{\int_o^t \omega(t)\,dt}_{\varphi_t} + \underbrace{\int_{k(0)}^{k(t)} \frac{i\langle u|\partial_k|u\rangle}{\langle u|u\rangle}\,dk}_{\varphi_g}. \tag{8}$$

The phase φ contains an additional term φ_g which is distinguishable from the phase φ_t acquired from the temporal evolution of the eigenmode $|m\rangle$. The geometrical phase φ_g collected when Bloch function $|m\rangle$ passes the periodic path in the space of k-number (i.e., when k is real and ranges from $-\pi/a$ to π/a) is called Zak phase θ:

$$\theta = \int_{-\pi/a}^{\pi/a} \frac{\Im \langle u|\partial_k|u\rangle}{\langle u|u\rangle}\,dk. \tag{9}$$

Dipolar-exchange spin waves

The demagnetizing field $\boldsymbol{H}_{\mathrm{dm}}(x,z,t) = -\nabla\varphi(x,z,t)$ is calculated under magnetostatic approximation by finding the magnetostatic potential $\varphi(x,z,t)$ from the Gauss equation. For the layer which is periodically modulated in the plane, the demagnetizing field was calculated using the method proposed by J. Kaczer[2], which is based on the Fourier expansion. For thin planar structure, the demagnetizing field does not change significantly inside the magnetic layer and we took its value in the middle of the layer ($z = 0$) as a representative for the whole cross-section of the layer. The dynamic demagnetizing field is expressed in terms of the coefficients of the Fourier expansion of the Bloch function $|m\rangle$, therefore the Eq. (3) must be written in the Fourier space as well:

$$\partial_t |\tilde{m}\rangle = \tilde{\Lambda} |\tilde{m}\rangle \tag{10}$$

where $|\tilde{m}\rangle := [u_{\parallel,G_0}, \ldots, u_{\parallel,G_n}, \ldots, u_{\perp,G_0}, \ldots, u_{\perp,G_n}, \ldots]^T e^{ikx}e^{i\omega t}$ with $u_{\parallel,G_i}$, $u_{\perp,G_i}$ being the Fourier coefficients, and matrix $\tilde{\Lambda}$ taking a form:

$$\tilde{\Lambda} = |\gamma|\mu_0 \begin{pmatrix} 0 & -\tilde{V} + \tilde{L} + \tilde{D}^{\parallel,\perp} \\ \tilde{V} - \tilde{L} - \tilde{D}^{\perp,\parallel} & 0 \end{pmatrix}. \tag{11}$$

The matrices $\tilde{L}$ and $\tilde{V}$ are related to (2) and describe the impact of external field and exchange interactions, respectively. The matrices $\tilde{D}^{\perp,\parallel}$ and $\tilde{D}^{\parallel,\perp}$ describe the dynamic dipolar interactions in 1D planar magnonic crystal[1,2] – the difference between them is reflected in the ellipticity of pressecion of dipolar spin waves. The explicit form of these matrices is:

$$\begin{aligned} \tilde{L}_{i,j} &= -\sum_l (k+G_i)(k+G_l)\lambda_{G_l-G_j}^2 M_{S,G_i-G_l}, \\ \tilde{V}_{i,j} &= H_0\delta_{i,j}, \\ \tilde{D}_{i,j}^{\perp,\parallel} &= -\left(1 - e^{-|k+G_j|d/2}\right)M_{S,G_i-G_j}, \\ \tilde{D}_{i,j}^{\parallel,\perp} &= -e^{-|k+G_j|d/2}M_{S,G_i-G_j}, \end{aligned} \tag{12}$$

where d is the thickness of the layer. The material parameters, i.e., saturation magnetization $M_S(x)$, exchange length $\lambda(x)$ and the components of Bloch function: $m_\parallel(x)$, $m_\perp(x)$ are expanded into Fourier series:

$$\begin{aligned} M_S(x) &= \sum_{n=0} M_{S,G_n} e^{iG_n x}, \\ \lambda(x) &= \sum_{n=0} \lambda_{G_i} e^{iG_n x}, \\ m_{\parallel(\perp)}(x) &= \sum_{n=0} u_{\parallel(\perp),G_n} e^{i(G_n+k)x}. \end{aligned} \tag{13}$$

The set $\{G_n\} = 0, \pm 2\pi/a, \pm 4\pi/a, \ldots, \pm n2\pi/a, \ldots$ denotes the reciprocal lattice numbers.

To prove that the formula (9) also applies to dipolar-exchange spin waves, we need to show that $\langle u|\partial_k|u\rangle = \langle \tilde{u}|\partial_k|\tilde{u}\rangle$ and $\langle u|u\rangle = \langle \tilde{u}|\tilde{u}\rangle$, where $|\tilde{u}\rangle = |\tilde{m}\rangle\, e^{-ikx} e^{-i\omega t}$:

$$\langle u|\partial_k|u\rangle = \int_{-a/2}^{a/2} \left(u_\parallel^*(x)\partial_k u_\parallel(x) + u_\perp^*(x)\partial_k u_\perp(x) \right) dx =$$

$$\sum_{i,j} \underbrace{\int_{-a/2}^{a/2} e^{i(G_i - G_j)x} dx}_{\delta_{i,j}} \left(u_{\parallel,G_i}^* \partial_k u_{\parallel,G_j} + u_{\perp,G_i}^* \partial_k u_{\perp,G_j} \right) = \sum_i \left(u_{\parallel,G_i}^* \partial_k u_{\parallel,G_i} + u_{\perp,G_i}^* \partial_k u_{\perp,G_i} \right) =: \langle \tilde{u}|\partial_k|\tilde{u}\rangle. \tag{14}$$

The relation $\langle u|u\rangle = \langle \tilde{u}|\tilde{u}\rangle$ can be proven in the same way. Starting from (10), we can then show that the Zak phase for dipolar-exchange spin waves is also equal:

$$\theta = \int_{-\pi/a}^{\pi/a} \frac{\Im\,\langle \tilde{u}|\partial_k|\tilde{u}\rangle}{\langle \tilde{u}|\tilde{u}\rangle} dk = \int_{-\pi/a}^{\pi/a} \frac{\Im\,\langle u|\partial_k|u\rangle}{\langle u|u\rangle} dk. \tag{15}$$

In (13, 14) we omitted the indexing of $u_{\parallel(\perp)}(x)$ and their Fourier coefficients $u_{\parallel(\perp),G_n}$ by the band number and did not marked their dependence on the wavenumber k.

2 Zak phase and logarithmic derivative for the crystal with centrosymmetric unit cells

For 1D crystal the Bloch function at $k=0$ or $k=\pm\pi/a$ is periodic ($\boldsymbol{m}(x+a)=\boldsymbol{m}(x)$) or anti-periodic ($\boldsymbol{m}(x+a)=-\boldsymbol{m}(x)$), respectively. Moreover, for the crystals with centrosymmetric unit cells, the Bloch function are even ($\boldsymbol{m}(x_s+x)=\boldsymbol{m}(x_s-x)\Rightarrow \partial_x\boldsymbol{m}=0|_{x=x_s}$) or odd ($\boldsymbol{m}(x_s+x)=-\boldsymbol{m}(x_s-x)\Rightarrow \boldsymbol{m}=0|_{x=x_s}$) function, with respect to each of two symmetry centers $x_s=na$ or $x_s=a/2+na$, and can be normalized to be real-valued. This gives four possible type of bands, by considering the (even or odd) symmetry of the Bloch function on each of two edges of the band. It is worth noting, that the symmetry of Bloch function is the same at both symmetry centers ($x_s=0+na$ and $x_s=a/2+na$) only for $k=0$ whereas it is reversed (from even to odd or from odd to even) when we change the symmetry point, for $k=\pi/a$. Therefore, it is better to use Wannier functions, defined as:

$$\boldsymbol{a}(x-na) = \sqrt{\frac{a}{2\pi}} \int_{-\pi/a}^{\pi/a} \boldsymbol{m}_k(x) e^{-ikna} dk, \tag{16}$$

to classify the symmetry of the bands[3,4]. The Wannier functions characterize whole band (do not depend on the wavenumber k). For the case of crystal of centrosymmetric unit cells, they are exponentially localized around one of symmetry centers ($x_c=0$ and $x_c=a/2$), and are either even or odd with respect to this symmetry center. The periodicity (and anti-periodicity) and symmetry of the Bloch function at $k=0$ ($k=\pi/a$) can be strictly connected to the properties of the Wannier functions by the relation:

$$\boldsymbol{m}_k(x) = \sqrt{\frac{a}{2\pi}} \sum_{n=-\infty}^{\infty} \boldsymbol{a}(x-na) e^{ikna}, \tag{17}$$

which can be used to express the Zak phase in terms of Wannier functions. Assuming that the Bloch functions are normalized $\langle m|m\rangle = 2\pi/a \Leftrightarrow \langle a|a\rangle = 2\pi/a$, we can obtain from (15) and (17):

$$\begin{aligned}
\theta &= \frac{2\pi}{a} \int_{-\pi/a}^{\pi/a} i\,\langle u|\partial_k|u\rangle\, dk \\
&= \int_{-a/2}^{a/2} \left(\sum_{n,n'=-\infty}^{\infty} (x-na)\boldsymbol{a}^*(x-n'a)\cdot\boldsymbol{a}(x-na) \underbrace{\int_{-\pi/a}^{\pi/a} e^{ik(n-n')a} dk}_{2\pi/a\,\delta_{n,n'}} \right) dx \\
&= \frac{2\pi}{a} \int_{-\infty}^{\infty} x|\boldsymbol{a}(x)|^2 dx = \frac{2\pi}{a} \int_{-\infty}^{\infty} x(|a_\parallel(x)|^2 + |a_\perp(x)|^2) dx,
\end{aligned} \tag{18}$$

where $a_\parallel(x)$ and $a_\perp(x)$ denote the components of Wannier function corresponding to in-plane and out-of-plane components of Bloch function. For the system with centrosymmetric unit cells, the integral $\theta = \frac{2\pi}{a} \int_{-\infty}^{\infty} x|\boldsymbol{a}(x)|^2 dx$ takes only two possible values 0 and π which correspond to different symmetry center: ($x_c=0$ or $x_c=a/2$) at which the Wannier function, related to given band, is localized. This allows splitting all band to two disjoint topological classes where the Zak phase θ is equal to 0

or π. Please note that in general case, i.e., when the unit cells are not centrosymmetric then the Zak phase can take arbitrary value. To prove the quantized values of Zak phase for centrosymmetric unit cell, we need to discuss the symmetry of function $x|\boldsymbol{a}(x)|^2$. This function is odd when $x_c = 0$, regardless if $\boldsymbol{a}(x)$ is even or odd, which gives $\theta = 0$. For $x_c = a/2$, we need make a substitution $x \rightarrow x + a/2$ for the variable inside the integral. Then, we can find that the expression can be split into two terms: $(x + a/2)|\boldsymbol{a}(x + a/2)|^2 = x|\boldsymbol{a}(x + a/2)|^2 + a/2|\boldsymbol{a}(x + a/2)|^2$, where the first one is odd and second one is even and does not vanish after integration, which gives $\theta = \pi$. The above discussion relates the symmetry of the Bloch function on the edges of the band to the Zak phase for this band in the structures with centrosymmetric unit cells. *If the symmetry of Bloch function, respect to the center of unit cell, is the same on both edges of the band then the Zak phase for this band is equal to 0, otherwise to π.* As we noticed at beginning of Section 2, the centering of the unit cell at alternative symmetry center x_s (i.e., shifting it by $a/2$) changes the symmetry of the Bloch function on one edge of the band only, i.e., for the edge at which $k = \pi/a$. As a result *the shift of the centrosymmetric unit cell by the half of the period: $x_s \rightarrow x_s + a/2$ flips the Zak phase for each band: $\theta \rightarrow \theta + \pi$.*
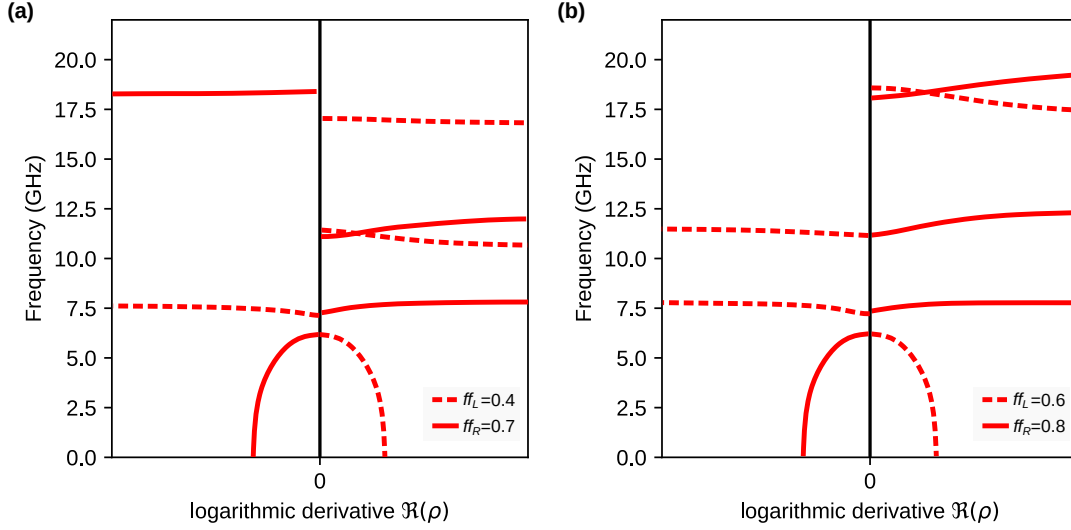

(a) **(b)**

Figure 1. Logarithmic derivative calculated numerically from eq. (19). The lines (dashed for $ff = 0.4$, solid for $ff = 0.7$) are monotonically goes between 0 and infinity within the band gap. The crossing point for left and right magnonic crystals (MCs) point out the frequency value of the interface state. Here, the interface state appears only in the second band gap. Logarithmic derivative calculated numerically from eq. (19). The lines (dashed for $ff = 0.6$, solid for $ff = 0.8$) are monotonically goes between 0 and infinity within the band gap. The crossing point for left and right MCs point out the frequency value of the interface state. Here, the interface state appears only in the third band gap.

For the crystal with centrosymmetric unit cells, the properties of the Bloch function on the edges of bands are decisive for the sign of the logarithmic derivative of Bloch functions inside the gaps and thus determine the conditions of existence for surface/interface modes. According to the work of J. Zak[5]: (i) the logarithmic derivative $\rho(k)$, taken in symmetry points $x_s = na$ or $x_s = a/2 + na$, is real and has a constant sign in the whole range of the frequency gap, whereas in the band $\rho(k)$ is purely imaginary; (ii) the sign of $\rho(k)$ in two successive gaps is different (the same) if $\rho(k)$ reaches two zeros or two poles (one zero and one pole) at the edges of the band between the gaps. The zeros and poles of $\rho(k)$ at the edges of bands correspond to $\boldsymbol{m}_k|_{x=x_0} = 0$ and $\partial_x\boldsymbol{m}_k|_{x=x_0} = 0$, which means the odd and even Bloch functions at symmetry point corresponding to the edge of unit cell, respectively; (iii) the sign of ρ is conserved (negated) in the direct gaps which is opened at $k_r = 0$ ($k_r = \pi/a$), in the center of the BZ; (iv) the change of the side of interface $x_{0+} \rightarrow x_{0-}$ and the direction of decaying of the mode from $x \rightarrow \infty$ to $x \rightarrow -\infty$ (when we switch from the MC on the right to the MC on the left) requires the change of the sign of imaginary part of the wavevector from $-k_i$ to k_i, that results in the change of the sign of the logarithmic derivative: $\rho(k_r + ik_i)|_{x=x_{0+}} = -\rho(k_r - ik_i)|_{x=x_{0-}}$. The properties (i), (ii) and conclusions highlighted at the end of the previous paragraph allow us to formulate the following statement. *When the Zak phase for a given band is equal 0 (π) then the signs of logarithmic derivatives of Bloch function in gaps surrounding this band are the same (are opposite).*

The knowledge of the Zak phases for all bands below a given gap allows determining the sign of the logarithmic derivative

of Bloch function $\rho(k)$ in this gap. To justify this formula, let us start with the discussion concerning the sign of $\rho(k)$ below the lowest band $n = 1$. For the frequencies below the 1st band, the Bloch function has a form of evanescent wave ($|k_i| > 0$) with homogeneous phase ($k_r = 0$) and without the oscillations within the unit cells. Therefore, it decays monotonously to the left $x \to -\infty$ ($k_i > 0$) or to the right $x \to \infty$ ($k_i > 0$) and its logarithmic derivative is positive or negative, respectively. This property is included by the sign $\pm$ in the formula which links the sign of $\rho(k)$ in the gap with the sequence of Zak phases for the bands below it (Eq.(5) in the manuscript). When all bands are characterized by the Zak phase $\theta = 0$, the logarithmic derivative of Bloch function ρ flips its sign from the gap to the gap. Therefore, in the gap just above n^{th} band, it will be equal to $\pm(-1)^m$. The number of flips of the sign will be reduced if some bands with the Zak phase $\theta = \pi$ appear below the selected gap. If the odd (even) number of such bands exit, then the sign $\pm(-1)^m$ will (will not) be reversed. This potential reversal of the sign can be described by adding factor $\prod_{m=1}^{n} \exp(i\theta_m) = \exp\sum_{m=1}^{n}(i\theta_m)$, where the expression $\exp(i\theta_m)$ is equal to $+1$ or -1, if $\theta_m = 0$ or π, respectively.

3 Calculations of the logarithmic derivative of Bloch function using the PWM

Using the Fourier expansion of the Bloch function (13), we can strictly calculate the derivative $\partial_x m_{\parallel(\perp)}$ and write the logarithmic derivative of Bloch function in the form:

$$\rho(x) = i\frac{\sum_i (k+G_i) u_{\parallel(\perp),k,G_i} \exp(iG_i x)}{\sum_n u_{\parallel(\perp),k,G_i} \exp(iG_i x)}. \tag{19}$$

4 The exemplary SWs' profiles on the edges of the frequency bands

For the centrosymmetric unit cell, the Zak phase θ_n of each nth band of the 1D crystal can be determined only by inspection of the Bloch functions' symmetry $m_{k,\parallel(\perp),n}(x)$ in the symmetry point of the 1st Brillouin zone: $k = 0$ or $k = \pm\pi/a$, where a is a period of 1D lattice. The Zak phase of the nth band is 0 if either $|m_{n,k=0}(x = x_0)| = |m_{n,k=\pi/a}(x = x_0)| = 0$ or $|\partial_x m_{n,k=0}(x = x_0)| = |\partial_x m_{n,k=\pi/a}(x = x_0)| = 0$, where x_0 denotes the center of the unit cell. Otherwise, it is π[6].

Figs. 2(a, b) presents the profiles of modes for four the lowest bands for the pair of $ff = 0.4$ and 0.7 (up and down, respectively) and Fig. 2(c, d) –for 0.6, 0.8, and Fig. 2(e, f) for the system with included dipolar interaction: ff=0.6 and 0.9. Black lines marks the profiles for $k = 0$, and green lines – for $k = \pi/a$. Light blue and yellow colors denotes the regions in which the Py and Co strips are placed, respectively (see Fig. 1 in the manuscript). The Zak phase can be deduced by analyzing symmetry of the profiles and the edges of each band, i.e., for $k = 0$ and $k = \pi/a$.

References

1. Krawczyk, M., Sokolovskyy, M. L., Kłos, J. W. & Mamica, S. On the formulation of the exchange field in the Landau-Lifshitz equation for spin-wave calculation in magnonic crystals. *Adv. Condens. Matter Phys.* **2012**, 14, DOI: 10.1155/2012/764783 (2012).

2. Kaczér, J. & Murtinová, L. On the demagnetizing energy of periodic magnetic distributions. *Phys. Status Solidi (a)* **23**, 79–86, DOI: https://doi.org/10.1002/pssa.2210230108 (1974).

3. Zak, J. Symmetry criterion for surface states in solids. *Phys. Rev. B* **32**, 2218–2226, DOI: 10.1103/PhysRevB.32.2218 (1985).

4. Kohn, W. Analytic properties of Bloch waves and wannier functions. *Phys. Rev.* **115**, 809–821, DOI: 10.1103/PhysRev.115.809 (1959).

5. Zak, J. Berry's phase for energy bands in solids. *Phys. Rev. Lett.* **62**, 2747–2750, DOI: 10.1103/PhysRevLett.62.2747 (1989).

6. Xiao, M., Zhang, Z. Q. & Chan, C. T. Surface impedance and bulk band geometric phases in one-dimensional systems. *Phys. Rev. X* **4**, 021017, DOI: 10.1103/PhysRevX.4.021017 (2014).
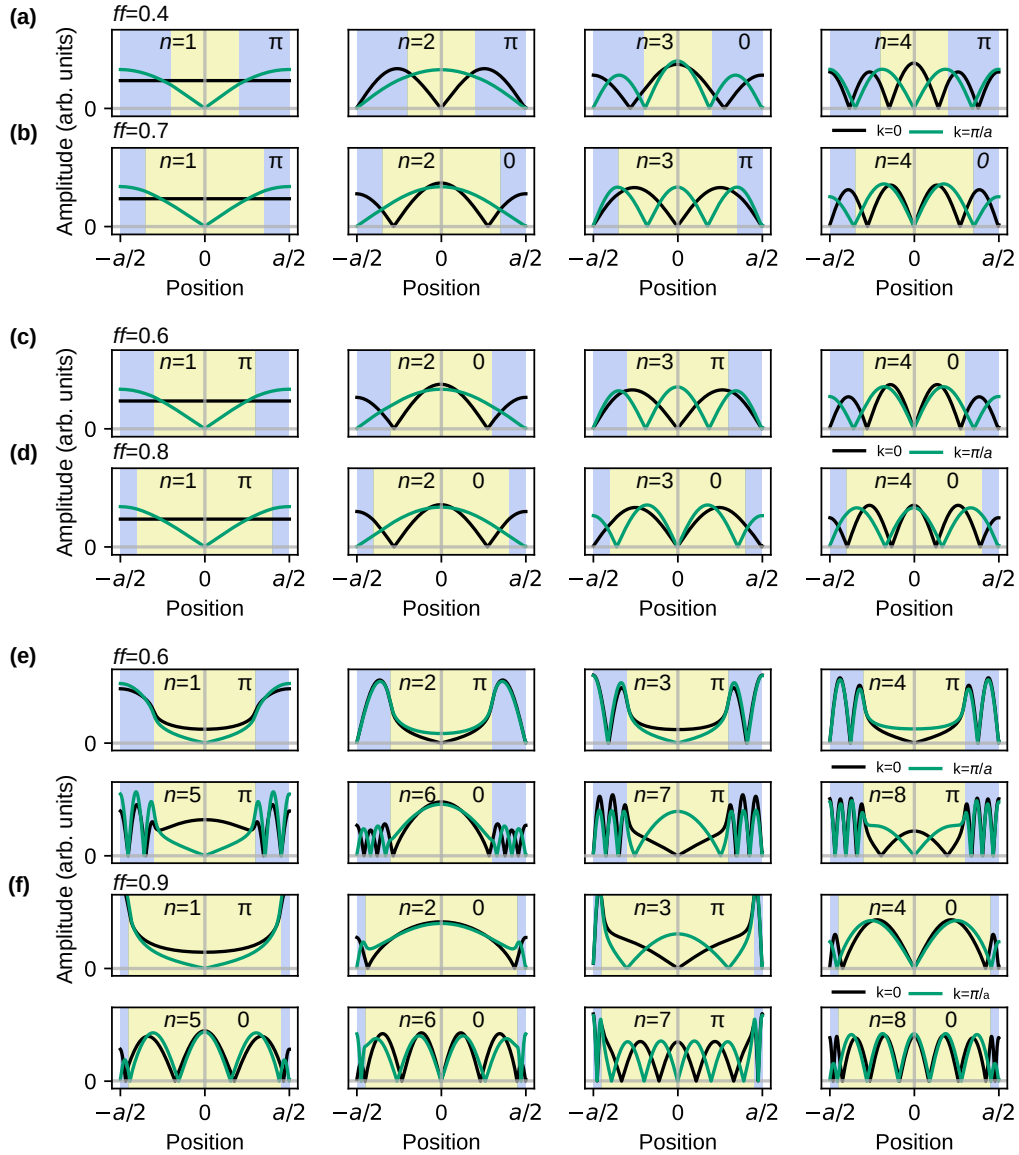
Figure 2. The SW's profiles $|m_\perp|$ within the unit cell at the edges of BZ. Black line is calculated for $k = 0$, green line for $k = \pi/a$. The values of the SW profiles and their derivatives allow determining the Zak phase for the band. (a) Results for $ff = 0.4$. For $n = 1$, $n = 2$ and $n = 4$ modes have different derivatives in the middle of unit cells, that suggest value of Zak phase equal to π. For $n = 3$ Zak phase is equal to 0. (b) Results for $ff = 0.7$. For $n = 1$ and $n = 3$ Zak phase is equal π, and for $n = 2$ and $n = 4$ Zak phase is equal 0. (c) Results for $ff = 0.6$. For $n = 1$ and $n = 3$ Zak phase equal to π. For $n = 2$ and $n = 4$ Zak phase is equal to 0. (d) Results for $ff = 0.8$. Only for $n = 1$ Zak phase is equal π, everywhere else is equal to 0. For exchange-dipolar waves, 8 SW's profiles are presented. (e) Results for $ff = 0.6$. For $n = 1$, $n = 2$, $n = 3$, $n = 4$, $n = 5$, $n = 8$ Zak phase is equal to π, everywhere else is equal to 0. (f) Results for $ff = 0.9$. For $n = 1$, $n = 3$, $n = 7$ Zak phase is equal to π, everywhere else is equal to 0.

4.4   P4 - Spin-wave localization on phasonic defects in one-dimensional magnonic quasicrystal

This work, P4 was inspired by the discussion with Dr. Radosław Strzałka[130], from AGH University of Science and Technology in Kraków, during the conference *45. Zjazd Fizyków Polskich*. Dr. Strzałka works theoretically on phasons in quasicrystals. He drew our attention to the enhanced susceptibility of narrower frequency gaps for closing due to the presence of defects in the structure of quasicrystals. Numerical studies presented in the paper were the continuation of the research on quasicrystals conducted in the Department of Physics of Nanomaterials at Adam Mickiewicz University in Poznań by Dr. Justyna Rychły[99], during her PhD-studies. Her pioneering works demonstrate fractal spectra of the integrated density of states (IDOS) and critically localized modes[79, 80]. We formulated a scientific objective asking ourselves what could be the role of disorder introduced into the quasiperiodic magnonic system. The role of disorder is not widely investigated in magnonics, especially in quasicrystals, so we thought that addressing this question is legit. Mentioned features of magnonic quasicrystals seemed to be especially interesting in the light of introducing defects because defects in the system lead to the appearance of mode localization, while the fine structure of IDOS gives the possibility to investigate the evolution of frequency gaps out of many frequencies and widths. To introduce structural defects, we applied the concept of uncorrelated phasonic defects. By increasing the number of such defects, we can gradually transit from the unperturbed Fibonacci quasicrystal to random rearrangement of the constituents elements decorating the initial Fibonacci lattice.

Although phasons are dynamic quasiparticles in quasicrystals, in this research, they are considered static, and we use this concept only to define the method of introducing defects. The Fibonacci lattice can be generated by the so-called "cut&projection" method, and the phasonic defects can be interpreted as the modulations of a line that cut the square lattice embedded in fictitious two-dimensional hyperspace. The Fibonacci sequence of length F_n has F_n different realization (aka phasons), related to the structural degree of freedom, that corresponds to the shift of the cut line. If the amplitude of modulation at a given lattice point is high enough, an element from a neighboring sequence can be picked up, leading to a phasonic defect. The amplitude of modulation determines the strength of the disorder because more phasonic defects are probable in the system.

Presentation of results in the work P4 starts from the comparison of the IDOS between ideal Fibonacci sequence and defected systems at different ranges of disorder. It can be noticed how the fine spectrum that is the hallmark of the magnonic quasicrystal is degrading under disorder. The impact on the smaller gap is strong, and even relatively small disorders in

the structure lead to closing the gaps. This is also reflected in the Bragg peaks, where smaller ones diminish more than bigger ones, with increasing levels of disorder. In the next step, the paper presents the aggregated results in the form of a histogram where the different realization of disorder is generated under the same level of disorder. This step allows for discussion of which peculiarities come from the phasonic defects. While small gaps close very fast, the bigger ones are more robust to the disorder. Additional states merge on the edges, leading to the destruction of the van Hove singularities, and additional modes appear well inside the gap. Increasing the level of disorder leads to a stronger impact on IDOS, and the modes' frequencies disperse over a wider range, penetrating the frequency gaps of undefected system. Under the defects, some modes migrate in the frequency domain, however, a measure of localization reveals the fact that all the modes are disturbed. The last part of the paper is a discussion on the mode evolution of several selected modes. The quasicrystal is self-similar, so there are many patterns that can be found repetitively across the structure. This behavior leads to the appearance of an additional type of modes that are unique for quasicrystals, namely critically localized states. Thus modes in magnonic quasicrystal can be grouped into two categories: bulk and critically localized. It is particularly interesting to track how each of them behaves under disorder in the system. In several examples, it is shown, how modes change the profile from bulk to critically localized, or from critically localized to localized on the defect.

In work P4, I performed calculations of spin wave spectra by plane wave expansion method, prepared graphics, and worked on the manuscript. I was the corresponding author.

Spin-wave localization on phasonic defects in a one-dimensional magnonic quasicrystal

Szymon Mieszczak ®,[*] Maciej Krawczyk, and Jarosław W. Kłos ®

Institute of Spintronics and Quantum Information, Faculty of Physics, Adam Mickiewicz University,
Poznań, Uniwersytetu Poznańskiego 2, Poznań 61-614, Poland

We report on the evolution of the spin-wave spectrum under structural disorder introduced intentionally into a one-dimensional magnonic quasicrystal. We study theoretically a system composed of ferromagnetic strips arranged in a Fibonacci sequence. We considered several stages of disorder in the form of phasonic defects, where different rearrangements of strips are introduced. By transition from the quasiperiodic order towards disorder, we show a gradual degradation of spin-wave fractal spectra and closing of the frequency gaps. In particular, the phasonic defects lead to the disappearance of the van Hove singularities at the frequency gap edges by moving modes into the frequency gaps and creating new modes inside the frequency gaps. These modes disperse and eventually can close the gap, with increasing disorder levels. The work reveals how the presence of disorder modifies the intrinsic spin-wave localization existing in undefected magnonic quasicrystals. The paper contributes to the knowledge of magnonic Fibonacci quasicrystals and opens the way to study of the phasonic defects in two-dimensional magnonic quasicrystals.

I. INTRODUCTION

Quasicrystals are aperiodic structures characterized by long-range order and lack of translational symmetry [1,2]. The order can be revealed in the Fourier spectrum of the structure that has a countable set of Fourier components [3–6]. This property leads to the presence of multiple frequency gaps (i.e., Bragg gaps) in the spectrum of eigenmodes. The disorder introduced into the structure generally leads to the localization of the eigenmodes. The increasing level of disorder eventually leads to Anderson localization [7–10] and the gradual closing of the Bragg gaps. Particularly interesting is the case of defects in quasicrystals because they possess fine band structures and already localized modes that are called critically localized. In this sense, the impact of the disorder can be more complex.

Due to the structural degrees of freedom in quasicrystals, the local arrangement of the structure cannot unambiguously determine the global ordering and the identification of disorder is more difficult than for periodic structures. The concept of structural degrees of freedom is more understandable when we notice that the quasicrystals can be generated from the higher-dimensional crystals defined in abstract higher-dimensional hyperspace or real space but by the cut-and-projection (C&P) method [3].

The most known one-dimensional (1D) quasicrystal whose lattice can be generated by the C&P method is the Fibonacci quasicrystal, where lattice points, separated by long ($L = a\tau/\sqrt{2+\tau}$) and short ($S = a/\sqrt{2+\tau}$) distances, are arranged aperiodically (a denotes the period of square lattice in hyperspace, τ is the golden ratio) [11]. The translation of the Fibonacci lattice is equivalent to rearrangements/swaps

within the pairs of neighboring sites, which leads to the exchange of the adjacent short and long distances: $LS \leftrightarrow SL$. These local rearrangements of the lattice are called *phasons* [12]. The C&P method suggests also how to generate the positional disorder in the Fibonacci lattice manifested only by the perturbation of the sequence of L and S. It can be achieved by the modulation of the shift c of the projection line $y = \tau^{-1}x + c(x)$—see Appendix A for more details. If this randomly introduced modulation is long wave and has small amplitude, then it generates the $LS \leftrightarrow SL$ swaps. Such kind of structural disorder is called *phasonic defects*.

The phasons (and phasonic defects) are the unique feature of all quasicrystals and were intensively investigated in relation to the stability of the atomic lattice of natural quasicrystals and their phononic properties [13]. In these systems, phasons are dynamic objects which can be activated thermally and move diffusely [10,14,15] in the structure of a quasicrystal. The concept of phasons was already investigated in photonics including the diffusive character of phasons [16]. Their role was also discussed as static defects, deliberately introduced into the photonic quasicrystals [17].

In the paper we focus on the general problem of proper introduction of positional disorder in magnonic quasicrystals and study the impact of such phasonic defects on the spin-wave spectra and their localization properties in magnonic Fibonacci quasicrystals [18,19]. We introduce the static and spatially uncorrelated phasonic defects, which allow for gradual transition from the nondefected Fibonacci sequence of strips to the completely disordered system. The static character of considered phasonic defects means that they are introduced intentionally (i.e., by design) and not spontaneously (i.e., by thermal activation).

The impact of the disorder on magnetization dynamics was extensively studied in the lattice models [20–23]. In the case of the continuous model, the impact of the isolated

---

[*]szymon.mieszczak@amu.edu.pl

defect on the spin-wave spectrum in magnonic crystals was investigated for 1D structures [24–26], two-dimensional (2D) magnonic crystals [27–29], and line defects in 2D magnonic crystals [30]. There were also reports on defect as a magnetization reversal of a single strip in a one-dimensional magnonic crystal [31]. However, a disorder in magnonic quasicrystals raises another class of questions, thus, we believe that our study on phasonic defects and their impact on the spin waves makes a valuable contribution to the magnonics field of research.

In Sec. II we present the magnonic structure under investigation, explaining (i) why this structure can be considered as a decorated Fibonacci lattice and (ii) how we introduce the uncorrelated phasonic defects. In this section we also outline the computational method based on the solution of the Landau-Lifshitz equation by the plane wave method. In Sec. III we provide a detailed analysis of the impact of the phasonic defect on the frequency spectra of SWs and localization of the modes, illustrated by the plots of the integrated density of states, localization measure, and the profiles of selected modes. Finally, in Sec. IV we conclude our findings.

II. STRUCTURE AND MODEL

We investigate spin waves (SWs) in a 1D planar magnonic structure composed of cobalt (Co) and permalloy (Py) strips of equal widths, being in direct contact and thus forming a continuous layer. The Co and Py strips are magnetically saturated by the external field applied along with them. The strips are arranged in a Fibonacci quasicrystal. It is worth noting that despite the equal width of the strips, the system can be understood as a decorated Fibonacci lattice where Co and Py strips are centered at sequences $SLLS$ and SLS sharing the shorter sections S between Co and Py with the ratio $(2 - \tau)/(2 + \tau)$. Then, the common width of Co and Py strips is equal to $a(\frac{3}{2}\tau + 1)/\sqrt{\tau + 2}$.

To generate the phasonic defects as the structural perturbations, we use the procedure which is technically simpler than the C&P method (discussed in Appendix A), although it is based on a more complex formalism (describing the properties of the generalized Harper model with incommensurate modulation of the on-diagonal and off-diagonal elements of tight-binding Hamiltonian [32]). The general model, which also describes the Fibonacci quasicrystal, is presented in Ref. [32]. The authors provide the characteristic equation that determines the successive elements of the Fibonacci sequence for given values of the parameter ϕ, describing the structural degree of freedom [33,34]:

$$\chi_n(\phi) = \text{sgn}\left[\cos\left(\frac{2\pi n}{\tau} + \phi\right) - \cos\left(\frac{\pi}{\tau}\right)\right]. \quad (1)$$

The characteristic function χ_n takes the values ± 1. For our structure, $\chi_n = 1$ ($\chi_n = -1$) selects Py (Co) strip at nth position in the Fibonacci sequence. The parameter ϕ is related to the shift c of the line $y = \tau^{-1}x + c$ in the C&P method: $\phi = 2\pi c/a$, see Fig. 9 in Appendix A. For infinite range of the index n, the different values of ϕ correspond to different realizations of the Fibonacci crystals which are only shifted by $\tilde{n}$ positions with respect to each other: $\chi_n(\phi) = \chi_{n+\tilde{n}}(\phi + \tilde{\phi})$, for every n (the change $\tilde{\phi}$ of the parameter ϕ corresponds
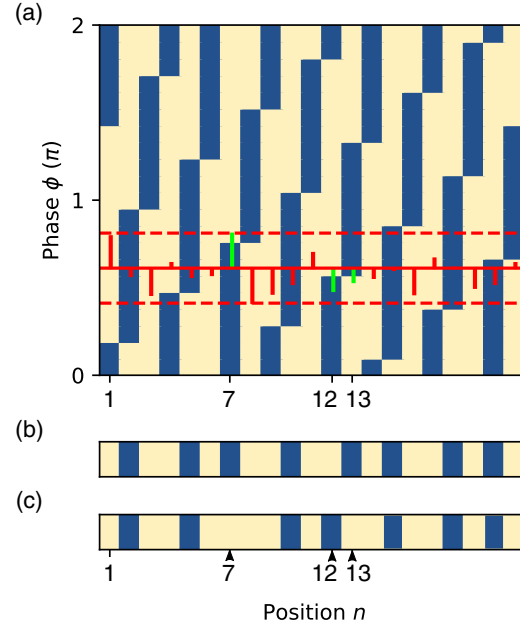

FIG. 1. (a) All possible approximates of a Fibonacci crystal composed of 21 elements. As the phase ϕ changes [see Eq. (1)], we obtain 21 possible sequences of Co (light yellow) and Py (dark blue)—note that Co strips can appear in doublets. The solid red line at $\phi = \pi/\tau$ corresponds to the approximate generated by standard substitution rules: Co $\rightarrow$ Co|Py, Py $\rightarrow$ Co, presented in (b)—see also Fig. 2. The red dashed lines show the range in which the parameter ϕ is randomly changed at each position n. The changes of ϕ which induces the phasonic defects are marked by green bars. They are responsible for the substitution Py $\rightarrow$ Co at position 7 and swap between positions 12 and 13 (Co|Py $\rightarrow$ Py|Co). A sequence with defects is presented in (c); note that position of swaps are marked by arrows.

to the shift of the sequence by $\tilde{n}$ positions). When n takes values in the finite range $1, \ldots, N$, where N is the Fibonacci number, then the sweep of the parameter ϕ in the range $[0, 2\pi]$ produces all unique, N-element sequences which can be identified as the Fibonacci crystal. The number of such unique approximates of the Fibonacci crystal is equal to N. It is illustrated in Fig. 1(a) where we presented all 21 approximates composed of 21 elements (strips). Please note that the characteristic function Eq. (1) is periodic: $\chi_n(\phi) = \chi_n(\phi + 2\pi)$, and the parameter ϕ plays a role of phase in Eq. (1).

We arbitrarily selected the structure represented by $\phi = \pi/\tau$ because this approximate is generated by the standard substitution rules. The phasonic defects can be introduced to any sequence generated by Eq. (1), because each of them is a defectless section of the Fibonacci quasicrystal. The approximate for $\phi = \pi/\tau$ [red solid line in Fig. 1(a)] is presented schematically in Fig. 1(b) and a corresponding structure is visualized in Fig. 2.

To introduce the phasonic defects we add an additional term ϕ_n to the parameter ϕ: $\phi \rightarrow \phi + \tilde{\phi} + \phi_n$ [33,34]. This term is a random number of uniform distribution in the range $-\Delta\phi < \phi_n < \Delta\phi$, where $\Delta\phi < \pi$. The range $\Delta\phi$ can be understood as a counterpart of thermodynamic temperature
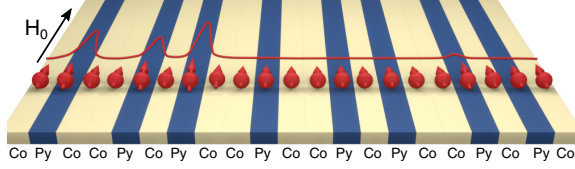
FIG. 2. The approximate of a Fibonacci quasicrystal corresponding to the $\phi = \pi/\tau$ (see Fig. 1), i.e., resulting from the standard substitution rules: Co → Co|Py, Py → Co. This exemplary structure is composed of Py and Co flat strips (30 nm thick and 300 nm wide), aligned side-by-side and being in direct contact. The field $\mu_0 H_0 = 0.1$ T is applied along the strips. The sequence of tilted arrows and line in front of them visualizes the spin-wave mode profile.

in atomistic quasicrystals, where higher temperature leads to higher probability of defect occurrence. This range is marked by the red dashed lines in Fig. 1(a) and the exemplary sample of the random values of ϕ_n are denoted by thin vertical bars. The perturbations ϕ_n which induce the phasonic defects (i.e., flip the sign of χ_n) are marked by the green line (positions $n = 7, 12, 13$). The ineffective perturbations are marked by red bars. The perturbed structures with three phasonic defects are shown in Fig. 1(c). Positions of phasonic defects are marked by arrows below the figure. The defects are not correlated in space because for each position χ_n is generated independently. Thus, the parameter ϕ_n does not change gradually, in a wavelike manner, as it is expected for a long wave (and long-living) phasons in atomic quasicrystals at finite temperature [13,14]. Because of it, along with swaps $LS \leftrightarrow SL$, we can also observe the substitutions $L \leftrightarrow S$. For $\Delta\phi = \pi$ the system becomes random, since the probability of a type of strip at nth position is τ. We discuss this case in Appendix B. For smaller values of the amplitude $\Delta\phi$, the introduction of defect is not equally probable at every position. At some locations (e.g., position 13 in Fig. 1) the generation of the defect is highly probable, whereas other locations can be quite robust (e.g., position 7), or even completely inaccessible (e.g., position 2) for defects [35].

Each strip is assumed to have a width of 300 nm, a thickness of 30 nm, and is infinitely long. The dimensions make the system in an exchange-dipolar regime, which is already feasible for experimental realization. For the constituent elements from which the system is constructed, we consider two widely used materials, namely Co and Py. The parameters that are important for SW propagation are magnetization saturation M_S and the exchange length λ_{ex}. These parameters are equal to $M_{S,Co} = 1445$ kA/m, $\lambda_{ex,Co} = 4.78$ nm, $M_{S,Py} = 860$ kA/m, and $\lambda_{ex,Py} = 5.29$ nm. We assume that our sample is saturated by the external magnetic field with value $\mu_0 H_0 = 0.1$ T, and is directed along the strips. In this geometry a static demagnetizing field is equal to zero.

We consider a magnonic quasicrystal that is composed of two different magnetic materials [36,37]. However, the magnetic contrast can also be obtained in other ways: By inducing local anisotropy [38,39], by decorating the uniform film [40,41], or by thermal gradient [42]. Having said that, the

physics that we present in the paper is not restricted to the bicomponent material.

When we neglect the damping, the dynamics of the magnetization vector can be described by the Landau-Lifshitz equation (LLE):

$$\frac{\partial \boldsymbol{M}}{\partial t} = -\mu_0 |\gamma| \boldsymbol{M} \times \boldsymbol{H}_{\text{eff}}, \qquad (2)$$

where $\mu_0 = 4\pi \times 10^{-7}$ H/m is the permeability of vacuum and $\gamma = 176$ rad GHz/T is the gyromagnetic ratio. The effective magnetic field, which contains all kinds of magnetic interactions considered in our study, governs the precession of the magnetization vector. In our case $\boldsymbol{H}_{\text{eff}}$ is composed of the following terms:

$$\boldsymbol{H}_{\text{eff}}(\boldsymbol{r}, t) = \boldsymbol{H}_0 + \boldsymbol{H}_{\text{dm}}(\boldsymbol{r}, t) + \boldsymbol{H}_{\text{ex}}(\boldsymbol{r}, t), \qquad (3)$$

where $\boldsymbol{H}_0$ stands for the external field, $\boldsymbol{H}_{\text{dm}}(\boldsymbol{r}, t)$ is the demagnetizing field, and $\boldsymbol{H}_{\text{ex}}(\boldsymbol{r}, t)$ is the exchange field. The last two terms are spatially and temporally dependent since they are connected with material parameters and magnetization dynamics at the same time. SWs are usually studied at room temperatures T. Considered materials have much higher Curie temperatures T_C, e.g., $T_C \approx 1400$ K for cobalt. In the regime $T \lesssim 3/4 T_C$, thermal effects can be neglected, and the usage of the LLE is fully justified [43].

We use the plane wave method (PWM) to solve the linearized LLE [44], where the magnetization vector $\boldsymbol{M}(\boldsymbol{r}, t)$ can be decomposed into static part $M_0(\boldsymbol{r})$ and dynamic $\boldsymbol{m}(\boldsymbol{r}) e^{i2\pi f t}$, changing harmonically with the frequency f. The dynamic part contains two components of magnetization vector: $m_{\text{in}}(\boldsymbol{r}, t)$ and $m_{\text{out}}(\boldsymbol{r}, t)$, representing in-plane and out-of-plane oscillation, respectively. The PWM method is designed for a periodic system, where the Bloch boundary condition must be used. The PWM is based on the application of the Fourier transform both to the Bloch functions (dynamic components of magnetization) and material parameters (saturation magnetization and exchange length). These procedures allow us to formulate an algebraic eigenproblem which can be solved numerically with the eigenvalues (being eigenfrequencies) and eigenvectors (being the Fourier coefficients of the Bloch functions).

Despite the fact that the quasicrystals are not periodic structures, the PWM can still be used in the so-called supercell approach [45]. This application of PWM still assumes periodicity, but for supercells being copies of the whole system, for which we take the periodic boundary condition. In magnonics, this approach was already used to investigate defect modes [24], interface modes [46], waveguides [47], and two-dimensional quasicrystals [48,49]. For the considered system, the supercells are composed of 377 strips. For such large supercells the peculiarities of the Fibonacci quasicrystal are well reproduced, and spurious interface states (which can appear at the edges of supercells) do not disturb the spectra. We used 3770 plane waves for expansion into the Fourier series. This amount was checked for convergence and was enough to reproduce the Fibonacci spectra [19].
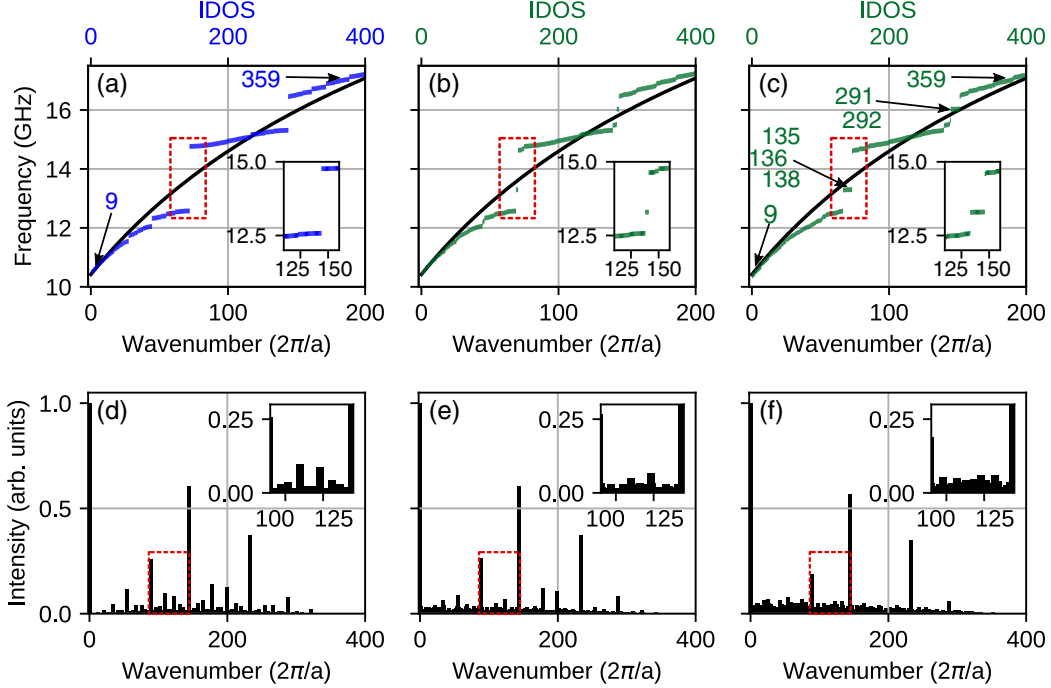
FIG. 3. Top row: (a), (b), and (c) Integrated density of states as a function of frequency plotted in the inverse form f(IDOS) (blue/green color), and the dispersion relation for SWs in a homogeneous film with weight averaged material parameters (black color). Please note that IDOS and dispersion relation has their own abscissa, and shares a common ordinate. The abscissa of each plot has the same scale, indicated only in the leftmost plot. (a) Results obtained for a perfect Fibonacci sequence composed of 377 strips. (b) Results obtained for a defected sequence with amplitude $\Delta\phi/(2\pi) = 5\%$ and (c) $\Delta\phi/(2\pi) = 10\%$. Bottom row: (d), (e), and (f) Bar plot of reciprocal lattice vector intensities, corresponding to the Bragg peaks, for the structures from (a), (b), and (c), respectively. Phasonic defects destroy the fine structure of Bragg peaks that in consequence lead to modification of the density of states at the edges of frequency gaps and creates new modes inside the gaps.

III. RESULTS AND DISCUSSION

To determine the spectral properties of the approximates of the Fibonacci quasicrystal, we plotted the dependence of integrated density of states (IDOS) on the frequency. For a finite system, IDOS(f) is the number of modes below a given frequency f, see Refs. [19,48,50]. For the successive approximates of a 1D crystal or quasicrystal (i.e., taking larger unit cell), the IDOS is a steplike function where the steps become finer with the increasing size of the approximates. Constant frequency ranges in the IDOS(f) corresponds to the frequency gap of the system for $k = 0$. The width of these ranges converges with larger approximates. The other feature allowing the identification of the frequency gaps is a specific character of IDOS(f) close to the gap's edges. The changes of the frequencies for successive modes (i.e., with increasing IDOS) become extremely small in the vicinity of the gap, which is the manifestation of van Hove singularities in the density of states for 1D nondefected systems [51,52]. It is worth noting that, due to the lack of translational symmetry in quasicrystals, we cannot easily relate the frequency f to the wave number k. However, it was shown that for a 1D infinite system, the IDOS(f) $\propto k(f)$ [53]. Therefore, the IDOS(f) dependence for large approximates give us insight into the dispersion relation $f(k)$, see Figs. 3(a)–3(c).

The f(IDOS), i.e., inverse function of IDOS(f), for a nondefected approximate (composed of 377 strips) is presented in Fig. 3(a). The solid black line in Figs. 3(a)–3(c) shows the dispersion relation $f(k)$ for an infinite uniform thin film [54]. Please note the split of the x axis between IDOS and the wave number. The film was assumed to have effective material parameters, which are the volume averages of the constituent material parameters of Co and Py. It is clearly seen that the f(IDOS) follows the dispersion relation $f(k)$. The agreement is very good for long SWs, in the so-called metamaterial regime ($k \to 0$). In this case, SWs are not that sensitive to a specific configuration of strips. Significant differences are observed when frequency gaps are opened, which does not appear in the homogeneous film. Just before and after frequency gaps, differences between the frequencies of successive states are very small, and bars in the graph [Fig. 3(a)] form the horizontal lines, which corresponds to the van Hove singularities.

Figures 3(b) and 3(c) show f(IDOS) in the presence of phasonic defects. We used green color for IDOS to visually differentiate results from the nondefected case in Fig. 3(a). We consider two levels of phasonic defects corresponding to different ranges $\Delta\phi$ of the random component of the parameter ϕ, which describes the structural degree of freedom [see, Eq. (1) and Fig. 1]. We assume the values $\Delta\phi/(2\pi) = 5\%$ [Fig. 3(b)] and 10% [Fig. 3(c)]. Due to phasonic defects, the
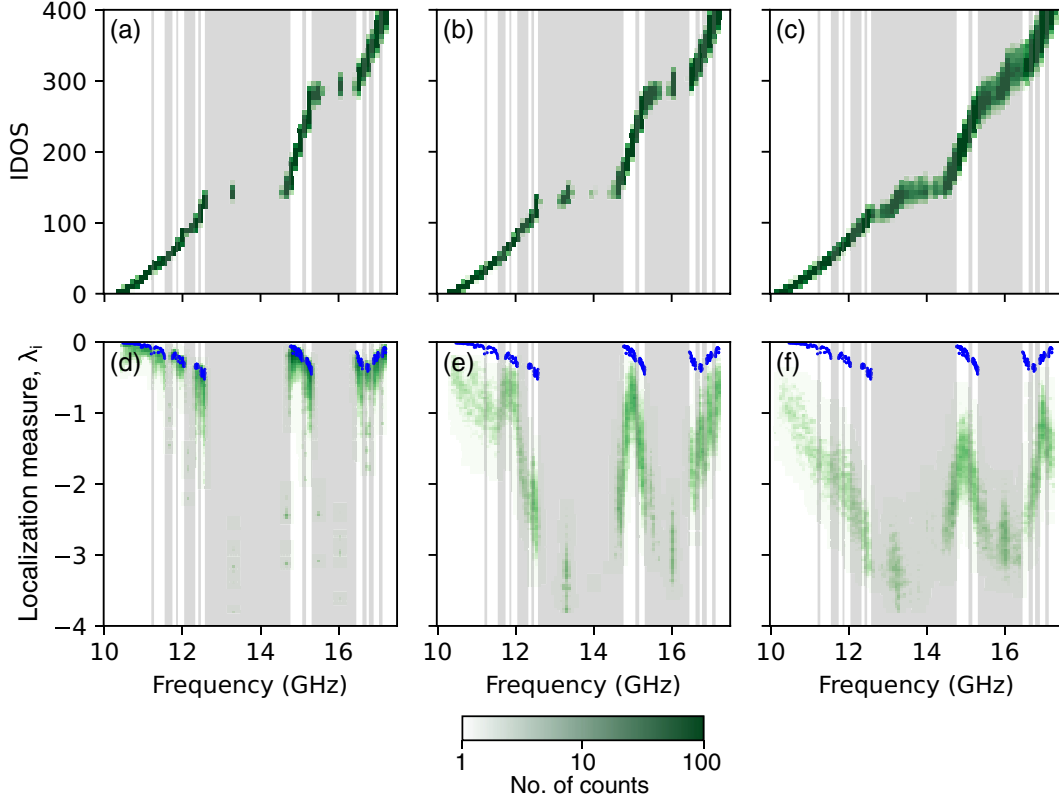
FIG. 4. Top row: (a), (b), and (c) Integrated density of states as a function of frequency plotted in the inverse form f(IDOS) calculated for the Fibonacci sequence with introduced defects. Gray areas represents the frequency gaps in an ideal Fibonacci sequence. The amplitude of phasonic defects $\Delta\phi/(2\pi)$ are (a) 5%, (b) 10%, and (c) 25%. A histogram of integrated density of states (IDOS) is obtained from 100 configurations of differently introduced defects. Intensity of the green color reflects how often a given position is occupied by an SW mode. Bottom row: (d), (e), and (f) Localization measure λ_i as a function of frequency for an SW in a 1D Fibonacci sequence with phasonic defects. The values of λ_i are calculated for structures with (d) 5%, (e) 10%, and (f) 25% of defects. Every plot aggregates 100 different system configurations. λ_i increases significantly even if a small amount of defects is introduced (d), and consequently increases with amount of defects (e) and (f).

narrowest gaps are closed, and new modes strongly localized at defects (see the discussion later in the paper) are induced [see the red dashed frames in Figs. 3(b) and 3(c), showing the states within the frequency gaps]. The narrower gaps are much more susceptible to disappearing with increasing disorder.

In the bottom row of Figs. 3(d)–3(f) we present a Fourier spectra of the structures considered in Figs. 3(a)–3(c). Formation of the frequency gaps can be attributed to the fulfillment of the Bragg condition, i.e., the position of the Bragg peak (multiplied by two) determines the position of frequency gaps [55]. However, their intensity does not necessarily determine the width of the frequency gap. We can see in the unperturbed Fibonacci structure [see Figs. 3(a) and 3(d)] that the biggest peak (except for a peak at $k = 0$) is responsible for the widest frequency gap (12.3–14.3 GHz), however the second biggest peak opens only a small one, around 15 GHz. We can see that the Bragg peaks are reduced as the level of phasonic defect increases. The relative reduction of the highest peaks (corresponding to wider gaps) is smaller than for lower peaks (corresponding to narrower gaps). Therefore,

only the highest peaks in the Fourier spectrum are distinguishable, and the widest gaps remain opened for a large level of phasonic defects—see the bottom part of Fig. 3(c) and the zoomed region, marked by the red dashed frame. Another effect of the phasonic defects in IDOS is the change of the slope of f(IDOS) at the edges of frequency gaps. This means that density of states is not singular anymore at these points.

Figures 3(a)–3(c) show that the f(IDOS) is a useful function for description of the spectral properties of defected quasicrystals. However, the spectra presented in Figs. 3(b) and 3(c) are specific for a given, randomly generated, set of phasonic defects. To obtain the representative picture, we need to collect the spectra for many configurations of phasonic defects generated for the same amplitude $\Delta\phi$. Figures 4(a)–4(c) present the IDOS for 100 different configurations aggregated on one plot in the form of a 2D histogram. Please note that figures in two rows of Fig. 4 share the same values of frequency on the horizontal axis. The intensity of the green color reflects which position in frequency and IDOS appear more often. Figures 4(a)–4(c) are plotted for $\Delta\phi/(2\pi) =$

5%, 10%, and 25%, respectively. The gray background marks the frequency gaps of the nondefected Fibonacci sequence. The general trend of IDOS in the function of frequency prevails even for the most disturbed system. The IDOS curve is not much dispersed, suggesting the same spectra for the different realizations of the disorder. However, we can notice that the green line in Fig. 4(c) is thicker than in Fig. 4(a), which indicates some frequency shift under strong disorder. In the range of frequency 10–12 GHz, where IDOS resembles the dispersion relation of the homogeneous film with weight averaged material parameters [black line in Figs. 3(a)–3(c)], defects do not change the picture. The impact of the defects is strongest around the frequency gaps. Initially, for $\Delta\phi/(2\pi) = 5\%$ the modes appear deeply inside and at the edges of the gaps. Then, for higher $\Delta\phi$, the modes start occupying other frequencies within the gaps and gradually fill them. These effects are more effective for narrower gaps. Finally, we do not observe the fine structure of the gaps in the spectrum which was a hallmark of quasiperiodicity. The location of the defect in the sequence and its neighborhood determines the frequency of strongly localized defect modes. For $\Delta\phi/(2\pi) = 5\%$ [Fig. 4(a)] modes from the widest frequency gaps (i.e., the gap around 13 or 16 GHz) are induced by those phasonic defects which form the sequence of double Py strips. Thus, their position on IDOS is very specific. Moreover, since such sequence of strips is common in the defected sequence, the modes are highly degenerated. For a more distorted sequence presented in Figs. 4(b) and 4(c), different sequences become available like triple Py strips, so defect states can occupy other frequencies.

The qualitative determination of localization is challenging because the profiles of the SW modes can be localized in many regions, so the rate of spatial decay cannot be determined unambiguously. Therefore, we decided to introduce the global measure of localization λ_i that is calculated for each ith SW mode $\boldsymbol{m}_i(x)$:

$$\lambda_i = -\frac{1}{L}\int_0^L |m_{i,\mathrm{out}}(x)| \log |m_{i,\mathrm{out}}(x)| dx, \qquad (4)$$

where L denotes the width of the whole sequence. For computational simplicity we considered only the out-of-plane component $m_{i,\mathrm{out}}(x)$ of the dynamic part of magnetization $\boldsymbol{m}_i(x)$. During the calculations, the profiles are normalized: $\frac{1}{L}\int_0^L |m_{i,\mathrm{out}}(x)| dx = 1$. The formulation of this measure is done with the analogy to the Shannon information entropy [56,57], where the SW profile plays a role of probability distribution—the uniform distribution (and Dirac delta distribution) corresponds to the highest entropy and complete absence of localization: $\lambda_i = 0$ (the lowest entropy and maximum localization: $\lambda_i = -\infty$).

In Figs. 4(d)–4(f) we present the localization measure λ_i for successive modes, calculated on the same data set as IDOS calculation. They are ordered with increasing frequency, similarly to the IDOS spectrum. We can see that localization is significantly enhanced as the amplitude of the phasonic defects is increasing [green 2D histogram in Figs. 4(d)–4(f)], especially if we compare it to the case of the nondefected system [blue points in Figs. 4(d)–4(f)]. We can identify the strongly localized defect modes with a large value of $|\lambda_i|$
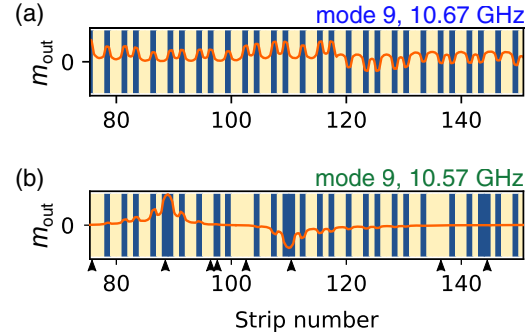

FIG. 5. The evolution of the bulk mode under the presence of the defects. (a) In the absence of defects the mode is not localized, its amplitude is more concentrated in Py than in Co. (b) For $\Delta\phi/(2\pi) = 10\%$ the defects (marked by arrows below the plot) lead to the formation of double Py strips and can concentrate the SW dynamics.

inside the frequency gap. It is worth noting that the localization of the modes at frequencies close to the edges of gaps with enhanced λ_i suggests that some of the critically localized modes [58–61] become defect modes. To inspect the localization of the SW modes directly, we plotted the profiles of selected modes. We chose one of the configurations for $\Delta\phi = 10\%$ that corresponds to an intermediate disorder level, presented in Figs. 4(b) and 4(e). All the modes are normalized to the maximum absolute value in the whole structure. Figures present only fragments of them, and the location can be deduced from strip numbers. All modes, which were selected for plotting, are also marked in the spectra [Figs. 3(a) and 3(c)]. We start the analysis by checking the impact of the disorder on the bulk modes. Figure 5 presents the comparison of one mode, labeled No. 9 at 10.67 and 10.57 GHz in nondefected and defected structures, respectively. Looking at Fig. 4(e) suggests significant modification of the profile. The envelope in Fig. 5(a) is not localized and the mode has several nodal points (one of them is visible close to strip No. 120). The visible nonuniformity of amplitude is related to the oscillatory and evanescent behavior in Py and Co strips, respectively, thus SW amplitude is concentrated in Py strips. Figure 5(b) presents mode No. 9 after introducing the defects, where double Py strips are formed. SW is localized on the defects, around the strips No. 90 and No. 110 that have a similar local arrangement.

In nondefected Fibonacci quasicrystals, the critically localized modes exist close to the edges of the gaps—see mode No. 136 at 12.57 GHz in Fig. 6(a) and its frequency marked in Fig. 3(c). The profile of this mode exhibits the pattern with amplitude concentrated on parts of the structure possessing locally the same arrangement of strips. For very large structures, these modes can reveal a self-similar pattern [58,61]. By adding the defects, we can shift critically localized modes to the frequency gap. Then, their frequencies are changed significantly, and the profiles are extremely strongly localized at defects, see Fig. 6(b). The SW in Fig. 6(b) is localized in double Py, and since such defects occur several times within
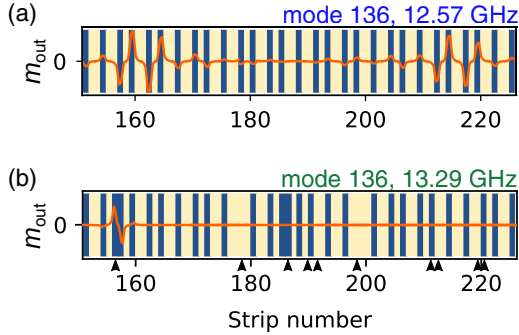
FIG. 6. The transition of the mode No. 136 from critically localized at the edge of the frequency gap to strongly localized in the frequency gap induced by phasonic defects. The critically localized mode (a) enters into the gap and (b) becomes strongly localized, due to the presence of defects $\Delta\phi/(2\pi) = 10\%$ which is accompanied by a significant change in frequency from 12.57 to 13.29 GHz.

the considered structure, the mode can occupy different defects leading to multiple degenerations.

The bulk modes can also increase their localization due to partial confinement between the defects. Figure 7(a) presents the critically localized mode No. 359 at 16.96 GHz, which has an enhanced amplitude on the sequences Co|Co|Py|Co (or on their reversed copies Co|Py|Co|Co). After introducing the defects, the mode amplitude is redistributed among these strips, which leads to the partial confinement of this mode between the defects, see Fig. 7(b).

The most typical kind of localization, existing in both periodic and quasiperiodic structures, is an exponential localization on defects, which are observed within the frequency gaps. We selected two wide gaps, around the frequency 13.5 or 16 GHz (Figs. 3 and 4), to investigate the profiles of defect modes. The selected modes (shown in Fig. 8) are localized at the defects, which have the form of double Py strips. We arbitrary chose the modes with one phase flip inside the single defect [Figs. 8(a) and 8(b)], and three phase's flips inside the defect [Figs. 8(c) and 8(d)]. The defect modes are located at a single or few positions in the structure. Due to strong localiza-
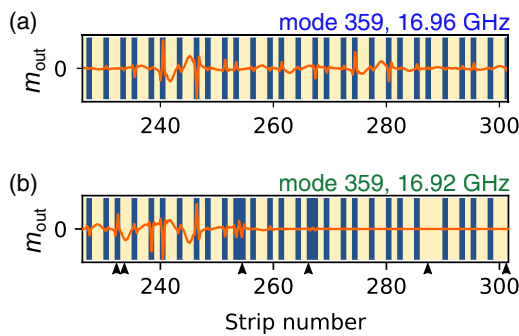

FIG. 7. (a) The critically localized mode (No. 359 at 16.96 GHz) which increases its localization and slightly changes its frequency to $f = 16.92$ GHz due to partial confinement between defects (b) at $\Delta\phi/(2\pi) = 10\%$.
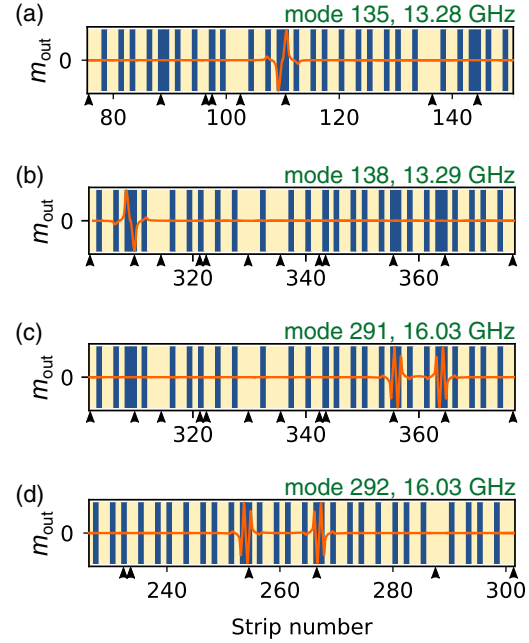

FIG. 8. The defect modes from the two largest frequency gaps shown in Figs. 3 and 4. (a) and (b) Modes No. 135 and No. 138 with frequency 13.28 and 13.29 GHz. (c) and (d) Modes No. 291 and No. 292 with frequency 16.03 GHz. The modes are strongly localized at one of few locations but have the same profile, differing only in phase (flipped upside down) [see (a) and (b)] or reversed along with the structure (flipped left-right) [see (c) and (d)]. Due to strong localization, the modes are practically degenerated. The results are shown for the structure with $\Delta\phi/(2\pi) = 10\%$.

tion and low probability of overlapping between the profiles concentrated at selected defects, the modes are degenerated—there are many modes of very similar frequencies occupying similar sequences in different locations of the quasicrystal. We discussed earlier the position-dependent susceptibility for inducing the defects, where we showed that some locations in the structure are very resistant or even completely robust to the introduction of defects at the low value of the amplitude $\Delta\phi$ [35]. This is an additional factor supporting the isolation of the SW dynamics at defects and contributing to the nonuniform distribution of the frequencies for defect modes within the frequency gaps.

IV. SUMMARY

It is known that magnonic quasicrystals offer additional possibilities in designing artificial magnonic band structures as compared to magnonic crystals. The increased complexity of the spin-wave spectrum and the appearance of bulk localization of the spin-wave modes are the main effects of the quasiperiodicity. In the paper we show additional steps towards customization, namely the introduction of the disorder in the form of phasonic defects, and demonstrate their impact on spectral properties and localization of the spin-wave modes. To explore the role of disorder in quasicrystals, we

studied many randomly generated configurations of defects. We focused on selected configurations to discuss the profiles of representative eigenmodes exhibiting the critical localization at the edges of the frequency gaps, and strong localization on phasonic defects inside the gaps. In particular, we show that smaller gaps are closed under a small perturbation of the quasiperiodicity, while wide ones are relatively robust to a disorder. It is assisted by transition from bulk modes to critically localized modes, and finally to the modes strongly localized on the defects. Interestingly, the modes from the frequency gap edges become strongly localized by the introduction of phasonic defects to the structure, which is correlated with the disappearance of van Hove singularities.

We demonstrated that in the complex magnonic system, where both short-range exchange interactions and long-range dipolar interactions come into play, the effects like closing the small gaps and enhancement of the modes' localization are reproduced for spin waves. The study opens the route for the investigation of phasonic defects in two-dimensional magnonic quasicrystals, which recently attracted interest due to their application potential in magnonics signal processing [49,62].
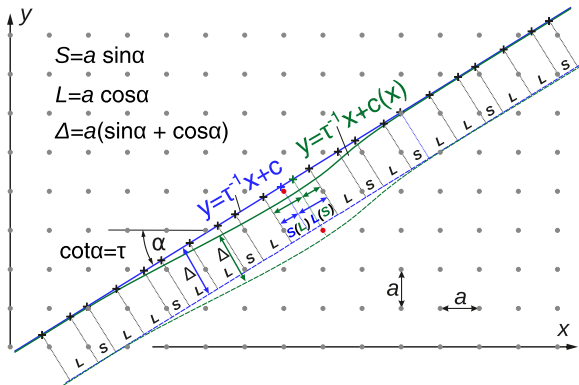
FIG. 9. The illustration of the cut-and-projection (C&P) method and the induction of phasonic defect. The array of dots represent the square lattice in a 2D hyperspace. The Fibonacci lattice (black and blue crosses) is generated by the projection of a square lattice from the belt between solid and dashed lines onto the line $y = \tau^{-1}x + c$ of irrational slope, being the inverse of the golden ratio τ. The visible (21-element) section of the Fibonacci lattice corresponds to the selection of $\phi = 2\pi c/a = 0.8$, see Fig. 1. For a defect-free Fibonacci lattice the belt (between solid blue and dashed blue line) is straight. By bending the belt (limited here by solid green and dashed green lines), we can induce the phasonic defects in the Fibonacci lattice (black and green crosses).

APPENDIX A: CUT-AND-PROJECT METHOD: PHASONS

The Fibonacci lattice can be generated from the square lattice of the period a by the C&P method [3]. The lattice points $\mathbf{r} = a(m\hat{\mathbf{x}} + n\hat{\mathbf{y}})$, where m, n are integers, are projected onto the line $y = \tau^{-1}x + c$ from the belt, below this line, of the width $a(\cos\alpha + \sin\alpha) = a(\tau + 1)/\sqrt{\tau + 2}$, where $\alpha = \text{arccot}(\tau)$ is the angle between the line and the x direction, and τ is the golden ratio. This procedure generates the proper sequence of long ($L = a\cos\alpha = a\tau/\sqrt{\tau + 2}$) and short distances ($S = a\sin\alpha = a/\sqrt{\tau + 2}$) between lattice points projected onto the line y, forming the Fibonacci lattice, see Fig. 9. The position of the line (given by the constant c) and the related shift in the perpendicular direction $\sqrt{\tau + 2}(-\hat{\mathbf{x}} + \tau\hat{\mathbf{y}})$ express the structural degree of freedom in defining a Fibonacci lattice. Regardless, on the value of this shift, we always obtain the defectless lattices, differing only in some uniform translation of the lattice sites along the real (parallel) direction $\sqrt{\tau + 2}(\tau\hat{\mathbf{x}} + \hat{\mathbf{y}})$.

The introduction of phasonic defect can be described by bending the belt. It is equivalent to the perturbation of structural degree of freedom, which can be expressed here as a position-dependent shift of the belt: $c(x)$. When this dependence is small and smooth at the distances larger than the lattice constant a, then the phasonic defects have a form of
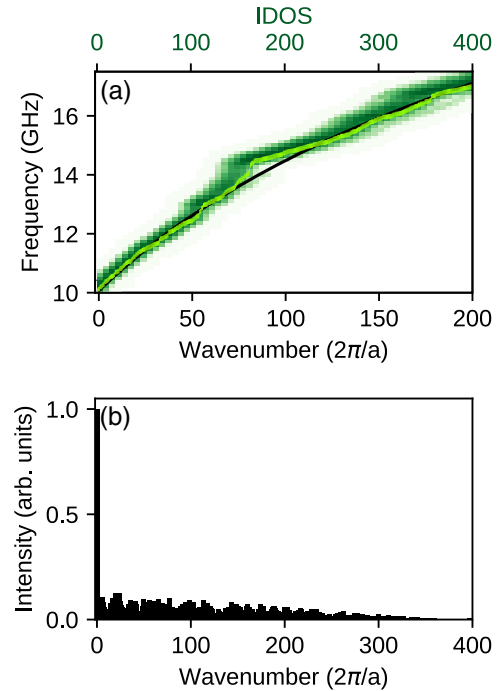
FIG. 10. (a) Integrated density of states for SWs in the randomly generated sequence of Co and Py, where the ratio between types of strips is kept as for a Fibonacci quasicrystal, i.e., it corresponds to the golden ratio. The dark-green color represents a histogram of aggregated results obtained from 100 different random sequences (the color scale is the same as in Fig. 4). Light-green points stand for one specific structure for which the bar of the Fourier transform (b) are plotted.

the swaps between neighboring short and long distances in the Fibonacci lattice ($S \leftrightarrow L$).

APPENDIX B: RANDOM SYSTEM

In Fig. 10(a) we show the IDOS spectrum of the SW eigenmodes in a randomized sequence of Co and Py with the same parameter as in the paper. To keep the same averaged composition, we used 144 Py and 233 Co strips. We generated 100 different configurations, and the intensity of the green color reflects how often a specific position is occupied on the plot. By light green we plotted one selected configuration, for which Fourier spectrum is presented below. The IDOS spectrum of this exemplary configuration coincides with the SW dispersion relation for a uniform ferromagnetic layer with the volume averaged material parameters (i.e., with the weights $1/\tau$ and $1 - 1/\tau$), except for a small deviation around 14 GHz. The IDOS does not show any signatures of the frequency gaps. It is also reflected in the Fourier spectrum [Fig. 10(b)] of this random structure that do not have any distinctive peaks except the peak at wave number $k = 0$, which corresponds to the average value of the spatial distribution of material parameters. The absence of Bragg peaks is the signature of the lack of (quasi)crystal long-range order.

The introduction of a phasonic defect for large approximates of the Fibonacci quasicrystal does not change the average number of Co and Py strips (it is obvious for the swaps Co $\leftrightarrow$ Py, whereas the substitutions Co $\rightarrow$ Py and Py $\rightarrow$ Co are equally probable, see Fig. 1). In the limit $\Delta\phi \rightarrow 2\pi$ the IDOS spectrum approaches the spectrum of the disordered system, as shown in Fig. 10(a).

[1] D. Shechtman, I. Blech, D. Gratias, and J. W. Cahn, Metallic Phase with Long-Range Orientational Order and No Translational Symmetry, Phys. Rev. Lett. **53**, 1951 (1984).

[2] D. Levine and P. J. Steinhardt, Quasicrystals: A New Class of Ordered Structures, Phys. Rev. Lett. **53**, 2477 (1984).

[3] C. Janot, *Quasicrystals: A Primer* (Oxford University Press, Oxford, 2012).

[4] Z. V. Vardeny, A. Nahata, and A. Agrawal, Optics of photonic quasicrystals, Nat. Photonics **7**, 177 (2013).

[5] L. Dal Negro, *Optics in Aperiodic Structures: Fundamentals and Device Applications* (CRC, Boca Raton, FL, 2014).

[6] T. Janssen, G. Chapuis, and M. De Boissieu, *Aperiodic Crystals From Modulated Phases to Quasicrystalss* (Oxford University Press, Oxford, 2007).

[7] P. W. Anderson, Absence of diffusion in certain random lattices, Phys. Rev. **109**, 1492 (1958).

[8] L. Levi, M. Rechtsman, B. Freedman, T. Schwartz, O. Manela, and M. Segev, Disorder-enhanced transport in photonic quasicrystals, Science **332**, 1541 (2011).

[9] M. Segev, Y. Silberberg, and D. N. Christodoulides, Anderson localization of light, Nat. Photonics **7**, 197 (2013).

[10] J. A. Kromer, M. Schmiedeberg, J. Roth, and H. Stark, What Phasons Look Like: Particle Trajectories in a Quasicrystalline Potential, Phys. Rev. Lett. **108**, 218301 (2012).

[11] A. Jagannathan, The Fibonacci quasicrystal: Case study of hidden dimensions and multifractality, Rev. Mod. Phys. **93**, 045001 (2021).

[12] E. Maciá, The role of aperiodic order in science and technology, Rep. Prog. Phys. **69**, 397 (2006).

[13] J. E. S. Socolar, T. C. Lubensky, and P. J. Steinhardt, Phonons, phasons, and dislocations in quasicrystals, Phys. Rev. B **34**, 3345 (1986).

[14] M. de Boissieu, Phonons, phasons and atomic dynamics in quasicrystals, Chem. Soc. Rev. **41**, 6778 (2012).

[15] J. Wolny, I. Buganski, and R. Strzalka, Phononic and phasonic Debye-Waller factors for 1D quasicrystals, Acta Phys. Pol. A **130**, 836 (2016).

[16] B. Freedman, R. Lifshitz, J. W. Fleischer, and M. Segev, Phason dynamics in nonlinear photonic quasicrystals, Nat. Mater. **6**, 776 (2007).

[17] M. A. Bandres, M. C. Rechtsman, and M. Segev, Topological Photonic Quasicrystals: Fractal Topological Spectrum and Protected Transport, Phys. Rev. X **6**, 011016 (2016).

[18] C. H. Chen, R. Z. Qiu, C. H. Chang, and W. J. Hsueh, Strongly localized modes in one-dimensional defect-free magnonic quasicrystals, AIP Adv. **4**, 087102 (2014).

[19] J. Rychły, J. W. Kłos, M. Mruczkiewicz, and M. Krawczyk, Spin waves in one-dimensional bicomponent magnonic quasicrystals, Phys. Rev. B **92**, 054414 (2015).

[20] J. Ding, M. Kostylev, and A. O. Adeyeye, Magnonic Crystal as a Medium with Tunable Disorder on a Periodical Lattice, Phys. Rev. Lett. **107**, 047205 (2011).

[21] M. Evers, C. A. Müller, and U. Nowak, Spin-wave localization in disordered magnets, Phys. Rev. B **92**, 014411 (2015).

[22] M. Evers, C. A. Müller, and U. Nowak, Weak localization of magnons in chiral magnets, Phys. Rev. B **97**, 184423 (2018).

[23] P. Buczek, S. Thomas, A. Marmodoro, N. Buczek, X. Zubizarreta, M. Hoffmann, T. Balashov, W. Wulfhekel, K. Zakeri, and A. Ernst, Spin waves in disordered materials, J. Condens. Matter Phys. **30**, 423001 (2018).

[24] R. A. Gallardo, T. Schneider, A. Roldán-Molina, M. Langer, A. S. Núñez, K. Lenz, J. Lindner, and P. Landeros, Symmetry and localization properties of defect modes in magnonic superlattices, Phys. Rev. B **97**, 174404 (2018).

[25] V. S. Tkachenko, V. V. Kruglyak, and A. N. Kuchko, Spectrum and reflection of spin waves in magnonic crystals with different interface profiles, Phys. Rev. B **81**, 024425 (2010).

[26] V. V. Kruglyak, M. L. Sokolovskii, V. S. Tkachenko, and A. N. Kuchko, Spin-wave spectrum of a magnonic crystal with an isolated defect, J. Appl. Phys. **99**, 08C906 (2006).

[27] H. Yang, G. Yun, and Y. Cao, Point defect states of exchange spin waves in all-ferromagnetic two-dimensional magnonic crystals, J. Appl. Phys. **111**, 013908 (2012).

[28] H. Yang, G. Yun, and Y. Cao, Coupling characteristics of point defects modes in two-dimensional magnonic crystals, J. Appl. Phys. **112**, 103911 (2012).

[29] H. Yang, G. Yun, and Y. Cao, Effects of point defect shapes on defect modes in two-dimensional magnonic crystals, J. Magn. Magn. Mater. **356**, 32 (2014).

[30] D. Xing, H. Yang, and Y. Cao, Waveguide properties in two-dimensional magnonic crystals with line defects, J. Magn. Magn. Mater. **377**, 286 (2015).

[31] K. Baumgaertl, S. Watanabe, and D. Grundler, Phase control of spin waves based on a magnetic defect in a one-dimensional magnonic crystal, Appl. Phys. Lett. **112**, 142405 (2018).

[32] Y. E. Kraus and O. Zilberberg, Topological Equivalence between the Fibonacci Quasicrystal and the Harper Model, Phys. Rev. Lett. **109**, 116404 (2012).

[33] A. Dareau, E. Levy, M. B. Aguilera, R. Bouganne, E. Akkermans, F. Gerbier, and J. Beugnon, Revealing the Topology of Quasicrystals with a Diffraction Experiment, Phys. Rev. Lett. **119**, 215304 (2017).

[34] E. Levy, A. Barak, A. Fisher, and E. Akkermans, Topological properties of Fibonacci quasicrystals: A scattering analysis of Chern numbers, arXiv:1509.04028.

[35] G. G. Naumis, Phason hierarchy and electronic stability of quasicrystals, Phys. Rev. B **71**, 144204 (2005).

[36] Z. K. Wang, V. L. Zhang, H. S. Lim, S. C. Ng, M. H. Kuok, S. Jain, and A. O. Adeyeye, Observation of frequency band gaps in a one-dimensional nanostructured magnonic crystal, Appl. Phys. Lett. **94**, 083112 (2009).

[37] S. Choudhury, S. Saha, R. Mandal, S. Barman, Y. Otani, and A. Barman, Shape- and interface-induced control of spin dynamics of two-dimensional bicomponent magnonic crystals, ACS Appl. Mater. Interfaces **8**, 18339 (2016).

[38] A. Wawro, Z. Kurant, M. Jakubowski, M. Tekielak, A. Pietruczik, R. Böttger, and A. Maziewski, Magnetic Properties of Coupled Co/Mo/Co Structures Tailored by Ion Irradiation, Phys. Rev. Applied **9**, 014029 (2018).

[39] L. Frąckowiak, P. Kuświk, G. D. Chaves-O'Flynn, M. Urbaniak, M. Matczak, P. P. Michałowski, A. Maziewski, M. Reginka, A. Ehresmann, and F. Stobiecki, Magnetic Domains without Domain Walls: A Unique Effect of He$^+$ Ion Bombardment in Ferrimagnetic Tb/Co Films, Phys. Rev. Lett. **124**, 047203 (2020).

[40] P. Graczyk, M. Krawczyk, S. Dhuey, W.-G. Yang, H. Schmidt, and G. Gubbiotti, Magnonic band gap and mode hybridization in continuous permalloy films induced by vertical dynamic coupling with an array of permalloy ellipses, Phys. Rev. B **98**, 174420 (2018).

[41] C. Liu, J. Chen, F. Heimbach, H. Yu, Y. Xiao, J. Hu, M. Liu, H. Chang, T. Stueckler, S. Tu, Y. Zhang, Y. Zhang, P. Gao, Z. Liao, D. Yu, K. Xia, N. Lei, W. Zhao, and M. Wu, Long-distance propagation of short-wavelength spin waves, Nat. Commun. **9**, 738 (2018).

[42] C. L. Chang, S. Mieszczak, M. Zelent, V. Besse, U. Martens, R. R. Tamming, J. Janusonis, P. Graczyk, M. Münzenberg, J. W. Kłos, and R. I. Tobey, Driving Magnetization Dynamics in an on-Demand Magnonic Crystal via the Magnetoelastic Interactions, Phys. Rev. Applied **10**, 064051 (2018).

[43] R. F. L. Evans, D. Hinzke, U. Atxitia, U. Nowak, R. W. Chantrell, and O. Chubykalo-Fesenko, Stochastic form of the Landau-Lifshitz-Bloch equation, Phys. Rev. B **85**, 014433 (2012).

[44] M. Krawczyk, M. L. Sokolovskyy, J. W. Kłos, and S. Mamica, On the formulation of the exchange field in the Landau-Lifshitz

[45] J. W. Kłos, M. Krawczyk, and M. Sokolovskyy, Bulk and edge modes in two-dimensional magnonic crystal slab, J. Appl. Phys. **109**, 07D311 (2011).

[46] S. Mieszczak and J. W. Kłos, Interface modes in planar one-dimensional magnonic crystals, Sci. Rep. **12**, 11335 (2022).

[47] S. Pan, J. W. Kłos, S. Mieszczak, A. Barman, and M. Krawczyk, Spin waves in periodic antidot waveguide of complex base, J. Phys. D **50**, 275003 (2017).

[48] J. Rychły, S. Mieszczak, and J. Kłos, Spin waves in planar quasicrystal of penrose tiling, J. Magn. Magn. Mater. **450**, 18 (2018).

[49] S. Watanabe, V. S. Bhat, K. Baumgaertl, and D. Grundler, Direct observation of worm-like nanochannels and emergent magnon motifs in artificial ferromagnetic quasicrystals, Adv. Funct. Mater. **30**, 2001388 (2020).

[50] P. Vignolo, M. Bellec, J. Böhm, A. Camara, J.-M. Gambaudo, U. Kuhl, and F. Mortessagne, Energy landscape in a penrose tiling, Phys. Rev. B **93**, 075141 (2016).

[51] L. van Hove, The occurrence of singularities in the elastic frequency distribution of a crystal, Phys. Rev. **89**, 1189 (1953).

[52] N. W. Ashcroft and D. N. Mermin, *Solid State Physics* (Harcourt College Publishers, San Diego, CA, 1976).

[53] F. Lisiecki, J. Rychły, P. Kuświk, H. Głowiński, J. W. Kłos, F. Groß, I. Bykova, M. Weigand, M. Zelent, E. J. Goering, G. Schütz, G. Gubbiotti, M. Krawczyk, F. Stobiecki, J. Dubowik, and J. Gräfe, Reprogrammability and Scalability of Magnonic Fibonacci Quasicrystals, Phys. Rev. Applied **11**, 054003 (2019).

[54] B. A. Kalinikos and A. N. Slavin, Theory of dipole-exchange spin wave spectrum for ferromagnetic films with mixed exchange boundary conditions, J. Phys.: Condens. Matter **19**, 7013 (1986).

[55] M. E. Limonov and R. E. De La Rue, *Optical Properties of Photonic Structures* (CRC, Boca Raton, FL, 2012).

[56] B. Mirbach and H. J. Korsch, Phase Space Entropy and Global Phase Space Structures of (Chaotic) Quantum Systems, Phys. Rev. Lett. **75**, 362 (1995).

[57] B. Mirbach and H. J. Korsch, A generalized entropy measuring quantum localization, Ann. Phys. **265**, 80 (1998).

[58] M. Kohmoto, B. Sutherland, and C. Tang, Critical wave functions and a cantor-set spectrum of a one-dimensional quasicrystal model, Phys. Rev. B **35**, 1020 (1987).

[59] E. Maciá and F. Domínguez-Adame, Physical Nature of Critical Wave Functions in Fibonacci Systems, Phys. Rev. Lett. **76**, 2957 (1996).

[60] L. Dal Negro, C. J. Oton, Z. Gaburro, L. Pavesi, P. Johnson, A. Lagendijk, R. Righini, M. Colocci, and D. S. Wiersma, Light Transport through the Band-Edge States of Fibonacci Quasicrystals, Phys. Rev. Lett. **90**, 055501 (2003).

[61] H. Aynaou, A. Mouadili, N. Ouchani, E. H. El Boudouti, A. Akjouj, and B. Djafari-Rouhani, Scaling law, confined and surface modes in photonic Fibonacci stub structures: Theory and experiment, Appl. Sci. **10**, 7767 (2020).

[62] S. Watanabe, V. S. Bhat, K. Baumgaertl, M. Hamdi, and D. Grundler, Direct observation of multiband transport in magnonic penrose quasicrystals via broadband and phase-resolved spectroscopy, Sci. Adv. **7**, eabg3771 (2021).

Chapter 5

Summary

The first magnonic structures could be dated to the 70ties of XX century when periodic structures were fabricated in micrometers dimensions. Although the pioneering papers are dated 50 years ago, not even mentioning the real beginning of the spin waves, that is 100 years old, I have a feeling that this is just beginning. During my short scientific journey, I already could notice several ideas like skyrmions, topological states, and neuromorphic computing that boost the interests of the field and can potentially lead to revolution. And I believe that more will come. In my research, I focused on the most fundamental properties in magnonic systems, propagation, and localization. I investigated a variety of systems, however, the common part was always to describe them from this point of view.

The thesis presents the results of the theoretical and numerical studies. They are preceded by Chapter 2, which contain a basic description of the terms that can help in understating the research, and Chapter 3 which explains the numerical tools used to obtain outcomes. The results were published in peer-reviewed journals and were incorporated into the thesis, in Chapter 4. For each paper: P1-P4, one subsection is devoted. P1 is the work written with the experimental team. We discuss the role of SW localization within the magnonic crystal. SW is induced by magnetoelastic coupling with SAW and due to nonuniformity in the internal field, the profile of SW is accordingly modified which is reflected in the strength of magnetoelastic coupling. P2 was written with the theoretical team. The paper is devoted to studies on SW propagation in the multimode waveguide that has a bent. Based on analytical and numerical works, we propose a method for guiding the SW through a curved section that would keep the coherence of the signal. We exploited the idea of graded-index elements to model the material parameter of the area and tilt the wavefront of the SW. In P3 are derived the existence conditions for interface mode between two semi-infinite magnonic crystals. Theoretical work is based on the work of Zak and is supported by numerical calculations. We comprehensively investigated the impact of exchange and dipolar interaction on the results

as well as structural parameters. P4 discusses the role of disorder in the quasicrystal. We introduce disorder in the form of phasonic defects, swapping constituent elements at specific positions. Investigating the different levels of disorder as well as the different realizations of disorder, we could qualitatively describe the evolution of the spectrum, and how band gaps are affected. Considering specific configuration, we could track the evolution of the mode, and in particular, speculate about the localization.

Even though my research was concentrated on the propagation and localization of SW, the investigated system was rather diverse. I think that the studies on considered systems and their properties definitely needs continuation. At the end of my studies, I was involved in the project "Anderson localization of spin waves in magnonic nanostructures", grant no. 2020/36/T/ST3/00542. This research was financed by the National Science Centrer, under the ETIUDA program. In this project, I cooperate with prof. Dirk Grundler, Andrea Mucchietto and Dr. Mingran Xu from EPFL in Lausanne. Our goal is to experimentally demonstrate Anderson localization, in the magnonic system. For the prototype structure, we consider decorated film, where the internal field is modified by a magnetic element on the top. We want to consider transverse Anderson localization, in the analogy to photonics, where SW is propagating along the coupled waveguides. The research is still in the preliminary stage, there are challenges that need to be addressed, but I am sure there will exciting outcomes.

The thesis addressed selected problems related to the spin wave localization and propagation in magnonic structures. The presented research demonstrate the potential for wave processing in nanostructures where the unique properties of spin waves can be used. I hope that my work will encourage other for the studies in this field.

References

[1] Abbas, K. (2020). *Handbook Of Digital CMOS Technology, Circuits, and Systems*. Springer.

[2] Abrahams, E. (2010). *50 Years of Anderson Localization*. World Scientific.

[3] Anderson, P. W. (1958). Absence of diffusion in certain random lattices. *Physical Review*, 109:1492–1505.

[4] Andreoni, W. and Yip, S. (2020). *Handbook of Materials Modeling, Applications: Current and Emerging Materials*. Springer International Publishing.

[5] Ashcroft, N. W. and Mermin, D. N. (1976). *Solid State Physics*. Harcourt College Publishers.

[6] Babu, N. K. P., Trzaskowska, A., Graczyk, P., Centała, G., Mieszczak, S., Głowiński, H., Zdunek, M., Mielcarek, S., and Kłos, J. W. (2021). The interaction between surface acoustic waves and spin waves: The role of anisotropy and spatial profiles of the modes. *Nano Letters*, 21(2):946–951.

[7] Banerjee, C., Gruszecki, P., Klos, J. W., Hellwig, O., Krawczyk, M., and Barman, A. (2017). Magnonic band structure in a Co/Pd tripe domain system investigated by Brillouin light scattering and micromagnetic simulations. *Physical Review B*, 96:024421.

[8] Bardeen, J. and Brattain, W. H. (1948). The transistor, a semi-conductor triode. *Physical Review*, 74:230–231.

[9] Barman, A., Gubbiotti, G., Ladak, S., Adeyeye, A. O., Krawczyk, M., Gräfe, J., Adelmann, C., Cotofana, S., Naeemi, A., Vasyuchka, V. I., Hillebrands, B., Nikitov, S. A., Yu, H., Grundler, D., Sadovnikov, A. V., Grachev, A. A., Sheshukova, S. E., Duquesne, J.-Y., Marangolo, M., Csaba, G., Porod, W., Demidov, V. E., Urazhdin, S., Demokritov, S. O., Albisetti, E., Petti, D., Bertacco, R., Schultheiss, H., Kruglyak, V. V., Poimanov, V. D., Sahoo, S., Sinha, J., Yang, H., Münzenberg, M., Moriyama, T., Mizukami, S., Landeros, P., Gallardo, R. A., Carlotti, G., Kim, J.-V., Stamps, R. L., Camley, R. E., Rana, B., Otani, Y., Yu, W., Yu, T., Bauer, G. E. W., Back, C., Uhrig, G. S., Dobrovolskiy, O. V., Budinska, B., Qin, H., van Dijken, S., Chumak, A. V., Khitun, A., Nikonov, D. E., Young, I. A., Zingsem, B. W., and Winklhofer, M. (2021). The 2021 magnonics roadmap. *Journal of Physics: Condensed Matter*, 33(41):413001.

[10] Bar'yakhtar, V. G. and Ivanov, B. A. (2015). The Landau-Lifshitz equation: 80 years of history, advances, and prospects. *Low Temperature Physics*, 41(9):663–669.

[11] Baumgaertl, K., Watanabe, S., and Grundler, D. (2018). Phase control of spin waves based on a magnetic defect in a one-dimensional magnonic crystal. *Applied Physics Letters*, 112:142405.

[12] Berry, M. V. (1984). Quantal phase factors accompanying adiabatic changes. *Proceedings of the Royal Society of London. A. Mathematical and Physical Sciences*, 392(1802):45–57.

[13] Bessonov, V. D., Mruczkiewicz, M., Gieniusz, R., Guzowska, U., Maziewski, A., Stognij, A. I., and Krawczyk, M. (2015). Magnonic band gaps in YIG-based one-dimensional magnonic crystals: An array of grooves versus an array of metallic stripes. *Physical Review B*, 91:104421.

[14] Bloch, F. (1929). Über die Quantenmechanik der Elektronen in Kristallgittern. *Zeitschrift für Physik*, 52(7):555–600.

[15] Bloch, F. (1930). Zur Theorie des Ferromagnetismus. *Zeitschrift für Physik*, 61(3):206–219.

[16] Brown, W. F. (1963). *Micromagnetics*. John Wiley and Sons, New Youk.

[17] Campbell, C. (1998). *Surface Acoustic Wave Devices for Mobile and Wireless Communications*. Academic Press.

[18] Centała, G., Sokolovskyy, M. L., Davies, C. S., Mruczkiewicz, M., Mamica, S., Rychły, J., Kłos, J. W., Kruglyak, V. V., and Krawczyk, M. (2019). Influence of nonmagnetic dielectric spacers on the spin-wave response of one-dimensional planar magnonic crystals. *Physical Review B*, 100:224428.

[19] Chumak, A. V., Kabos, P., Wu, M., Abert, C., Adelmann, C., Adeyeye, A. O., Åkerman, J., Aliev, F. G., Anane, A., Awad, A., Back, C. H., Barman, A., Bauer, G. E. W., Becherer, M., Beginin, E. N., Bittencourt, V. A. S. V., Blanter, Y. M., Bortolotti, P., Boventer, I., Bozhko, D. A., Bunyaev, S. A., Carmiggelt, J. J., Cheenikundil, R. R., Ciubotaru, F., Cotofana, S., Csaba, G., Dobrovolskiy, O. V., Dubs, C., Elyasi, M., Fripp, K. G., Fulara, H., Golovchanskiy, I. A., Gonzalez-Ballestero, C., Graczyk, P., Grundler, D., Gruszecki, P., Gubbiotti, G., Guslienko, K., Haldar, A., Hamdioui, S., Hertel, R., Hillebrands, B., Hioki, T., Houshang, A., Hu, C.-M., Huebl, H., Huth, M., Iacocca, E., Jungfleisch, M. B., Kakazei, G. N., Khitun, A., Khymyn, R., Kikkawa, T., Kläui, M., Klein, O., Kłos, J. W., Knauer, S., Koraltan, S., Kostylev, M., Krawczyk, M., Krivorotov, I. N., Kruglyak, V. V., Lachance-Quirion, D., Ladak, S., Lebrun, R., Li, Y., Lindner, M., Macêdo, R., Mayr, S., Melkov, G. A., Mieszczak, S., Nakamura, Y., Nembach, H. T., Nikitin, A. A., Nikitov, S. A., Novosad, V., Otálora, J. A., Otani, Y., Papp, A., Pigeau, B., Pirro, P., Porod, W., Porrati, F., Qin, H., Rana, B., Reimann, T., Riente, F., Romero-Isart, O., Ross, A., Sadovnikov, A. V., Safin, A. R., Saitoh, E., Schmidt, G., Schultheiss, H., Schultheiss, K., Serga, A. A., Sharma, S., Shaw, J. M., Suess, D., Surzhenko, O., Szulc, K., Taniguchi, T., Urbánek, M., Usami, K., Ustinov, A. B., van der Sar, T., van Dijken, S., Vasyuchka, V. I., Verba, R., Kusminskiy, S. V., Wang, Q., Weides, M., Weiler, M., Wintz, S., Wolski, S. P., and Zhang, X. (2022). Advances in magnetics roadmap on spin-wave computing. *IEEE Transactions on Magnetics*, 58(6):1–72.

[20] Chumak, A. V., Serga, A. A., and Hillebrands, B. (2014). Magnon transistor for all-magnon data processing. *Nature Communications*, 5:4700.

[21] Chumak, A. V., Vasyuchka, V. I., Serga, A. A., and Hillebrands, B. (2015). Magnon spintronics. *Nature Physics*, 11(6):453–461.

[22] Damon, R. and Eshbach, J. (1961). Magnetostatic modes of a ferromagnet slab. *Journal of Physics and Chemistry of Solids*, 19:308–320.

[23] Daw, R. (2014). What is a crystal? *Nature*, 511(7509):18–19.

[24] Díaz, S. A., Klinovaja, J., and Loss, D. (2019). Topological magnons and edge states in antiferromagnetic skyrmion crystals. *Physical Review Letters*, 122:187203.

[25] Dieny, B., Prejbeanu, I. L., Garello, K., Gambardella, P., Freitas, P., Lehndorff, R., Raberg, W., Ebels, U., Demokritov, S. O., Akerman, J., Deac, A., Pirro, P., Adelmann, C., Anane, A., Chumak, A. V., Hirohata, A., Mangin, S., Valenzuela, S. O., Onbaşlı, M. C., d'Aquino, M., Prenat, G., Finocchio, G., Lopez-Diaz, L., Chantrell, R., Chubykalo-Fesenko, O., and Bortolotti, P. (2020). Opportunities and challenges for spintronics in the microelectronics industry. *Nature Electronics*, 3(8):446–459.

[26] Dreher, L., Weiler, M., Pernpeintner, M., Huebl, H., Gross, R., Brandt, M. S., and Goennenwein, S. T. B. (2012). Surface acoustic wave driven ferromagnetic resonance in nickel thin films: Theory and experiment. *Physical Review B*, 86:134415.

[27] Ellis, M. O. A., Evans, R. F. L., Ostler, T. A., Barker, J., Atxitia, U., Chubykalo-Fesenko, O., and Chantrell, R. W. (2015). The Landau–Lifshitz equation in atomistic models. *Low Temperature Physics*, 41(9):705–712.

[28] Fert, A., Reyren, N., and Cros, V. (2017). Magnetic skyrmions: advances in physics and potential applications. *Nature Reviews Materials*, 2(7):1–15.

[29] Fischer, P., Sanz-Hernández, D., Streubel, R., and Fernández-Pacheco, A. (2020). Launching a new dimension with 3D magnetic nanostructures. *APL Materials*, 8(1):010701.

[30] Floquet, G. (1883). Sur les équations différentielles linéaires à coefficients périodiques. *Annales scientifiques de l'École Normale Supérieure*, 2e série, 12:47–88.

[31] Frackowiak, L., Kuświk, P., Chaves-O'Flynn, G. D., Urbaniak, M., Matczak, M., Michałowski, P. P., Maziewski, A., Reginka, M., Ehresmann, A., and Stobiecki, F. (2020). Magnetic domains without domain walls: A unique effect of He^+ ion bombardment in ferrimagnetic Tb/Co films. *Physical Review Letters*, 124:47203.

[32] Gallardo, R. A., Schneider, T., Roldán-Molina, A., Langer, M., Núñez, A. S., Lenz, K., Lindner, J., and Landeros, P. (2018). Symmetry and localization properties of defect modes in magnonic superlattices. *Physical Review B*, 97:174404.

[33] Garcia-Sanchez, F., Borys, P., Soucaille, R., Adam, J.-P., Stamps, R. L., and Kim, J.-V. (2015). Narrow magnonic waveguides based on domain walls. *Physical Review Letters*, 114:247206.

[34] Graczyk, P., Krawczyk, M., Dhuey, S., Yang, W.-G., Schmidt, H., and Gubbiotti, G. (2018). Magnonic band gap and mode hybridization in continuous permalloy films induced by vertical dynamic coupling with an array of permalloy ellipses. *Physical Review B*, 98:174420.

[35] Graczyk, P., Kłos, J., and Krawczyk, M. (2017). Broadband magnetoelastic coupling in magnonic-phononic crystals for high-frequency nanoscale spin-wave generation. *Physical Review B*, 95:104425.

[36] Gramotnev, D. K. and Bozhevolnyi, S. I. (2010). Plasmonics beyond the diffraction limit. *Nature Photonics 2010 4:2*, 4:83–91.

[37] Gubbiotti, G. (2019). *Three-Dimensional Magnonics: Layered, Micro- and Nanostructures*. Jenny Stanford Publishing.

[38] Gurevich, A. G. and Melkov, G. A. (1996). *Magnetization Oscillations and Waves*. CRC Press.

[39] Guslienko, K. Y., Demokritov, S. O., Hillebrands, B., and Slavin, A. N. (2002a). Effective dipolar boundary conditions for dynamic magnetization in thin magnetic stripes. *Physical Review B*, 66:132402.

[40] Guslienko, K. Y., Ivanov, B. A., Novosad, V., Otani, Y., Shima, H., and Fukamichi, K. (2002b). Eigenfrequencies of vortex state excitations in magnetic submicron-size disks. *Journal of Applied Physics*, 91:8037.

[41] Guslienko, K. Y. and Slavin, A. N. (2005). Boundary conditions for magnetization in magnetic nanoelements. *Physical Review B*, 72:014463.

[42] Haldar, A. and Adeyeye, A. O. (2021). Functional magnetic waveguides for magnonics. *Applied Physics Letters*, 119(6):060501.

[43] Heinz, B., Brächer, T., Schneider, M., Wang, Q., Lägel, B., Friedel, A. M., Breitbach, D., Steinert, S., Meyer, T., Kewenig, M., Dubs, C., Pirro, P., and Chumak, A. V. (2020). Propagation of spin-wave packets in individual nanosized yttrium iron garnet magnonic conduits. *Nano Letters*, 20:4220–4227.

[44] Heisenberg, W. (1926). Mehrkörperproblem und Resonanz in der Quantenmechanik. *Zeitschrift für Physik*, 38(6):411–426.

[45] Henry, Y., Stoeffler, D., Kim, J.-V., and Bailleul, M. (2019). Unidirectional spin-wave channeling along magnetic domain walls of Bloch type. *Physical Review B*, 100:24416.

[46] Hirohata, A., Yamada, K., Nakatani, Y., Prejbeanu, L., Diény, B., Pirro, P., and Hillebrands, B. (2020). Review on spintronics: Principles and device applications. *Journal of Magnetism and Magnetic Materials*, 509:166711.

[47] Hu, H., Strybulevych, A., Page, J. H., Skipetrov, S. E., and Van Tiggelen, B. A. (2008). Localization of ultrasound in a three-dimensional elastic network. *Nature Physics*, 4:945–948.

[48] Jackson, J. D. (1998). *Classical Electrodynamics*. Wiley.

[49] Jagannathan, A. (2021). The Fibonacci quasicrystal: Case study of hidden dimensions and multifractality. *Reviews Modern Physics*, 93:045001.

[50] Janot, C. (1992). *Quasicrystals - A Primer*. Clarendon Press Oxford.

[51] Janutka, A. (2021). Analytical description of domain wall propagation in cylindrical nanowires. *IEEE Magnetics Letters*, 12:1–5.

[52] Janušonis, J., Jansma, T., Chang, C. L., Liu, Q., Gatilova, A., Lomonosov, A. M., Shalagatskyi, V., Pezeril, T., Temnov, V. V., and Tobey, R. I. (2016). Transient Grating Spectroscopy in Magnetic Thin Films: Simultaneous Detection of Elastic and Magnetic Dynamics. *Scientific Reports*, 6(1):29143.

[53] Joannopoulos, J. D., Johnson, S. G., Winn, J. N., and Meade, R. D. (2008). *Photonic Crystals: Molding the Flow of Light*. Princeton University Press.

[54] Kaczér, J. and Murtinová, L. (1974). On the demagnetizing energy of periodic magnetic distributions. *physica status solidi (a)*, 23(1):79–86.

[55] Kalinikos, B. A. and Slavin, A. N. (1986). Theory of dipole-exchange spin wave spectrum for ferromagnetic films with mixed exchange boundary conditions. *Journal of Physics C: Solid State Physics*, 19(35):7013–7033.

[56] Kalinikos, B. A. and Ustinov, A. B. (2013). Nonlinear spin waves in magnetic films and structures: Physics and devices. In Wu, M. and Hoffmann, A., editors, *Recent Advances in Magnetic Insulators – From Spintronics to Microwave Applications*, volume 64 of *Solid State Physics*, pages 193–235. Academic Press.

[57] Khitun, A., Bao, M., and Wang, K. L. (2008). Spin wave magnetic nanofabric: A new approach to spin-based logic circuitry. *IEEE Transactions on Magnetics*, 44(9):2141–2152.

[58] Kim, J.-W., Vomir, M., and Bigot, J.-Y. (2012). Ultrafast magnetoacoustics in nickel films. *Physical Review Letters*, 109:166601.

[59] Kittel, C. (1948). On the theory of ferromagnetic resonance absorption. *Physical Review*, 73:155–161.

[60] Kittel, C. (2004). *Introduction to Solid State Physics*. John Wiley and Sons.

[61] Kohn, W. (1959). Analytic properties of Bloch waves and Wannier functions. *Physical Review*, 115:809–821.

[62] Krawczyk, M. and Grundler, D. (2014). Review and prospects of magnonic crystals and devices with reprogrammable band structure. *Journal of Physics: Condensed Matter*, 26(12):123202.

[63] Krawczyk, M., Klos, J., Sokolovskyy, M. L., and Mamica, S. (2010). Materials optimization of the magnonic gap in three-dimensional magnonic crystals with spheres in hexagonal structure. *Journal of Applied Physics*, 108(9):093909.

[64] Krawczyk, M., Mamica, M., Mruczkiewicz, M., Kłos, J. W., Tacchi, S., M., M., Gubbiotti, G., Duerr, G., and Grundler, D. (2013). Magnonic band structures in two-dimensional bi-component magnonic crystals with in-plane magnetization. *Journal of Physics D: Applied Physics*, 46:495003.

[65] Krawczyk, M. and Puszkarski, H. (2008). Plane-wave theory of three-dimensional magnonic crystals. *Physical Review B*, 77:054437.

[66] Krawczyk, M., Sokolovskyy, M. L., Kłos, J. W., and Mamica, S. (2012). On the formulation of the exchange field in the Landau-Lifshitz equation for spin-wave calculation in magnonic crystals. *Advances in Condensed Matter Physics*, 2012(764783):14.

[67] Kruglyak, V. V., Demokritov, S. O., and Grundler, D. (2010). Magnonics. *Journal of Physics D: Applied Physics*, 43:264001.

[68] Krupinski, M., Sobieszczyk, P., Zieliński, P., and Marszałek, M. (2019). Magnetic reversal in perpendicularly magnetized antidot arrays with intrinsic and extrinsic defects. *Scientific Reports 2019 9:1*, 9:1–11.

[69] Kłos, J. W., Krawczyk, M., and Sokolovskyy, M. (2011). Bulk and edge modes in two-dimensional magnonic crystal slab. *Journal of Applied Physics*, 109(7):07D311.

[70] Kłos, J. W. and Tkachenko, V. S. (2013). Symmetry-related criteria for the occurrence of defect states in magnonic superlattices. *Journal of Applied Physics*, 113(13):133907.

[71] Lahini, Y., Avidan, A., Pozzi, F., Sorel, M., Morandotti, R., Christodoulides, D. N., and Silberberg, Y. (2008). Anderson localization and nonlinearity in one-dimensional disordered photonic lattices. *Physical Review Letters*, 100:13906.

[72] Lakshmanan, M. (2011). The fascinating world of the Landau-Lifshitz-Gilbert equation: an overview. *Philosophical Transactions: Mathematical, Physical and Engineering Sciences*, 369(1939):1280–1300.

[73] Landau, L. D. and Lifshitz, E. (1935). On the theory of the dispersion of magnetic permeability in ferromagnetic bodies. *Physikalische Zeitschrift der Sowjetunion*, 8:153.

[74] Langer, M., Gallardo, R. A., Schneider, T., Stienen, S., Roldán-Molina, A., Yuan, Y., Lenz, K., Lindner, J., Landeros, P., and Fassbender, J. (2019). Spin-wave modes in transition from a thin film to a full magnonic crystal. *Physical Review B*, 99:24426.

[75] Langer, M., Roder, F., Gallardo, T., Schneider, S., Steinen, C., Gatel, R., Hubner, R., Bischoff, L., Lenz, K., Lindner, J., Landeros, P., and J., F. (2017). The role of internal demagnetizing field for the dynamics of a magnonic crystal. *Physical Review B*, 95:184405.

[76] Leliaert, J. and Mulkers, J. (2019). Tomorrow's micromagnetic simulations. *Journal of Applied Physics*, 125(18):180901.

[77] Lenk, B., Ulrichs, H., Garbs, F., and Münzenberg, M. (2011). The building blocks of magnonics. *Physics Reports*, 507:107 – 136.

[78] Li, Z., Qiao, Z., and Tang, T. (2018). *Numerical Solution of Differential Equations: Introduction to Finite Difference and Finite Element Methods.* Cambridge University Press, Cambridge.

[79] Lisiecki, F., Rychły, J., Kuświk, P., Głowiński, H., Kłos, J. W., Groß, F., Bykova, I., Weigand, M., Zelent, M., Goering, E. J., Schütz, G., Gubbiotti, G., Krawczyk, M., Stobiecki, F., Dubowik, J., and Gräfe, J. (2019a). Reprogrammability and scalability of magnonic Fibonacci quasicrystals. *Physical Review Applied*, 11:054003.

[80] Lisiecki, F., Rychły, J., Kuświk, P., Głowiński, H., Kłos, J. W., Groß, F., Träger, N., Bykova, I., Weigand, M., Zelent, M., Goering, E. J., Schütz, G., Krawczyk, M., Stobiecki, F., Dubowik, J., and Gräfe, J. (2019b). Magnons in a quasicrystal: Propagation, extinction, and localization of spin waves in Fibonacci structures. *Physical Review Applied*, 11:054061.

[81] Lord Rayleigh, J. R. S. (1887). On the maintenance of vibrations by forces of double frequency, and on the propagation of waves through a medium endowed with a periodic structure. *The London, Edinburgh, and Dublin Philosophical Magazine and Journal of Science*, 24(147):145–159.

[82] Maciá, E. (1999). Physical nature of critical modes in Fibonacci quasicrystals. *Physical Review B*, 60:10032–10036.

[83] Mack, C. A. (2011). Fifty years of moore's law. *IEEE Transactions on Semiconductor Manufacturing*, 24(2):202–207.

[84] Mafi, A. (2015). Transverse Anderson localization of light: a tutorial. *Advances in Optics and Photonics*, 7:459–515.

[85] Mahmoud, A., Ciubotaru, F., Vanderveken, F., Chumak, A. V., Hamdioui, S., Adelmann, C., and Cotofana, S. (2020). Introduction to spin wave computing. *Journal of Applied Physics*, 128(16):161101.

[86] Mamica, S., Krawczyk, M., and Grundler, D. (2019). Nonuniform spin-wave softening in two-dimensional magnonic crystals as a tool for opening omnidirectional magnonic band gaps. *Physical Review Applied*, 11:54011.

[87] Manzin, A., Barrera, G., Celegato, F., Coïsson, M., and Tiberto, P. (2016). Influence of lattice defects on the ferromagnetic resonance behaviour of 2D magnonic crystals. *Scientific Reports*, 6:11.

[88] Markov, I. L. (2014). Limits on fundamental limits to computation. *Nature*, 512(7513):147–154.

[89] Mulkers, J., Van Waeyenberge, B., and Milošević, M. V. (2018). Tunable Snell's law for spin waves in heterochiral magnetic films. *Physical Review B*, 97:104422.

[90] Pan, S., Kłos, J. W., Mieszczak, S., Barman, A., and Krawczyk, M. (2017). Spin waves in periodic antidot waveguide of complex base. *Journal of Physics D: Applied Physics*, 50(27):275003.

[91] Papp, A., Csaba, G., and Porod, W. (2021). Characterization of nonlinear spin-wave interference by reservoir-computing metrics. *Applied Physics Letters*, 119(11):112403.

[92] Pozar, D. M. (2011). *Microwave Engineering*. John Wiley and Sons.

[93] Qin, H., Holländer, R. B., Flajšman, L., and van Dijken, S. (2022). Low-loss nanoscopic spin-wave guiding in continuous yttrium iron garnet films. *Nano Letters*.

[94] Rado, G. T. and Weertman, J. R. (1959). Spin-wave resonance in a ferromagnetic metal. *Journal of Physics and Chemistry of Solids*, 11:315–333.

[95] Reddy, J. N. (2013). *An Introduction to Continuum Mechanics*. Cambridge University Pressr.

[96] Rigneault, H., Lourtioz, J.-M. J.-M., Delalande, C., and Levenson, A. (2010). *Nanophotonics*. Wiley.

[97] Rychły, J. and Kłos, J. W. (2017). Spin wave surface states in 1D planar magnonic crystals. *Journal of Physics D: Applied Physics*, 50(16):164004.

[98] Rychły, J., Kłos, J. W., and Krawczyk, M. (2016). Spin wave damping in periodic and quasiperiodic magnonic structures. *Journal of Physics D: Applied Physics*, 49(17):175001.

[99] Rychły, J., Kłos, J. W., Mruczkiewicz, M., and Krawczyk, M. (2015). Spin waves in one-dimensional bicomponent magnonic quasicrystals. *Physical Review. B*, 92:054414.

[100] Rychły, J., Mieszczak, S., and Kłos, J. (2018). Spin waves in planar quasicrystal of Penrose tiling. *Journal of Magnetism and Magnetic Materials*, 450:18–23.

[101] Sadd, M. H. (2021). *Elasticity: theory, applications, and numerics*. Academic Press is an imprint of Elsevier.

[102] Sadovnikov, A. V., Davies, C. S., Kruglyak, V. V., Romanenko, D. V., Grishin, S. V., Beginin, E. N., Sharaevskii, Y. P., and Nikitov, S. A. (2017). Spin wave propagation in a uniformly biased curved magnonic waveguide. *Physical Review B*, 96:060401.

[103] Schultheiss, K., Verba, R., Wehrmann, F., Wagner, K., Körber, L., Hula, T., Hache, T., Kákay, A., Awad, A. A., Tiberkevich, V., Slavin, A. N., Fassbender, J., and Schultheiss, H. (2019). Excitation of whispering gallery magnons in a magnetic vortex. *Phys. Rev. Lett.*, 122:097202.

[104] Schwartz, T., Bartal, G., Fishman, S., and Segev, M. (2007). Transport and anderson localization in disordered two-dimensional photonic lattices. *Nature*, 446:52–55.

[105] Scroggs, M. W., Baratta, I. A., Richardson, C. N., and Wells, G. N. (2022). Basix: a runtime finite element basis evaluation library. *Journal of Open Source Software*, 7:3982.

[106] Segev, M., Silberberg, Y., and Christodoulides, D. N. (2013). Anderson localization of light. *Nature Photonics*, 7:197–214.

[107] Shechtman, D., Blech, I., Gratias, D., and Cahn, J. W. (1984). Metallic phase with long-range orientational order and no translational symmetry. *Physical Review Letters*, 53:1951–1953.

[108] Sheka, D. D. (2021). A perspective on curvilinear magnetism. *Applied Physics Letters*, 118(23):230502.

[109] Shockley, W. (1939). On the surface states associated with a periodic potential. *Physical Review*, 56:317–323.

[110] Sokolovskyy, M. L. and Krawczyk, M. (2011). The magnetostatic modes in planar one-dimensional magnonic crystals with nanoscale sizes. *Journal of Nanoparticle Research*, 13(11):6085–6091.

[111] Stancil, D. D. and Prabhakar, A. (2009). *Spin Waves Theory and Applications*. Springer.

[112] Stigloher, J., Decker, M., Körner, H. S., Tanabe, K., Moriyama, T., Taniguchi, T., Hata, H., Madami, M., Gubbiotti, G., Kobayashi, K., Ono, T., and Back, C. H. (2016). Snell's law for spin waves. *Physical Review Letters*, 117:037204.

[113] Sykes, C. G., Adam, J. D., and Collins, J. H. (1976). Magnetostatic wave propagation in a periodic structure. *Applied Physics Letters*, 29(6):388–391.

[114] Tacchi, S., Duerr, G., Klos, J. W., Madami, M., Neusser, S., Gubbiotti, G., Carlotti, G., Krawczyk, M., and Grundler, D. (2012). Forbidden band gaps in the spin-wave spectrum of a two-dimensional bicomponent magnonic crystal. *Physical Review Letters*, 109:137202.

[115] Tacchi, S., Gruszecki, P., Madami, M., Carlotti, G., Kłos, J. W., Krawczyk, M., Adeyeye, A., and Gubbiotti, G. (2015). Universal dependence of the spin wave band structure on the geometrical characteristics of two-dimensional magnonic crystals. *Scientific Reports*, 5(1):10367.

[116] Tacchi, S., Montoncello, F., Madami, M., Gubbiotti, G., Carlotti, G., Giovannini, L., Zivieri, R., Nizzoli, F., Jain, S., Adeyeye, A. O., and Singh, N. (2011). Band diagram of spin waves in a two-dimensional magnonic crystal. *Physical Review Letters*, 107:127204.

[117] Tamm, I. (1932). On the possible bound states of electrons on a crystal surface. *Physikalische Zeitschrift der Sowjetunion*, 1:733.

[118] Thomas, S., Katrin, S., Björn, O., Burkard, H., and Helmut, S. (2015). Micro-focused Brillouin light scattering: Imaging spin waves at the nanoscale. *Frontiers in Physics*, 3:35.

[119] Ulrichs, H., Lenk, B., and Münzenberg, M. (2010). Magnonic spin-wave modes in cofeb antidot lattices. *Applied Physics Letters*, 97:92506.

[120] Vaňatka, M., Szulc, K., Wojewoda, O. c. v., Dubs, C., Chumak, A. V., Krawczyk, M., Dobrovolskiy, O. V., Kłos, J. W., and Urbánek, M. (2021). Spin-wave dispersion measurement by variable-gap propagating spin-wave spectroscopy. *Physical Review Applied*, 16:054033.

[121] Vansteenkiste, A., Leliaert, J., Dvornik, M., Helsen, M., Garcia-Sanchez, F., and Van Waeyenberge, B. (2014). The design and verification of mumax3. *AIP Advances*, 4(10):107133.

[122] Vardeny, Z. V., Nahata, A., and Agrawal, A. (2013). Optics of photonic quasicrystals. *Nature Photonics*, 7(3):177–187.

[123] Vasseur, J. O., Dobrzynski, L., Djafari-Rouhani, B., and Puszkarski, H. (1996). Magnon band structure of periodic composites. *Physical Review B*, 54:1043–1049.

[124] Wagner, K., Kákay, A., Schultheiss, K., Henschke, A., Sebastian, T., and Schultheiss, H. (2016). Magnetic domain walls as reconfigurable spin-wave nanochannels. *Nature Nanotechnology*, 11(5):432–436.

[125] Walker, A. D. M., McKenzie, J. F., and Budden, K. G. (1985). Properties of electromagnetic waves in ferrites. *Proceedings of the Royal Society of London. A. Mathematical and Physical Sciences*, 399(1817):217–241.

[126] Wang, Q., Chumak, A. V., and Pirro, P. (2021). Inverse-design magnonic devices. *Nature Communications*, 12:1–9.

[127] Wang, Q., Heinz, B., Verba, R., Kewenig, M., Pirro, P., Schneider, M., Meyer, T., Lägel, B., Dubs, C., Brächer, T., and Chumak, A. V. (2019). Spin pinning and spin-wave dispersion in nanoscopic ferromagnetic waveguides. *Physical Review Letters*, 122:247202.

[128] Wawro, A., Kurant, Z., Jakubowski, M., Tekielak, M., Pietruczik, A., Böttger, R., and Maziewski, A. (2018). Magnetic properties of coupled co/mo/co structures tailored by ion irradiation. *Physical Review Applied*, 9:14029.

[129] Weiler, M., Dreher, L., Heeg, C., Huebl, H., Gross, R., Brandt, M. S., and Goennenwein, S. T. B. (2011). Elastically driven ferromagnetic resonance in nickel thin films. *Physical Review Letters*, 106:117601.

[130] Wolny, J. and R., S. (2016). Phononic and phasonic debye–waller factors for 1D quasicrystals. *Acta Physica Polonica A*, 130(4):836–840.

[131] Xu, M., Yamamoto, K., Puebla, J., Baumgaertl, K., Rana, B., Miura, K., Takahashi, H., Grundler, D., Maekawa, S., and Otani, Y. (2020). Nonreciprocal surface acoustic wave propagation via magneto-rotation coupling. *Science Advances*, 6.

[132] Yablonovitch, E. (1987). Inhibited spontaneous emission in solid-state physics and electronics. *Physical Review Letters*, 58:2059–2062.

[133] Yu, H., Duerr, G., Huber, R., Bahr, M., Schwarze, T., Brandl, F., and Grundler, D. (2013). Omnidirectional spin-wave nanograting coupler. *Nature Communications*, 4:2702.

[134] Yu, H., Xiao, J., and Schultheiss, H. (2021). Magnetic texture based magnonics. *Physics Reports*, 905:1–59. Magnetic texture based magnonics.

[135] Yuan, H., Cao, Y., Kamra, A., Duine, R. A., and Yan, P. (2022). Quantum magnonics: When magnon spintronics meets quantum information science. *Physics Reports*, 965:1–74. Quantum magnonics: When magnon spintronics meets quantum information science.

[136] Zak, J. (1982). Band center—a conserved quantity in solids. *Physical Review Letters*, 48:359–362.

[137] Zak, J. (1985). Symmetry criterion for surface states in solids. *Physical Review B*, 32:2218–2226.

[138] Zak, J. (1989). Berry's phase for energy bands in solids. *Physical Review Letters*, 62:2747–2750.

[139] Zhang, V. L., Lim, H. S., Ng, S. C., Kuok, M. H., Zhou, X., and Adeyeye, A. O. (2016). Spin-wave dispersion of nanostructured magnonic crystals with periodic defects. *AIP Advances*, 6:115106.

Appendix A

List of publications

Publications included in the dissertation:

- **P1**: C. L. Chang, <u>S. Mieszczak</u>, M. Zelent, V. Besse, U. Martens, R. R. Tamming, J. Janusonis, P. Graczyk, M. Münzenberg, J. W. Kłos, and R. I. Tobey, *Driving Magnetization Dynamics in an On-Demand Magnonic Crystal via the Magnetoelastic Interactions*, Physical Review Applied, **10**, 064051 (2018),

- **P2**: <u>S. Mieszczak</u>, O. Busel, P. Gruszecki, A. N. Kuchko, J. W. Kłos, and M. Krawczyk, *Anomalous Refraction of Spin Waves as a Way to Guide Signals in Curved Magnonic Multimode Waveguides*, Physical Review Applied, **13**, 054038 (2020),

- **P3**: <u>S. Mieszczak</u>, and J. W. Kłos, *Interface modes in planar one-dimensional magnonic crystals*, Scientific Reports, **12**, 11335 (2022),

- **P4**: <u>S. Mieszczak</u>, M. Krawczyk, and J W. Kłos, *Spin-wave localization on phasonic defects in a one-dimensional magnonic quasicrystal*, Physical Review B, **106**, 064430 (2022).

Publications not included in the dissertation:

- S. Pan, J. W Kłos, <u>S. Mieszczak</u>, A. Barman and M. Krawczyk, *Spin waves in periodic antidot waveguide of complex base*, Journal of Physics D: Applied Physics **50**, 275003 (2017),

- J. Rychły, <u>S. Mieszczak</u>, J. W. Kłos, *Spin waves in planar quasicrystal of Penrose tiling*, Journal of Magnetism and Magnetic Materials, **450**, 18-23 (2017),

- N. K. P. Babu, A. Trzaskowska, P. Graczyk, G. Centała, <u>S. Mieszczak</u>, H. Głowiński, M. Zdunek, S. Mielcarek, and J. W. Kłos, *The Interaction between Surface Acoustic Waves and Spin Waves: The Role of Anisotropy and Spatial Profiles of the Modes*, Nano Letters, **21**, 946-951 (2021),

- J. W. Kłos, I. L. Lyubchanskii, M. Krawczyk, P. Gruszecki, <u>S. Mieszczak</u>, J. Rychły, Y. S. Dadoenkova, and N. N. Dadoenkova, Chapter: *Magnonics and Confinement of Light in Photonic–Magnonic Crystals*, in *Optomagnonic Structures: Novel Architectures for Simultaneous Control of Light and Spin Waves*, Editor: E. Almpanis, World Scientific 2021

- A. V. Chumak, P. Kabos, M. Wu, C. Abert, C. Adelmann, A. O. Adeyeye, J. Akerman, F. G. Aliev, A. Anane, A. Awad, C. H. Back, A. Barman, G. E. W. Bauer, M. Becherer, E. N. Beginin, V. A. S. V. Bittencourt, Y. M. Blanter, P. Bortolotti, I. Boventer, D. A. Bozhko, S. A. Bunyaev, J. J. Carmiggelt, R. R. Cheenikundil, F. Ciubotaru, S. Cotofana, G. Csaba, O. V. Dobrovolskiy, C. Dubs, M. Elyasi, K. G. Fripp, H. Fulara, I. A. Golovchanskiy, C. Gonzalez-Ballestero, P. Graczyk, D. Grundler, P. Gruszecki, G. Gubbiotti, K. Guslienko, A. Haldar, S. Hamdioui, R. Hertel, B. Hillebrands, T. Hioki, A. Houshang, C. -M. Hu, H. Huebl, M. Huth, E. Iacocca, M. B. Jungfleisch, G. N. Kakazei, A. Khitun, R. Khymyn, T. Kikkawa, M. Kloui, O. Klein, J. W. Kłos, S. Knauer, S. Koraltan, M. Kostylev, M. Krawczyk, I. N. Krivorotov, V. V. Kruglyak, D. Lachance-Quirion, S. Ladak, R. Lebrun, Y. Li, M. Lindner, R. Macedo, S. Mayr, G. A. Melkov, <u>S. Mieszczak</u>, Y. Nakamura, H. T. Nembach, A. A. Nikitin, S. A. Nikitov, V. Novosad, J. A. Otalora, Y. Otani, A. Papp, B. Pigeau, P. Pirro, W. Porod, F. Porrati, H. Qin, B. Rana, T. Reimann, F. Riente, O. Romero-Isart, A. Ross, A. V. Sadovnikov, A. R. Safin, E. Saitoh, G. Schmidt, H. Schultheiss, K. Schultheiss, A. A. Serga, S. Sharma, J. M. Shaw, D. Suess, O. Surzhenko, K. Szulc, T. Taniguchi, M. Urbanek, K. Usami, A. B. Ustinov, T. van der Sar, S. van Dijken, V. I. Vasyuchka, R. Verba, V. S. Kusminskiy, Q. Wang, M. Weides, M. Weiler, S. Wintz, S. P. Wolski, X. Zhang, *Advances in Magnetics Roadmap on Spin-Wave Computing*, IEEE Transactions on Magnetics **58**, 1-72 (2022).

Appendix B

Statements about the contributions to the publication

For the publications P2-P4, I attach the statements of all co-authors specifying her/his individual contribution to the work with the declaration that she/he is aware that the publication will be included in my doctoral thesis.

For the publication P1, which has eleven co-authors, I have attached the statements of five co-authors, i.e., all co-authors for Adam Mickiewicz University and the leaders of the groups from the University of Groningen and from the University of Greifswald.

My contribution to the publications P1-P4 is described in Chapter 4, in the commentaries preceding each publication.

1. Statement about the contribution to the publication

I hereby declare that I am aware that the work:
Driving Magnetization Dynamics in an On-Demand Magnonic Crystal via the Magnetoelastic Interactions, Physical Review Applied, **10**, 064051 (2018), C. L. Chang, S. Mieszczak, M. Zelent, V. Besse, U. Martens, R.R. Tamming, J. Janusonis, P. Graczyk, M. Münzenberg, J.W. Kłos, and R. I. Tobey, of which I am a co-author, has been included in the doctoral thesis of Szymon Mieszczak. I contributed to the work by leading the experimental team that acquired the data at the University of Groningen, in The Netherlands. We subsequently collated the data and initiated fruitful discussions with the team from Poznan. Together with Szymon and team we wrote the manuscript detailed above.

Raanan Tobey

Sept 16, 2022

UNIVERSITÄT GREIFSWALD
Wissen lockt. Seit 1456

Universität Greifswald, Institut für Physik, Felix-Hausdorff-Str. 6, 17489 Greifswald

Mathematisch
Naturwissenschaftliche
Fakultät

Institut für Physik
Prof. Dr. Markus Münzenberg

Telefon: +49 3834 420 4780
markus.muenzenberg@uni-greifswald.de

Greifswald 19. September 2022

Statement about the contribution to the publication

I hereby declare that I am aware that the work:

Driving Magnetization Dynamics in an On-Demand Magnonic Crystal via the Magnetoelastic Interactions, Physical Review Applied, **10**, 064051 (2020), C. L. Chang, S. Mieszczak, M. Zelent, V. Besse, U. Martens, R.R. Tamming, J. Janusonis, P. Graczyk, M. Münzenberg, J.W. Kłos, and R. I. Tobey, of which I am a co-author, has been included in the doctoral thesis of Szymon Mieszczak.
I contributed to the work by: discussed and approved the final version of the manuscript.

Greifswald 19. September 2022

(Prof. Dr. Markus Münzenberg)

Statement about the contribution to the publication

I hereby declare that I am aware that the work:

Driving Magnetization Dynamics in an On-Demand Magnonic Crystal via the Magnetoelastic Interactions, Physical Review Applied, **10**, 064051 (2020),
C. L. Chang, S. Mieszczak, M. Zelent, V. Besse, U. Martens, R.R. Tamming, J. Janusonis, P. Graczyk, M. Münzenberg, J.W. Kłos, and R. I. Tobey, of which I am a co-author, has been included in the doctoral thesis of Szymon Mieszczak. I contributed to the work by performing few micromagnetic simulations.

09.09.2022

Zelent

Mateusz Zelent
(date and signature)

Statement about the contribution to the publication

I hereby declare that I am aware that the work:

Driving Magnetization Dynamics in an On-Demand Magnonic Crystal via the Magnetoelastic Interactions, Physical Review Applied, **10**, 064051 (2018), C. L. Chang, S. Mieszczak, M. Zelent, V. Besse, U. Martens, R.R. Tamming, J. Janusonis, P. Graczyk, M. Münzenberg, J.W. Kłos, and R. I. Tobey,

of which I am a co-author, has been included in the doctoral thesis of Szymon Mieszczak.

I contributed to the work by: problem and solution analysis (simulation), result discussion, edited subsequent drafts of the manuscript and approved the final version of the manuscript.

Piotr Graczyk
(date and signature)

15.09.2022

Piotr Graczyk

Statement about the contribution to the publication

I hereby declare that I am aware that the work:

Driving Magnetization Dynamics in an On-Demand Magnonic Crystal via the Magnetoelastic Interactions, Physical Review Applied, **10**, 064051 (2018), C. L. Chang, S. Mieszczak, M. Zelent, V. Besse, U. Martens, R.R. Tamming, J. Janusonis, P. Graczyk, M. Münzenberg, J.W. Kłos, and R. I. Tobey,

of which I am a co-author, has been included in the doctoral thesis of Szymon Mieszczak.

I contributed to the work by: participation in designing the theoretical and numerical studies, writing parts of the first draft and editing subsequent drafts of the manuscript.

Jarosław W. Kłos
(date and signature)

Statement about the contribution to the publication
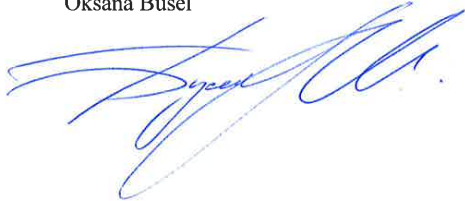
I hereby declare that I am aware that the work:
Anomalous Refraction of Spin Waves as a Way to Guide Signals in Curved Magnonic Multimode Waveguides, Physical Review Applied, **13**, 054038 (2020),
Szymon Mieszczak, Oksana Busel, Paweł Gruszecki, Andriy N. Kuchko, Jarosław W. Kłos, and Maciej Krawczyk
of which I am a co-author, has been included in the doctoral thesis of Szymon Mieszczak.
I contributed to the work by developing the analytical model of spin wave transmission through the barrier. I participated in the preparation of the plots and writing the manuscript.

Oksana Busel

9.16.2022

Statement about the contribution to the publication

I hereby declare that I am aware that the work:

Anomalous Refraction of Spin Waves as a Way to Guide Signals in Curved Magnonic Multimode Waveguides, Physical Review Applied, **13**, 054038 (2020),

Szymon Mieszczak, Oksana Busel, Paweł Gruszecki, Andriy N. Kuchko, Jarosław W. Kłos, and Maciej Krawczyk

of which I am a co-author, has been included in the doctoral thesis of Szymon Mieszczak.

I contributed to the work by taking part in the analyzing of anomalous refraction of spin waves and designing of the graded index slab. I participated in the preparation of the plots and writing the manuscript.

15.09.2022, Paweł Gruszecki
Paweł Gruszecki

Statement about the contribution to the publication

I hereby declare that I am aware that the work:

Anomalous Refraction of Spin Waves as a Way to Guide Signals in Curved Magnonic Multimode Waveguides, Physical Review Applied, **13**, 054038 (2020),

Szymon Mieszczak, Oksana Busel, Paweł Gruszecki, Andriy N. Kuchko, Jarosław W. Kłos, and Maciej Krawczyk

of which I am a co-author, has been included in the doctoral thesis of Szymon Mieszczak.

I contributed to the work by: participation in designing the theoretical and numerical studies, editing subsequent drafts of the manuscript.

Jarosław W. Kłos
(date and signature)

Statement about the contribution to the publication

I hereby declare that I am aware that the work:
Anomalous Refraction of Spin Waves as a Way to Guide Signals in Curved Magnonic Multimode Waveguides, Physical Review Applied, **13**, 054038 (2020),
Szymon Mieszczak, Oksana Busel, Paweł Gruszecki, Andriy N. Kuchko, Jarosław W. Kłos, and Maciej Krawczyk
of which I am a co-author, has been included in the doctoral thesis of Szymon Mieszczak.

I contributed to the work by discussing concept of the study and editing the draft of the manuscript.

19.09.2022   Maciej Krawczyk

Statement about the contribution to the publication

I hereby declare that I am aware that the work:
Interface modes in planar one-dimensional magnonic crystals, Scientific Reports, **12**, 11335 (2022),
Szymon Mieszczak, and Jarosław W. Kłos,
of which I am a co-author, has been included in the doctoral thesis of Szymon Mieszczak.
I contributed to the work by: (study design, performing the theoretical studies for Sections 1 and 2 of Supplementary Information, writing the parts first draft and editing subsequent drafts of the manuscript.

Jarosław W. Kłos
(date and signature)

Statement about the contribution to the publication

I hereby declare that I am aware that the work:
Spin-wave localization on phasonic defects in a one-dimensional magnonic quasicrystal, Physical Review B, **106**, 064430 (2022),
Szymon Mieszczak, Maciej Krawczyk, and Jarosław W. Kłos,
of which I am a co-author, has been included in the doctoral thesis of Szymon Mieszczak.
I contributed to the work by: participation in study design, writing the parts of the first draft and editing subsequent drafts of the manuscript.

Jarosław W. Kłos
(date and signature)

Statement about the contribution to the publication

I hereby declare that I am aware that the work:
Spin-wave localization on phasonic defects in a one-dimensional magnonic quasicrystal, Physical Review B, **106**, 064430 (2022),
Szymon Mieszczak, Maciej Krawczyk, and Jarosław W. Kłos,
of which I am a co-author, has been included in the doctoral thesis of Szymon Mieszczak.

I contributed to the work by discussing concept of the study and editing the draft of the manuscript.

19.09.2022   Maciej Krawczyk